Tapan K. Sengupta
Thierry Poinsot
Editors

International Centre for Mechanical Sciences

Instabilities of Flows: with and without Heat Transfer and Chemical Reaction

CISM Courses and Lectures, vol. 517

SpringerWienNewYork

SpringerWienNewYork

CISM COURSES AND LECTURES

The series presents lecture notes, monographs, edited works and proceedings in the field of Mechanics, Engineering, Computer Science and Applied Mathematics.
Purpose of the series is to make known in the international scientific and technical community results obtained in some of the activities organized by CISM, the International Centre for Mechanical Sciences.

INTERNATIONAL CENTRE FOR MECHANICAL SCIENCES

COURSES AND LECTURES - No. 517

INSTABILITIES OF FLOWS: WITH AND WITHOUT HEAT TRANSFER AND CHEMICAL REACTION

EDITED BY

TAPAN K. SENGUPTA
HIGH PERFORMANCE COMPUTING LABORATORY,
DEPT. OF AEROSPACE ENGG.
IIT KANPUR 208 016, INDIA

THIERRY POINSOT
CNRS/INST. DE MECANIQUE DES FLUIDES DE TOULOUSE,
TOULOUSE, FRANCE

SpringerWienNewYork

This volume contains 133 illustrations

Printed in Italy
SPIN 12822072

All contributions have been typeset by the authors.

ISBN 978-3-7091-0126-1 SpringerWienNewYork

Prefaces

This monograph is an outcome of the summer school organized on behalf of CISM in June 2008, for the advanced course titled "Instabilities of Flows with and without Heat Transfer and Chemical Reactions". The course was conducted over five days of a working week in the beautiful and peaceful surrounding of Udine with an *ashram*-like atmosphere and the course was held quite intensively, with active participation of the lecturers and all the participants, including one of the rectors of the institute.

The scope of the course was vast and the lectures turned out to be reflections of the expertise of the lecturers. The material covered in the course ranged from classical hydrodynamic instability (although taught from asymptotic theory perspective) to newer areas of interests and finally to the complex field of flow instability involving heat transfer and chemical reactions. While significant progresses have been made over the last century and half in understanding the field of instability, the motivation still remains that is given by the aphorism: *the flow that occurs in nature must not only follow the equations of fluid dynamics, but also be stable* (Landau & Lifshitz, 1959).

Currently there are more than one monographs and textbooks available that deals with the basic subject of instability and a question arises naturally, if there is a need for another monograph. Before proposing the course, I discussed this aspect with Prof. Schneider who actually encouraged us to propose what we ended up doing: To teach a course on the subject of our expertise that will have minimal overlap with available materials, at the same time to remain relevant to the needs of the participants. The enthusiasm of the participants in the summer school convinced us that the goal was met by and large. That also encourages us to go ahead and put those materials in one place in this monograph those happen to be the research interests of the contributing authors. In presenting this monograph, as the editor, I realise that if a scholar has nothing new to say, then he should keep quiet. I fully realise that some of the materials presented in the manuscript is alternative ways for the quest for truth and if they provoke the readers to think differently, then the purpose for the monograph will be more than met. The monograph essentially is in two parts, as contributed by the two authors. The first part is a synthesis of classical material mixed with emerging areas of research, but dealt with in a completely different manner than that is found in other books and monographs. The second part is also a mixture of classical physical ideas as applied to a very complex engineering problem, addressed by computational means.

Instability and transition have a track of torturous development, im-

mediately following the successful explanation of inviscid mechanisms by Kelvin, Helmholtz and Rayleigh- who assumed that viscous action can only be stabilizing. The subject of instability suffered from this misconception for quite a long time. Notable researchers who were victims of indifference by proposing alternate ideas were many, including Heisenberg. His fate was followed by the researchers belonging to the German school led by Prandtl. When this was eventually circumvented in 1940's with viscous instability theory accepted as an established area of research, it was found to be moderately good enough for many more decades to come. But then *a thing moderately good is not so good as it ought to be (Tom Paine).*

The overbearing successes of linear instability theory impeded development in other important areas of (i) receptivity and (ii) many other mechanisms of transition, e.g. bypass transition and spatio-temporal growth of disturbances seen in flows where linear theories apply. In chapter 2, we have dealt with a unified description of instability and receptivity- which has not been dealt systematically before. This should be considered a first for this monograph.

Technological advances in aerospace industry were achieved by the linear instability theory, whose sole criterion of existence of Tollmien-Schlichting waves as disturbances have dominated the post-world war II research in this area. Any routes of transition other than that by TS waves were christened as bypass transition by Morkovin in late 1950. It meant many things to many researchers and the resultant lack of focus seems to pervade the field even today. We have tried to state the case of one mechanism of bypass transition systematically in chapter 3 from the first principle. In developing this area, we have also revived the energy-based stability and receptivity concept from a completely new interpretation of mechanical energy, and not relying on kinetic energy alone. The classical energy-based stability theory based on only kinetic energy is known to be deficient! This has been rectified in recent times and the appearance of a new energy based theory is given in chapter 3 and 4.

The other canonical flow geometry considered in the first part consists of bluff-body flow instability dealt in chapter 5. This introduces the flow past a cylinder that actually suffers linear temporal instability moderated by nonlinear stabilization. This flow is different from that is discussed primarily in chapters 2 to 4, where the linear instability is via spatial growth. Also, for such flows nonlinearity leads to further destabilization, whereas for the flow past a cylinder, the nonlinearity stabilizes the linear instability and takes the flow to another equilibrium flow. In chapter 6, the effects of heat transfer via the restrictive condition of Boussinesq approximation for the canonical flow past flat plates is studied. This problem has been solved

by the robust compound matrix method (CMM), revealing newer insight. Advancing CMM as a method for solving stiff differential equations arising in instability problem is also a significant new addition to the subject, as given in this monograph.

In a complete departure to the first six chapters, the last four chapters show the practical method of studying flows involving combustion. Such flows and their instability at the present time are solved numerically and this approach is followed in these chapters. Nonetheless, the author pays particular attention to subtle issues of wave propagation in reacting flows and their special simulation techniques. The author particularly emphasizes on studying multiphase flows in combustion chambers by newer innovative numerical techniques. Not content with just simulating such flows numerically by LES, the author also investigates numerical instabilities in such simulation by often neglected round-off error. This is a significant addition to the subject area to deal with complex flows numerically and should help practising scientists and engineers involved in research on the topic of combustion and its instability.

TK Sengupta wants to acknowledge the help provided by V.K. Suman, Neelu Singh, Y. Bhumkar, S. Bhaumik and Kamal K. Mishra for help with preparation of the manuscript.

Tapan K. Sengupta
Department of Aerospace Engineering
Indian Institute of Technology Kanpur

The theory of instability of fluid flows is one of the oldest branches of fluid mechanics. Results that are considered as fundamental even at present days were already obtained in the 19th century, and the names of eminent scientists like Helmholtz, Kelvin, Rayleigh and Reynolds are associated with those early results. Remarkably, instabilities of fluid flows have not lost their appeal to the fluid mechanics community up to this day. Those colleagues who are fond of great challenges might consider the subject so fascinating because it is so difficult, but there are other reasons that may be of relevance, e.g. the importance of flow instabilities in many applications, including many branches of engineering. After all, steady-state solutions of the equations of motion, whether they might have been obtained analytically as so-called exact solutions, or numerically by means of CFD, will be observed in the real world only if they are stable.

Those, among others, were the reasons why the Scientific Council of CISM unanimously accepted Professor Sengupta's proposal for an Advanced Course entitled "Instabilities of Flows with and without Heat Transfer and Chemical Reactions". For the favourable decision of the Scientific Council it was also essential that Professor Sengupta himself, an authority in the field, was available for organizing the course, which included the important task of proposing eminent, internationally recognized scientist as lecturers.

The course organized, and directed, by Professor Sengupta was a great success, not only in terms of the number of participants, but also from a scientific point of view. I myself had the privilege of representing CISM at the course. I attended presentations of all lecturers, and it was a pleasure to see the participants—of various levels of professional experience—follow the lectures with great interest, themselves also making useful contributions in the discussions. I should like to add that, like the participants, I also learned a lot from the lectures that were both instructive and stimulating.

The Rectors Committee, which comprises the rectors, the former rectors, the secretary general and the vice secretary general of CISM, has always been in favour of publishing the lecture notes of each course in the Springer book series "CISM Courses and Lectures", with the course organizer(s) acting as editor(s). Thus the lecturers, including the organizer, are usually asked to submit manuscripts that are suitable for publication in the series, accounting for the results of the discussions during the course, if appropriate. However, not always agree all lecturers to have their course notes published. The present case is a particular one. Despite great efforts by Professor Sengupta as the editor, only two, out of a total of five, lecturers - including the editor himself - were willing, and able, to submit manuscripts in due time. The result, however, is nothing less than an excellent contribution to the CISM book series. Professor Sengupta's article has, in fact, developed into a monograph on the subject of his lectures, and Dr. Poinsot has also nicely refined the interesting material he had presented during the course. Hence I should like to express my sincere gratitude to both authors for their valuable contributions. I have no doubts that the present book will be accepted most favourably by the scientific community - colleagues and students alike.

Wilhelm Schneider
Vienna University of Technology
Former Rector of CISM

Contents

Chapter 1

GENERAL INTRODUCTION ON INSTABILITY AND TRANSITION

Prof. Tapan K. Sengupta
HPCL, Aerospace Engineering
I.I.T. Kanpur

1.1 Introduction

This monograph is an idiosyncratic look at the topics of research interests of the contributing authors ranging from (i) classical linear hydrodynamic instability in chapter 1; on (ii) receptivity (chapter 2); (iii) other topics of current interest on bypass transition (chapter 3) and spatio-temporal instability (chapter 4); (iv) bifurcation and nonlinear stabilization in a bluff-body flow (chapter 5) and (vi) qualitative changes in flow instability due to restricted heat transfer (chapter 6). These topics are admixtures of linear and nonlinear aspects of flow instabilities studied via analytical and computational routes. Even though in chapters 2 to 5, theoretical results are supplemented by computational results obtained by specifically developed high accuracy direct numerical simulation (DNS) techniques, in chapters 7 to 11 attention is focused on computational results obtained for combustors and combustion processes in engineering- a very specialized topic of current interest. This requires understanding complex, reacting, multiphase flows and their computations by large eddy simulation (LES). For this purpose, special attention is devoted in understanding waves in reacting flows and the role of computing errors in LES. However, over-riding all these special aspects, one needs to understand the concepts of basic fluid mechanics and fundamental principles of receptivity and instability.

Thus, the summer school at CISM in June 2008 and the present monograph grew out of a desire of the contributing authors to add those areas essential to the understanding of core materials, emphasizing those areas which have not been covered earlier. This is with a hope that this would

form a timely addition to the subject across a large range of studies in flow instabilities and its dependence on heat transfer and chemical reactions.

Fluid dynamics continues to be the crucible of studies for continuum mechanics. The subject as a whole straddles fields involving many areas of engineering applications and to basic principles of instability of dynamical systems. It was not before 1687 (the year of publication of *The Principia* by Isaac Newton), the equations of motion was first written down for mechanical systems. The first proper mathematical modeling of what is now called the inviscid flow was first published by Euler in 1752. Understanding of fluid flow by empirical models during and before this period was so unsatisfactory that Robins (1746) noted that *all the theories of resistance hitherto established are extremely defective, and that it is only by experiments analogous to those here recited that this important subject can ever be completed.* It was in 1840 that the equation of fluid motion in the presence of friction –the Navier-Stokes equation - was published. The sanctity and correctness of this equation is now well-accepted in the continuum regime of fluid flow. Apart from the fact that correct governing equations are needed, one has also to ensure that correct boundary and initial conditions are used in the solution process. In this context, investigations on the validity of no-slip boundary condition have been revisited many a times. One must note that this boundary condition is a modeling approximation and has never been proven rigorously. Batchelor (1988) has therefore noted for Newtonian fluid flow that *the absence of slip at a rigid wall is now amply confirmed by direct observation and by the correctness of its many consequences under normal conditions.* There are now some exceptions to this boundary condition for low density and in micro- to nano-scale flows, that has been interestingly attributed to electrokinetic effects or flow instabilities by Tropea *et al.* (2007). Despite this, by and large we will not question the correctness of no-slip condition for continuum flows. Issues of flow instabilities and their resolution has occurred side by side with the development of the subject of fluid mechanics itself. We therefore begin with some general observations on fluid mechanics and its relation to studies of flow instabilities.

After Navier- Stokes equation has been written down in the first half of nineteenth century, few exact solutions were obtained for few fluid flows. In one such case, Stokes compared theoretical prediction with available experimental data for pipe flow and found no agreement whatsoever. Now we know that the theoretical solution of Stokes corresponded to undisturbed laminar flow, while the experimental data given to him corresponded to a turbulent flow. This problem was seized upon by Osborne Reynolds, who explained the reason for such mismatches by his famous pipe flow experiments (Reynolds, 1883). It was shown that the basic flow obtained as a

legitimate solution of the governing Navier- Stokes equation is unable to maintain its stability with respect to omnipresent small disturbances in the flow. Mere mathematical existence of a solution does not always guarantee its physical realization and observation. Existence of a mathematical solution shows a possibility of a solution (that we will refer as the equilibrium solution), as it embodies satisfaction of conservation laws satisfying force, moment and energy balance . However, additionally one needs to study the stability of each and every such solutions to ascertain their observability. Reynolds demonstrated experimentally the equilibrium parabolic profile disintegrating into sinuous motion of water in the pipe that eventually led to random or turbulent flow.

In view of the above, very aptly the following is noted in Landau & Lifshitz (1959) that *the flow that occurs in nature must not only follow the equations of fluid dynamics, but also be stable*. This observation is central to many physical phenomena- where *observability* of solution is of fundamental importance. If solutions are not *observable*, then the corresponding equilibrium flows are not *stable*. Here, implication of flow *instability* is in the context of continuous deviation of the instantaneous solution from the equilibrium solution caused by growth of infinitesimally small perturbations present in the surroundings of the system. It is this sensitive dependence on, often unquantifiable, disturbance environment that makes the subject of instability very challenging. At the same time, smallness of the background disturbances allows one to study the problem of growth of these from a small perturbation approach. This greatly helps, if the governing nonlinear equations can be solved for the equilibrium solution with ease and then its stability can be studied by linearizing the governing equation for the perturbation field. In the present monograph this is amply demonstrated in chapters 1-4 in studying linear instability.

To understand better the issues affecting flow instability, certain features of the dye-experiments performed by Reynolds (1883) is worth recounting- which is perhaps the first recorded thorough experimental observations on the phenomenon of flow instability. Reynolds in his experiments, took pipes of different diameters fitted with a trumpet shaped mouth-piece or bell-mouth. The mouth-piece accelerates the flow locally, creating a favorable pressure gradient that has the propensity of attenuating background disturbances, as we will explain in chapter 2. It is also for the reason to reduce disturbances, experiments were performed by Reynolds during mid-night to avoid noise from daytime vehicular traffic. Reynolds also observed that the rapid diffusion of dye with surrounding fluid depends on the non-dimensional parameter, Va/ν with V as the center-line velocity in the pipe whose diameter is a and ν is the kinematic viscosity. This ubiquitous

non-dimensional parameter is now called the Reynolds number (Re) to underscore the singular importance of this now-famous pipe flow experiment. Reynolds found that the flow can be kept orderly or laminar up to Re = 12,830. He noted that this value is very sensitive to the disturbances in the flow before it enters the tube. Thus, he noted quite prophetically that *this at once suggested the idea that the condition might be one of instability for disturbance of a certain magnitude and stable for smaller disturbances.* The relationship of instability with disturbance amplitude is a typical attribute of non-linear instability. It is now well established that pipe and plane Couette flows are linearly stable for all Reynolds numbers, when the usual linear stability analysis is performed. This therefore suggests that either non-linear and/ or different unknown linear mechanism(s) of instabilities are at play for these flows.

Later, the critical Re was further raised for pipe flows, establishing that there is perhaps no upper limit above which transition to turbulence can not be prevented. This example also suggests the importance of receptivity of flow to different types of input disturbances to the system. If there is no input to a fluid dynamical system of a particular kind that triggers instability, then the response will demonstrate the flow to be orderly, even if the fluid dynamical system is unstable to that kind of input. Thus, if the basic flow is receptive to a particular disturbance, then the equilibrium flow will not be observable in the presence of such disturbances.

Reynolds' experiment pointed out the instability as the main reason for the non-observability of basic flow, but it still did not clarify the steps following which one gets to the turbulent flow stage. Like every other subject, instability and transition also has gone through uneven progress from this pioneering experiment to its present state. We note that like many other fields, the associated scientific ideas, laws, and their discovery as narrated in textbooks on flow instabilities are mere distillation of complex multi-faceted, subtle and convoluted historical narrative. The initial impetus in any field itself could be due to missed starts, dead ends etc. and afterward it is invariably followed by mistakes, sophistries those are at times no more than self-fulfilling prophesies (aptly called the Pygmalion or Rosenthal effects in social sciences) and deceptions- that makes the whole journey a maze with errors appearing understandable, as an after-thought.

There have been significant contributions initially made by Helmholtz, Kelvin and Rayleigh (1880, 1887) using inviscid analysis. In their quest to justify their inviscid analysis, an assumption was made that viscous action due to its dissipative nature can be only stabilizing. Such was the impact of this observation that when Heisenberg (1924) submitted his dissertation solving perturbation equations including viscous terms for boundary layer

(under the guidance of Sommerfeld), the examination committee could find nothing wrong in the analysis, but found it difficult to accept that viscous action can add to instability. Of course, it makes perfect sense now, when one realizes that viscous action can cause a phase delay that can lead to positive feedback and hence destabilize the flow. Similar fate awaited the researchers from the Göttingen-school led by Prandtl (1935) in developing viscous linear stability theory that explained many aspects of the early stages of transition process involving formation and growth of waves, attributed to Tollmien and Schlichting. This theory is based on the key equation developed independently by Orr (1907) and Sommerfeld (1908) and is named after them. It took the pioneering experimental effort of Dryden and his associates in establishing viscous linear stability theory by detecting the so-called Tollmien-Schlichting waves through the famous vibrating ribbon experiments of Schubauer & Skramstad (1947).

Linear stability theory results match quite well with controlled laboratory experiment for thermal and centrifugal instabilities. But, instabilities dictated by shear force do not match so well, e.g. linear stability theory applied to plane Poiseuille flow gives a critical Reynolds number of 5772, while experimentally such flows have been observed to become turbulent even at Re = 1000- as shown in Davies and White (1928). Couette and pipe flows are also found to be linearly stable for all Reynolds numbers, the former was found to suffer transition in a computational exercise at $Re = 350$ (Lundbladh & Johansson, 1991) and the latter found to be unstable in experiments for $Re \geq 1950$. Interestingly, according to Trefethen *et al.* (1993) the other example for which linear analysis fails *include to a lesser degree, Blasius boundary layer flow.* This is the flow which many cite as the success story of linear stability theory.

Flow instability of attached boundary layers has been predicted with some success and the corresponding empirical transition prediction methodologies have matured to such an extent that they are now routinely used in aircraft industry. A flat plate placed in a stream with moderately low ambient disturbance level (turbulence intensity below 0.5%), flow transition takes place at a distance x from the leading edge given by,

$$Re_{tr} = \frac{U_\infty x}{\nu} = 3.5 \times 10^5 \quad to \quad 10^6$$

The onset of instability is predicted at $Re_{cr} = 519$ (based on displacement thickness as the length scale). It is important to realize that instability and transition are not synonymous. Actual process of transition begins with the onset of instability but the completion may depend upon multiple factors those form the basis for adjunct topics like secondary, tertiary and

nonlinear instabilities. Hence it is difficult to predict Re_{tr} as compared to Re_{cr}. In many external flows, the latter processes takes place over such a short streamwise distances, that the above mentioned empirical prediction methodologies neglect the distinction between the two.

It is also important to note that the linear stability theory studies a particular class of problems where the disturbances decay as one moves away in the wall-normal direction from one of the boundaries. Thus, the developed theory is mainly for disturbances that originate at the wall. The problem of destabilizing a shear layer by disturbances outside the shear layer has not received sufficient attention or adequately tackled in the past. This is also one of the major focus of this monograph, as we discuss it in chapter 2.

Despite many attempts made over more than a century, the exact route to turbulence is still far from clear. This prompted Morkovin (1991) to state: *"One hundred eight years after O. Reynolds demonstrated turbulence in a circular pipe, we still do not understand the nature of the irregular fluctuations at the wall nor the formation of larger coherent eddies convected downstream further from the wall. Neither can we describe the mechanisms of the instabilities that lead to the onset of turbulence in any given pipe nor the Reynolds number (between about 2000 and 100 000) at which it will take place. It is sobering to recall that Reynolds demonstrated this peculiar non-laminar behaviour of fluids before other physicists started on the road to relativity theory, quantum theory, nuclear energy, quarks etc"*. While some additional researches have clarified some key concepts, the situation about flow transition in a pipe remains the same.

The search for complete understanding on the origin and nature of turbulence continues- with the hope that the numerical solution of full Navier-Stokes equation without any modeling, as in DNS, may provide insight to it. Multitude of published DNS results in the literature suffers from a major drawback though, with most of them not requiring any explicit forcing of the flow via definitive and realistic input disturbance field. Most of these depend upon computational noises and /or "random noise". We wish to point out that unlike in mathematical closed-form solutions, numerical solution is always visited upon by *numerical noise* of the method and the hardware. Thus, the implicit assumption in DNS that these *numerical noise* sources will produce a *turbulent flow* and that is the same as the physical turbulent flow is a statement of hope and yet to be established rigorously. In fact, the contrary seems to be the case, as is shown in chapter 3 via DNS of bypass transition where a physical process is traced following explicit excitation. In contrast in chapters 7 to 11, computed LES solutions did not require any explicit specification or modeling of input disturbance or noise.

In studying stability of flows, it is convenient to pose the problem either as a temporal or as a spatial instability problem. While it is numerically expedient to take a temporal approach, many practical flows are known to follow spatial route. For example in lab experiments for external wall-bounded flows, it is noted that the disturbances grow in space as they travel downstream. This was established unambiguously through the experiments of Schubauer & Skramstad (1947) for flat plate boundary layer and is an excellent example of spatial instability problems. However, there are many flows where the instability grows both in space and time. These type of problems to identify whether the flow suffers temporal and/ or spatial instability arise in linear stability analysis. Flow instability studied following descriptions of two independent routes, is an artificial way of treating general instability problems.

1.2 What is Instability?

To analyze a physical problem analytically, we must obtain the governing equations that model the phenomenon adequately. Additionally, if the auxiliary equations pertaining to initial and boundary conditions are prescribed those are also well-posed, then conceptually getting the solution of the problem is straightforward. Mathematicians are justifiably always concerned with the *existence* and *uniqueness* of the solution. Yet not every solution of the equation of motion, even if it is exact, is observable in nature. This is at the core of many physical phenomena where *observability* of solution is of fundamental importance. If the solutions are not *observable*, then the corresponding basic flow is not *stable*. Here, the implication of *stability* is in the context of the solution with respect to infinitesimally small perturbations.

In studying the stability of problem with respect to ambient disturbances, it is hardly ever possible that one can incorporate all the contributing factors in a given physical scenario for posing a physical problem. Occasionally these neglected *causes* can be incorporated by *process noise* and results are made to correlate with the physical situation. This is possible when the *causes* are statistically independent and then it follows upon using Central Limit Theorem.

1.3 Temporal and Spatial Instability

Instability of an autonomous system is strictly for time-dependent systems that would display growth of disturbances in time. This may also mean that either we are studying the stability of a flow at a fixed spatial location or the full system displays identical variation in time for each

and every spatial locations. In reality, many fluid flows display a growth in space, or in time, or a complex spatio-temporal growth of disturbances. For disturbances that originate from a fixed location in space the disturbance grows, as it convects downstream. Thus, the disturbance is termed unstable, if it grows unbounded as it moves downstream. This is called the convective instability. This type of instability is seen in wall bounded shear layers, exemplified by the classic vibrating ribbon experiment of Schubauer & Skramstad (1947). This experiment was performed in a very quiet facility to create Tollmien- Schlichting (TS) waves by vibrating a ribbon inside a flat plate boundary layer. This experiment was the first one to show the existence of viscous unstable waves those were predicted earlier theoretically by Heisenberg (1924), Tollmien (1931) and Schlichting (1933), but were not supported experimentally immediately. Hence, the existence of TS waves were doubted before these experimental results were known. Additionally, this experiment was also the first one that displayed the receptivity of wall-bounded shear layer to vibratory disturbances within the shear layer, while showing the inadequacy of acoustic excitation in creating TS waves.

For convectively unstable flows, disturbances are swept away from their actual origin. However, in many cases it can so happen that the disturbance can grow first in time at a fixed location, before they are convected downstream. Such growth of disturbances both in space and time are seen in many free shear layers and bluff-body flows. If we subject the equilibrium solution of such an unstable fluid dynamical system to a localized impulse, then the response field spreads both upstream and downstream of the location with respect to the local flow, where it originated while growing in amplitude. Such instabilities are termed as *absolute instabilities*. Here, an additional distinction needs to be made between convective and absolute instabilities. On application of an impulse, both the situation display disturbances in upstream and downstream directions. However, in convectively unstable system the growth of the disturbance is predominantly in one direction, while for absolutely unstable system the growth will be omni-directional. These ideas will be further clarified by understanding some basic concepts related to wave motion.

1.4 Elements of Wave Mechanics

In the previous section, we have distinguished between systems that grow either with time or with space. In reality, many flows display a complex space-time dependence for the disturbance evolution. In contrast to laminar flows, transitional and turbulent flows display broad-band spectra in wave number and circular frequencies. Thus, it facilitates to discuss such flow

dynamics in spectral plane. Below, we provide a very brief introduction to wave mechanics, as applied to a model spatio-temporal dynamical system. Of special interest, is the utility of the concept of dispersion relation that relates the wave number with the circular frequencies. As we note that such dispersion relations are consequences of the governing differential equations and/ or the associated auxiliary conditions.

A wave may be viewed as a unit of the response of the system to applied input or disturbances. These responses could be in terms of physical deflections, pressure, velocity, vorticity, temperature etc., those physical properties relevant to the dynamics, showing up in general, as function of space and time. Any arbitrary function of space and time can be written in terms of Fourier-Laplace transform as given by,

$$f(x,t) = \int_{Br} \int F(\omega,k) e^{i(kx-\omega t)} d\omega dk, \tag{1.4.1}$$

for a system whose property $f(x,t)$ varies with time and single space dimension x. In this definition, ω and k are the complex circular frequency and wave number, respectively. A special point is stated here to interpret the meaning of Eqn. (1.4.1). The integrals in this equation are performed along special contours in the complex $\omega-$ and $k-$plane and are called the Bromwich contours- whose definition and usages can be further seen in Van der Pol & Bremmer (1959) and Papoulis (1962). The Bromwich contours are chosen in the strip of their convergence, where they are defined. This is discussed in section 2.6.1.2 for an elaborate explanation and many applications for boundary layer instability are shown in section 2.6. Choice of the contour in the $\omega-$plane depends on the physical principle of *causality*. In the same way, the k-plane contour has to be chosen in such a way that the poles and singularities of the response should be positioned to account for the correct directionality of the associated response field. The transforms related to time dependence are thus sought in terms of unilateral Laplace-Fourier transform and the transforms associated with space dependence are defined via bi-lateral Laplace transform. Equation (1.4.1) is the inverse transform to obtain the function in the physical space based on the value of the direct transform $F(\omega,k)$, obtained in the spectral plane. The direct transform can be obtained in turn from the following,

$$F(\omega,k) = \int_{-\infty}^{\infty} \int_{0}^{\infty} f(x,t) e^{-i(kx-\omega t)} dx dt \tag{1.4.2}$$

In writing the above transform, it is implied that the input to the system is applied at $t = 0$, and thus, the time integral starts at that time, essentially

following the *causality* principle. However no such restriction needs to be applied for space dependence of the function.

The definition integrals of Eqns. (1.4.1) and (1.4.2), tell us that any arbitrary space-time dependent functions can be thought of as an ensemble of large numbers of waves with different combinations of wave numbers and circular frequencies. This assembly could be a result of countably infinite numbers of waves or it could represent a continuous spectrum. There is a definitive relationship between the wave numbers and the circular frequencies, as identified before, as the dispersion relation.

Let us explain the implication of dispersion relation through a simple example of one-dimensional wave propagation whose governing equation is given by,

$$\frac{\partial f}{\partial t} + c\frac{\partial f}{\partial x} = 0 \tag{1.4.3}$$

In this equation c is the phase speed of the wave. We know that the exact solution of Eqn. (1.4.3) shows the initial solution to travel to the right at the phase speed (c). If we use the representation given by Eqn. (1.4.1), in Eqn. (1.4.3) we then get,

$$\int_{Br}\int i(kc-\omega)Fe^{-i(kx-\omega t)}d\omega dk = 0 \tag{1.4.4}$$

Since the integral is true along the Bromwich contours and is equal to zero, hence a non-trivial and unique solution would require the following relation to hold,

$$\omega = kc$$

This is the desired relationship between the circular frequency and the wave number and is the *dispersion relation*. For a general problem governed by other forms of equation, the *dispersion relation* will be of the kind,

$$\omega = \omega(k) \tag{1.4.5}$$

Thus, the dispersion relation for Eqn. (1.4.3), is the statement of governing equation in the spectral plane and tells us that the scale of space variation and the scale of time variation are not independent and they are related. For many other problems, the dispersion relation will be consequence of boundary conditions, as is often derived for water waves developing for an equilibrium solution given by the Laplace's equation. Equation (1.4.5) implies that each frequency component will travel in space with the

corresponding phase speed. Any system that has relationship showing that the phase corresponding to each wave number travels by the same speed is called a *non-dispersive system*. In contrast, a *dispersive system* is one for which different frequency components travel with different speed, such that any compact disturbance at $t = 0$ will be found dispersed at a later time. One can generalize the above for a system that displays broad-band dynamics.

Once again for such a general system, the governing differential equation(s) and the boundary condition(s) will determine the *dispersion relation*. Once we have this relation, it is possible to talk about the general properties of the response field (Lighthill(1978)). Let us consider two neighboring wave numbers, k_1 and k_2 of the response field. For the physical problem, response field depends continuously on the forcing and auxiliary conditions. Hence the corresponding circular frequencies, ω_1 and ω_2, as obtained from the *dispersion relation* will also be two closely spaced neighboring points in the frequency plane. We denote the corresponding response components by,

$$f_1 = a\cos(k_1 x - \omega_1 t) \tag{1.4.6a}$$

$$f_2 = a\cos(k_2 x - \omega_2 t) \tag{1.4.6b}$$

We consider here only the real part of the response field. A more generalized response based on the expression (1.4.1) will have also an imaginary component signifying the phase shift of the output with respect to applied input. In the above equations, both the components have been assumed to have same amplitude, the difference being negligible- as we are considering two components that are separated by an infinitesimal amount in the spectral plane. The total contribution coming from these two components is then given by,

$$f = f_1 + f_2 = [2a\cos\frac{1}{2}\{(k_1-k_2)x-(\omega_1-\omega_2)t\}]\cos\frac{1}{2}\{(k_1+k_2)x-(\omega_1+\omega_2)t\} \tag{1.4.7}$$

Total effect of these two components shows up as a combination of two factors- one on a slow scale given by the first quantity inside the square bracket and the second quantity that varies on the original scale given by the second cosine function. As the two components are infinitesimally apart in the spectral plane, the slowly varying part can be viewed as the amplitude of the total effect. As energy of a wave system is proportional to the square of the amplitude of the wave, one can view the energy of the system to vary following the phase variation of the amplitude. Therefore the speed

of propagation of energy is given by the rate at which the phase of the amplitude changes and is given by,

$$V_g = \frac{(\omega_2 - \omega_1)}{(k_2 - k_1)}$$

This is the group velocity of the simple system considered here, where the spatial variation is along a single direction and the group velocity direction is given along this direction. For the one-dimensional system in the limit, when the wave numbers of the two components are only dk apart in $k-$space, then one can consider an equivalent response field centered around this cluster and a general expression for the group velocity is given by,

$$V_g = \frac{d\omega}{dk} \tag{1.4.8}$$

The group velocity for multi-dimensional problem is a vector, decided by the variation of circular frequency with the wave number vector. It is only the real part of Eqn. (1.4.8) that is termed the group velocity - as discussed in Whitham (1978). Thus, this is the velocity at which the energy of a group of waves travel, centered about the middle of the wave number group. It is noted that the one-dimensional wave given by Eqn. (1.4.3), is non-dispersive with $V_g = c$.

Regarding the classification of instabilities into convective and absolute instability, one can now see the difference clearer in terms of the group velocity. For absolute instability the group velocity is found to be zero, so that the disturbances do not get swept away, as in convective instability and continue to grow in the place of their origin. However, in many flow systems, these two aspects can remain simultaneously.

1.5 Some Instability Mechanisms

Here two simple cases of instabilities are considered to emphasize the concepts described above. We begin by distinguishing the difference between static and dynamic instability by considering the stability of atmosphere as an example.

When a parcel of air in the atmosphere is moved rapidly from an equilibrium condition and its tendency to come back to its undisturbed position is noted, then we term the atmosphere as statically stable. The movement of the packet is considered as impulsive, to preclude any heat transfer from the parcel to the ambience. This tendency of static stability- when exists, is due to the buoyancy force caused by the density differential due to temperature variation with height and such body force acts upon the displaced air-parcel.

In static stability studies, we do not look for detailed timed-dependent motion of the parcel following the displacement (as the associated accelerations are considered negligible).

1.5.1 Dynamic Stability of Still Atmosphere

For the dynamic stability study, we consider once again a parcel of air to be at equilibrium, at a height z and is displaced to a height $(z+\xi)$ to follow its detailed time history of motion. We note that the motion is caused again by the buoyancy force, caused by the temperature variation of the ambient air given by $T = T(z)$. Here, the vertical displacement of the air-parcel is ξ and the dynamics follows the force balance equation,

$$\rho' \ddot{\xi} = g(\rho - \rho')_{z+\xi} \tag{1.5.1}$$

where $\ddot{\xi}$ is the instantaneous acceleration experienced by the parcel of air. Density of the displaced parcel is considered to be given by ρ', while the ambient fluid has the density ρ, so that the right hand side of the above equation represents the buoyancy force. Equilibrium thermodynamics tells us that for a simple compressible substance with only one mode of work, any state property can be represented by any two other properties and let us consider them to be the pressure (p) and the entropy (s). Thus, using a Taylor series we can relate the density of the ambient air at the two heights as

$$\rho(z+\xi) = \rho(z) + \left(\frac{\partial \rho}{\partial p}\right)_s [p(z+\xi) - p(z)] + \left(\frac{\partial \rho}{\partial s}\right)_p [s(z+\xi) - s(z)] + \ldots \tag{1.5.2}$$

Once again, we will assume that the displacement process of the air-parcel is isentropic (there are no viscous or heat losses associated with the rapid movement of the parcel) and thus for the air-parcel,

$$\rho'(z+\xi) = \rho'(z) + \left(\frac{\partial \rho}{\partial p}\right)_s [p(z+\xi) - p(z)] \tag{1.5.3}$$

In Eqns. (1.5.2) and (1.5.3), mechanical equilibrium ensures same δp and $\rho(z) = \rho'(z)$. Thus, the density differential causing the buoyancy is given by,

$$(\rho - \rho')_{z+\xi} = \left(\frac{\partial \rho}{\partial s}\right)_p [s(z+\xi) - s(z)] = \left(\frac{\partial \rho}{\partial s}\right)_p \frac{ds}{dz} \xi \tag{1.5.4}$$

We can also relate the density of the air-parcel at the two heights as,

$$\rho'(z+\xi) = \rho(z) + \left(\frac{\partial \rho}{\partial p}\right)_s \frac{dp}{dz}\xi = \rho(z) + \frac{1}{c^2}\frac{dp}{dz}\xi$$

where c is the speed of sound. Equation (1.5.1) can also be written in terms of the specific volume ($v = \frac{1}{\rho}$), using Eqn. (1.5.4) as,

$$\ddot{\xi} = \frac{g}{\rho'}(\rho - \rho')_{z+\xi} = -\left[\frac{g}{v}\left(\frac{\partial v}{\partial s}\right)_p \frac{ds}{dz}\xi\right] / \left[1 + \frac{v\xi}{c^2}\frac{dp}{dz}\right]$$

From the mechanical equilibrium, $\frac{dp}{dz} = -\rho g$, above can be further simplified to

$$\ddot{\xi} = -\left[\frac{g}{v}\left(\frac{\partial v}{\partial s}\right)_p \frac{ds}{dz}\xi\right] / \left[1 - \frac{g\xi}{c^2}\right]$$

We can further simplify by using the thermodynamic relations: $\left(\frac{\partial v}{\partial s}\right)_p = \left(\frac{\partial T}{\partial s}\right)_p \left(\frac{\partial v}{\partial T}\right)_p$ and $\frac{ds}{dz} = \left(\frac{\partial s}{\partial T}\right)_p \frac{dT}{dz} + \left(\frac{\partial s}{\partial p}\right)_T \frac{dp}{dz}$, noting that $\left(\frac{\partial s}{\partial T}\right)_p = \left(\frac{\partial s}{\partial h}\right)_p \left(\frac{\partial h}{\partial T}\right)_p = \frac{C_p}{T}$. From the Maxwell's relation, $\left(\frac{\partial s}{\partial p}\right)_T = -\left(\frac{\partial v}{\partial T}\right)_p$, we obtain $\frac{ds}{dz} = \frac{C_p}{T}\frac{dT}{dz} + \rho g\left(\frac{\partial v}{\partial T}\right)_p$.

All these simplifications lead to,

$$\ddot{\xi} = -\frac{g\xi}{v}\left(\frac{\partial v}{\partial T}\right)_p \frac{T}{C_p}\left[\frac{C_p}{T}\frac{dT}{dz} + \frac{g}{v}\left(\frac{\partial v}{\partial T}\right)_p\right] / \left[1 - \frac{g\xi}{c^2}\right]$$

If we consider air as a perfect gas ($p = \rho RT$), then $\left(\frac{\partial v}{\partial T}\right)_p = v/T$ and the above further simplifies to

$$\ddot{\xi} = -\frac{g}{T}\left(\frac{dT}{dz} + \frac{g}{C_p}\right)\xi / \left[1 - \frac{g\xi}{c^2}\right]$$

If we further consider the speed of sound (c) to be very large, then the above equation can be further approximated to

$$\ddot{\xi} + N^2 \xi = 0 \tag{1.5.5}$$

where $N^2 = \frac{g}{v}(\frac{\partial \nu}{\partial s})_p \frac{ds}{dz}$. We can consider the following possibilities:

Case-1: If $N^2 > 0$ then the dynamics of the displacement will be purely oscillatory, implying neutral stability of the static atmosphere.

Case-2: If $N^2 < 0$, then the vertical displacement will vary as,

$$\xi(t) = Ae^{|N|t} + Be^{-|N|t}$$

where the first component clearly indicates instability. N is called the *Brunt-väisälä* or buoyancy frequency. As given above, following Thompson (1972), we can obtain this frequency with air treated as an ideal gas by,

$$N^2 = \frac{g}{T}\left[\frac{dT}{dz} + \frac{g}{C_p}\right] \tag{1.5.6}$$

For dry air, $\frac{g}{C_p} = -0.01$ K/meter and hence for stability of dry atmosphere the temperature distribution has to be so that $\frac{dT}{dz} > -0.01$ K/meter. Thus $\frac{dT}{dz} = 0.01$ represents the border line of instability and the numerical value on the right hand side within the square bracket is termed as the dry adiabatic lapse rate, because this ensures $\frac{ds}{dz} = 0$.

1.5.2 Kelvin - Helmholtz Instability

This arises when two layers of fluids (may not be of same species or density) are in relative motion. Thus, this is an interfacial instability and the resultant flow features due to imposed disturbance will be much more complicated due to relative motion. Physical relevance of this problem was seized upon by Helmholtz (1868) who observed that the interface as a surface of separation tears the flow *asunder*. Sometime later Kelvin (1871) posed this problem as one of instability and solved it. We follow this latter approach here. The basic equilibrium flow is assumed to be inviscid and incompressible - as two parallel streams having distinct density and velocity - flowing one over the another, as depicted in figure below.

Before any perturbation is applied, the interface is located at $z = 0$ and subsequent displacement of this interface is expressed parametrically as,

$$z_s = \hat{\eta}(x, y, t) = \epsilon \eta(x, y, t) \tag{1.5.7}$$

where ϵ is a small parameter, defined to perform a linearized perturbation analysis. One can view the interface itself as a shear layer of vanishing thick-

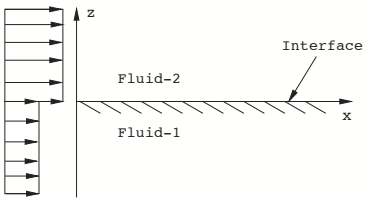

Figure 1.1 Kelvin-Helmholtz instability at the interface of two flowing fluids.

ness. For the considered inviscid irrotational flows, the velocity potentials in the two domains are given by,

$$\tilde{\phi}_j(x, y, z, t) = U_j x + \epsilon\phi_j(x, y, z, t) \tag{1.5.8}$$

The governing equations in either of the flow-domains are given by,

$$\nabla^2\tilde{\phi}_j = 0 \tag{1.5.9}$$

And the potential must satisfy the following far-stream boundary conditions given by,

$$\phi_j s \quad are \quad bounded \quad as \quad z \to \pm\infty \tag{1.5.10}$$

The other set of boundary condition is applied at the interface, which is the no-fluid through the interface condition i.e.

$$\frac{\partial\hat{\eta}}{\partial t} - \frac{\partial\tilde{\phi}_j}{\partial z} = -\frac{\partial\hat{\eta}}{\partial x}\frac{\partial\tilde{\phi}_j}{\partial x} - \frac{\partial\hat{\eta}}{\partial y}\frac{\partial\tilde{\phi}_j}{\partial y} \tag{1.5.11}$$

In addition, in the absence of surface tension, pressure must be continuous across the interface. Upon linearization, the interface boundary condition (1.5.11) simplifies to,

$$\frac{\partial\eta}{\partial t} + U_j\frac{\partial\eta}{\partial x} - \frac{\partial\phi_j}{\partial z} = 0 \quad for \quad j = 1, \quad 2 \tag{1.5.12}$$

where $\tilde{\phi}_j$ and ϕ_j are as related in Eqn. (1.5.8). Defining the pressure on the either flow-domain by unsteady Bernoulli's equation, one can write

$$p_j = C_j - \rho_j\left\{\frac{\partial\tilde{\phi}_j}{\partial t} + \frac{1}{2}(\nabla\tilde{\phi}_j)^2 + g\hat{\eta}\right\} \tag{1.5.13}$$

Simplifying and retaining up to $0(\epsilon)$ terms, we get the following conditions

$$0(1) \;\; condition : C_1 - \frac{1}{2}\rho_1 U_1^2 = C_2 - \frac{1}{2}\rho_2 U_2^2 \tag{1.5.14a}$$

$$0(\epsilon) \;\; condition : \rho_1 \left\{ \frac{\partial \phi_1}{\partial t} + U_1 \frac{\partial \phi_1}{\partial x} + g\eta \right\} = \rho_2 \left\{ \frac{\partial \phi_2}{\partial t} + U_2 \frac{\partial \phi_2}{\partial x} + g\eta \right\} \tag{1.5.14b}$$

One can consider a very general interface displacement given in terms of bilateral Laplace transform as,

$$\eta(x, y, t) = \int \int F(\alpha, \beta, t) e^{i(\alpha x + \beta y)} d\alpha d\beta \tag{1.5.15}$$

Correspondingly, the perturbation velocity potential is expressed as,

$$\phi_j(x, y, z, t) = \int \int Z_j(\alpha, \beta, z, t) e^{i(\alpha x + \beta y)} d\alpha d\beta \tag{1.5.16}$$

Writing $k^2 = \alpha^2 + \beta^2$ and using Eqn. (1.5.16) in (1.5.9), one gets the solution that satisfies the far-stream boundary conditions (1.5.10) as,

$$Z_j = f_j(\alpha, \beta, t) e^{\pm kz} for \quad j = 1 \;\; and \;\; 2 \tag{1.5.17}$$

Using Eqn. (1.5.15) in the interface boundary condition (1.5.12) one gets,

$$\dot{F} + i\alpha U_1 F - k f_1 = \dot{F} + i\alpha U_2 F + k f_2 = 0 \tag{1.5.18}$$

where the dots denote differentiation with respect to time. If we denote the density ratio $\rho = \rho_2/\rho_1$, then the linearized pressure continuity condition (1.5.14b) gives,

$$\frac{\partial \phi_1}{\partial t} - \rho \frac{\partial \phi_2}{\partial t} + U_1 \frac{\partial \phi_1}{\partial x} - \rho U_2 \frac{\partial \phi_2}{\partial x} + (1 - \rho) g\eta = 0 \tag{1.5.19}$$

Using (1.5.15) and (1.5.16) in the above equation, one gets

$$\dot{f}_1 - \rho \dot{f}_2 + i\alpha U_1 f_1 - i\alpha \rho U_2 f_2 + (1 - \rho) g F = 0 \tag{1.5.20}$$

Eliminating f_1 and f_2 from Eqn. (1.5.20) using Eqn. (1.5.18), one gets after simplification,

$$(1 + \rho)\ddot{F} + 2i\alpha(U_1 + \rho U_2)\dot{F} - \{\alpha^2(U_1^2 + \rho U_2^2) - (1 - \rho) g k\} F = 0 \tag{1.5.21}$$

This ordinary differential equation for the time variation of the interface displacement F can be understood better in terms of its Fourier transform defined by,

$$F(.,t) = \int \hat{F}(.,\omega)e^{i\omega t}d\omega \tag{1.5.22}$$

One obtains the following dispersion relation by substitution of (1.5.22) in (1.5.21) as,

$$-\omega^2(1+\rho) - 2\alpha\omega(U_1 + \rho U_2) + (1-\rho)gk - \alpha^2(U_1^2 + \rho U_2^2) = 0 \tag{1.5.23}$$

This provides the characteristic exponents in (1.5.22) as,

$$\omega_{1,2} = -\frac{\alpha(U_1 + \rho U_2)}{(1+\rho)} \mp \frac{\sqrt{gk(1-\rho^2) - \alpha^2\rho(U_1 - U_2)^2}}{(1+\rho)} \tag{1.5.24}$$

Based on this dispersion relation, the following sub-cases can be considered:

CASE 1: When the interface is disturbed in the spanwise direction only i.e. $\alpha = 0$ and then

$$\omega_{1,2} = \mp\sqrt{g\beta\frac{(1-\rho)}{(1+\rho)}} \tag{1.5.25}$$

Thus, the streaming velocities U_1 and U_2 do not affect the response of the system. If in addition, $\rho > 1$, i.e. a heavier liquid is over a lighter liquid, then the buoyancy force causes temporal instability (if β is considered real) - as is the case for Rayleigh-Taylor instability (see Chandrasekhar (1960)).

CASE 2: For a general interface perturbation if $gk(1-\rho^2) - \alpha^2\rho(U_1 - U_2)^2 < 0$, then the interface displacement will grow in time. This condition can be alternately stated as a condition for instability as: $(U_1 - U_2)^2 > \frac{gk}{\alpha^2}\left(\frac{1-\rho^2}{\rho}\right)$.

Thus, for a given shear at the interface given by, $(U_1 - U_2)$ and for a given oblique disturbance propagation direction at the interface indicated by the wave number vector k, instability would occur for all wave numbers k^*, given by

$$k^* > \left(\frac{k^*}{\alpha}\right)^2 \frac{g}{(U_1 - U_2)^2}\left(\frac{\rho_1}{\rho_2} - \frac{\rho_2}{\rho_1}\right)$$

Note that the wave number vector makes an angle γ with the x-axis, such that $cos\gamma = \frac{\alpha}{k^*}$ and the above condition can be conveniently written as,

$$k^* > \frac{g}{(U_1 - U_2)^2 cos^2\gamma}\left(\frac{\rho_1}{\rho_2} - \frac{\rho_2}{\rho_1}\right) \tag{1.5.26}$$

The lowest value of wave number ($k^* = k_{min}$) would occur for two-dimensional disturbances i.e. when $cos\gamma = 1$ and this is given by,

$$k^*_{min} = \frac{g}{(U_1 - U_2)^2}\left(\frac{\rho_1}{\rho_2} - \frac{\rho_2}{\rho_1}\right) \tag{1.5.27}$$

CASE 3: Consider the case of shear only of same fluid in both the domain i.e. $\rho = 1$. The characteristic exponents then simplify to,

$$\omega_{1,2} = -\alpha\frac{U_1 + U_2}{2} \mp \frac{i\alpha}{2}(U_1 - U_2) \tag{1.5.28}$$

Presence of the imaginary part with negative sign implies temporal instability for all wave lengths. Also, to be noted that since the group velocity and phase speed in y-direction is identically zero, therefore the Kelvin-Helmholtz instability for pure shear always will lead to two-dimensional instability.

Chapter 2

INSTABILITY AND TRANSITION IN FLUID MECHANICS

Prof. Tapan K. Sengupta
HPCL, Aerospace Engineering
I.I.T. Kanpur

2.1 Introduction

The basic aim of the material in this chapter is to acquaint readers with the state-of-art in the study of receptivity and relate the same with instability and transition of fluid flow. This subject area remains the pacing item in understanding many natural phenomena, as well as, in the analysis and design of many engineering systems. For example, this is pursued in civil aviation to design newer lifting surfaces with drag reduced by passive means. In this context, keeping the flow laminar (stable) over a wing, to as large an extent possible is the primary goal. With reduced drag, the aircraft speed and range can be increased for the same power consumed or have a less powerful engine for the same endurance and range of the flight envelope.

It is well known that for a zero pressure gradient flat plate boundary layer, the skin friction for laminar flow is given by, $C_f = \frac{1.328}{\sqrt{Re}}$ that at a Reynolds number of 10^7 works out as 0.00043 (See Schlichting (1979)) and the same profile drag increases to 0.0035 for the equivalent turbulent flow (Van Driest (1951)). This is the rationale for trying to keep a flow laminar so that one can obtain an order of magnitude drag reduction in the relevant portion of the aerodynamic surface. Such drag reductions are also realizable for airfoil- the quintessential lifting surface element of all aircraft wings. According to Viken (1983), flow past an airfoil at moderate Reynolds number, that is fully turbulent without any separation, displays a profile drag coefficient of nearly 0.0085 and that can be reduced to 0.0010 if the flow over the airfoil is maintained fully laminar. Even a modest viscous drag

reduction via transition delay can provide large benefits, if large numbers of aircrafts are involved- as is the case for civil air transport industry.

Thus, transition delay for the flow over aircraft wings takes on added importance when it is realized that by resorting to transition delay techniques on wings alone, about 10 to 12% drag reduction is feasible on a modern transport aircraft. It is also now well established that transition to turbulence relates to the understanding of vorticity distribution in the shear layer and their reorganization, in response to forcing by environmental disturbances. While the flows, either in its spatio-temporal orderly form (in laminar flows) or in its chaotic form, are governed by the same generalized Navier- Stokes equation (Goldstein (1938)). The late stages of transition processes or the fully turbulent flows are not amenable to easy understanding due to the intractable nonlinearity of the Navier-Stokes equation (Morkovin (1991)). However, the onset of the transition process (also known as the receptivity stage - see Morkovin (1958, 1978, 1990)) is bedeviled by our inability to catalogue and quantify the background omnipresent disturbances. At this point in time, significant understanding of the receptivity and the linear stage of transition have been made- that allows attempts made to design aircrafts with reduced drag via transition delay. In Fig. 2.1, we reproduce the system portrait given in Morkovin (1991) for the route to wall bounded turbulent flows. As of today, the primary approaches in transition delay relates to suppressing disturbance growth during the receptivity and primary instability stages. Late stages of transition and turbulent states of flows can be controlled by active means. This aspect is still an active area of research and is currently not used in any operational transport aircrafts. Flow control is gaining in importance in recent times.

Primarily laminar boundary layers are sustained by either small amount of suction (Pfenninger (1947)) or by favourable pressure gradients. Stabilizing by suction though very efficient [critical Reynolds number increases by 90 times to $Re_{cr} = 46,000$ for asymptotic suction, as compared to the no-suction case for Blasius boundary layer for which $Re_{cr} = 520$ - see Hughes & Reid (1965) and White (1991)] - is not practiced due to operational difficulties. For example, one must have the provision of porous surface together with the necessary suction system- complexity and maintenance of such system makes this technology unattractive, at present.

In contrast, stabilization of boundary layer by contouring the airfoil surface to achieve favourable pressure gradient as a passive way is found to be practical and attractive. The resultant section is known as the Natural Laminar Flow (NLF) airfoil and this is an area which has been under renewed investigation over the last three decades. Early efforts of designing

airfoils to delay transition are as given in Jacobs (1939), Tani (1952), Abbott & Doenhoff (1959). Typical examples of such airfoils designed are given by the six digit NACA series airfoils. These aerofoils were successful at low Reynolds numbers- as evidenced by their continued usage in gliders. This is due to the fact that the early NLF airfoils exhibited low drag only for a narrow range of C_l's (designed considering cruise condition only). However, such a section does not perform optimally in other sector of flight envelope. This highlights that a practical NLF airfoil must only have low cruise drag, but also must provide high lift characteristics- very essential during landing, take off and climb. Unfortunately, to maximize desired performance in terms of low drag degrades high lift performance and vice versa.

The above discussion pertaining to drag reduction of external flow over an aircraft wing is equally relevant to the power requirements for flow of water or oil in a pipeline. If the flow can be retained laminar and flow instability prevented and/or delayed, then there is a direct benefit in terms of energy efficiency. This is a justified motivation to discuss about flow instability, without the understanding of which it is not possible to design any system whose performance is dictated by fluid flow. Here we provide a general introduction to topics of receptivity and flow instability relevant to many engineering systems.

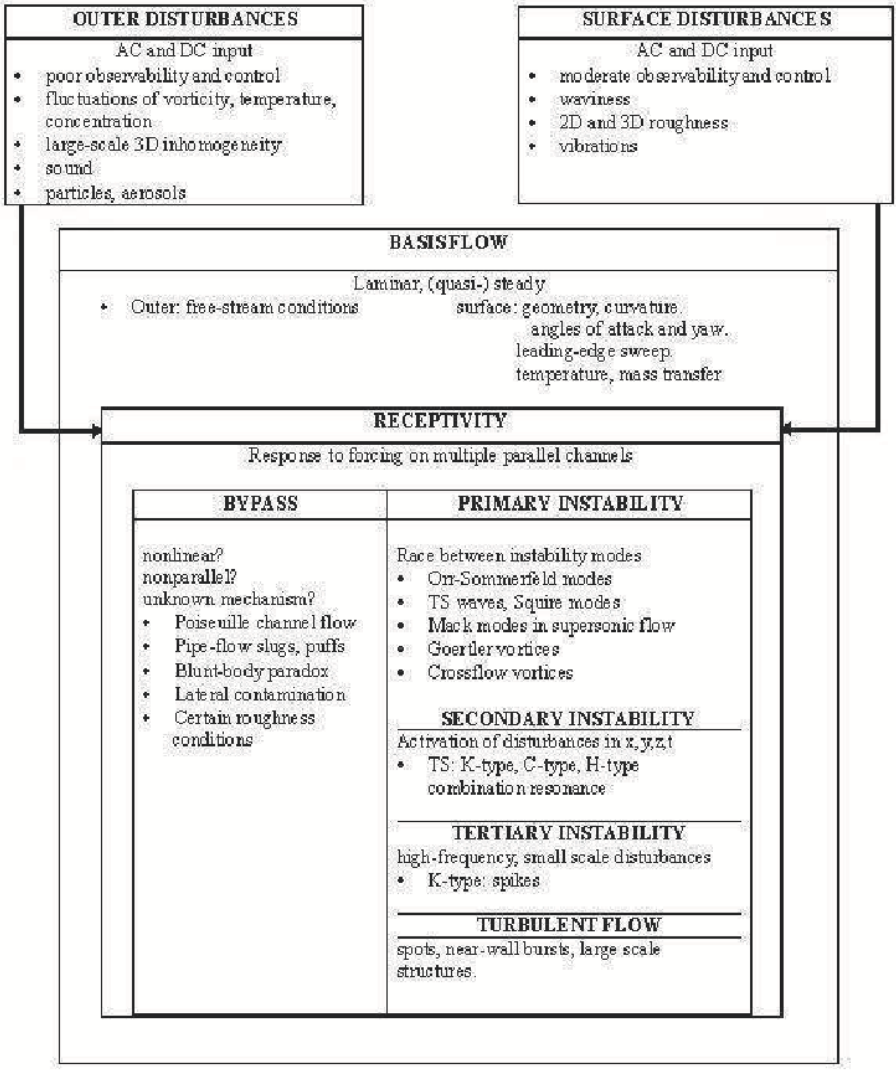

Figure 2.1 System portrait for road to turbulence (Morkovin, 1991)

It is not straightforward to perform pure theoretical stability analyses for any given flow. To do this, one needs additional simplifying assumptions to make the problem tractable- with the major one described next.

2.2 Parallel Flow Approximation and Inviscid Instability Theorems

The above discussion on rudiments of instability indicates the need to obtain the equilibrium flow, followed by the study of its stability or instability. It so happens that obtaining the equilibrium flow itself could be arduous and that is compounded by lacking general procedure to study its instability, without making many simplifying assumptions. For example, the instability studies has been facilitated by considering only those flows for which the shear layer grows very slowly, so that the streamlines within the shear layer can be approximated to be parallel to each other- the so-called parallel flow approximation. It should be noted that boundary layer flows under mild pressure gradient remains unseparated and can be approximated as quasi-parallel flow for the purpose of studying its instability, even when the equilibrium flow has been obtained without such restrictions. A major part of linear (and weakly nonlinear) instability theories have been developed for quasi-parallel flows, starting with the pioneering work of Helmholtz (1868), Kelvin (1871) and Rayleigh (1880).

To study the stability of a two-dimensional parallel flow that only supports two-dimensional disturbance field, one considers the total flow field to be given by,

$$u(x,y,t) = U(y) + \epsilon u'(x,y,t) \tag{2.2.1}$$

$$v(x,y,t) = \quad \epsilon v'(x,y,t) \tag{2.2.2}$$

$$p(x,y,t) = P(x,y) + \epsilon p'(x,y,t) \tag{2.2.3}$$

Note the space-time dependence for the perturbation field is without any restrictions, at this stage. In the absence of body force for constant density flows, the governing equations for the disturbance field in small perturbation analysis is obtained from the linearized perturbation equations given by,

$$\frac{\partial u'}{\partial x} + \frac{\partial v'}{\partial y} = 0 \tag{2.2.4}$$

$$\frac{\partial u'}{\partial t} + U\frac{\partial u'}{\partial x} + v'\frac{dU}{dy} = -\frac{1}{\rho}\left(\frac{\partial p'}{\partial x}\right) \tag{2.2.5}$$

$$\frac{\partial v'}{\partial t} + U\frac{\partial v'}{\partial x} \quad = -\frac{1}{\rho}\left(\frac{\partial p'}{\partial y}\right) \tag{2.2.6}$$

For the purpose of linear analysis, we represent the perturbation quantities by their Fourier- Laplace transform via

$$u'(x,y,t) = \int \overline{u}(y;\alpha,\omega)e^{i(\alpha x-\omega t)}d\alpha d\omega \tag{2.2.7}$$

$$v'(x,y,t) = \int \overline{v}(y;\alpha,\omega)e^{i(\alpha x-\omega t)}d\alpha d\omega \tag{2.2.8}$$

$$\frac{p'(x,y,t)}{\rho} = \int \overline{p}(y;\alpha,\omega)e^{i(\alpha x-\omega t)}d\alpha d\omega \tag{2.2.9}$$

In these representations, α and ω are the wave number and circular frequency, respectively. One can use (2.2.7) to (2.2.9) in (2.2.4)-(2.2.6) and eliminate $\overline{u}$ and $\overline{p}$ from the three equations to get a single differential equation for $\overline{v}$ as,

$$(U-\frac{\omega}{\alpha})(\frac{d^2\overline{v}}{dy^2}-\alpha^2\overline{v})-\frac{d^2U}{dy^2}\overline{v}=0 \tag{2.2.10}$$

This is the celebrated Rayleigh's stability equation. To study this inviscid stability of a fluid dynamical system, one has to solve Eqn. (2.2.10) subject to the homogenous boundary conditions for $\overline{v}$. In general for a fluid dynamical system admitting spatio-temporal growth of small perturbations, both α and ω are complex. However, for the ease of analysis we study temporal growth i.e. we consider α as real and ω as complex. If we write $c=\omega/\alpha$, then the complex phase speed $(=c_r+ic_i)$ will determine the stability obtained as an eigenvalue of the equation given by,

$$(U-c)(\frac{d^2\overline{v}}{dy^2}-\alpha^2\overline{v})-\frac{d^2U}{dy^2}\overline{v}=0 \tag{2.2.11}$$

The criterion for instability then becomes: *There exists a solution with* $c_i<0$ *for some positive* α.

2.2.1 Inviscid Instability Mechanism

Let $\overline{v}^*$ be complex conjugate of $\overline{v}$, then $\overline{v}\,\overline{v}^*=|\overline{v}|^2$.

Multiplying Eqn. (2.2.11) by $\overline{v}^*$ and integrating over the possible limit (say, $-\infty$ to $+\infty$) we get,

$$\int_{-\infty}^{+\infty}\overline{v}^*[\frac{d^2\overline{v}}{dy^2}-\alpha^2\overline{v}-\frac{U''}{U-c}\overline{v}]dy=0 \tag{2.2.12}$$

Above equation is non-singular as we are looking for solutions with $c_i \neq 0$, such that the quantity in the denominator of the third term does not vanish. Simplifying Eqn. (2.2.12) one gets,

$$\int [\,|\frac{d\overline{v}}{dy}|^2 + \alpha^2|\overline{v}|^2]dy + \int \frac{U''|\overline{v}|^2}{|U-c|^2}(U-c)^* dy = 0 \tag{2.2.13}$$

In Eqn. (2.2.13) the first term is real and positive and the imaginary part of this equation is

$$c_i \int \frac{U''}{|U-c|^2}\,|\overline{v}|^2\,dy = 0 \tag{2.2.14}$$

This integral of (2.2.14) will vanish if and only if the integrand changes sign in the interval of integration. That is possible only when U'' changes sign. Thus, there must be a location where $U'' = 0$ for some $y = y_s$ within the limits of integration. This point is known as the inflection point and this leads to,

Rayleigh's Inflection Point Theorem: A *necessary condition* for instability is that the basic velocity profile should have an inflection point.

In this theorem, the inflection point refers to the existence of a point within a shear layer (at $y = y_s$ where the local velocity is given by U_s) and where the second derivative of the equilibrium flow profile vanishes i.e. $\frac{d^2U}{dy^2} = U'' = 0$, where y is the wall-normal co-ordinate inside the shear layer. A stronger version of the Rayleigh's theorem was given later by Fjϕrtoft (1950).

Fjϕrtoft's Theorem: A *necessary condition* for instability is that $U''(U-U_s)$ is less than zero somewhere in the flow field.

Thus, if the velocity profile is a monotonically growing function of its argument with a single inflection point then the above necessary condition for instability can be written for this velocity profile as $U''(U-U_s) \leq 0$ for the range of integration, with equality only at $y = y_s$. Both the Rayleigh's and Fjϕrtoft's theorem are necessary condition and they do not provide a sufficient condition for instability.

Above inviscid mechanism of instability is often encountered in free shear layers and jets. A fundamental difference between flows having an inflection point (such as in free shear layer, jets and wakes and the cross flow component of some three-dimensional boundary layers) and flows without inflection points (as in wall bounded flows in channel or in boundary layers) exists. Flows with inflection points are susceptible to temporal instabilities for very low Reynolds numbers. One can find detailed accounts of invis-

cid instability theories in Drazin & Reid (1981) and Betchov & Criminale (1967).

2.3 Viscous Instability of Parallel Flows

In the beginning when flow stability was being investigated, it was thought the action of viscous forces is to dissipate energy and thus its effect is essentially stabilizing. This prompted early stability studies using Rayleigh's equation. However, Heisenberg and various researchers from Prandtl's school established (under the parallel flow assumption), that the action of viscosity can be destabilizing. This provides one mechanism for the instability of zero and favourable pressure gradient boundary layers those are otherwise stable with respect to the inviscid mechanism of section 2.2.1. In this section, the stability of viscous flows (those are essentially parallel or those could be well-approximated as parallel flow), is discussed. Thus, one considers mean flow profiles given by

$$U = U\ (y)\hat{i} \tag{2.3.1}$$

The flow is in the x-direction and the velocity magnitude solely depends on the distance from the datum $y = 0$.

Tollmien (1931) calculated a critical Reynolds number (the lowest Reynolds number at which the flow first becomes unstable), details of which can be found in Schlichting (1979). The value obtained for the critical Reynolds number by Tollmien was $(Re_x)_{crit} = \frac{U_\infty x}{v} = 60,000$ - a value much lower than the wind tunnel results that varied between $Re_{tr} = 3.5 \times 10^5$ (in noisy tunnels) and 10^6 (comparatively cleaner tunnels of that period). We have indicated Reynolds numbers by different subscripts for the purpose that explain the discrepancy. The reason for it is that instability and transition are not synonymous. While a flow can become unstable early enough, it would take a while for these unstable disturbances to grow up to sufficiently large amplitude to complete the process of transition. Schlichting later calculated the amplitude ratio A/A_0 of the *most amplified frequency* as a function of Reynolds number for a flat plate boundary layer, where A_0 is the amplitude of disturbance at the onset of instability. He found out that the ratio A/A_0 varied between e^5 and e^9 at the observed Re_{tr}. These wave solutions are now called the TS waves, irrespective of whether they are amplified or attenuated. It is now generally accepted that flow parameters such as pressure gradient, suction and heat transfer qualitatively affect transition in the same way that was predicted by viscous stability theory developed. In this theory this is cast as an eigenvalue problem.

2.3.1 Eigenvalue Formulation for Instability of Parallel Flows

In this theory, equilibrium flow is obtained using thin shear layer (TSL) approximation of the governing Navier- Stokes equation. However, to investigate the stability of the fluid dynamical system the disturbance equations are obtained from the full time dependent Navier- Stokes equations, with the equilibrium condition defined by the steady laminar flow. We obtain these in Cartesian coordinate system given by,

$$\frac{\partial u}{\partial t} + u\frac{\partial u}{\partial x} + v\frac{\partial u}{\partial y} + w\frac{\partial u}{\partial z} = -\frac{\partial p}{\partial x} + \frac{1}{Re}\bigtriangledown^2 u \tag{2.3.2}$$

$$\frac{\partial v}{\partial t} + u\frac{\partial v}{\partial x} + v\frac{\partial v}{\partial y} + w\frac{\partial v}{\partial z} = -\frac{\partial p}{\partial y} + \frac{1}{Re}\bigtriangledown^2 v \tag{2.3.3}$$

$$\frac{\partial w}{\partial t} + u\frac{\partial w}{\partial x} + v\frac{\partial w}{\partial y} + w\frac{\partial w}{\partial z} = -\frac{\partial p}{\partial z} + \frac{1}{Re}\bigtriangledown^2 w \tag{2.3.4}$$

and

$$\frac{\partial u}{\partial x} + \frac{\partial v}{\partial y} + \frac{\partial w}{\partial z} = 0 \tag{2.3.5}$$

Here the equilibrium flow is considered to be in the $(x - z)$ - plane with y indicating the wall-normal direction. Above equations are written in non-dimensional form with the shear layer edge velocity, U_e (or an appropriate velocity for other flows), as the velocity scale and L as the length scale so that $Re = \frac{U_e L}{V}$ is the Reynolds number.

To perform a linearized stability analysis of the fluid dynamical system, we express all flow quantities q, into a steady mean (Q) and an unsteady disturbance term $(\epsilon q')$ that is considered one order of magnitude smaller than the mean quantities, so that

$$q(x, y, z, t) = Q(x, y, z) + \epsilon q'(x, y, z, t) \tag{2.3.6}$$

The smallness of the perturbation quantities are indicated by the small parameter ϵ. Furthermore, the mean velocity field is assumed parallel/ quasi-parallel so that,

$$U = U(y); V \approx 0; W = W(y) \tag{2.3.7}$$

If the splitting of variables, as indicated by Eqn. (2.3.6) are substituted in Eqns. (2.3.2) -(2.3.5) and the $O(\epsilon)$- terms are collated one gets the

following disturbance equations,

$$\frac{\partial u'}{\partial t} + U\frac{\partial u'}{\partial x} + W\frac{\partial u'}{\partial z} + v'\frac{dU}{dy} = -\frac{\partial p'}{\partial x} + \frac{1}{Re}\bigtriangledown^2 u' \tag{2.3.8}$$

$$\frac{\partial v'}{\partial t} + U\frac{\partial v'}{\partial x} + W\frac{\partial z'}{\partial z} = -\frac{\partial p'}{\partial y} + \frac{1}{Re}\bigtriangledown^2 v' \tag{2.3.9}$$

$$\frac{\partial w'}{\partial t} + U\frac{\partial w'}{\partial x} + W\frac{\partial w'}{\partial z} + v'\frac{dW}{dy} = -\frac{\partial p'}{\partial z} + \frac{1}{Re}\bigtriangledown^2 w' \tag{2.3.10}$$

and

$$\frac{\partial u'}{\partial x} + \frac{\partial v'}{\partial y} + \frac{\partial w'}{\partial z} = 0 \tag{2.3.11}$$

Next, one performs the normal mode analysis, i.e. the flow instabilities are governed by discrete eigenmodes those do not interact with each other and are studied separately. Equations (2.3.8) to (2.3.11) are variable coefficient linear partial differential equations; but, they do not admit analytic solutions. However, with the help of normal mode analysis, this can be further simplified. As the coefficients of these equations are functions of the wall normal co-ordinate, it is natural to expand the disturbance quantities in the following manner,

$$\{u', v', w', p'\}^T = \{f(y), \varphi(y), h(y), \pi(y)\}^T exp\{i(\alpha x + \beta z - \omega t)\} \tag{2.3.12}$$

Here the disturbance amplitudes f, ϕ, h and π are the complex amplitude functions and ω is the dimensionless circular frequency, $(= \omega^* L/U_e)$. When Eqn. (2.3.12) is substituted in Eqns. (2.3.8) - (2.3.11), the following ordinary differential equations result,

$$i\{\alpha U + \beta W - \omega\}f + U'\phi = -i\alpha\pi + \frac{1}{Re}\{f'' - (\alpha^2 + \beta^2)f\} \tag{2.3.13}$$

$$i\{\alpha U + \beta W - \omega\}\phi = -\pi' + \frac{1}{Re}\{\phi'' - (\alpha^2 + \beta^2)\phi\} \tag{2.3.14}$$

$$i\{\alpha U + \beta W - \omega\}h + W'\phi = -i\beta\pi + \frac{1}{Re}\{h'' - (\alpha^2 + \beta^2)h\} \tag{2.3.15}$$

and

$$i\{\alpha f + \beta h\} + \phi' = 0 \tag{2.3.16}$$

In these equations, primes indicate differentiation with respect to y. One can rewrite these equations as a set of six first order equations and thus one would require six boundary conditions to solve them simultaneously. For the stability analysis, above equations are solved subject to homogeneous boundary conditions that are compatible with the governing equations. For example at the wall, one uses the no-slip boundary conditions,

$$f(0) = \phi(0) = h(0) = 0 \tag{2.3.17}$$

At the free stream (i.e. as $y \to \infty$) one requires the disturbance velocity components to decay to zero i.e.

$$f(y), \phi(y), h(y) \to 0 \quad as \quad y \to \infty \tag{2.3.18}$$

Non-trivial solutions of Eqns. (2.3.13) - (2.3.16) subject to homogenous boundary conditions (2.3.17) and (2.3.18) will exist only for particular combinations of the parameters α, β, ω, and Re. This then produces the dispersion or eigenvalue relation as

$$g(\alpha, \beta, \omega, Re) = 0 \tag{2.3.19}$$

It is also possible to reduce Eqns. (2.3.13) - (2.3.16) to a single ordinary differential equation for the unknown ϕ. One can combine the first and the third equation in that set to form an equation for $\{\alpha f + \beta h\}$. This variable can be replaced by using the fourth equation (2.3.16), and after differentiation with respect to y and eliminating π' by using the second equation one gets the following equation for ϕ,

$$\begin{aligned} &\phi^{iv} - 2\{\alpha^2 + \beta^2\}\phi'' + \{\alpha^2 + \beta^2\}^2\phi = \\ &\quad iRe\{\{\alpha U + \beta W - \omega\}[\phi'' - \{\alpha^2 + \beta^2\}\phi] - \{\alpha U'' + \beta W''\}\phi\} \end{aligned} \tag{2.3.20}$$

This is the well-known Orr-Sommerfeld equation (OSE) that forms the major tool for the investigation of flow instability. If one considers two-dimensional disturbance field in a two-dimensional mean flow then the above equation transforms to the simpler form,

$$\phi^{iv} - 2\alpha^2\phi'' + \alpha^4\phi = iRe\{\{\alpha U - \omega\}[\phi'' - \alpha^2\phi] - \alpha U''\phi\} \tag{2.3.21}$$

Thus, the Orr-Sommerfeld equation is a fourth order ODE and has same form whether the mean flow is three- or two-dimensional. Same observation can be made with respect to the disturbance field as well for special cases.

This fact can be exploited to relate more general cases to Eqn. (2.3.21). It is illustrated for 2D mean flow with 3D disturbance field below. Setting $W \equiv 0$ and using the following transformations in (2.3.20),

$$\alpha^2 + \beta^2 = \tilde{\alpha}^2 \;\; ; \;\; \omega\, \tilde{\alpha} = \tilde{\omega}\, \alpha \quad and \quad Re \;\; \alpha = \;\; \tilde{Re}\, \tilde{\alpha} \tag{2.3.22}$$

One gets the following governing equation,

$$\phi^{iv} - 2\tilde{\alpha}^2\phi'' + \tilde{\alpha}^4\phi = i\, \tilde{Re}\{\{\tilde{\alpha}\, U - \tilde{\omega}\}[\phi'' - \tilde{\alpha}^2\phi] - \tilde{\alpha}U''\, \phi\} \tag{2.3.23}$$

In essence, Eqns. (2.3.20) and (2.3.23) are identical - expressed for different parameters, where the parameters are related via Eqn. (2.3.22). The mean flow U is real and unchanged and if α and β are real, then a three-dimensional stability problem at a Reynolds number Re has been reduced to a two-dimensional problem at the lower Reynolds number $\tilde{Re}$. This is known as the **Squire's theorem**, and formally stated as:

In a two-dimensional boundary layer with real wave numbers, instability appears first for two-dimensional disturbances.

We must, however, note that the utility of the Squire's theorem is lost if the mean flow is three dimensional or if α and β are complex, as in spatial stability problems.

2.3.2 Temporal and Spatial Amplification of Disturbances

If α, β and ω are all real, then from Eqn. (2.3.12) one can see that the disturbances propagate through the shear layer with constant amplitude at all times. However, if α and β are real and ω is complex, then according to Eqn. (2.3.12) the disturbances will grow or decay with time. In contrast, if ω is real and α, β are complex then the disturbance amplitude will not change with time, but they will change with x and z. The former case, where the disturbance amplitude change with time, is a subject dealt with in *temporal amplification theory* and the latter is the subject of *spatial amplification theory.* If all the three quantities α, β and ω are complex, then the disturbances grow in both space and time and is the subject matter of *spatio-temporal theory.*

2.3.2.1 Temporal Amplification Theory

With $\omega = \omega_r + i\omega_i$ and (α, β) real, the disturbance can be written as,

$$q'(x, y, z, t) = \{\hat{q}(y)e^{\omega_i t}\} \;\; e^{i(\alpha x + \beta z - \omega_r t)} \tag{2.3.24}$$

The magnitude of the wave number vector is $\bar{\alpha} = \{\alpha^2 + \beta^2\}^{\frac{1}{2}}$ and the angle between the wave number vector and the x-axis is given by $\psi = \tan^{-1}\{\beta/\alpha\}$. The phase speed of the disturbance field is given by $c_{ph} = \omega_r/\bar{\alpha}$. If A represents the magnitude of the disturbance at a particular height y, then it follows from Eqn. (2.3.24),

$$\frac{1}{A}\frac{dA}{dt} = \omega_i \tag{2.3.25}$$

Thus, ω_i is the *amplification rate* in the temporal theory. If

$$\omega_i < 0 \Rightarrow \tag{2.3.26a}$$

then the disturbances are *damped*.
If, on the other hand

$$\omega_i = 0 \Rightarrow \tag{2.3.26b}$$

then the disturbances are *neutral*.

Finally, if

$$\omega_i > 0 \Rightarrow \tag{2.3.26c}$$

then the disturbances *amplify* with time.

2.3.2.2 Spatial Amplification Theory

In this theory, ω is treated as real and the wave number components are complex:

$$\alpha = \alpha_r + i\alpha_i \quad and \quad \beta = \beta_r + i\beta_i. \tag{2.3.27}$$

Thus, one can write the disturbance field as,

$$q'(x, y, z, t) = \{\hat{q}(y)e^{-(\alpha_i x + \beta_i z)} \; e^{i(\alpha_r x + \beta_r z - \omega t)} \tag{2.3.28}$$

If one defines,

$$\bar{\alpha}_r = \{\alpha_r^2 + \beta_r^2\}^{1/2} \quad and \quad \psi = \tan^{-1} \; \beta_r/\alpha_r \tag{2.3.29}$$

Then the phase speed of the disturbance field is given by, $c_{ph} = \omega/\bar{\alpha}_r$. Additionally, if one defines $\bar{\alpha}_i = \{\alpha_i^2 + \beta_i^2\}^{1/2}$ and $\bar{\psi} = \tan^{-1} \; (\beta_i/\alpha_i)$, then one can define two new directions, $\tilde{x}$ along $\bar{\alpha}_r$ and $\bar{x}$ along $\bar{\alpha}_i$ and rewrite (2.3.28) as,

$$q'(x, y, z, t) = \hat{q}(y) \; e^{-\bar{\alpha}_i \bar{x}} \; e^{i(\bar{\alpha}_r \tilde{x} - \omega t)} \tag{2.3.30}$$

Thus, one can similarly write a spatial amplification rate in the particular direction given by $\bar{\psi}$ as,

$$\frac{1}{A}\frac{dA}{d\bar{x}} = -\bar{\alpha}_i \tag{2.3.31}$$

The amplification rates are different in different directions and of course, different $\bar{\alpha}_i$ are themselves function of $\bar{\psi}$. For three- dimensional waves the spatial theory comes with lot more complications as compared to temporal theory. In addition to the wave orientation angle ψ, the amplification direction $\bar{\psi}$ must also be specified before any calculation can be made. Once again, if

$$\bar{\alpha}_i > 0 \Rightarrow \tag{2.3.32a}$$

then this corresponds to a *damped* solution.
On the other hand, if

$$\bar{\alpha}_i = 0 \Rightarrow \tag{2.3.32b}$$

then this corresponds to *neutral stability.*
Finally, if

$$\bar{\alpha}_i < 0 \Rightarrow \tag{2.3.32c}$$

then we have situation of *instability.*

2.3.2.3 Relationship Between Temporal and Spatial Theories

Consider the general dispersion relation

$$\omega = \omega(\alpha, \beta, Re, ...) \tag{2.3.33}$$

From this, we can obtain the group velocity components for the three-dimensional disturbance field in the x- and z- directions, respectively as

$$\vec{V_g} = (\frac{\partial\omega}{\partial\alpha}\ ,\ \frac{\partial\omega}{\partial\beta}) \tag{2.3.34}$$

In *temporal theory*, one uses $\omega = \omega_r$ and in *spatial theory* one uses $\alpha = \alpha_r$ and $\beta = \beta_r$ in Eqn. (2.3.34). The imaginary part of the group velocity is usually neglected. For parallel flows, one can form a spatial amplification rate by following the wave with the group velocity i.e.

$$\frac{d}{dt} = \vec{V_g}\ \frac{d}{d\bar{x}} \tag{2.3.35}$$

where $\bar{x}$ is chosen in the direction of $\vec{V_g}$. Consequently,

$$\bar{\alpha}_i = -\frac{\omega_i}{|\vec{V_g}|^2}\ \vec{V_g} \tag{2.3.36}$$

and the direction of $\bar{\alpha}_i$ is obtained from

$$\bar{\psi} = \tan^{-1}\left[\frac{\partial\omega_r/\partial\beta}{\partial\omega_r/\partial\alpha}\right] \tag{2.3.37}$$

For two-dimensional flows, such a relation was used by Schlichting (1939) without any proof and was later provided in Gaster (1962). But, this can be shown for general disturbance field by noting that ω is an analytic complex function of α and β. Therefore, one can use the Cauchy- Riemann equation valid for complex analytic functions and here, these are given by,

$$\frac{\partial\omega_r}{\partial\alpha_r} = \frac{\partial\omega_i}{\partial\alpha_i}, \quad \frac{\partial\omega_r}{\partial\alpha_i} = -\frac{\partial\omega_i}{\partial\alpha_r} \tag{2.3.38}$$

and

$$\frac{\partial\omega_r}{\partial\beta_r} = \frac{\partial\omega_i}{\partial\beta_i}, \quad \frac{\partial\omega_r}{\partial\beta_i} = -\frac{\partial\omega_i}{\partial\beta_r} \tag{2.3.39}$$

For three- dimensional disturbances, the left hand side of the first equations of (2.3.38) and (2.3.39) are the group velocity components as defined by (2.3.34). Also note that $\frac{\partial\omega_i}{\partial\alpha_i}$ can be approximated by noting that ω_i decreases from its temporal value to zero in the spatial theory as α_i goes from zero to its value as obtained in the spatial theory. If the amplification rates are small, as they are in a linear theory, then the above variations are linear and thus, $\frac{\partial\omega_i}{\partial\alpha_i} \simeq -\frac{\omega_i}{\alpha_i}$.

Therefore,

$$[V_g]_x = -\frac{\omega_i}{\alpha_i} \tag{2.3.40}$$

For three- dimensional disturbances, if $\bar{\psi}$ is specified arbitrarily and the x-axis is rotated to lie in the $\bar{\psi}$ direction, then Eqn. (2.3.36) will apply with α_i replaced by $\bar{\alpha}_i$ and V_g by the component of group velocity in the $\bar{\psi}$ direction.

2.4 Properties of Orr-Sommerfeld Equation and Boundary Conditions

For the stability analysis of fluid dynamical system whose equilibrium solution is given by a parallel or quasi-parallel flow, one has to solve the Orr-Sommerfeld equation depending on whether the mean flow is two- or three-dimensional. For the two-dimensional problem equivalent boundary conditions are given by,

$$At \quad y = 0: \quad f, \;\; \phi = 0 \tag{2.4.1a}$$

$$And \ \ as \quad y \to \infty : \quad f, \ \ \phi \to 0 \tag{2.4.1b}$$

To solve Eqn. (2.3.21), above boundary conditions have to be transformed in terms of ϕ for two-dimensional disturbance field as,

$$\phi' = -i\alpha f \tag{2.4.2}$$

Thus, one has to satisfy homogeneous boundary conditions for ϕ and ϕ' at both the boundaries for wall-bounded shear flows. The consequence of far stream boundary conditions as given by (2.4.1b) is understood by using the mean flow information at $y \to \infty : \quad U(y) = 1$ and $U''(y) \equiv 0$ in (2.3.21). One gets the following constant coefficient ODE at $y \to \infty$:

$$\phi^{iv} - 2\alpha^2\phi'' + \alpha^4\phi = i\,Re\{(\alpha - \omega)(\phi'' - \alpha^2\phi)\} \tag{2.4.3}$$

Solution of the above can be obtained in the form, $\phi \ \sim e^{\lambda y}$, so that one gets the characteristic roots as, $\lambda_{1,2} = \mp\alpha$ and $\lambda_{3,4} = \mp Q$, where $Q = [\alpha^2 + i\alpha\, Re(1-c)]^{1/2}$. For boundary layer instability problems, $Re \to \infty$ and then $|Q| >> |\alpha|$. This is the source of stiffness that makes obtaining the numerical solution of (2.3.21) a daunting task. This causes the fundamental solutions of the Orr-Sommerfeld equation to vary by different orders of magnitude near and far away from the wall. This type of behaviour makes the governing equation a *stiff differential equation* that suffers from the growth of *parasitic error*, while numerically solving it.

In general, Orr-Sommerfeld equation is a fourth order ODE and thus, will have four fundamental solutions whose asymptotic variation for $y \to \infty$, is given by the characteristic exponents of (2.4.3) i.e.

$$\phi = a_1\phi_1 + a_2\phi_2 + a_3\phi_3 + a_4\phi_4 \tag{2.4.4}$$

Where, at the free stream $(y \to \infty) : \phi_1 \sim e^{-\alpha y}$; $\phi_2 \sim e^{\alpha y}$; $\phi_3 \sim e^{-Qy}$ and $\phi_4 \sim e^{Qy}$.

To satisfy the boundary condition given in (2.4.1b), one must have: $a_2 = a_4 = 0$. Then the general solution is of the form,

$$\phi = a_1\phi_1 + a_3\phi_3 \tag{2.4.5}$$

This is an admissible solution of Eqns. (2.4.21) and/ or (2.4.23) that satisfies one set of boundary conditions, (2.4.1b) automatically. The two remaining constants in the solution (2.4.5) can be fixed by satisfying the boundary conditions given by (2.4.1a) as,

$$a_1\phi_1(y = 0, \ \alpha\,; \omega, \ Re) + a_3\phi_3(y = 0, \ \alpha\,; \omega, \ Re) = 0 \tag{2.4.6}$$

$$a_1\phi_1'(y=0,\ \alpha\,;\omega,\ Re) + a_3\phi_3'(y=0,\ \alpha\,;\omega,\ Re) = 0 \tag{2.4.7}$$

We will get a non-trivial solution for these, if and only if the determinant of the associated matrix of the linear algebraic system given by above equations is zero i.e.,

$$(\phi_1\phi_3' - \phi_1'\phi_3)_{y=0} = 0 \tag{2.4.8}$$

This is the characteristic equation for the eigenvalues posed by the Orr-Sommerfeld equation that also can be viewed as the dispersion relation of the problem. So the task at hand is to obtain a combination of α and ω for a given Re, such that the solution of OSE satisfies (2.4.8). The stiffness of OSE causes the numerical solution to lose the *linear independence* of different solution components corresponding to the different fundamental solutions. This is the source of *parasitic error* growth of any *stiff differential equation*. To remove this problem in a straight forward manner, one can use the Compound Matrix Method (CMM).

As discussed in Drazin & Reid (1981), there are three principal methods for solving linear stability problems and they are: (a) Matrix method based on finite difference or spectral discretizations; (b) Shooting techniques along with orthogonalization of the fundamental solutions and (c) Shooting with CMM. As discussed in Allen & Bridges (2002), eigenvalue problems in infinite domain matrix methods based on finite difference and spectral method produce spurious eigenvalues due to problems in satisfying boundary conditions correctly, to preserve linearity in the parameters and due to fracturing of the continuous spectra. Shooting methods based on orthogonalization are cumbersome to program and require comparatively large computer memory while producing non-analytic solutions. Considering these, CMM is the best available method for hydrodynamic stability problems. This method has been reformulated by Allen & Bridges (2002a) using exterior algebra to make the method coordinate free. CMM has been in use for stability calculations for over last two decades- as reported in Drazin & Reid (1981), Ng & Reid (1980, 1985), Sengupta (1992), Sengupta & Venkatasubbaiah (2006). Advantages of CMM as compared to other methods have been described in these references above. Otherwise there are other methods based on ODE solver in physical plane (See Scott & Watts (1977)) or spectral collocation method that involves Chebyshev discretization of the Orr-Sommerfeld equation as given in Schmid & Henningson (2000).

2.4.1 Compound Matrix Method

Compound matrix method (CMM) has been in use for stability calculations for over last two decades, as the original method was reported in Ng & Reid (1980, 1985). Advantages of CMM as compared to other methods of solving stiff differential equations have been described above. Additionally, its main strength lies in its simplicity of application and interpretation of the results. CMM not only yields satisfactory results for the evaluation of eigenvalues and eigenfunctions of the Orr- Sommerfeld equation, but it also brings in to fore the analytic structure of the solution. For these reasons CMM is recommended here to readers. Moreover, because of the specific structure it is possible to solve both the stability and the receptivity problems without a great deal of effort in coding. Some essential modifications for appropriate choice of equation in CMM are reported in Sengupta (1992).

In this method, instead of working with ϕ one works with a new set of variables that are combinations of the fundamental solutions ϕ_1 and ϕ_3. These new variables all vary with y at the identical rate, removing the stiffness problem. For the Orr-Sommerfeld equation the new variables are (for details about these new variables see Drazin & Reid (1981), Sengupta (1992)),

$$\begin{aligned} y_1 &= \phi_1\phi_3' - \phi_1'\phi_3 \\ y_2 &= \phi_1\phi_3'' - \phi_1''\phi_3 \\ y_3 &= \phi_1\phi_3''' - \phi_1'''\phi_3 \\ y_4 &= \phi_1'\phi_3'' - \phi_1''\phi_3' \\ y_5 &= \phi_1'\phi_3''' - \phi_1'''\phi_3' \\ y_6 &= \phi_1''\phi_3''' - \phi_1'''\phi_3'' \end{aligned} \tag{2.4.9}$$

It is easy to verify with the help of solution of Eqn. (2.4.3) in the free-stream that y_1 to y_6 have identical growth rate, as one integrates from the free-stream to the wall. From the definition given above in (2.4.9), one gets the following,

$$y_1' = \phi_1'\phi_3' + \phi_1\phi_3'' - \phi_1'\phi_3' - \phi_1''\phi_3 = y_2 \tag{2.4.10a}$$

$$\begin{aligned} y_2' &= (\phi_1\phi_3''' - \phi_1'''\phi_3) + (\phi_1'\phi_3'' - \phi_1''\phi_3') = y_3 + y_4 \\ y_3' &= \phi_1\phi_3^{iv} + (\phi_1'\phi_3''' - \phi_1'''\phi_3') - \phi_3\phi_1^{iv} \end{aligned} \tag{2.4.10b}$$

From Eqn. (2.3.21),

$\phi_1^{iv} = \{2\alpha^2 + i\alpha\, Re\{U-c\}\}\phi_1' - \{\alpha^4 + i\alpha^3\, Re\{U-c\} + i\alpha\, Re\, u''\}\phi_1$
or $\phi_1^{iv} = b_1\phi_1'' - b_2\phi_1$

Similarly a relation for ϕ_3^{iv} can be obtained and one can simplify to obtain, $\phi_1\phi_3^{iv} - \phi_1^{iv}\phi_3 = b_1 y_2$. Thus,

$$y_3' = b_1 y_2 + y_5 \tag{2.4.10c}$$

$$\begin{aligned} y_4' &= \phi_1'\phi_3''' + \phi_1''\phi_3'' - \phi_1''\phi_3'' - \phi_1'''\phi_3' = y_5 \\ y_5' &= \phi_1'\phi_3^{iv} + \phi_1''\phi_3''' - \phi_1^{iv}\phi_3' - \phi_1'''\phi_3'' \\ &= \{\phi_1''\phi_3''' - \phi_1'''\phi_3''\} + \phi_1'\{b_1\phi_3'' - b_2\phi_3\} - \phi_3'\{b_1\phi_1'' - b_2\phi_1\} \end{aligned} \tag{2.4.10d}$$

$$= y_6 + b_1 y_4 + b_2 y_1 \tag{2.4.10e}$$

$$y_6' = \phi_1''\phi_3^{iv} + \phi_1'''\phi_3''' - \phi_1'''\phi_3''' - \phi_1^{iv}\phi_3'' = b_2 y_2 \tag{2.4.10f}$$

Equations (2.4.10a) to (2.4.10f) are six first order ODEs for the six unknown variables y_1 to y_6. Note that the order of system is increased from four to six in CMM, while the governing equation is transformed from a boundary value problem to an initial value problem. To solve these six equations, we therefore need to generate initial conditions for the unknowns. As we know the property of the fundamental solutions in the free stream, we can use that information to generate the initial conditions for y_1 to y_6. As at $y \to \infty : \phi_1 \sim e^{-\alpha y}$ and $\phi_3 \sim e^{-Qy}$, therefore we can estimate the free stream values of the unknown as,

$$y_1 \sim \{-Q + \alpha\}\, e^{-(\alpha+Q)y} \tag{2.4.11a}$$

$$y_2 \sim \{Q^2 - \alpha^2\}\, e^{-(\alpha+Q)y} \tag{2.4.11b}$$

$$y_3 \sim \{-Q^3 + \alpha^3\}\, e^{-(\alpha+Q)y} \tag{2.4.11c}$$

$$y_4 \sim \{-\alpha Q^2 + \alpha^2 Q\}\, e^{-(\alpha+Q)y} \tag{2.4.11d}$$

$$y_5 \sim \{\alpha Q^3 - \alpha^3 Q\}\, e^{-(\alpha+Q)y} \tag{2.4.11e}$$

$$y_6 \sim \{-\alpha^2 Q^3 + \alpha^3 Q^2\}\, e^{-(\alpha+Q)y} \tag{2.4.11f}$$

Note that in (2.4.11), all the variables have the same exponential rate of growth or attenuation- a special feature of CMM where the problem of stiffness is removed by the specific choice of new variables. In integrating (2.4.10), one can start off with the values given by (2.4.11), with variables normalized with respect to one of them. Let us normalize every variable with respect to y_1, so that the initial conditions for solving Eqns. (2.4.10) are then,

$$y_1 = 1.0 \tag{2.4.12a}$$

$$y_2 = -\{\alpha + Q\} \tag{2.4.12b}$$

$$y_3 = \alpha^2 + \alpha Q + Q^2 \tag{2.4.12c}$$

$$y_4 = \alpha Q \tag{2.4.12d}$$

$$y_5 = -\alpha Q\{\alpha + Q\} \tag{2.4.12e}$$

$$y_6 = \alpha^2 Q^2 \tag{2.4.12f}$$

One solves Eqns. (2.4.10), starting off from the free stream to the wall, with the initial condition provided in (2.4.12). After marching up to the wall, observe that the satisfaction of characteristic equation (2.4.8) is equivalent to locating (α, ω) combinations for a given Re is exactly equivalent to enforcing

$$y_1 = 0 \;\; at \;\; y = 0 \tag{2.4.13}$$

Having recast the problem in CMM in terms of the new variables, one can calculate the eigenvalues very quickly. That leaves one with the task of finding out the corresponding eigenvector(s). This also can be done readily by noting that the eigenvector ϕ is a linear combination of ϕ_1 and ϕ_3 such that,

$$\phi = a_1\phi_1 + a_3\phi_3 \tag{2.4.14a}$$

$$\phi' = a_1\phi_1' + a_3\phi_3' \tag{2.4.14b}$$

$$\phi'' = a_1\phi_1'' + a_3\phi_3'' \tag{2.4.14c}$$

$$\phi''' = a_1\phi_1''' + a_3\phi_3''' \tag{2.4.14d}$$

One can eliminate a_1 and a_3 from Eqns. (2.4.14) using Eqns. (2.4.10) in many ways. This leads us to the following differential equations for ϕ,

$$y_1\phi'' - y_2\phi' + y_4\phi = 0 \tag{2.4.15a}$$

$$y_1\phi''' - y_3\phi' + y_5\phi = 0 \tag{2.4.15b}$$

$$y_2\phi''' - y_3\phi'' + y_6\phi' = 0 \tag{2.4.15c}$$

$$y_4\phi''' - y_5\phi'' + y_6\phi' = 0 \tag{2.4.15d}$$

In principle, having obtained y_1 to y_6 for all y's, it is possible to obtain ϕ by solving any one of the four equations listed above. It is noted that the retained fundamental solutions automatically satisfies the far stream boundary conditions and thus one can solve any one of the equations in (2.4.15) starting from the wall and marching towards free stream. The homogeneous boundary conditions given by Eqn. (2.4.1a) can not be used as the initial condition to march out from the wall to free-stream, as the differential equations in (2.4.15) are homogeneous. For stability problems, one should provide a non-trivial normalized boundary conditions as discussed in Sengupta & Venkatasubbaiah (2006), instead of (2.4.1a). While for receptivity problems, the wall boundary conditions are inhomogeneous and raises no problems at all. This is the benefit of CMM where a difficult boundary value problem is replaced by two relatively easier initial value problems.

Presence of four alternatives in (2.4.15) raises the question of which equation is more accurate and consistent for the solution process. Thus, it is important to know which equations from the set given in (2.4.15) are to be solved. This was shown in Sengupta (1992) that the eigenvectors cannot be obtained by all the four equations, for high Reynolds numbers and/ or high Wave numbers. It was shown clearly in Sengupta (1992) that the third equation (2.4.15c), produced divergent results for high wave numbers due to the following reason.

All the four equations (2.4.15a) to (2.4.15d), reduce to constant coefficient ODEs at the free stream, for which one can use the values provided in Eqn. (2.4.12) for the compound matrix variables. It is easy to see that Eqn. (2.4.15c) has three characteristic roots at the free stream given by $-\alpha$, $-Q$ and $\frac{\alpha Q}{\alpha+Q}$. The first two roots correspond to the fundamental solutions ϕ_1 and ϕ_3, but the third root is not only extraneous, but is also unstable!

Thus, for the solution of (2.3.21) subject to boundary conditions (2.4.1a) and (2.4.1b), this spurious mode will not satisfy the free stream boundary condition. For moderate to high Reynolds numbers (as will be case for all post-critical, but pre-transitional flows), $|Q| >> |\alpha|$ and the third characteristic root can be simplified to $\frac{\alpha Q}{\alpha+Q} \simeq \alpha$. Thus, this third mode is a close approximation to ϕ_2 that does not satisfy the boundary condition (2.4.1b). It is possible to miss out this problem- as was the case in Gaster (1987) and Davey (1982), where results were reported using the third equation. The problem associated with the above growing mode was not observed because the leading eigenvalue of such problems is usually very small and if the far stream boundary is not taken far enough outside the shear layer, this problem remains masked. However, when one wants to solve a receptivity problem, one needs to solve Orr-Sommerfeld equation for a large range of α's and there this problem becomes very apparent. This was the case investigated in Sengupta *et al.* (1994) for the receptivity of Blasius boundary layer.

Above investigation for the behaviour of the solution at the free stream can be extended to other equations of (2.4.15) to check their usefulness in obtaining the eigen function. At the free stream the characteristic roots for Eqn. (2.4.15a) are $\{-\alpha, -Q\}$. Equation (2.4.15b) being a third order equation has three roots given by $[-\alpha, -Q, \{\alpha + Q\}]$. Thus, this equation is also violently unstable, even for low wave numbers and Reynolds numbers. Equation (2.4.15c) has the asymptotic behaviour for large y's as dictated by the characteristic roots given by $[-\alpha, -Q, \frac{\alpha Q}{\alpha+Q}]$. Finally, the characteristic roots for Eqn. (2.4.15d) are given by $\{-\alpha, -Q, 0\}$ i.e. one mode is neutral for large values of y. One sees that the first and the fourth equations are compatible with the required formulation and boundary condition, while the second and third equations are unstable (when the shear layer is excited at the wall) and need to be avoided. While Drazin & Reid (1981) mentioned that *it is certainly not obvious which one is best for numerical purposes"*, this simple analysis tells us about the correct choice of the equation as either (2.4.15a) or (2.4.15d). In obtaining eigenfunctions of the stability problem defined via Orr-Sommerfeld equation, it is noted that Eqn. (2.4.15a) is not suitable because y_1 at the wall is zero. It was suggested by Ng & Reid (1981) that this difficulty can be overcome, by integrating (2.3.21) itself a few steps from the wall before switching over to Eqn. (2.3.15a). At the wall, it is observed that while ϕ and ϕ' are zero, ϕ'' is indeterminate. The value of ϕ'' therefore can be arbitrarily set equal to any value and then either (2.4.15a) or (2.4.15d) can be solved, avoiding the above suggestion of Ng & Reid (1981). This procedure has been followed in Sengupta & Venkatasubbaiah (2006). While solving receptivity problems, the boundary conditions are the

prescribed non-zero values and the problem of starting solution for stability analyses does not arise. However, another problem may bedevil the CMM for obtaining eigenfunctions of (2.3.21) for high Reynolds numbers. This is due to the dynamic ranges of the compound matrix variables inside the shear layer. For example, in Eqn. (2.4.15a) one would require accurate calculation of the ratio of $\frac{y_2}{y_1}$ and $\frac{y_4}{y_1}$. These ratios exhibit very large variations near the wall, where y_1 is close to zero. This causes the eigensolution to be highly oscillatory. For Eqn. (2.4.15d) the ratios $\frac{y_5}{y_4}$ and $\frac{y_6}{y_4}$ are of order one and non-oscillatory. Thus, the eigenfunction obtained by solving equation (2.4.15d) are quite regular, as seen from the results in Sengupta *et al.* (1994) for a receptivity problem. The problems of solving Orr-Sommerfeld equation analytically for very large values of α can be handled in a satisfactory way by looking for asymptotic solution, that will be dealt later.

2.5 Instability Analysis from Solution of Orr-Sommerfeld Equation

The Orr- Sommerfeld equation can be solved either as a temporal or as a spatial instability problem. For disturbance field created as a consequence of a localized excitation inside boundary layers, the temporal growth of the disturbance field is not realistic. It has been observed phenomenologically that for attached flows, instability is usually of a convective type and obtaining solution by spatial analysis is the appropriate one. In chapter 4, we will note that even for such a problem there can be spatio-temporally growing wave-fronts that dominate in attached boundary layers that are noted to be spatially stable. Such a problem is not evident for flows those are spatially unstable. The monograph by Betchov & Criminale (1967) specifically talks about temporal growth of disturbances in shear layers and the readers are referred there for detailed expositions.

Let us therefore discuss about spatial instability of parallel flows, mainly the flow past a flat plate at zero angle of attack- a problem that enjoys a canonical status for instability analyses. For the spatial instability problem associated with two-dimensional disturbance field of two-dimensional primary flows, the disturbance quantities will have the appearance of Eqn. (2.3.28) with $\beta = 0$. Thus for a fixed Re, one would be looking for complex α when the shear layer is excited by a fixed frequency source of circular frequency, ω_0. If we define Re in terms of the displacement thickness δ^* as the length scale, then $Re = \frac{U_e \delta^*}{v}$ and the results obtained will be plotted as contours of constant amplification rates α_i in $(Re - \omega_0)-$ plane, as shown in Fig. 2.2.

The solid line in the figure corresponds to $\alpha_i = 0$ and represents the

condition of neutral stability and hence this is called the *neutral curve*. The area inside the neutral curve corresponds to $\alpha_i < 0$ and hence represents flow instability for these parameter combinations. Similarly the area outside the *neutral curve* corresponds to stable disturbances in the shear layer. It is noted that the foremost position of the *neutral curve* occurs for $Re = 519.23$ and corresponds to the fact that the flow is stable below this value of Re for all circular frequencies. Hence this value of the Reynolds number is called the *critical Reynolds number*. There is also similarly an upper bound corresponding to the circular frequency above which the disturbance field is going to be stable. It is customary to call the lower part of the *neutral curve* as the *branch I*, while the upper part of the neutral curve is called the *branch II*. This picture corresponds to the stability portrait of the system, as obtained using a linear theory, making a parallel flow approximation.

Note that the circular frequency of Fig. 2.2 is non-dimensional, based on the length scale, δ^* and velocity scale, U_e. Thus,

$$\omega_0 = 2\pi\ f\ \frac{\delta^*}{U_e} = (\frac{2\pi\ f}{\nu U_e^2})\frac{U_e\delta^*}{\nu} = F\ Re \tag{2.5.1}$$

In this equation, F is the non-dimensional physical frequency of excitation. Thus, a constant physical frequency line in the $(Re - \omega_0)$-plane is a straight line passing through the origin and different constant frequency lines have slopes that corresponds to different values of F. Let us consider a physical frequency of excitation f_1, as shown in Fig. 2.2. If the point of origin of the disturbance (say, at the point A) is outside the neutral curve, then the created disturbances will be decaying to begin with, and one must follow the corresponding constant- frequency F-line, ABC. Once the disturbance crosses a location corresponding to B at the *branch I* of the neutral curve, from that point onwards the disturbance will amplify as it propagates downstream, until the line hits the *branch II* of the neutral curve at C. Beyond that point, once again the disturbance will be damped. Now, let us say that the exciter is located at the same physical location but the frequency of excitation is increased to f_2, marked by the point P in the figure. Then, once again the disturbance will be damped in its early evolution till it reaches the point Q. In between Q and R the disturbance will amplify and beyond that it will again be damped. It is noted that the flow, within the parallel flow approximation, readjusts itself to the local condition in fixing the growth or decay rate.

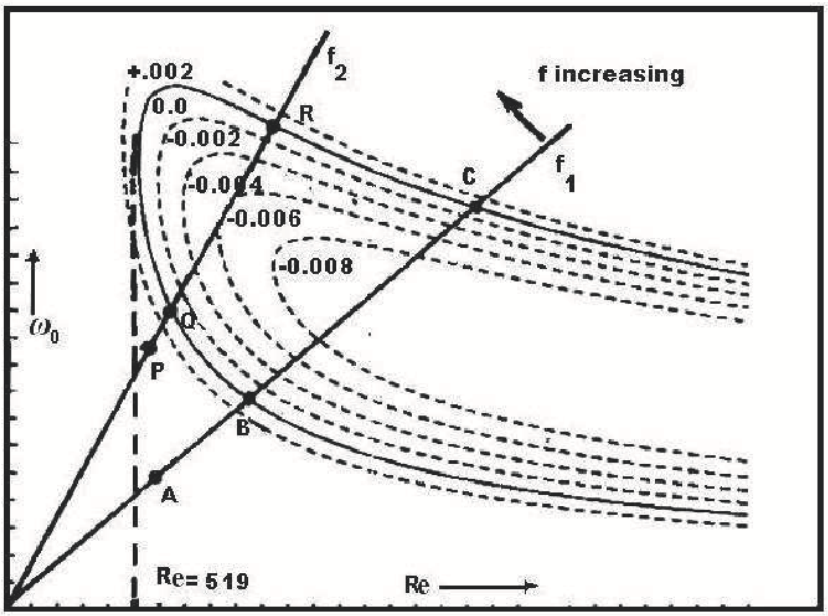

Figure 2.2 Contour plots of asymptotic growth rate in Reynolds number- circular frequency plane

There are additional aspects those need recounting here for viscous flow instability problems, other than the zero pressure gradient flow given by Blasius equation. If the *neutral curve* of Fig. 2.2 is extended to higher Reynolds numbers then the *branch I* and *branch II* tends towards each other i.e. the *neutral curve* closes on itself. In contrast, if the mean flow profile possesses an inflection point, the upper and the lower branches of the *neutral curve* remains distinct even when $Re \to \infty$. This is the case for wall-bounded flows with adverse pressure gradient, mixing layers, jets and wakes. Also, for such flows the critical Reynolds number, (Re_{cr}) is significantly lower than that for the zero pressure gradient flat plate boundary layer. This is relevant for flows past complex shapes, e.g. the flow over airfoils or wings.

Along with the constant-α_i contours, the constant-α_r contours can be plotted in the $(Re - \omega_0)$-plane, as shown in Fig. 2.3. The *neutral curve* is included in this figure to provide a reference. From this figure, it is noted

that the maximum wave number for instability of Blasius profile is given by $\alpha_{max}\delta^* \approx 0.35$ that corresponds to the smallest unstable waves such a shear layer supports whose wavelength is given by $\lambda_{min} = \frac{2\pi}{\alpha_{max}} \approx 18\delta^*$. Thus, the TS waves are significantly longer than the boundary layer thickness, justifying the quasi-parallel flow approximation for stability analysis.

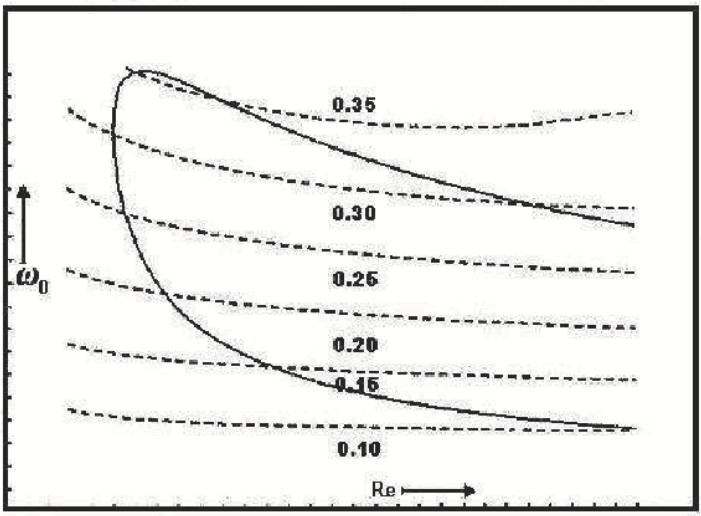

Figure 2.3 Contour plots of disturbance wave number in Reynolds number- circular frequency plane

Early corroboration of the linear viscous stability theory came from experiments where background disturbances were minimized to an extremely low value and simultaneously two-dimensional controlled disturbances were introduced in the flow. This was first performed and reported in the classic work of Schubauer & Skramstad (1947). These experiments were performed in the NBS wind tunnel with specially fitted damping screens that reduced the turbulence intensity of the oncoming flow by increasing the solidity ratio or number of such screens. In the experiments without explicit excitation, they could progressively shift the location of transition by reducing turbulence intensity all the way down to 0.08 percent. Further reduction in turbulence intensity had no effect on the position of the *natural transition*. The following figure taken from Schubauer & Skramstad (1947) reveals the

natural transition as observed when no extraneous excitation was imposed on the flow, for a flow speed of 53 ft/sec. Shown sequences in Fig. 2.4 are a set of film records made by photographing the oscillograph screen with a moving film camera.

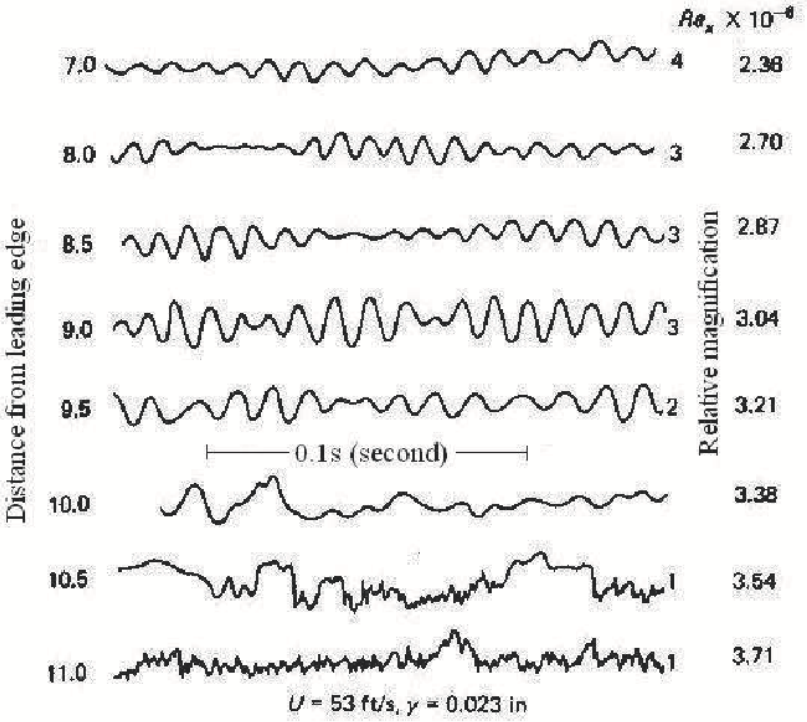

Figure 2.4 Hot-wire oscillogram traces showing natural transition from laminar to turbulent flow on a flat plate (From Schubauer & Skramstad, 1947)

For the first few frames the signal has been amplified in the figure for the ease of viewing, as indicated by the relative magnification on the right margin of the figure. While one can see sinusoidal oscillations at and up to 9 ft from the leading edge of the flat plate, it is also clear that the so-called *natural disturbances* are not purely *monochromatic* i.e., the disturbances with the oncoming flow have many harmonic components. To detect TS waves and circumvent noticing multi-harmonic disturbances, they next in-

troduced perfectly controlled two-dimensional disturbances by electromagnetically vibrating a phosphor-bronze ribbon (of 0.002 inches thickness and that was 0.1 inches wide) inside the shear layer, at a height of 0.006 inches from the plate. The positioning of this vibrator did not alter the mean flow, while it created pure sinusoidal oscillations starting from a little distance downstream from the ribbon. In this experiment, the *neutral curve* was charted out and compared with Schlichting's theoretical *neutral curve*. The agreement was remarkable and this led to complete justification of viscous stability theory of the Göttingen-school. Historically, it was Heisenberg who actually led this type of analysis under the guidance of Sommerfeld.

The natural background disturbance must be viewed as an irregular pattern of two- and three-dimensional wave packets with non-uniform spectral content. Also, the study of isolated spectral component is only a valid concept as long as non-linearity can be ignored and superposition principle valid. Furthermore, the stability analysis identifies a complex α for a given non-dimensional frequency ω_0 and Reynolds number, under the assumption of parallel flow. However, for low speed incompressible flow the shear layer thickness increases downstream even when the edge velocity is kept constant. Such growth is spectacular near the leading edge and the growth rate of the shear layer thickness is moderate to negligible, at larger distances from the leading edge of the flat plate. Hence the parallel flow analysis is more relevant for larger Reynolds numbers. For such flows, changes in boundary layer properties being very small, the stability analysis works locally and the TS wave generated at a given location, in its movement downstream, will adjust itself to the local property dictated by the dispersion relation. This local adjustment- as an assumption- is synonymous to what is known as *quasi-parallel assumption*.

2.5.1 Local and Total Amplification of Disturbances

The Reynolds number at observed transition location (defined as a location where the intermittency factor is about 0.1 i.e. the flow is 10 % of time turbulent and rest of the time it is laminar) for zero pressure gradient flat plate boundary layer is of the order of 3.5×10^5. This corresponds to $Re^*_\delta = 950$. The distance between the point of instability and the point of transition depends on the degree of amplification and the kind of disturbance present with the oncoming flow. This calls for a study of local and total amplification of disturbances. The following description is as developed in Arnal (1984) for two-dimensional incompressible flows.

Consider the application of spatial theory for a wall-bounded external flow. On the top panel of Fig. 2.5, we once again show the *neutral curve*

in the $(Re - \omega_0)$-plane. If we focus our attention on a particular frequency f_1, then we will follow that ray emanating from the origin. According to this figure, this disturbance will decay up to $x = x_0$ from the leading edge. This, thereafter, will grow till $x = x_1$ i.e. up to the location where the ray intersects the branch II.

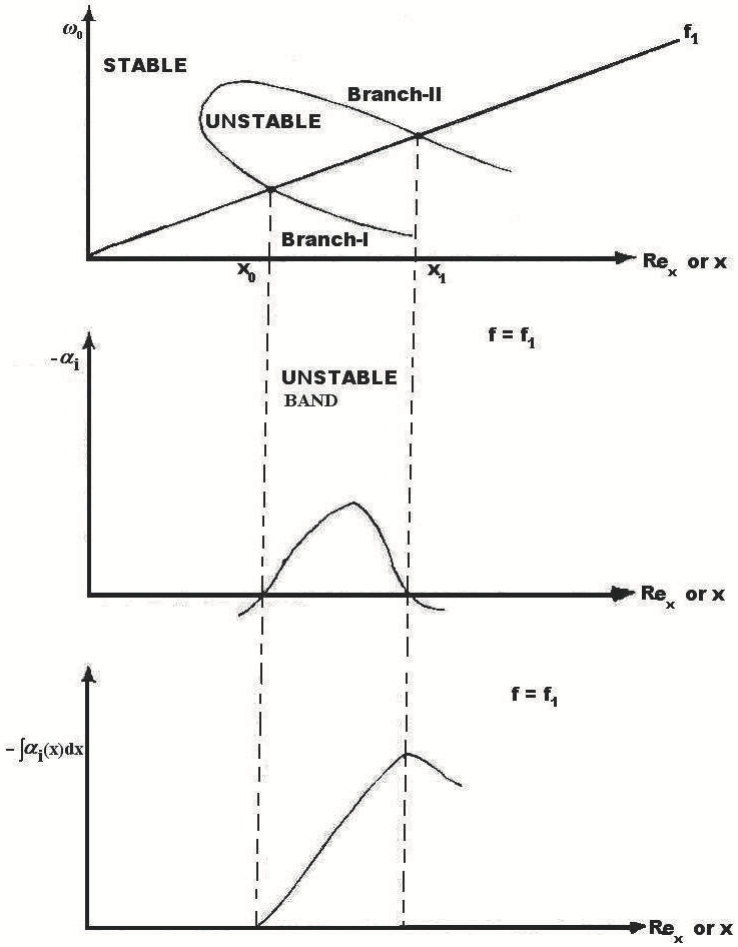

Figure 2.5 Sketch of local and total amplification of the disturbance field

The amplification rate suffered by the disturbances within the neutral curve is shown in the middle panel of Fig. 2.5. Note the sign of the plotted rate, with negative values plotted along the positive ordinate direction. For two-dimensional disturbances in two-dimensional mean flow, the amplification rate can be expressed as,

$$\frac{1}{A}\frac{dA}{dx} = -\alpha_i \tag{2.5.2}$$

If the level of disturbance amplitude at $x = x_0$ is indicated by A_0, then the amplitude at any location downstream of x_0 is given by,

$$A(x) = A_0 e^{-\int_{x_0}^{x} \alpha_i(x)dx} \tag{2.5.3}$$

In the lower panel of Fig. 2.5, the exponent n is shown as a function of x where

$$n = -\int_{x_0}^{x} \alpha_i(x)dx \tag{2.5.4}$$

This factor $n(x)$ is calculated for a particular frequency and the exercise can be repeated for a range of frequencies and a composite plot can be made, as shown in Fig. 2.6.

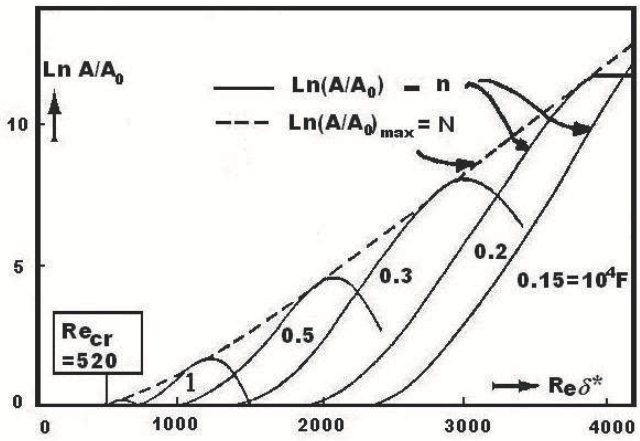

Figure 2.6 Total amplification rates for different frequencies for the Blasius flow [Arnal, 1984].

The total amplification suffered by individual frequencies is shown by the solid lines in Fig. 2.6. The envelope to these curves, shown by the dotted line, represents the maximum amplification suffered by different frequencies, since their entry into the unstable zone. The envelope is generally designated by,

$$N = [Ln\frac{A}{A_0}]_{max} = Max_f[\int_{x-0}^{x} -\alpha_i(x)dx] \tag{2.5.5}$$

Note that x_0 is different for different frequencies as it starts from the *branch I* where that particular frequency enters the unstable region. Secondly, the lower frequencies dwell inside the neutral loop for longer distances and these components tend to amplify the most.

2.5.2 Effect of Mean Flow Pressure Gradient

So far, we have been talking about the stability of zero pressure gradient flows. It is possible to extend the studies to include flows with pressure gradient using quasi-parallel flow assumption. To study the effects in a systematic manner, one can also use the equilibrium solution provided by the self-similar velocity profiles of the Falkner-Skan family. These similarity profiles are for wedge flows, whose external velocity distribution is of the form, $U_e = k\, x^m$. This family of similarity flow is characterized by the Hartree parameter $\beta_h = \frac{2m}{2m+1}$ and the shape factor, $H = \frac{\delta^*}{\theta}$. Some typical non-dimensional flow profiles of this family are plotted against non-dimensional wall-normal co-ordinate in Fig. 2.7. The wall-normal distance is normalized by the boundary layer thickness of the shear layer.

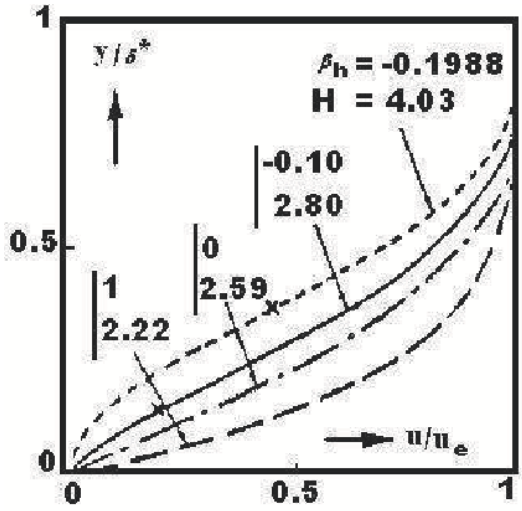

Figure 2.7 Typical mean velocity profiles of some thin shear layers [Arnal,1984].

The flow profiles with $H > 2.591$, correspond to velocity distributions with inflection point and these are the decelerated flows or flows with adverse pressure gradient. On the contrary, the flow profiles with $H < 2.591$, correspond to $\frac{dp}{dx} < 0$ (the accelerated flows). The figure with $\beta_h = 0$ and $H = 2.59$, corresponds to the Blasius profile. The profile with $\beta_h = 1$ and $H = 2.22$ corresponds to the stagnation point flow. The other two profiles in Fig. 2.7 are for flows with adverse pressure gradient and the crosses on the profile indicate the locations of the inflexion point. The profile for $\beta_h = -0.1988$ ($H = 4.032$) corresponds to the case of incipient separation.

In Fig. 2.8, the neutral curves for the above four velocity profiles of Fig. 2.7 are compared. The deciding trend is that as H increases, Re_{cr} decreases. And for flows with $\frac{dp}{dx} > 0$, the critical Reynolds numbers are significantly lower.

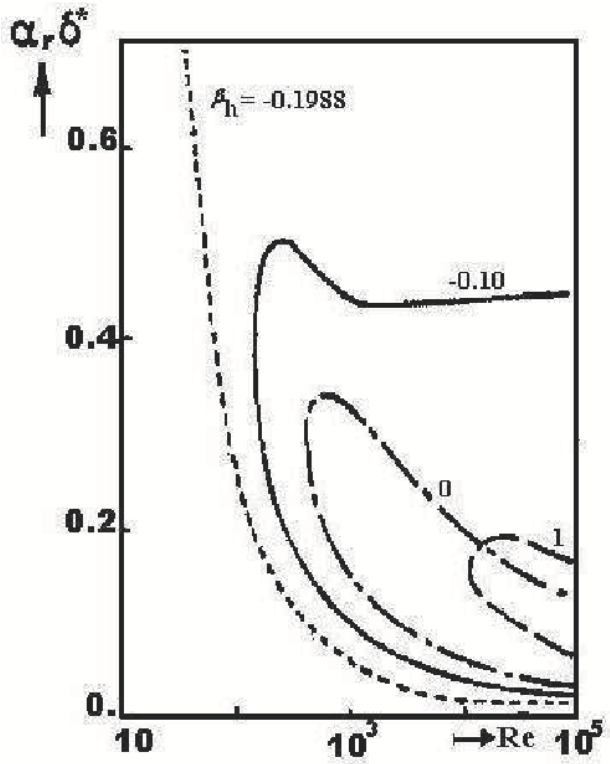

Figure 2.8 Neutral curves of some shear layer velocity profiles shown in Fig.2.7

The fact that such profiles are prone to instability earlier is the reason for calling these as adverse pressure gradient flows. Along with this, the growth rate of unstable waves becomes larger, as the shape factor increases. Also, for decelerated flows, the neutral curve does not close- as seen for $H = 2.80$ ($\beta_h = -0.10$) case. For the separated profiles, there is no *branch II* of the neutral curve at all. The stagnation region on a body in the presence of fluid flow is a site of high stability, as can be seen for the Hiemenz flow (stagnation point flow profile with $\beta_h = 1$) that is far more stable than the Blasius flow in Fig. 2.8.

The envelope curve (that represents the envelope of the maximum amplification suffered by all the frequencies considered present in the background

disturbance), shown by the dotted line in Fig. 2.6 was drawn for a particular pressure gradient. This process can be repeated for different pressure gradient parameters. In Fig. 2.9, the envelope curves have been shown for few representative adverse pressure gradient parameters starting from the Blasius profile ($H = 2.59$) to the incipient separated flow ($H = 4.032$). As the shape factor, H for the flow increases, Re_{cr} also decreases (indicated by the starting point of these curves). The slope of these envelope curves ($\frac{dN}{dRe_{cr}}$), also increases with H. One can use the local stability property of the flow by solving OSE and characterize the effects of pressure gradient in the same way that we did for Blasius profiles. It is apparent that the shape factor of the shear layer, H is a very important parameter that indicates flow separation and enhanced or reduced instability.

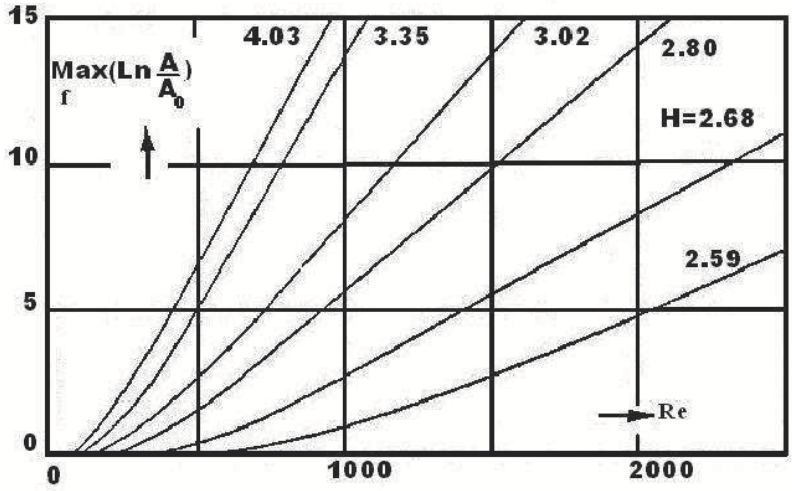

Figure 2.9 Envelope curves for total amplification for Falkner-Skan similarity profiles [Arnal, 1984].

In Fig. 2.10, Reynolds number based on momentum thickness at transition onset is shown plotted against the shape factor, as reported in Arnal (1984).

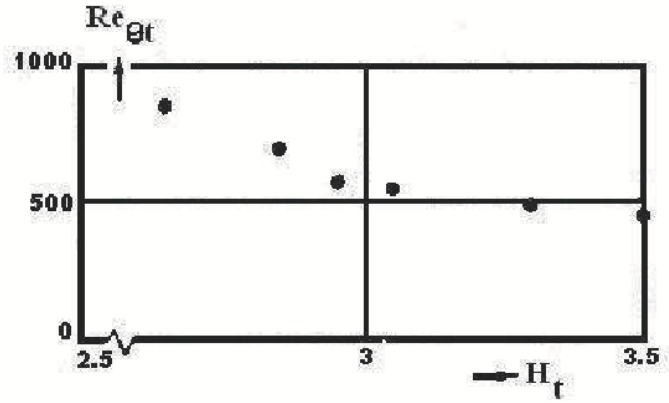

Figure 2.10 Momentum thickness Reynolds number and shape factor at transition onset [Arnal, 1984].

The shape factor turns out to be an important parameter in deciding flow instabilities and transition. Thus, by plotting H variation in the streamwise direction it is possible to indicate the transition location in a given flow. It is adequate to define the transition onset location as the place where the shape factor variation exhibits a sudden negative slope. The following results in Fig. 2.11 (also from Arnal (1984))- show that flow transition in an adverse pressure gradient shear layer always precedes before theoretical location of laminar separation, indicated by a vertical bars in the frames.

In the set of frames in Fig. 2.11, (A) represents a zero pressure gradient shear layer for which the flow is not predicted to separate theoretically. The sudden decrease of H is the harbinger of flow transition. From figures (B) through to (F), the pressure gradient is progressively made more adverse and consequently the theoretical location of laminar separation point moves forward and H variation becomes sharper with a larger fall in value at the location of transition. For severe adverse pressure gradient, the point of separation is almost coincident with the point of transition. This is often made use of for severe adverse pressure gradient flow calculations. However, this is not always the case for predicting transition location. For example, at low Reynolds number, flow often separates first and then transition occur subsequently. The separated flow being very unstable, following transition is very quick - one has practically a free shear layer with a point of inflexion. As turbulent flows are capable of withstanding much higher adverse

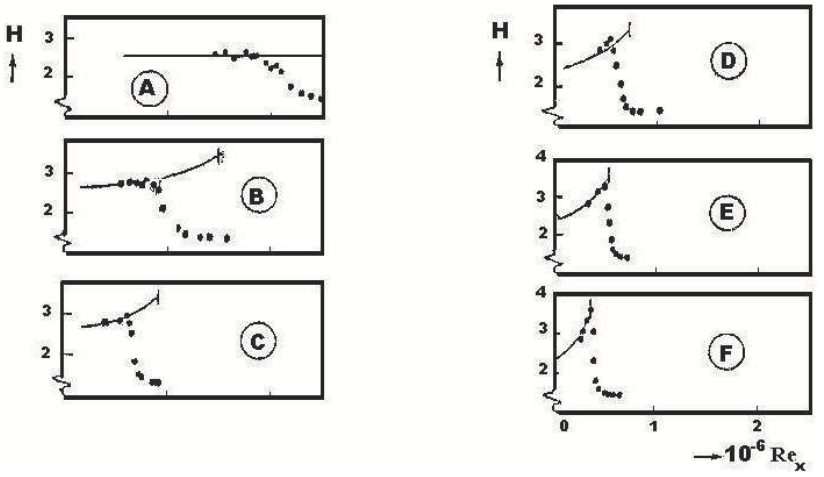

Figure 2.11 Effects of positive pressure gradient on separation and transition. Discrete symbols are experimental data points and continuous lines are laminar calculations. Vertical bar in laminar calculation indicate the location of point of laminar separation [Arnal, 1984].

pressure gradients, such separated turbulent flows can reattach to the wall. It results in mean wall streamline forming a separation bubble. Beyond the reattachment point the flow is turbulent and such flows are observed for uniform flow past circular cylinders in Reynolds number range of 3×10^5 to 3×10^6, on the leeward side. The flow after turbulent reattachment, separates again and remains fully separated. Separation bubbles are also seen in flow past aerofoil downstream of the suction peak at moderate Reynolds numbers and at non-zero angles of attack. There is an intense interaction of the viscous flow in the shear layer with the outer inviscid flow in such cases and boundary layer approximation fails.

The importance of shape factor, H can also be gauged for its ability to correlate it with instability and transition by looking at Fig. 2.12 where the values of $Re_{\delta^* crit}$ are plotted versus H (from Obremski, Morkovin & Landahl (1969) and White (1991)) that shows a regular variation of the data for different varieties of flows.

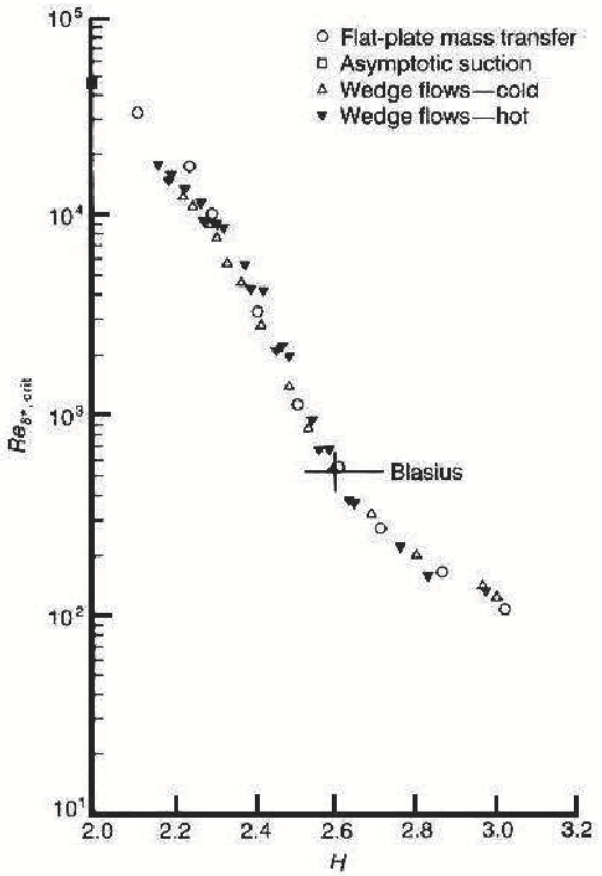

Figure 2.12 Collation of critical Reynolds number variation data with shape factor for different indicated flow types (From Obremski *et al.*, 1969).

This importance of H has been further utilized in predicting transition by Wazzan *et al.* (1981), by noting that similar correlation exist for the parameters such as pressure gradient, suction/ blowing, heating/ cooling etc., if it is plotted in terms of transition shape factor. In Fig. 2.13, this correlation is shown by the upper curve that is premised on linear instability studies with $N = 9$. The lower curve gives Re_{crit} as computed from Fig.

2.12 by converting $Re_{\delta*}$ to Re_x. To use Fig. 2.13, computed $H(x)$ by any laminar boundary layer code is used to predict transition, when the local $H(x)$ intersects upper curve, which is also given by the following empirical fit:

$$log_{10}(Re_{x,tr}) = -40.4557 + 64.8066H - 26.7538H^2 + 3.3819H^3 \quad (2.5.6)$$

This correlation is valid only in the range for $2.1 < H < 2.8$. This method is promising, as it is premised on e^9 method (but with significantly lesser effort), as described in the next sub-section.

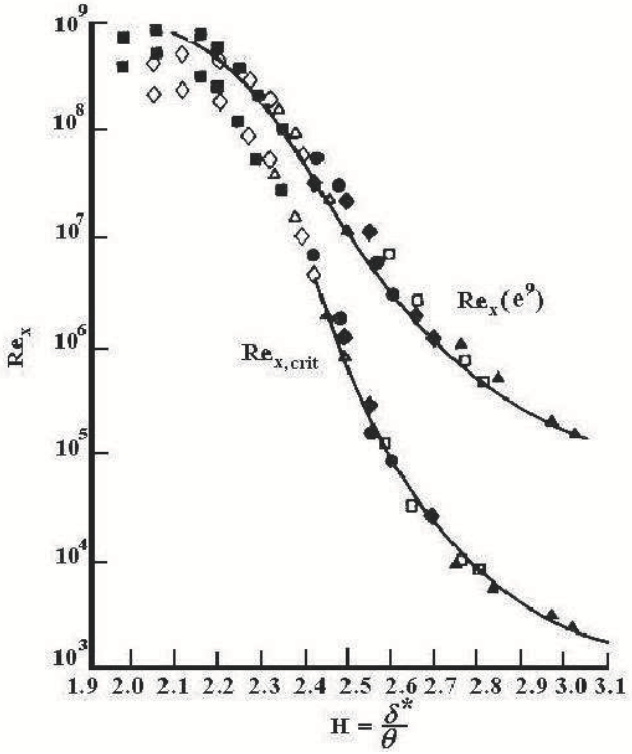

Figure 2.13 Correlation of critical and transitional Reynolds number versus boundary-layer shape factor. (From White, 1991).

2.5.3 Transition Prediction Based on Stability Calculation

Following the path-breaking experiments of Schubauer & Skramstad (1947), there have been sustained efforts to link the stability theory in predicting transition. Michel (1952) reported first that his compiled data showed the transition to be indicated when the total amplification of TS waves corresponded to $A/A_0 \approx 10^4$, where A_0 is the disturbance amplitude at the onset of instability. This motivated Smith & Gamberoni (1956) and van Ingen (1956) to use temporal theory results to show that at transition the total amplification is given by,

$$\frac{A}{A_0} = exp[\int_{x_{cr}}^{x_{tr}} \alpha \; c_i \; dt] \tag{2.5.7}$$

Note that the integration ranges from the critical point (x_{cr}) to the point of transition (x_{tr}). As the right hand side roughly became equal to e^9 (as noted by Smith & Gamberoni (1956)) on transition, this method has also acquired the name, e^9 method. Van Ingen (1956) reported the value of the exponent between 7 and 8. The disparity in the value of the exponent arises due to different levels and spectrum of background disturbances. Currently, it is known as the e^N method where the exponent has been given a general value depending on other factors affecting the transition process. Later on Jaffe et al. (1970) performed the spatial stability calculations and reported the exponent as equal to 10.

Experiments on transition for 2D attached boundary layer have revealed that the onset process is dominated by TS wave creation and its evolution, when the free stream turbulence level is low. Generally speaking, the estimated quantities like frequency of most dominant disturbances, eigenvalues and eigenvectors matched quite well with experiments. It is also noted from experiments that the later stages of transition process is dominated by nonlinear events. However, this phase spans a very small streamwise stretch and therefore one can observe that the linear stability analysis more or less determines the extent of transitional flow. This is the reason for the success of all linear stability based transition prediction methods. However, it must be emphasized that nonlinear, nonparallel and multi-modal interaction processes are equally important in some cases.

Despite the reasons cited for the success of linear stability theory in predicting transition, it is important to underscore its limitation as well. This should help one to look for hitherto unknown mechanism(s) that may play a bigger role in transition prediction than it might have been suspected. For example, the envelope method does not require any information about the frequency content of the background disturbances and always predicts

transition based on lower frequency events. What if a particular disturbance environment precludes such components of disturbances? Will the non-linear process create those frequencies first and then they would amplify? In such a case, the transitional region will be prolonged as compared to other cases and transition prediction based on normal mode analysis will be in question. This possibility is not explored in the present form of the instability theory. Also, it is stated that the above method works only when the free stream turbulence levels are low. It is legitimate to ask, what happens when the turbulence intensities are higher? Would one see different transition scenarios? Would one see transition without even creating TS waves? This is the point of view for bypass transition research, discussed in Chapter 3. First, let us discuss about incorporating semi-empirically the role of low-level free-stream turbulence on transition along with the e^N method.

2.5.4 Effects of Free Stream Turbulence

It has been stated above that the success of the e^N method depends strongly on the fact that this method was based on experimental results obtained in low turbulence intensity tunnels. Here the turbulence intensity is defined as,

$$Tu = \frac{[\frac{(u'^2+v'^2+w'^2)}{3}]^{1/2}}{U_\infty} \tag{2.5.8}$$

Quantities indicated by primes are the fluctuating components and thus, the numerator indicates the r.m.s. fluctuation level of the disturbance and is calculated taking a long time history. The effect of Tu is very strong on transition. For example, in the experiments by Schubauer & Skramstad (1947), the Reynolds number at transition location dropped by 50% when Tu was increased to 0.35% from its highest value at 0.04% as shown in Fig. 2.14 (a reproduction of Figure 2.2 of Schubauer & Skramstad (1947)).

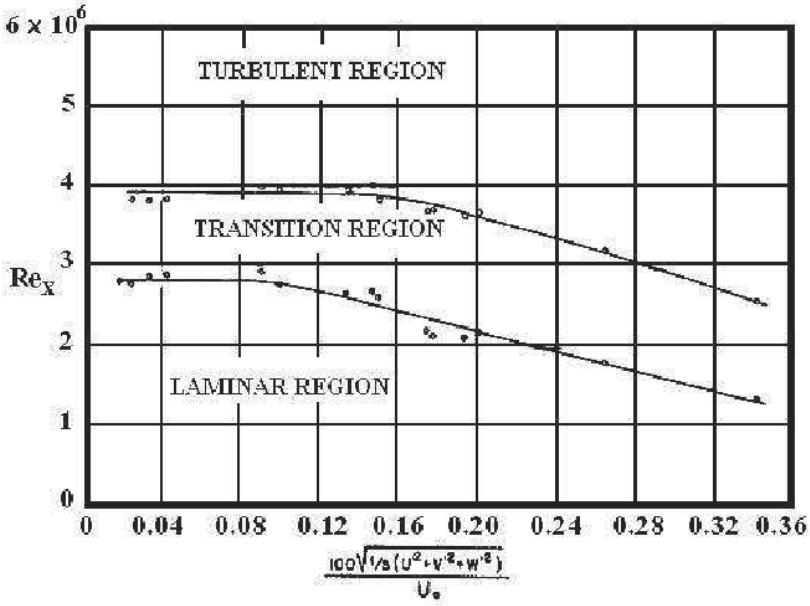

Figure 2.14 Effect of free stream turbulence on transition for flat plate boundary layers. (Taken from Schubauer & Skramstad (1947))

As seen here, the transition Reynolds number decreases rapidly for Tu greater than 0.10%, and this variation cannot be directly explained by e^N method. Mack (1977) has suggested the following empirical correlation, linking Tu with the exponent N of the e^N method,

$$N = -8.43 - 2.4\ Ln(Tu) \tag{2.5.9}$$

The above correlation is applicable in the range of: $0.0007 \leq Tu \leq 0.00298$. This correlation is based on the experimental results of Dryden (1959). Arnal (1986) reports its successful application for flows with adverse pressure gradient.

At the upper end of the range of application for $Tu = 0.00298$, one notes $N \approx 0$, implying that the transition would occur right at the location of Re_{cr}. In applying this correlation, the following has to be kept in mind:

- For $Tu < 0.10$ % , the transition location is insensitive to Tu. Such low levels of disturbances are typical of acoustic noise that controls

transition rather than the vortical disturbances. This distinction is not made in literature between the two and everything is included in the catch-all terminology of free stream turbulence (FST).

- For higher values of *Tu*, (greater than 2 to 3 %), transition often occurs without the appearance of TS waves at Reynolds numbers below Re_{cr}, for wall-bounded flows. Thus, the linear process of instability is *bypassed* and such transition processes are called *Bypass Transition*, as discussed in the next chapter.

If the excitation source is not inside the shear layer, then also a bypass transition can be caused by flows with low levels of FST embedding convected vortices in it- as is discussed in section 2.9. Important distinction must be made between periodic and aperiodic convecting vortices in the free stream. Following Fig. 2.15 taken from Spangler & Wells (1968), clearly distinguishes some of the causes that trigger transition due to FST. In this figure, the generic causes shown are due to i) grid-generated turbulence, ii) acoustic noises and other vortical/ acoustic sources that create iii) standing and iv) traveling waves. As compared to "low noise" transition Reynolds number of 2.8×10^6 obtained in Schubauer & Skramstad (1947) the facility used by Wells (1967) produced transition to occur at Reynolds number equal to 4.9×10^6. The facility used for the experiment excluded traveling acoustic noise, but there were standing acoustic waves in the test section.

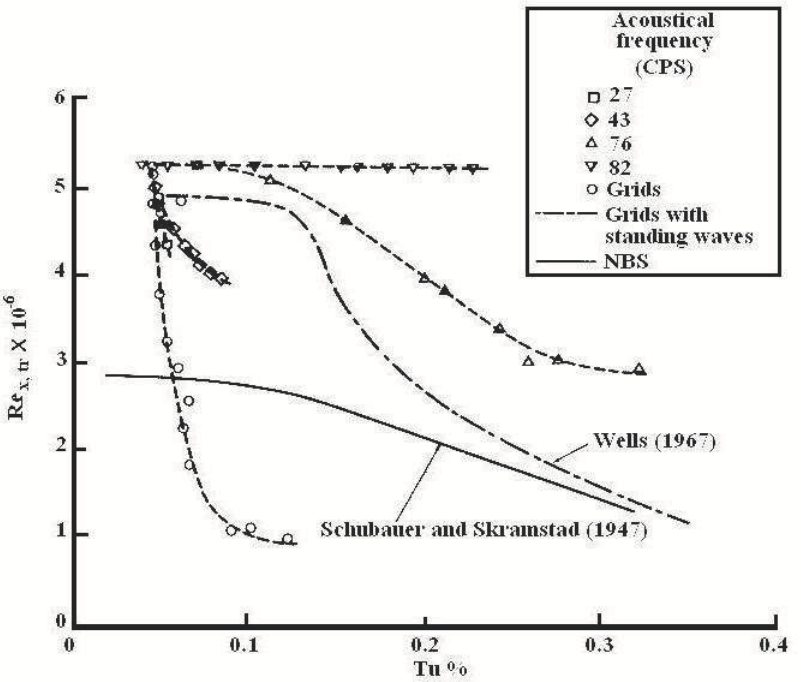

Figure 2.15 Correlation of transition Reynolds number with FST data from Spangler & wells (1968)

Results referred to Spangler & Wells (1968) in Fig. 2.15, used acoustics signals of fixed frequency to trigger transition and these clearly demonstrate that transition is sensitively dependent on frequency of excitation when *Tu* ranges from very small to significantly large values. Although the high frequency data in this figure (for 82 Hz) shows no variation at all in the plotted range- a value that is outside the neutral curve in the stable region. The grid data shows itself as a strong transition promoter; Re_{tr} value dropping sharply with a very small variation in *Tu*. Spangler and Wells report that the spectral distribution of disturbances show different amplitudes at different frequencies. To this, one must also add that there can be significant interferences between acoustic and vortical excitation- as seen for the *Tu* dependence of transition for the 76 Hz data, with gradual decrease of Re_{tr} with *Tu*.

2.6 Receptivity Analysis of Shear Layer

In Fig. 2.15, one notes the transitional Reynolds number plotted versus the disturbance amplitude for a flat plate boundary layer, excited by different means. It is evident that each case differs significantly from the others. The entrainment of different disturbance sources inside the shear layer to produce instability is at the core of receptivity studies- that relates the **cause** and its **effect(s)**. For example, from Fig. 2.15 it is apparent that the grid generated disturbances are very effective in triggering transition while free stream acoustic excitation is not so. Thus, one would state that shear layers are more receptive to vortical disturbances than acoustic disturbances. It is recognized that there are the following sources that can trigger transition in laminar flows: (a) perturbations in the form of vortical field; (b) acoustic or isentropic weak pressure field and (b) entropic field or temperature fluctuations. Note that the surface vibration or surface inhomogeneity also creates locally a vortical perturbation those are a potent trigger for transition in shear layers. It is the aim of receptivity studies to show the process of creation of instability in a shear layer by any one or a combination of these sources. What is essentially lacking so far is a proper mathematical framework that can deal with the problem of the processes for the initiation of instability. There have been some efforts on studying various aspects of receptivity, as given in Morkovin (1969), Tam (1971), Reshotko (1976), Nishioka & Morkovin (1986), Goldstein & Hultgren (1989), Choudhari & Streett (1990), Crouch (1992, 1993), Collis & Lele (1996), Leib, Wundrow & Goldstein (1999), Lin, Stuckert & Herbert (1995), Saric, White & Reed (1999), Buter & Reed (1993), Choudhari (1996), Sengupta *et al.* (1997, 1999, 1999a, 2002)- among many others.

The experimental results of Schubauer & Skramstad (1947) were a demonstration of receptivity of a flat plate shear layer to induced vibration inside the shear layer. They could produce TS waves, in a reproducible fashion, only when they vibrated a metallic ribbon at a fixed frequency very close to the wall with the help of an electromagnet. It is instructive to recall the following from Schubauer & Skramstad (1947): *In the search for schemes to excite oscillations in the boundary layer, a number of devices were tried before completely satisfactory results were obtained. Methods using sound, both pure notes and random noise, were none too satisfactory because of resonance effects and the complexity of the wave pattern in the tunnel.* It is generally considered that the major problem with acoustic excitation from free stream is the problem of matching of scales between the acoustic excitation field and the TS waves. The wavelength and propagation speed of acoustic wave is almost two orders of magnitude larger than the unstable TS waves. Also it is to be noted that the experiments

of Schubauer & Skramstad (1947) was attempting to verify the theoretical developments for two-dimensional instability while the acoustic excitations are always three-dimensional! There is absolutely no scope of creating 2D acoustic excitations! Since the instability of shear layer is associated with spatial theory, Squires theorem also does not help, in looking for 2D disturbance field that is more unstable than the 3D one. Schubauer & Skramstad (1947) carefully devised the means of creating mainly a 2D excitation field by vibrating a ribbon inside the shear layer that produced instability waves with properties predicted theoretically by Schlichting (1935).

However, one aspect of the theoretical developments of instability theory is quite easily overlooked that it requires neither the knowledge of excitation fields nor the location where it is applied. In eigenvalue analyses, the excitation field information is obscured through the application of homogeneous conditions at the boundaries. It is even worse, if the excitation is applied in the interior of the shear layer- there are no theories of instability at all! The instability theory developed in the previous sections relates to exciting the flow field by the boundary condition at the wall only- as explained next.

This is evident from the formulation: see for example, the retention of two modes in Eqn. (2.4.5) that only considers excitations at the boundary $y = 0$, those decay with height. It is therefore clear that the characteristic determinant of (2.4.8) will extract only those modes that are triggered by wall excitation and those decay with height. Thus in an experiment, TS waves are naturally going to be produced by excitation of the shear layer at the wall- as was demonstrated in Schubauer & Skramstad's experiment. When the frequency of the ribbon in the experiment is fixed, TS waves are predicted as a consequence of satisfying the dispersion relation of (2.4.8) via the spatial theory.

It is therefore also not directly apparent, why TS waves will be created when the flow is excited at the free stream- until and unless the coupling mechanism between free stream and wall excitation is established. It is not enlightening to read in literature about creation of TS waves in shear layer by free stream excitation and to explain it all by theories that are developed exclusively for wall excitation. The exception to this is the work reported in Sengupta *et al.* (2002), where the coupling mechanism was explained for the excitation by a train of convecting vortices moving at a constant speed at a fixed height. It was pointed out that there is only a narrow convection speed range for which convected vortices can have very strong receptivity. This is discussed in details later.

Furthermore, in the absence of any other mechanisms, most of the efforts so far have gone in looking for TS waves as the harbinger of transition for any kind of excitation. This situation is needed to be rectified, as suggested by

Morkovin in various papers including in Morkovin (1991) and a schematic is already shown here in Fig. 2.1. This relates to explaining bypass transition that causes transition without the appearance of TS waves. On bypass transition, one can look for additional discussions in Breuer & Kuraishi (1993), Landahl (1975), Landahl (1980), Jacobs & Durbin (2001), Sengupta *et al.* (2002, 2003), Lim *et al.* (2004) and Sengupta *et al.* (2006). Having stated the inadequacies of the eigenvalue approach, in the following we describe the receptivity approach starting with the linear theory.

2.6.1 Receptivity Mechanism by Linearized Approach: Connection to Stability Theory

Few articles on receptivity present a qualitative view of particular transition routes created by not so well-defined excitation field (see e.g. Saric *et al.* (1999)). Such approaches do not demonstrate complete theoretical and /or experimental evidence connecting the cause (excitation field) and its effect(s) (response field). Here, a model based on linearized Navier- Stokes equation is presented to show the receptivity route for excitation applied at the wall. This requires a dynamical system approach to explain the response of the system with the help of Laplace-Fourier transform.

2.6.1.1 A Brief Review of Laplace-Fourier Transform

Fourier and Laplace transforms are linear transforms and are very often used for analyzing problems in various branches of science and engineering. Since receptivity is studied with respect to onset of instability, it is quite natural that these transform techniques will be the tool of choice for such studies. Fourier transform provides an approach wherein the differential equation of a time dependent system is solved in the transformed plane as,

$$Y(\omega) = H(\omega)\ X(\omega) \tag{2.6.1}$$

where $X(\omega)$ and $Y(\omega)$ are the transform or spectrum of the input and output of the system, while $H(\omega)$ is called the *transfer function* of the system. If one focuses on an input of a particular frequency at $\omega = \omega_0$, then one can obtain the corresponding transfer function $H(\omega_0)$ and the output of the system can be obtained using (2.6.1). Such a study for all possible frequencies will give us, what is known as the *Frequency Response* of the system. In contrast, one can obtain the response of the system if the input to the system is instead a Dirac delta function in the physical plane, then the system will be excited simultaneously at all frequencies and the corresponding output (also in the physical plane) will be called the *Impulse Response*. Thus, the study

of a linear system is as simple as finding out the transfer function for the system and knowing the input spectrum. While the output in the transform plane is obtained by a simple multiplication, we will shortly see that the output can be obtained in the physical plane by performing a convolution integral between the impulse response and input spectrum. Use of Fourier transform, as opposed to Fourier series allows system analysis for aperiodic system. Almost all physical systems are *causal* i.e. these are the systems whose output does not anticipate input. For a linear and fixed system characterized by an *impulse response* $h(t)$ the causality requires,

$$h(t) = 0 \quad for \;\; t < 0. \tag{2.6.2}$$

Thus, it becomes apparent the output and the impulse response are one-sided in the time domain and this property can be exploited in such studies. Solving linear system problems by Fourier transform is a convenient method. Unfortunately, there are many instances of input/ output functions for which the Fourier transform does not exist. This necessitates developing a general transform procedure that would apply to a wider class of functions than the Fourier transform does. This is the subject area of one-sided Laplace transform that is being discussed here as well. The idea used here is to multiply the function by an exponentially convergent factor and then using Fourier transform technique on this altered function. For causal functions that are zero for $t < 0$, an appropriate factor turns out to be $e^{-\sigma t}$ where $\sigma > 0$. This is how Laplace transform is constructed and is discussed. However, there is another reason for which we use another variant of Laplace transform, namely the bi-lateral Laplace transform.

All fluid dynamical systems are continuous system with *infinite* degrees of freedom and the governing equations depend continuously upon both space and time. While for any system, the time-dependent signal cannot move back in time, the space dependent signal can propagate in all directions with respect to the location of the source. This therefore requires that we develop a theory based on bilateral Laplace transform - a topic described in great details in Papoulis (1962) and Van der Pol & Bremmer (1959).

2.6.1.2 Fourier and Laplace Transform

If $F(\omega)$ is the Fourier transform of a time varying function $f(t)$, then

$$F(\omega) = \int_{-\infty}^{+\infty} f(t)\, e^{-i\omega t} dt \tag{2.6.3}$$

The above integral exists in the sense of having a Cauchy principal value for every value of ω. Conversely if we have the Fourier transform, then we can construct the function in the time-domain from,

$$f(t) = \frac{1}{2\pi} \int_{-\infty}^{+\infty} F(\omega)\, e^{i\omega t} d\omega \tag{2.6.4}$$

Note that in Eqns. (2.6.3) and (2.6.4), ω is real. As mentioned above, we will also use *bi-lateral Laplace transform* $F_{II}(\alpha)$ to describe the space dependence of the function by,

$$F_{II}(\alpha) = \int_{-\infty}^{+\infty} f(x)\, e^{-i\alpha x} dx \tag{2.6.5}$$

Thus, $F_{II}(\alpha)$ and $f(x)$ form the transform-original pair for a space-dependent function. Here, α is a complex quantity i.e. $\alpha = \alpha_r + i\alpha_i$ and represents a complex wave number. Note that α being complex, $F_{II}(\alpha)$ is only defined in a limited region of the complex α plane, as shown in the sketch of Fig. 2.16.

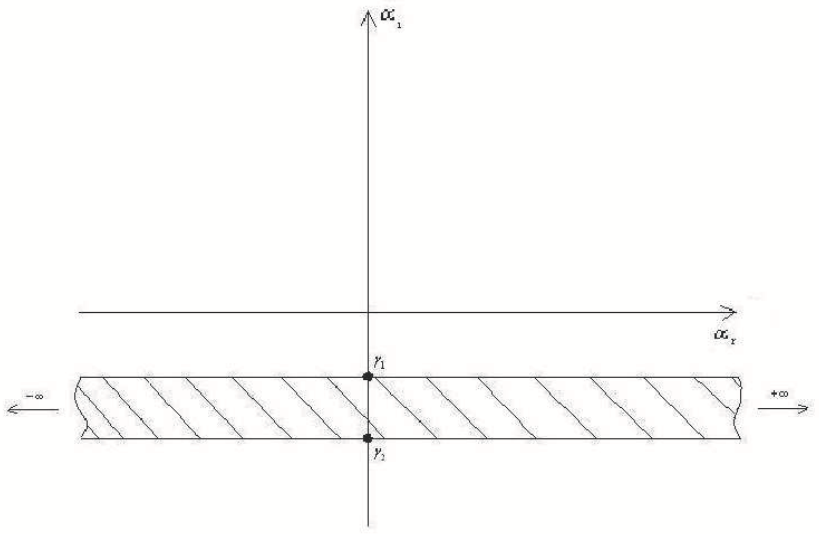

Figure 2.16 The strip of convergence for the Fourier-Laplace integral in the wave number plane

In the sketch above, a horizontal hatched strip is defined by $\gamma_2 < \alpha_i < \gamma_1$. Any contour chosen within this strip of convergence is called the *Bromwich contour*. On the right hand side integral of Eqn. (2.6.5), if we restrict the lower limit to x = 0, then we would retrieve the unilateral Laplace transform given by,

$$F_I(\alpha) = \int_0^\infty f(x)\, e^{-i\alpha x} dx \tag{2.6.6}$$

The right hand side can also be rewritten as

$$F_I(\alpha) = \int_0^\infty f(x)\, e^{\alpha_i x}\, e^{-i\alpha_r x} dx \tag{2.6.7}$$

This shows that $F_I(\alpha)$ is the Fourier transform of the function $f(x)\, e^{\alpha_i x}$, if α_i is held constant. Applying Fourier inversion formula (2.6.4), we obtain

$$f(x)\, e^{\alpha_i x} = \frac{1}{2\pi} \int_{-\infty+i\alpha_i}^{+\infty+i\alpha_i} F_I(\alpha)\, e^{i\alpha_r x} d\alpha_r \tag{2.6.8}$$

Here, the integration contour is traced along a $\alpha_i = const.$ line i.e. the integration contour is along a horizontal line, $\alpha_i = \gamma$. This is the Bromwich contour for one-sided Laplace transform, if the corresponding inverse Fourier transform in (2.6.8) exists. The integral in (2.6.7) will then converge for all other contours for which $\alpha_i < \gamma$ defining the region of convergence for the transform where it is analytic. We can extrapolate this to define the strip of convergence for bi-lateral Laplace transform.

The bi-lateral Laplace transform of (2.6.5) can be rewritten as,

$$F_{II}(\alpha) = \int_0^\infty f(x)\, e^{-i\alpha x} dx + \int_{-\infty}^0 f(x)\, e^{-i\alpha x} dx \tag{2.6.9}$$

The first integral in (2.6.9) is the unilateral Laplace transform of $f(x)U(x)$ where $U(x)$ is the unit step function or the Heaviside function. Therefore, it converges in a region $\alpha_i > \gamma_1$ as shown in Fig. 2.17.

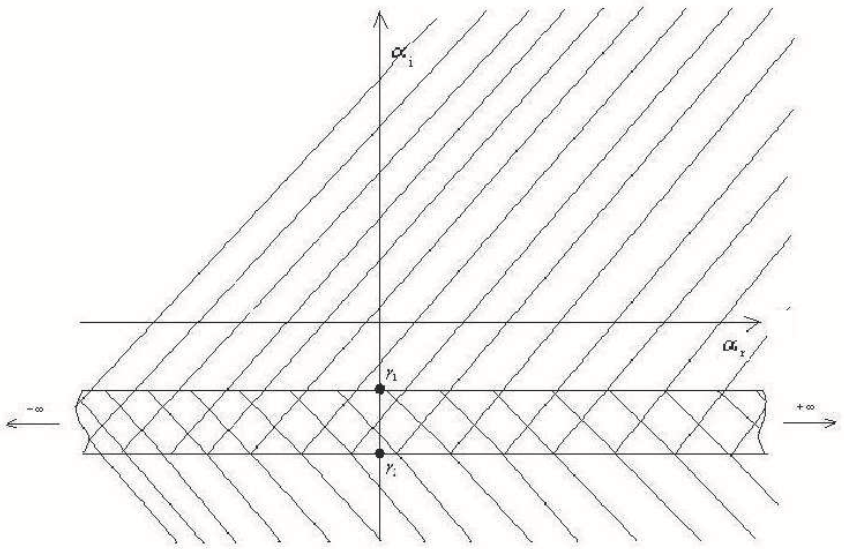

Figure 2.17 Fixing the Bromwich contour in the wave number plane inside the cross-hatched region

Similarly, the second integral of (2.6.10) is analytic for $\alpha_i > \gamma_2$, as shown in Fig. 2.17. Therefore, $F_{II}(\alpha)$ is analytic in the region shown by cross-hatches in the above figure, recovering the definition shown in Fig. 2.16.

2.6.1.2(a) The Inversion Formula for Laplace Transform

Once we identify the strip of convergence, we can write down the inversion formula by integrating along a Bromwich contour (here taken as a $\alpha_i = const.$ line for convenience) in the complex α-plane by,

$$f(x) = \frac{1}{2\pi} \int_{Br} \; F_{II}(\alpha_r + i\alpha_i) e^{i\alpha_r x} e^{-\alpha_i x} \; d\alpha_r \tag{2.6.10}$$

or

$$f(x) e^{\alpha_i x} = \frac{1}{2\pi} \int \; F_{II}(\alpha_r + i\alpha_i) e^{i\alpha_r x} \; d\alpha_r \tag{2.6.11}$$

This is the equivalent inverse Fourier transform of the right hand side. This integral can be evaluated by contour integration (see Papoulis (1962)

and Van der Pol & Bremmer (1959) for more details). For an application in fluid flow instability study, see Sengupta (1991) and Sengupta *et al.* (1994). Suppose that the only singularities of $F_{II}(\alpha)$ are simple poles and if

$$F_{II}(\alpha) \to 0 \quad for \quad |\alpha| \to \infty \tag{2.6.12}$$

Then one can invoke Jordan's lemma and Cauchy's theorem (see Whittaker & Watson (1946)) for the line integral in (2.6.11) that can be converted to the contour integral, as shown in Figure 2.18, with only a single pole indicated at the point P_1. Let us also say that the disturbance corresponding to this pole has a positive group velocity i.e. the associated disturbance propagates in downstream direction.

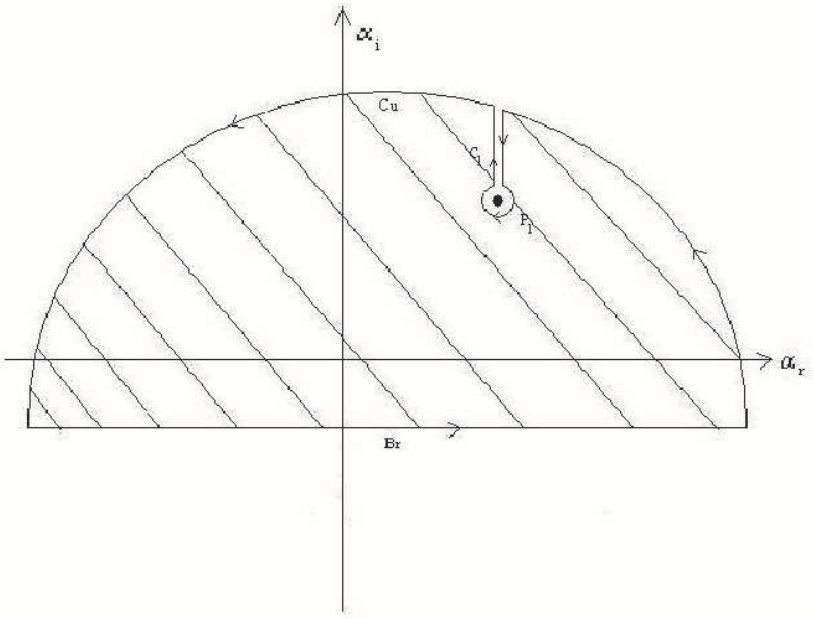

Figure 2.18 Bromwich contour and its closure for the integral in Eqn. (2.6.13)

We construct a closed contour C_u which is the Bromwich contour plus the semi-circular part as indicated in the figure, with a small indented contour

around the pole connected by a pair of vertical lines to this semi-circular arc. These vertical lines constitute a cut that links the small circular contour (C_1) to the semi-circle. The arrows show the direction along which the contour integral is taken for estimating the inverse transform corresponding to the downstream propagating signal. Because there are no other singularities, $F_{II}(\alpha)$ is analytic along and within C'_u, as indicated by hatching. Therefore,

$$f(x) = \frac{1}{2\pi} \int_{C_u} F_{II}(\alpha) e^{i\alpha x} \, d\alpha \quad for \;\; x > 0 \tag{2.6.13}$$

Where, $C_u = C'_u + C_1$. For an analytic function $f(z)$ in a domain bounded by a closed contour C, *Cauchy's theorem* states that,

$$\int_C \; f(z) \, dz = 0$$

Thus, we can apply this theorem to the integrand of (2.6.13) in the contour C'_u i.e.

$$\tfrac{1}{2\pi} \textstyle\int_{C'_u} \; F_{II}(\alpha) e^{i\alpha x} \; d\alpha = 0$$

Hence

$$\frac{1}{2\pi} \int_{C'_u} \; F_{II}(\alpha) e^{i\alpha x} \; d\alpha = -\frac{1}{2\pi} \int_{C_1} \; F_{II}(\alpha) e^{i\alpha x} \; d\alpha \tag{2.6.14}$$

Note that while C_u is in anti-clockwise direction and hence positive, the integral on the right hand of (2.6.14) is in clockwise direction. If we perform this integral also in anti-clockwise direction, then the negative sign can be removed. The integral on the right hand side can be evaluated by the calculus of residues i.e.

$$\int_{-C_1} \; F_{II}(\alpha) e^{i\alpha x} \; d\alpha = 2\pi \;\; i \; * \;\; Residue \; (\alpha = \alpha_{P_1}) \tag{2.6.15}$$

where the residue has to be calculated at the pole located at P_1. If the pole is of order m, then

$$Residue \;\; (\alpha_{P_1}) = \frac{1}{(m-1)!} \; \frac{d^{m-1}}{d\alpha^{m-1}} [F_{II}(\alpha) e^{i\alpha x}] \tag{2.6.16}$$

If we would have joined the Bromwich contour by a semi-circle in the lower part of the α plane as indicated by the contour C_d, then

$$f(x) = \frac{1}{2\pi} \int_{C_d} F_{II}(\alpha) e^{i\alpha x} d\alpha \;\; for \;\; x < 0 \tag{2.6.17}$$

However, one need not perform contour integrals to obtain $f(x)$. For example, if we perform the integral of (2.6.10) directly along the Bromwich

contour, then we will be simultaneously getting both the downstream and upstream propagating solutions together. We advocate this procedure, because this also allows us the freedom from finding out the detailed information about all possible singularities (not only the simple poles) of the transform and their order. Only thing that has to be ensured is finding the correct strip of convergence for the Bromwich contour. This procedure has been followed in Sengupta (1991) in calculating the impulse response of Blasius boundary layer; in Gaster & Sengupta (1993) for solving the signal problem for the spatial growth and in Sengupta *et al.* (1994) for solving the full spatio-temporal problem when a zero pressure gradient shear layer is excited harmonically.

It is interesting to note that the response of a system to a harmonic input is itself harmonic at the same frequency under the twin conditions of linearity and time invariance of the system properties for stable systems. For instability and receptivity problems, there is no general proof of the same due to the nonlinear nature of the dispersion relation, despite the fact that one is studying linearized Navier- Stokes equation. Thus it can at best be an assumption that is adopted in many analyses of this problem, except in Sengupta *et al.* (1994, 2006, 2006a) where the full time-dependent problem is solved as a transient problem by considering Bromwich contours in $\alpha-$ and ω- planes simultaneously.

There is another reason for our preference in calculating system response by integrating (2.6.10) directly and not use contour integral (2.6.13) and (2.6.17). This is due to the restrictive condition (2.6.12) needed to hold for Jordan's Lemma to be used. We will show here, that the condition of Jordan's Lemma does not hold for the Orr-Sommerfeld equation - a result that has not been used in stability studies of fluid dynamics.

2.6.1.3 A Short Tutorial on Fourier Integral and Transforms

Given a function of the real variable t, consider the integral

$$F(\omega) = \int_{-\infty}^{+\infty} f(t) e^{-i\omega t} dt \tag{2.6.18}$$

The Fourier transform $F(\omega)$ is in general complex that can be expressed as,

$$F(\omega) = R(\omega) + iI(\omega) \tag{2.6.19}$$

or

$$= A(\omega) e^{i\varphi} \tag{2.6.20}$$

where $A(\omega)$ is the amplitude or Fourier spectrum of $f(t)$, $A^2(\omega)$ its energy spectrum and φ its phase angle. The inversion formula,

$$f(t) = \frac{1}{2\pi}\int_{-\infty}^{+\infty} F(\omega)e^{i\omega t}d\omega \tag{2.6.21}$$

is valid at all continuous points. At the discontinuities, one should take the average of its right and left limits i.e.

$$f(t) = \frac{1}{2}[f(t^+) + f(t^-)] \tag{2.6.22}$$

If $f(t)$ is absolutely integrable i.e $\int_{-\infty}^{+\infty}|f(t)|dt < \infty$, then $F(\omega)$ exists. Let us now talk about some special forms of Fourier integrals. If $f(t) = f_1(t) + if_2(t)$, then

$$R(\omega) = \int_{-\infty}^{+\infty}[f_1\cos(\omega t) + f_2\sin(\omega t)]dt \tag{2.6.23a}$$

$$I(\omega) = -\int_{-\infty}^{+\infty}[f_1\sin(\omega t) - f_2\cos(\omega t)]dt \tag{2.6.23b}$$

And

$$f_1(t) = \frac{1}{2\pi}\int_{-\infty}^{+\infty}[R\cos(\omega t) - I\sin(\omega t)]d\omega \tag{2.6.24a}$$

$$f_2(t) = \frac{1}{2\pi}\int_{-\infty}^{+\infty}[R\sin(\omega t) + I\cos(\omega t)]d\omega \tag{2.6.24b}$$

Thus, if $f(t)$ is real i.e. $f_2(t) \equiv 0$, then $R(\omega) = \int_{-\infty}^{+\infty}[f_1\cos(\omega t)]dt$ and hence it is an even function. In the same way $I(\omega)$ is an odd function. Furthermore, if $f(t)$ is real and even, then $f(t)\cos\omega(t)$ is even and $f(t)\sin\omega(t)$ is odd. Hence for such combinations,

$$R(\omega) = 2\int_0^{\infty} f(t)\cos\omega t dt \quad and \quad I(\omega) \equiv 0 \tag{2.6.25}$$

In contrast, if $f(t)$ is real and odd, then

$$R(\omega) \equiv 0 \quad and \quad I(\omega) = -2\int_0^{\infty} f(t)\sin\omega t dt \tag{2.6.26}$$

For a causal function,

$$f(t) = 0 \quad for \quad t < 0 \tag{2.6.27}$$

Also from (2.6.18), it is easy to see that

$$F(-\omega) = \int_{-\infty}^{+\infty} f(t)e^{i\omega t}dt = \int_{-\infty}^{+\infty} f(-t)e^{-i\omega t}dt \tag{2.6.28}$$

Thus, the Fourier transform of $f(-t)$ is given by $R(\omega) - iI(\omega)$. If we split $f(t)$ into an even and odd function as given by

$$f_e(t) = \frac{1}{2}[f(t) + f(-t)] \qquad f_0(t) = \frac{1}{2}[f(t) - f(-t)] \tag{2.6.29}$$

It is clear that $R(\omega)$ is the Fourier transform of $f_e(t)$ and $iI(\omega)$ is the Fourier transform of $f_0(t)$. For a causal function, due to (2.6.27), one can see that $f(t) = 2f_e(t) = 2f_0(t)$ for $t > 0$. Therefore, a real causal function can be determined either in terms of $R(\omega)$ or in terms of $I(\omega)$ from

$$f(t) = \frac{2}{\pi}\int_0^{\infty} R(\omega)\cos \ \ \omega t \ \ d\omega \tag{2.6.30a}$$

or

$$= -\frac{2}{\pi}\int_0^{\infty} I(\omega)\sin \ \ \omega t \ \ d\omega \tag{2.6.30b}$$

In addition to the above simplifications for estimating the Fourier transforms and their inverses, following properties are often used as further aids. They are also known as theorems, as described in Papoulis (1962). For notational ease, let us use the following to indicate the connection between original and its transform: $f(t) \Leftrightarrow F(\omega)$.

Linearity:

$$If \ \ f_1(t) \Leftrightarrow F_1(\omega) \ \ and \ \ f_2(t) \Leftrightarrow F_2(\omega) \ \ then \ \ f_1(t) + f_2(t) \Leftrightarrow F_1(\omega) + F_2(\omega) \tag{2.6.31}$$

This theorem directly transfers to Laplace transform without any further qualification.

Symmetry:

$$If \ \ f(t) \Leftrightarrow F(\omega) \ \ , then \ \ \ F(t) \Leftrightarrow 2\pi \ f(-\omega) \tag{2.6.32}$$

Time Scaling: For any real α,

$$f(\alpha t) \Leftrightarrow \frac{1}{|\alpha|}F(\frac{\omega}{\alpha}) \tag{2.6.33}$$

This property also applies directly to Laplace transform, for $\alpha > 0$.

Time Shifting: For any real time t_0,

$$f(t-t_0) \Leftrightarrow F(\omega)e^{-i\omega t_o} \tag{2.6.34}$$

It is also the same for Laplace transform.

Frequency Shifting: For any real frequency ω_0,

$$e^{i\omega_0 t}f(t) \Leftrightarrow F(\omega-\omega_0) \tag{2.6.35}$$

This theorem also applies directly to Laplace transform.

Time Differentiation: The Fourier transform of n^{th} order derivative can be found in terms of the Fourier transform of the original function by,

$$\frac{d^n f}{dt^n} \Leftrightarrow (i\omega)^n F(\omega) \tag{2.6.36}$$

For Laplace transform, a more general expression is obtained using all the initial conditions as given below, $(i\omega)^n F(\omega) - (i\omega)^{n-1} f(0^-) - ..... - f^{(n-1)}(0^-)$

Frequency Differentiation: In a similar fashion, one can relate the n^{th} derivative in the spectral plane with the following function in the physical plane via,

$$(-it)^n f(t) \Leftrightarrow \frac{d^n F(\omega)}{d\omega^n} \tag{2.6.37}$$

Moment Theorem: For the n^{th} moment of a function, $m_n = \int_{-\infty}^{+\infty} t^n f(t)dt$, one has the following pair

$$(-i)^n m_n \Leftrightarrow \frac{d^n F(0)}{d\omega^n} \tag{2.6.38}$$

Next, we describe the important property of the convolution. Consider two functions $f_1(x)$ and $f_2(x)$ from which we can construct the following,

$$f(x) = \int_{-\infty}^{+\infty} f_1(y) f_2(x-y)dy \tag{2.6.39}$$

The function $f(x)$ is called the convolution of $f_1(x)$ and $f_2(x)$. It is denoted symbolically as,

$$f(x) = f_1(x) * f_2(x) \tag{2.6.40}$$

Let us now state the following convolution theorems.

Time convolution theorem: If $f_1(t) \Leftrightarrow F_1(\omega)$ and $f_2(t) \Leftrightarrow F_2(\omega)$ then,

$$\int_{-\infty}^{\infty} f_1(\tau) f_2(t-\tau)d\tau \Leftrightarrow F_1(\omega)F_2(\omega) \tag{2.6.41}$$

Frequency convolution theorem: Similarly, one can state the following frequency convolution theorem,

$$f_1(t)f_2(t) \Leftrightarrow \frac{1}{2\pi}\int_{-\infty}^{+\infty} F_1(y)F_2(\omega - y)dy \tag{2.6.42}$$

2.6.1.4 Some Useful Fourier Transforms

Some useful transforms are summarized here those will be of use in formulating and solving receptivity problems.

(a) **Dirac Delta function:** For the delta function treated as a distribution $f(t) = \delta(t)$, allows it's Fourier transform to be obtained by,

$$F(\omega) = \int_{-\infty}^{+\infty} \delta(t)e^{-i\omega t}dt = 1 \tag{2.6.43}$$

Thus, application of delta function is equivalent to exciting all the circular frequencies with equal emphasis. This is the basis of finding the natural frequency of any oscillator via impulse response. When the oscillator is subjected to an impulse, all frequencies are equally excited and the system dynamics picks out the natural frequency of vibration, leaving others to decay in due course of time. It is noted that this result also applies to Laplace transform and we are going to use it often by replacing time by space and circular frequency by wave numbers.

Now using the time shift theorem (as given by Eqn. (2.6.34)), it is immediately evident using Eqn. (2.6.43) that,

$$\delta(t - t_0) \Leftrightarrow e^{-i\omega t_0} \tag{2.6.44}$$

Also using the symmetry property of Eqns. (2.6.32) and (2.6.35), one gets

$$1 \Leftrightarrow 2\pi\delta(\omega) \tag{2.6.45}$$

Similarly using the symmetry property of Eqns. (2.6.32) and (2.6.44), we get

$$e^{i\omega_0 t} \Leftrightarrow 2\pi\delta(\omega - \omega_0) \tag{2.6.46}$$

Since $\cos\omega_0 t = \frac{1}{2}\{e^{i\omega_0 t} + e^{-i\omega_0 t}\}$, therefore

$$\cos\omega_0 t \Leftrightarrow (\frac{2\pi}{2})[\delta(\omega - \omega_0) + \delta(\omega + \omega_0)] \tag{2.6.47}$$

In the same way, from $\sin\omega_0 t = \frac{1}{2i}\{e^{i\omega_0 t} - e^{-i\omega_0 t}\}$, one obtains the following transform pair,

$$\sin\omega_0 t \Leftrightarrow i\pi[\delta(\omega+\omega_0)-\delta(\omega-\omega_0)] \tag{2.6.48}$$

(b) **The sign function** ($sgn\ t$)**:** is equal to +1 when $t>0$ and is equal to -1 when t is negative. Its Fourier transform is then given by,

$$sgn\ (t) \Leftrightarrow \frac{2}{i\omega} \tag{2.6.49}$$

Proof of (2.6.49): For $F(\omega)=\frac{2}{i\omega}$, the original is given by,
$f(t)=\frac{1}{2\pi}\int_{-\infty}^{+\infty}\frac{2}{i\omega}e^{i\omega t}d\omega \qquad =\frac{1}{\pi}\int_{-\infty}^{+\infty}\frac{\sin\omega t}{\omega}d\omega$

This integral on the right hand side has the property to be equal to +1 when $t>0$ and is equal to -1 when $t<0$. Hence $f(t)$ is $sgn\ (t)$.

(c) **Unit Step function or Heaviside function** $U(t)$: This function is equal to zero for all negative values of the argument and for positive values of the argument it is equal to +1, taking a discontinuous jump at $t=0$. Hence this function can be written as,

$$U(t)=\frac{1}{2}+\frac{1}{2}sgn\ (t) \tag{2.6.50}$$

Hence, using the results of (2.6.45) and (2.6.49) we get the following pair,

$$U(t) \Leftrightarrow \pi\delta(\omega)+\frac{1}{i\omega} \tag{2.6.51}$$

Furthermore, using the frequency shift theorem of Eqn. (2.6.35),

$$e^{i\omega_0 t}U(t) \Leftrightarrow \pi\delta(\omega-\omega_0)+\frac{1}{i(\omega-\omega_0)} \tag{2.6.52}$$

Above result is of central importance for the study of harmonic excitation of a shear layer with the excitation having a finite start-up time. Usage of the above, allows one to distinguish between the transient and asymptotic part of the receptivity solution of a shear layer to a harmonic excitation starting at a finite time. This was used in Sengupta *et al.* (1994) to study the receptivity of zero pressure gradient shear layer to harmonic excitation.

It is now easy to show that a harmonic excitation starting at $t=0$ is given by,

$$U(t)\cos\omega_0 t \Leftrightarrow \frac{\pi}{2}[\delta(\omega-\omega_0)+\delta(\omega+\omega_0)]+\frac{i\omega}{\omega_0^2-\omega^2} \tag{2.6.53}$$

(d) **Derivatives of Delta function:** In this class of functions one can include the doublet, quadrupole etc. those are often used as singularity

functions used in fluid mechanics and acoustics. It is worthwhile to point out that the potential flow results for source, sink, doublet etc can be obtained using the same procedure detailed here using Laplace's equation as the governing differential equation.

It has been shown in Papoulis (1962),

$$\int_{-\infty}^{+\infty} \frac{d^n}{dt^n}\delta(t-t_0)\varphi(t)dt = (-1)^n \frac{d^n\varphi(t_0)}{dt^n}$$

Therefore,

$$F(\omega) = \int_{-\infty}^{+\infty} \frac{d^n\delta}{dt^n} e^{-i\omega t}dt = (-1)^n \frac{d^n}{dt^n}(e^{-i\omega t})_{t=0} \quad = (i\omega)^n$$

Thus,

$$\frac{d^n\delta}{dt^n} \Leftrightarrow (i\omega)^n \tag{2.6.54}$$

(e) **Gaussian function** $(e^{-t^2/2})$: This function belongs to the class of Hermitian functions and has the important self-reciprocity property with its transform. The Fourier transform of it is given by,

$$\begin{aligned} F(\omega) &= \textstyle\int_{-\infty}^{+\infty} e^{-t^2/2}e^{-i\omega t}dt \\ &= \textstyle\int_{-\infty}^{\infty} e^{-\frac{1}{2}(t^2+2i\omega t)}dt \\ &= e^{-\frac{\omega^2}{2}} \textstyle\int_{-\infty}^{+\infty} e^{-\frac{(t+i\omega)^2}{2}}dt \\ &= \sqrt{2}e^{-\frac{\omega^2}{2}} \textstyle\int_{-\infty}^{+\infty} e^{-\frac{(t+i\omega)^2}{2}} d(\frac{(t+i\omega)}{\sqrt{2}}) \end{aligned}$$

Since $\int_{-\infty}^{+\infty} e^{-x^2/2}dx = \sqrt{\pi}$

Therefore

$$e^{-\frac{t^2}{2}} \Leftrightarrow \sqrt{2\pi}e^{-\frac{\omega^2}{2}} \tag{2.6.55}$$

This is the important property of the Gaussian function, namely that its transform has the identical functional form as the original. This is called the property of *self-reciprocity*. All its derivatives also share the same property. The derivatives of the Gaussian function produce the well known Hermite functions,

$$h_n(t) = (-1)^n e^{t^2/2}\frac{d^n}{dt^n}(e^{-t^2}) \Leftrightarrow H_n(\omega)$$

Therefore, $\sqrt{2\pi}h_n(t) = i^n H_n(t)$

2.6.2 Receptivity to Wall Excitation and Impulse Response

This is based on the work reported in Sengupta (1991), Gaster & Sengupta (1993) and Sengupta *et al.* (1994). Consider the behaviour of small amplitude disturbances in a given parallel mean flow, in response to a time harmonic localized disturbance source (with frequency ω_0). In the simplest form of a model for response, the perturbation stream function is defined by (as in Sengupta (1991) and Gaster & Sengupta (1993))

$$\psi(x, y, t) = \frac{1}{2\pi} \int_{Br} \phi(y, \alpha; \omega_0) e^{i(\alpha x - \omega_0 t)} d\alpha \tag{2.6.56}$$

Two-dimensional disturbance field arising in a 2D mean flow described by the velocity profile $U(y)$ is considered first. The disturbance source is located at the origin of a Cartesian system and the circular frequency of the exciter is given by ω_0. In writing the disturbance stream function above, one assumes the system to respond at the frequency of the excitation only- this is known as the **signal problem** (as considered in Sengupta (1991) and Gaster & Sengupta (1993)). Also note that this represents disturbance field that can move both in the downstream, as well as in the upstream direction. Hence the above is a bi-lateral Laplace transform and the Bromwich contour is to be located in the strip of convergence for the transform amplitude ϕ, as described in Papoulis (1962). Substituting (2.6.56) in linearized Navier-Stokes equation and making the parallel flow assumption provides the Orr-Sommerfeld equation - as given in Eqn. (2.4.3). The only difference in this receptivity approach from the stability approach is that the boundary conditions are not homogeneous, unlike that was given in Eqn. (2.4.1a).

For the case of receptivity to localized wall excitation, a delta function is used at the point of excitation; this gives rise to what is known as the *impulse response* of the shear layer. The boundary conditions applied at the wall are given by,

$$at\ y = 0: \qquad u = 0 \quad and \quad \psi(x, 0, t) = \delta(x)\, e^{-i\omega_0 t} \tag{2.6.57}$$

And far from the wall ($y \to \infty$) :

$$u, v \to 0 \tag{2.6.58}$$

The decaying boundary condition (2.6.58) at the free stream excludes two fundamental modes of the OSE. With the other two retained modes one defines,

$$\phi = a_1 \phi_1 + a_3 \phi_3 \tag{2.6.59}$$

Constants a_1 and a_3 are fixed by the boundary conditions given by (2.6.57) as follows

$$a_1\phi'_{10} + a_3\phi'_{30} = 0 \tag{2.6.60a}$$

$$a_1\phi_{10} + a_3\phi_{30} = 2\pi \tag{2.6.60b}$$

Additional subscript 0 indicates the quantities to be evaluated at the wall. Equations (2.6.60) are solved for a_1 and a_3 that simplifies (2.6.56) to,

$$\psi(x,y,t) = \int_{Br} \frac{\phi_1(y,\alpha)\phi'_{30} - \phi'_{10}\phi_3(y,\alpha)}{\phi_{10}\phi'_{30} - \phi'_{10}\phi_{30}} e^{i(\alpha x - \omega_0 t)} d\alpha \tag{2.6.61}$$

The denominator in this expression is evaluated at the wall and is the characteristic determinant of the eigenvalue problem shown in Eqn. (2.4.8). This connects the receptivity problem with the corresponding instability problem. It is also apparent that the eigenvalues (those are the zeros of the characteristic determinant in the denominator of (2.6.61)) constitute the poles for the receptivity problem.

The choice of Bromwich contour is made based on the qualitative knowledge of the eigen-spectra of the problem. For example, if one were to calculate the impulse response of Blasius boundary layer, then one has to position this contour in such a way that all the downstream propagating modes (the group velocity of these are positive) lie above this contour and the upstream propagating modes lie below this contour in the wave number plane. Detailed discussion of this is given in Sengupta *et al.* (1994). The response due to all the discrete modes, the essential singularities and the continuous spectra are built inside ϕ evaluated along the Bromwich contour itself. A possible Bromwich contour can be taken parallel and below the real axis, so that the downstream propagating modes stay above this contour. There is the added advantage for this choice of contour in applying DFFT along this contour- otherwise any other contour would be alright in the strip of its convergence.

A typical impulse response is shown in Fig. 2.19 for Blasius boundary layer, for $\omega_0 = 0.1$ and $Re_{\delta^*} = 1000$, with disturbance stream function shown at the inner and the outer maxima of the least stable mode.

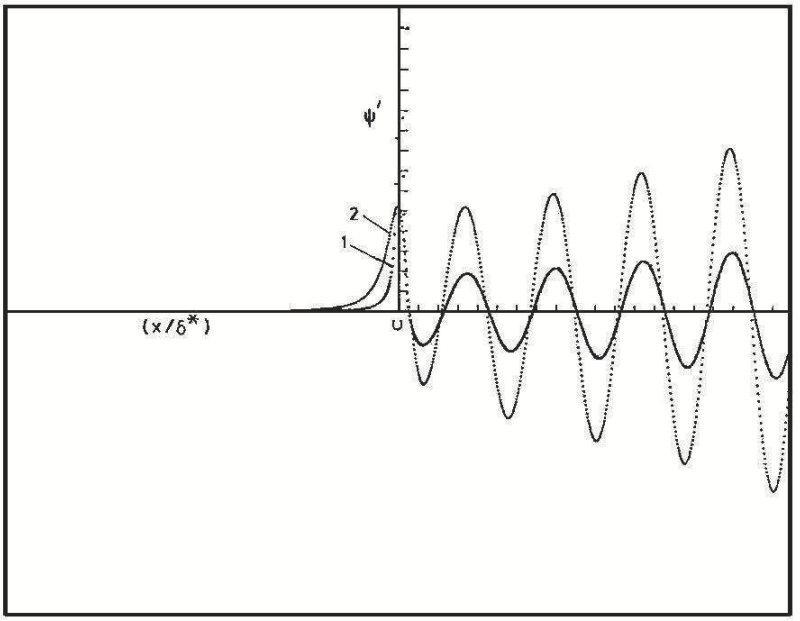

Figure 2.19 Disturbance stream function plotted versus streamwise distance for (1) the inner maximum at $y/\delta^*0.277$ and (2) for the outer maximum at $y/\delta^*1.79$

About $30\delta^*$ from the exciter in the downstream direction the computed disturbance profile matches with the eigen-solution corresponding to the complex wave number value (0.2798261, -0.00728702), with that obtained by the stability analysis for the TS mode. It is interesting to note that there is a local component of the receptivity solution that decays rapidly in either direction. This is called the near-field response or the local solution. Thus, the receptivity solution in this figure consists of the asymptotic solution (away from the exciter) and a local solution.

The description of the local solution and other details of selecting the Bromwich contours are given in Sengupta *et al.* (1994) and Sengupta & Rao (2006). The near-field response created due to wall excitation is shown in these references as due to the essential singularity of the bilateral Laplace transform of the disturbance stream function. While the experiments of Schubauer & Skramstad (1947) verified the instability theory, the instability theory is incapable of explaining all the aspects of the experiments or

the solution obtained by the receptivity analysis e.g. the near-field and the transient solution discussed in Sengupta *et al.* (2006a). In this context receptivity analysis is unique and assumes special importance. In the following, the near-field of the receptivity solution is explained.

2.6.2.1 Near-Field Response Created by Localized Excitation

The near-field response created due to wall excitation is shown here as due to the essential singularity of the bilateral Laplace transform of the disturbance stream function. So far we have seen that the occurrence of transition from laminar to turbulent boundary layer over plane surface proceed as growth of spatially growing instability waves -as was theoretically shown by Heisenberg (1924), Tollmien (1931) and Schlichting (1935) and later verified experimentally by Schubauer & Skramstad (1947).

In Case (1960) and Gaster (1965), some theoretical aspects of the receptivity of a fluid dynamic system from initial- boundary value point of view was addressed. The first set of receptivity calculations were provided in Sengupta (1991) and Gaster & Sengupta (1993) under some restrictive conditions on time variation. Sengupta *et al.* (1994) removed this constraint and produced the first time-dependent solution of the receptivity to wall excitation problem. In Ashpis & Reshotko (1990), a "revised" formulation (with respect to Gaster's (1965) work) was given following Briggs' method developed to study plasma dynamics instability. The authors stated that the discrete spectrum and branch points constitute the time asymptotic solution. It was also conjectured that the near-field contribution comes from the branch cuts introduced from three fixed branch points of the governing Orr- Sommerfeld equation. Interestingly, they identified the branch-cuts as the continuous spectral lines responsible for the local solution. This has not been proven since and the one-to-one correspondence between the so-called continuous spectra and the near-field established. On the other hand, the formal integral of the bilateral Laplace transform in space and Fourier integral in time, along carefully chosen Bromwich contours can automatically provide both the near- and far-field results, an example is shown in Fig. 2.19.

Here an explanation is provided on the structure of the near-field solution with the help of some fundamental theorems. These theorems provide the basis for interpreting both the near- and far-field solutions. These are due to Abel and Tauber and their utility was highlighted by Van der Pol & Bremmer (1959) in connection with the properties of bilateral Laplace transform. In exploring relationships between the original in the physical plane and the image or transform in the spectral plane these two important

theorems are used here. In particular if one is interested in the behaviour of the original in the neighborhood of the exciter (i.e. near $x = 0$), then one needs to investigate the image at $\alpha \to \infty$. This is the **Tauber's theorem**. Similarly, if one is interested in the solution far away from the exciter $x \to \infty$, then one needs to consider only the neighborhood of the origin in the α-plane. This is the **Abel's theorem** and this simply points to the relevance of those poles only that are very close to the origin in the $\alpha-$ plane. In traditional stability analysis, not only the Abel's theorem is implicitly used, but also the attention is focused only on the right-half of the $\alpha-$ plane.

Following the above, let us explore the relation between the original and the image of bilateral Laplace transforms in relation to the evolution of small disturbances in boundary layers. In particular, one would be interested in the behaviour of the original in the neighbourhood of the exciter ($x = 0$) as determined by the image $\phi(y, \alpha)$ for $\alpha \to \infty$ according to the Tauber's theorem.

In this sense we will determine the contribution of $\alpha \to \infty$ for the original-image pair of Eqn. (2.6.56). It is also relevant to discuss about the role of Jordan's Lemma (as discussed in Arfken (1985)) that shows the contour integral along the semi-circular arc- with its radius approaching infinity in Figure 2.18- approaches zero under some special condition satisfied by the integrand. Let us recall that the integral along C, as shown in Fig. 2.18, is given by

$$I_C = \int \phi(\alpha) e^{i\alpha x} d\alpha \tag{2.6.62}$$

would vanish, if and only if the degree of the denominator of (2.6.61) is at least two orders higher than the degree of the numerator i.e.,

$$|\phi(\alpha)| < \frac{k}{|\alpha^2|} \tag{2.6.63}$$

for $\alpha \to \infty$. One of the main reasons for the present discussion here is to show that the image $\phi(\alpha)$ for this limit, as governed by Orr-Sommerfeld equation, does not satisfy the condition given in (2.6.63). To show this, it is possible to expand $\phi(\alpha)$ as a function of $\epsilon_1 (= \frac{1}{\alpha})$ by a singular perturbation analysis for $\alpha \to \infty$ and it can be shown that such a series expansion starts with a $0(\epsilon_1)$ term i.e. the condition given in Eqn. (2.6.63) is not supported- so that the Jordan's lemma is inapplicable here.

Thus, the next objective here is to estimate the contribution coming from the contour integral in (2.6.62) from the semi-circular arc in the α-plane, when the radius of the arc goes to infinity. Along this arc one can

represent,

$$\alpha = \rho \quad e^{i\theta} = \rho\beta \tag{2.6.64}$$

where ρ is the radius of the arc. To determine ϕ for large α, examine the asymptotic form of the Orr-Sommerfeld equation as an expansion in the small parameter $\epsilon_1 = \frac{1}{\rho}$ for $\rho \to \infty$. Equation (2.3.21) then takes the form

$$\begin{aligned}&\epsilon_1^4\phi^{iv} - [2\epsilon_1^2\beta^2 + iRe\epsilon_1^3(\beta U - \epsilon_1\omega_0)]\phi'' \\ &+ [\beta^4 + iRe\beta\epsilon_1^3 U'' + iRe\beta^2\epsilon_1(\beta U - \epsilon_1\omega_0)]\phi = 0\end{aligned} \tag{2.6.65}$$

Note that the image ϕ can also be expanded in a perturbation series and the analysis here is for the leading order term of such an expansion. The higher order terms of ϕ would produce trivial contribution to the contour integral because of the satisfaction of the condition for Jordan's Lemma, as given above in (2.6.63).

Let us now discuss the case of wall excitation where a localized delta function excites the flow. To simplify analysis, consider the following boundary conditions applied at the wall that is located at the origin of the co-ordinate system:

$$y = 0: \qquad u = 0 \quad and \quad \psi(x, 0, t) = \delta(x)e^{-i\omega_0 t} \tag{2.6.66}$$

And far from the wall ($y \to \infty$):

$$u, v \to 0 \tag{2.6.67}$$

The boundary conditions (2.6.66) and (2.6.67) of the impulse response problem, can also be expressed as $\phi(0, \alpha) = 1$ and $\phi'(0, \alpha) = 0$ at $y = 0$ and as $y \to \infty$: $\phi(y, \alpha), \phi'(y, \alpha) \to 0$.

From Eqn. (2.6.65), it is apparent that this is a singular perturbation problem (as the highest derivative term is multiplied by the small parameter) and then one can use matched asymptotic expansion to obtain ϕ by describing the solution in terms of outer and inner solutions.

2.6.2.1a Outer Solution

By definition, in the outer region ϕ and all its derivatives are 0(1) and Eqn. (2.6.65) simplifies to

$$\phi_0 = 0 \tag{2.6.68}$$

This solution is true up to any order and it automatically satisfies the outer boundary conditions. However, this does not satisfy the wall boundary condition and one must have a *boundary layer* or the inner layer of say, the thickness, δ. The thickness δ, can be obtained by the distinguished limits in the inner layer by following the method given in Bender & Orszag (1987).

2.6.2.1b Inner Solution

In the inner layer, we define a new independent variable $Y = y/\delta$ and work with the dependent variable $\phi = \phi_i(Y)$. Then Eqn. (2.6.65) takes the form,

$$(\frac{\epsilon_1}{\delta})^4\phi_i^{iv} - [2\beta^2(\frac{\epsilon_1}{\delta})^2 + iRe(\beta U - \epsilon_1\omega_0)(\frac{\epsilon_1^3}{\delta^2})]$$
$$\phi_i'' + [\beta^4 + iRe\beta\epsilon_1^3 U'' + iRe\beta^2\epsilon_1(\beta U - \epsilon_1\omega_0)]\phi_i = 0 \qquad (2.6.69)$$

Here the derivatives of ϕ_i are now with respect to Y. One can look at various distinguished limits by choosing terms pairwise in Eqn. (2.6.69).

(i) For the distinguished limit $\delta << \epsilon_1$: Equation (2.6.69) reduces to $\phi_1 = 1$.

This is a non-trivial solution satisfying the wall boundary conditions. But, it does not allow matching the inner and outer solutions and has to be discarded.

(ii) For the distinguished limit $\delta >> \epsilon_1$, one gets $\phi_i(Y) = 0$. However, this is not a valid solution as it fails to satisfy the wall boundary condition.

(iii) For the distinguished limit $\delta = \epsilon_1$: Equation (2.6.69) takes the form

$$\phi_i^{iv} - 2\beta^2\phi_i'' + \beta^4\phi_i = 0$$

The solution of which is, $\phi_i(Y) = A\ e^{\beta Y} + BY\ e^{\beta Y} + C\ e^{-\beta Y} + DY\ e^{-\beta Y}$

Note that β is a complex constant and for $\beta_r > 0$, the inner solution that satisfies Eqn. (2.6.66) is given by,

$$\phi_i(Y) = (1 + \beta Y)\ e^{-\beta Y} \qquad (2.6.70)$$

Similarly one can obtain the inner solution for $\beta_r < 0$ as,

$$\phi_i(Y) = (1 - \beta Y)\ e^{\beta Y} \qquad (2.6.71)$$

It is easy to show that the other two distinguished limits, $\delta^2 = \epsilon_1^3$ and $\delta^2 = \epsilon_1^4$ produce only the trivial solution.

Thus, the only possible distinguished limit is $\delta = \epsilon_1$, implying that the inner layer of the Orr-Sommerfeld equation is of thickness, $\delta = \frac{1}{|\alpha|}$. In terms of the physical variables, the asymptotic value of ϕ is then:

For $\alpha_r > 0$

$$\phi = (1 + \alpha y)\ e^{-\alpha y} \qquad (2.6.72)$$

And for $\alpha_r < 0$

$$\phi = (1 - \alpha y)\ e^{\alpha y} \qquad (2.6.73)$$

To evaluate the contribution to ψ coming from the semicircular contour, we must consider three segments of the contour- as shown in Fig. 2.20-

since ϕ is discontinuous across α_i- axis. The imaginary axis demarcates the spectral plane in terms of required sub-dominance of the fundamental solutions as given in Eqn. (2.4.4) and a consequence of which is observed from Eqns. (2.6.70) and (2.6.71).

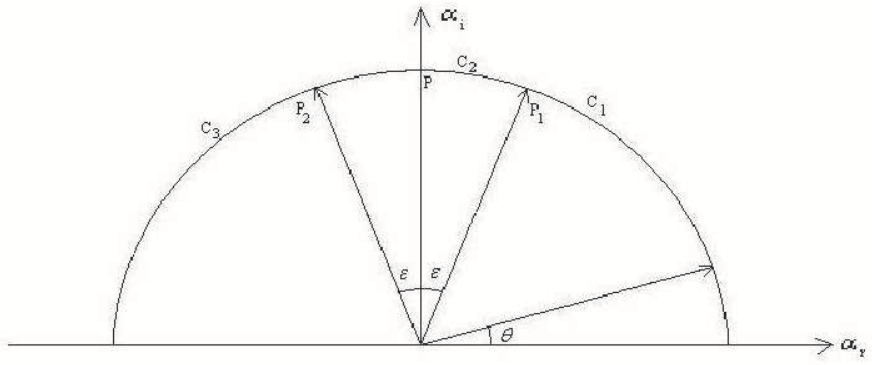

Figure 2.20 The contour used in the evaluation of the integral in Eqn. (2.6.74)

For the purpose of evaluating the contour integral, we choose the Bromwich contour along the real wave number axis, without any loss of analyticity of ϕ. Thus,

$$\psi(x,y,t) = \frac{1}{2\pi}\int \phi(y,\alpha)e^{i(\alpha x-\omega_0 t)}d\alpha \tag{2.6.74}$$

Where

$$On \quad C_1: \quad \phi(y,\alpha) = (1+\alpha y)e^{-\alpha y} \tag{2.6.75}$$

$$On \quad C_2: \quad \phi(y,\alpha) = (1-\alpha y)e^{\alpha y} \tag{2.6.76}$$

$$At \quad P: \quad \phi(y,i\rho) = \frac{1}{2}(e^{i\rho y}+e^{-i\rho y}) \tag{2.6.77}$$

The last contribution is required as ϕ is discontinuous across P. To calculate the contribution coming from the neighbourhood of point P, we consider a sector of the contour around P terminating at P_1 and P_2 in Fig. 2.20, defined by the small angle ϵ. One fixes the value of β at P_1 and P_2 in the following manner. The value of β corresponding to P_1 is,

$$\beta_1 = e^{i(\frac{\pi}{2}-\epsilon)} = i + \epsilon \text{ for the small value of } \epsilon.$$

And the value of β corresponding to P_2 is

$$\beta_2 = e^{i(\frac{\pi}{2}-\epsilon)} = i - \epsilon \text{ for the small value of } \epsilon.$$

The contribution coming from C_1 is obtained from

$$I_1 = \frac{1}{2\pi} e^{-i\omega t} \int_0^{\beta_1} (1 + \rho\beta y) e^{i\beta\rho z} \rho d\beta$$

$$= \frac{e^{-i\omega_0 t}}{2\pi} [e^{i\rho\beta_1 z} \frac{(1 + \rho\beta_1 z + \frac{iy}{z})}{iz} + e^{i\rho z} \frac{(1 + \rho y + \frac{iy}{z})}{z}]$$

The contribution I_2, coming from the contour C_2, in the limit of $\epsilon \to 0$ is

$$I_2 = \frac{e^{-\rho x - i\omega_0 t}}{2\pi} \cos \rho y$$

And finally the contribution I_3, coming from the contour C_3 is

$$I_3 = \frac{e^{-i\omega_0 t}}{2\pi} [e^{-i\rho\bar{z}} \frac{(1 + \rho y - i\ y/\bar{z})}{i\bar{z}} - ei\rho\beta_2\bar{z} \frac{(1 + \rho\beta_2 y - i\ y/\bar{z})}{i\bar{z}}]$$

where $z = x + iy$ and $\bar{z} = x - iy$, is its complex conjugate.

Collecting various contributions, one obtains the perturbation stream function from the semicircular contour of radius ρ as,

$$\psi(x, y, \rho, t) = [e^{-\rho x} \cos \rho y + \frac{ie^{i\rho z}}{z}(1 + \rho y + \frac{iy}{z}) - \frac{ie^{-i\rho\bar{z}}}{\bar{z}}(1 + \rho y - \frac{iy}{\bar{z}})$$
$$- \frac{ie^{\rho z + iz}}{z}(1 + \frac{iy}{z} + i\rho y + y) + \frac{ie^{-\rho\bar{z} - i\bar{z}}}{\bar{z}}(1 - \frac{iy}{\bar{z}} - i\rho y + y)] \frac{e^{-i\omega_0 t}}{2\pi} \tag{2.6.78}$$

To check for the correctness of this result, let us investigate the solution at $y = 0$, where the wall excitation is applied to the shear layer. Here $\psi(x, 0, \rho, t)$ simplifies to

$$\psi(x, 0, \rho, t) = \frac{e^{-i\omega_0 t}}{2\pi} \{e^{-\rho x} - \frac{2 \sin \rho x}{x} + 2e^{-\rho x}(\frac{\sin x}{x})\} \tag{2.6.79}$$

In the limit of $\rho \to \infty$, the first and the third terms above, do not contribute. But the second term turns out as equal to what is known as

Dirichlet function, which is an approximation of Delta function, $\delta(x)$. Various approximate representations of Dirac delta function are provided in Van der Pol & Bremmer (1959) on pp 61-62. This clearly shows that we recover the applied boundary condition at $y = 0$. Therefore, the delta function is totally supported by the point at infinity in the wave number space (which is nothing but the circular arc of Fig. 2.20 i.e. the essential singularity of the kernel of the contour integral).

This result has the following consequence for the completeness of basis function constructed from the eigenvectors obtained by stability analysis of external flows. It has been clearly shown by Mack (1976) that internal flows, like the channel flow, has denumerable infinite number of eigen modes and any arbitrary applied disturbance can be expressed in terms of this complete basis set. However, for external flows, as we have seen for the Blasius flow in Table 2.1 that there are only a few discrete eigenmodes and it is not possible to express any arbitrary functions in terms of these only, in the absence of any other singularities for this flow.

Table 2.1: Spatial modes and their group velocity for the impulse response analysis for $Re = 1000$ and $\omega_0 = 0.10$ (From Sengupta et al. (1994))

Mode Number	α_r	α_i	V_g (Group Velocity)
1	0.2798261	-0.00728702	0.4202
2	0.1380375	0.10991244	0.4174
3	0.1220209	0.17393307	0.8534

The theoretical analysis here in the present section clearly indicates that the localized delta function excitation in the physical space is supported by the essential singularity ($\alpha \to \infty$) in the image plane. This is made possible because $\phi(y, \alpha)$ does not satisfy the condition required for the satisfaction of Jordan's lemma. As any arbitrary function can be shown as a convolution of delta functions with the function depicting the input to the dynamical system. The present analysis indicates that any arbitrary disturbances can be expressed in terms of a few discrete eigenvalues and the essential singularity. In any flow, in addition to these singularities there can be contributions from continuous spectra and branch points - if these are present.

For the purpose of highlighting the above theoretical analysis explaining the origin for the creation of the near-field of the response created by wall excitation, some numerical results are presented next, those have been obtained by solving (2.3.21), subject to the boundary conditions given by Eqns. (2.6.66) - (2.6.67). Cases have been considered where a harmonic source is excited with $\omega_0 = 0.1$ placed at three different locations with the local Reynolds numbers based on displacement thickness are 400, 1000 and 4000, respectively. As in calculating the impulse response case shown in Figure 2.19, here also the Bromwich contour is located below and parallel to the real wave number axis, along $\alpha_i = -0.02$. Once again, the compound matrix method has been utilized to obtain the solution and shown in Fig. 2.21 below.

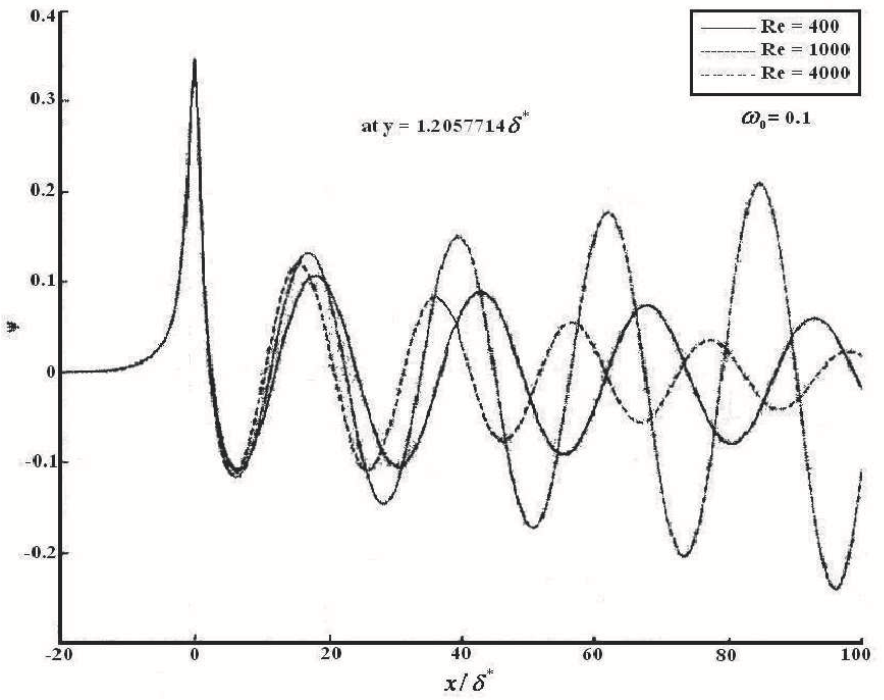

Figure 2.21 The solution of the signal problem at the indicated Reynolds numbers, for the same circular frequency. Note that the local solution components in all the cases are the same.

Presented solution once again, demonstrates the far-field to correspond to the TS mode obtained by linear stability analysis. For $Re = 1000$ and $\omega_0 = 0.1$, the calculated impulse response displays TS wave with $\alpha_r = 0.279826$ and $\alpha_i = -0.007287$. The results are shown at a height of $y = 1.205\delta^*$- the location of the outer maximum of the eigenvector. Considering the stability properties of the Blasius profile, one expects the flow to be stable for $Re = 400$ and 4000 - with the latter case showing higher damping than the former, as clearly seen in Fig. 2.21.

Despite the differences in the values of the wave length and the growth/ decay rate of the three cases, one can notice the remarkable similarity of the near-field solution. While the upstream part of all the three solutions are exactly identical, the minor differences on the downstream side of the near-field are due to the different wave lengths and growth (decay) rates of the asymptotic solutions. This is very consistent with the observed properties of ϕ, as obtained for $\alpha \to \infty$ behaviour. Specifically one can note that the near-field solution obtained in Eqns. (2.6.78) and (2.6.79) are Reynolds number independent, as is also seen in the calculated cases shown in Fig. 2.21. One also notes that the local solution originates in the inner layer whose governing differential equation is given by (obtained from the appropriate distinguished limit of (2.6.69)),

$$\phi^{iv} - 2\beta^2\phi'' + \beta^4\phi = 0 \tag{2.6.80}$$

From this equation, it is possible to discuss further about the general properties of the near-field solution. Noticing that the kinematic equation $\bigtriangledown^2\psi = -\omega$, when substituted in the governing vorticity transport equation one obtains,

$$\frac{D}{Dt}\bigtriangledown^2\psi = \frac{1}{Re}\bigtriangledown^4\psi \tag{2.6.81}$$

It is easy to see that Eqn. (2.6.80) is nothing but the right hand side of Eqn. (2.6.81), implying that the near-field of the solution is given by the corresponding Stokes problem (in the limit of $Re \to 0$),

$$\bigtriangledown^4\psi = 0 \tag{2.6.82}$$

Thus, in the near-field of the exciter, the flow behaves like a highly viscous flow and it is for the same reason the near-field does not penetrate far upstream and downstream. For the cases shown in Fig. 2.21 the zone affected in the near-field is roughly about $20\delta^*$.

The above results also bring forth a very important aspect of real fluid flows. Despite the mathematical requirement of Jordan's Lemma (that we must have $|\phi(\alpha)| \to 0$ for $\alpha \to \infty$), in real flows there always exists a cut-off wave number due to the fact that smaller waves have larger strain-rates.

Hence unlimited range of wave numbers are not sustainable for an excitation problem driven by a finite source of energy. At the cut-off wave number, the kinetic energy of the wave would be converted to heat - an idea that has been traditionally employed to fix the cut-off wave number in Kolmogorov's theory of energy cascade in homogeneous turbulence. Present analysis also shows that the motion in the very small scale of any flow, is governed by Stokes equation given by (2.6.82). It is also interesting to note that the local or the near-field solution cannot be canceled by wave superposition principle.

So far, we have discussed the case of very localized-in-space excitation cases. However, in an actual flow the exciter will be of finite width, as it was in the vibrating ribbon experiments of Schubauer & Skramstad (1947). This is the topic of discussion in the following.

2.6.3 Vibrating Ribbon at The Wall

If one wants to model the vibrating ribbon experiments of Schubauer & Skramstad (1947) by embedding the disturbance source on the surface of the plate, then the following is implied. Let the disturbance source be located at $x = x_0$, instead of the origin. Then instead of (2.6.56) one should rewrite the disturbance stream function as,

$$\psi(x, x_0, y, t) = \frac{1}{2\pi} \int_{Br} \phi(y, \alpha; \omega_0) e^{i[\alpha(x-x_0)-\omega_0 t]} d\alpha \tag{2.6.83}$$

It is seen that the governing equation for the bi-lateral Laplace amplitude is, once again, given by the Orr-Sommerfeld equation. To model this flow, we have to consider the width of the vibrating ribbon and not treat it as a simple line source. Finite width of the ribbon will excite a stream of contiguous wave numbers. Such closely spaced wave numbers will create groups of waves or a wave packet and in the response one would see modulated waves, as discussed and shown in Sengupta *et al.* (2006a).

Thus, for the finite-width ribbon located between $x = x_1$ and $x = x_2$, the disturbance stream function can be written as,

$$\psi(x, y, t) = \frac{1}{2\pi} \int_{x_1}^{x_2} \{ \int_{Br} \phi(y, \alpha; \omega_0) e^{i[\alpha(x-x_0)-\omega_0 t]} d\alpha \} dx_o \tag{2.6.84}$$

Here it is implied that all the points between x_1 and x_2 are excited by the same amplitude. It need not necessarily be the case and a more general

excitation would have the solution of the form written as,

$$\psi(x,y,t) = \frac{1}{2\pi}\int_{x_1}^{x_2}[\int_{Br} W(x_0;x_1,x_2)\phi(y,\alpha;\omega_0)e^{i[\alpha(x-x_0)-\omega_0 t]}d\alpha]dx_o \tag{2.6.85}$$

Where $W = W(x_0;x_1,x_2)$ is the prescribed weight function that fixes the type of excitation applied at the wall. This requires performing an weighted integral of the impulse response given by (2.6.83) with the prescribed weight function. Some typical weight-functions are shown in Fig. 2.22 corresponding to different types of commonly used excitations.

These model excitations are commonly used in receptivity analysis using linear and nonlinear models. For example, the combined blowing and suction excitation case shown in Fig. 2.22 has been used in quite a few direct simulation attempts because of the fact that this does not excite high wave numbers in the spectral plane to cause numerical instability that is a common problem faced in DNS at high wave numbers. Also, such an excitation does not cause numerical mass conservation problem at any time instant, as the amount of blowing is analytically counter-balanced by the amount of suction. Such an exercise for exciting TS waves was undertaken in Fasel & Konzelmann (1990). Sometimes the Gaussian excitation, shown in Fig. 2.22, is also preferred due to the advantage of band-limited nature of the excitation field in the spectral plane as well; as a consequence of the *self reciprocity* property of Hermite functions. The excitation shown in Fig. 2.22(a) is preferred for receptivity calculations based on linearized Navier-Stokes equation- as it excites a large band of wave numbers with equal emphasis.

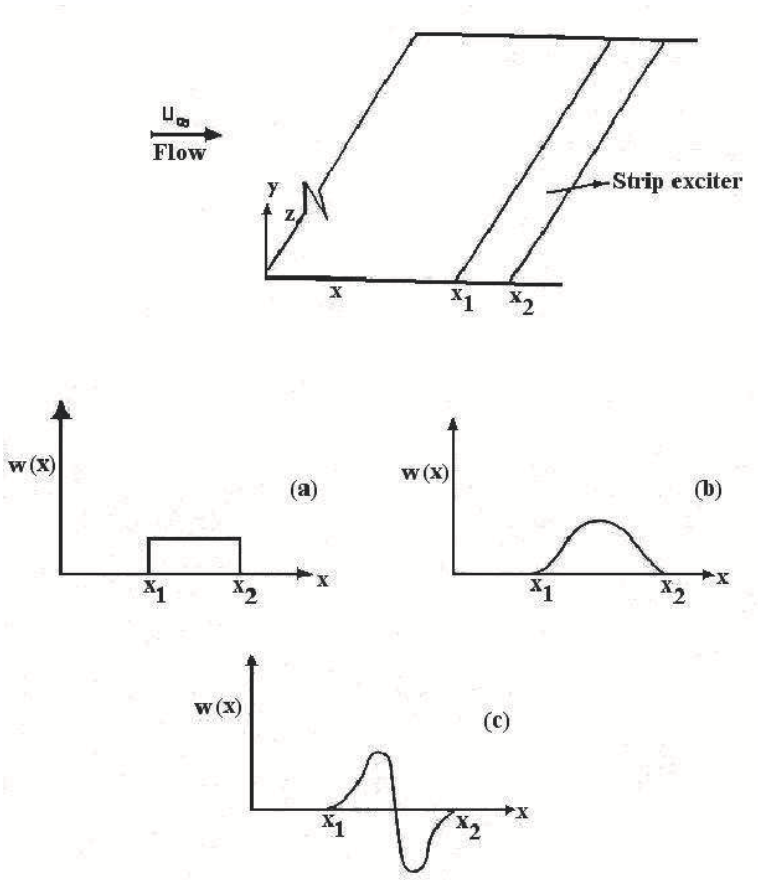

Figure 2.22 Typical time-harmonic excitations used on the surface for receptivity studies: (a) Strip excitation; (b) Gaussian amplitude distribution and (c) Simultaneous blowing and suction excitation.

Solutions for different excitations, at different x- locations, have simply to be added or convolved in the linear analysis, as demonstrated in Sengupta & Sinha (1995) and Sengupta *et al.* (2006a) for the type of strip excitation shown in Fig. 2.22(a) applied on a flat plate.

To calculate the actual receptivity of a boundary layer in a correct time-accurate fashion, one should not start with the ansatz of the **signal prob-**

lem, as given by Eqn. (2.6.56) and instead one should define the disturbance stream function by,

$$\psi(x,y,t) = \frac{1}{(2\pi)^2}\int\int_{Br} \phi(y,\alpha,\omega)e^{i(\alpha x-\omega t)}d\alpha \;\; d\omega \tag{2.6.86}$$

For this case, the Bromwich contours have to be traced simultaneously in both the $\alpha-$ and the $\omega-$ plane. The choice of Bromwich contour in the $\omega-$ plane is not difficult, because in choosing it, one has to satisfy the causality requirement. However, the choice of Bromwich contour in the wave number plane remains as difficult as before for the *signal problem*.

Once again, when the ansatz of Eqn. (2.6.86) is used in the linearized Navier-Stokes equation and the equilibrium solution is treated as parallel, one obtains OSE as the governing equation. The boundary conditions applicable at the wall should now additionally incorporate the information of the finite start-up time of excitation as given below by,

$$u = 0 \quad and \quad \psi(x,0,t) = U(t)\delta(x)e^{-i\omega_0 t} \tag{2.6.87}$$

At the free stream the disturbance quantity should decay to zero as before. Note that the presence of the Heaviside function $U(t)$ in Eqn. (2.6.87) ensures that the excitation begins at t = 0, once again at the frequency ω_0. These boundary conditions in the physical plane translates in the spectral planes as,

$$\phi'(\alpha,0,\omega) = 0 \tag{2.6.88a}$$

and

$$\phi(\alpha,0,\omega) = BC_w \tag{2.6.88b}$$

Where $BC_w = [i(\omega_0-\omega)]^{-1}$ is the correct boundary condition for the full time-dependent problem. To satisfy the far-stream ($y \to \infty$) conditions, the solution of OSE would be cast once again in the form,

$$\phi(\alpha,y,\omega) = c_1\phi_1 + c_3\phi_3 \tag{2.6.89}$$

where ϕ_1 and ϕ_3 are the inviscid and the viscous fundamental decaying modes, as before. The constants c_1 and c_3 are fixed from the wall conditions given in (2.6.88a) and (2.6.88b). This gives,

$$\psi(x,y,t) = \frac{1}{(2\pi)^2}\int\int_{Br} \frac{\phi_1(\alpha,y,\omega)\phi'_{30} - \phi'_{10}\phi_3(\alpha,y,\omega)}{\phi_{10}\phi'_{30} - \phi_{30}\phi'_{10}} BC_w e^{i(\alpha x-\omega t)}d\alpha\, d\omega \tag{2.6.90}$$

This is the problem that was solved for $Re = 1000$ and $\omega_0 = 0.1$ in Sengupta *et al.* (1994), for which the results for the corresponding *signal*

problem was provided before in Sengupta (1991) and Gaster & Sengupta (1993). In Fig. 2.23, the full time-dependent solution is compared with the solution obtained for the corresponding *signal problem*, termed as the time-asymptotic solution in the figure.

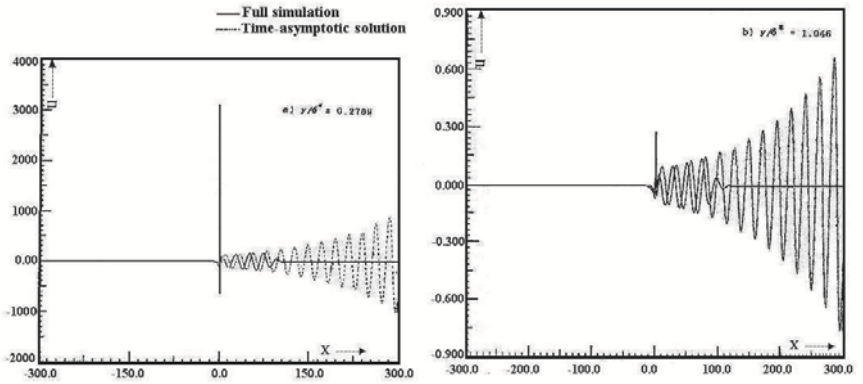

Figure 2.23 Comparison of solutions obtained by full receptivity analysis (solid line) and signal problem analysis (dotted line)- at the indicated heights.

Presented time accurate solution can be termed appropriately as the correct receptivity solution, as compared to its idealization in the *signal problem.* Later on, the results of this solution process is considered to look at the cases of "spatially stable systems", those actually admit spatio-temporally growing wave-fronts-as given in Sengupta *et al.* (2006, 2006a). What is apparent for all spatially unstable cases is that there are no differences between the *signal problem* and the actual time-dependent problem-as two solutions shown in Fig. 2.23 match up to a certain distance-with the streamwise distance over which the match is seen stretches with time.

One of the reasons that the transition process is somewhat intractable is due to the fact that the receptivity process is inadequately understood for cases other than the wall excitation case, as discussed above. This intractability is specifically the case for shear layers excited by sources outside the viscous layer in the free stream, for many reasons. Firstly, unlike the wall excitation case where the applied disturbance is uniquely located at the wall, for free stream excitation the response would be different depending upon the height of the exciter in the free stream - a parameter that can

continuously change with space and time, depending upon the dynamics of such disturbances interacting with other disturbance sources. Secondly, the type of excitation that is present in the free stream also matters significantly. For example, acoustic, entropic and vortical disturbances will have significantly different receptivity. In the following, attention is focused upon the cases of vortical excitation only.

2.6.4 Receptivity to Free Stream Excitation

The main aspect of instability by free stream disturbances has not been investigated as successfully as has been the case of wall excitation. The reason has been explained earlier while discussing the observations from the experiments of Schubauer & Skramstad (1947). They could not successfully detect TS waves when they irradiated the test section with acoustic waves. Of course, transition was detected without tracing the over-riding presence of a monochromatic disturbances like the TS wave. The reasons are many-folds: firstly, an acoustic wave is three-dimensional and even when it creates TS waves, they would be due to streamwise and cross flow instability. Moreover, it would create many interacting TS waves simultaneously without showing monochromatic wave- as obtained in normal mode analysis. Secondly, the receptivity of laminar boundary layer to this type of free stream disturbances show indirect and very weak coupling. Some experimental efforts have been made starting with the interesting work of Taylor (1936), who tried to estimate the dependence of critical Reynolds number upon free stream turbulence, treating the latter as a vortical disturbance only. Monin & Yaglom (1971), in discussing Taylor's work, conjectured that the convected vortices embedded in the free stream cause small adverse pressure gradient that gives rise to unsteady separation at multiple scales. Such unsteady separations cause very rapid and catastrophic transition. The assumption implicit in this scenario is that the *effect is connected with the generation of fluctuations of longitudinal pressure gradient by these disturbances, leading to the random formation of individual spots of unstable S-shaped velocity profile* (Monin & Yaglom, 1971). Thus, the effects of free stream disturbances are viewed as causing the buffeting of the shear layer by these ever-present disturbance sources- not as such as that is due to instabilities.

In contrast to this earlier view-point, Morkovin (1969) proposed that the response to free stream excitation occurs in two stages. In the first stage (popularized by Morkovin (1969) as the receptivity stage) the external perturbations are internalized as unsteady fluctuations giving rise to TS waves accompanying the equilibrium state. In the second stage, these internalized

excitations have the direct receptivity in causing transition- as described in previous sub-sections.

The problem of excitation of shear layer by disturbance sources convecting outside the shear layer has been experimentally investigated by Kendall (1987, 1990) and Dietz (1999). Kendall (1990) through his experiments on jet-induced free stream turbulence, has provided direct evidence of TS waves and wave packets forming in a nominally flat plate boundary layer.

Dietz (1999) successfully created a single frequency gust by using a vibrating ribbon in the free stream and provided quantitative data on TS wave amplitudes generated by the interaction of the gust with a surface roughness element. It is interesting to note that the prevalent notion that convected vorticity field traveling with the free stream speed will not show any receptivity, was also shown in Sengupta *et al.* (2002). However, for free stream acoustic excitation, the receptivity problem is furthermore complicated due to the problem of scale conversion i.e. the sound wave and the TS waves are of different wave lengths and also the phase/ group velocity of the two are also different by orders of magnitude. Additionally, it was noted in the numerical calculations by Murdock (1980) and by theoretical analysis in Goldstein (1983) and Goldstein *et al.* (1983), that the response field amplitude in the shear layer is an order of magnitude lower than the forcing disturbance amplitude in the free stream. However, the experimental results of Leehey & Shapiro (1979) had clearly demonstrated earlier that this coupling is of order one. At the same time, the experiments of Aizin & Polyakov (1979) demonstrated experimentally that an introduction of a thin surface roughness element increases the receptivity linearly with forcing amplitude and roughness height. Most of the theoretical developments using asymptotic analysis were based on this observation - see e.g. the triple deck theory in Goldstein (1985) and Ruban (1985). In Saric *et al.* (1999), the authors noted that the *receptivity has many different paths through which to introduce disturbance into the boundary layer. They include the interaction of freestream turbulence and acoustic disturbances with model vibrations, leading-edge curvature, discontinuities in surface curvature, or surface inhomogeneities... The incoming freestream disturbance (sound or turbulence) at wave number* α_{fs} *interacts with a body in such way (roughness, curvature, etc.) so as to broaden its spectrum to include the response wave number* α_{TS}. In discussing the receptivity to freestream excitation, Goldstein & Hultgren (1989) noted that the scale adjustment mechanism can be attributed to *(i) rapid streamwise variations in the mean boundary-layer flow (which invalidates the parallel-flow assumption of the Orr-Sommerfeld equation) and (ii) sudden changes in surface boundary conditions.* As a result, there is some region near the leading edge of the plate where the correct asymptotic ap-

proximation to the Navier-Stokes equations is the unsteady boundary-region equations, which are just the Navier-Stokes equations with the streamwise derivatives neglected in the viscous and pressure gradient terms. The former is used in leading-edge receptivity problems and the latter comes into view via the appearance of triple-deck structure of the flow at downstream location, in the large Reynolds number limit.

In particular, the receptivity to vortical disturbances was investigated theoretically by Rogler & Reshotko (1975) who modeled the free stream disturbance as a convected array of harmonic vortices. Highly damped near-wall disturbances were calculated from this model. Kerschen (1991) used asymptotic method to calculate vortical receptivity and showed that to vary with the convection speed of vortices. Other Orr-Sommerfeld based models in the literature also could not reveal the physical picture seen in the experiments of Kendall (1987) and Dietz (1999), except in Sengupta *et al.* (2002) - that is discussed in details here.

Kendall (1987) performed experiments in which a circular cylinder was rotated in a circular trajectory above a flat plate shear layer to create a convecting periodic disturbance source. The speed of convection of these vortices was controlled and it was demonstrated that the underlying shear layer was strongly receptive to imposed disturbances in a narrow range of convecting speed around $c = 0.3U_\infty$. In the receptive range, the response field consisted of wave packets composed of many TS waves. In this experiment the disturbance (cause) always stayed outside the shear layer.

Subsequently, Liu & Rodi (1991) repeated Kendall's experiment, but now the periodic disturbance was directed toward the shear layer with large wall-normal velocity component. This latter experiment was supposed to mimic the physical events in the flow inside a turbomachinery. The experiments by Kendall (1987) and Liu & Rodi (1991) show such strong receptivity, while contemporary theoretical calculations by various mathematical models showed lower receptivity. This discrepancy was explained in Sengupta *et al.* (2002) as due to the constraint imposed in the theoretical models on the speed of vortical disturbances in the free stream. It has been seen that in turbomachinery or in flows over helicopter rotor blades, the flow in subsequent stages or blades is strongly influenced by vortices that travel over it at speeds much lower than the free stream speed. For example, the experimental data and their correlation in Schlichting (1979) reveals that the vortices in the far wake of a single bluff body convect at 14 % of the free stream speed. This convection speed is expected to be different in the near wake and when large ensembles of unconstrained vortices are present in the wake. In the experiments of Kendall (1987), this was dramatically shown that maximum receptivity of shear layer occurred when the convec-

tion speed of the freestream vortices were around 30 % of the free stream speed. In a 3D DNS (where there was no need to prescribe any convection speed of vortices) by Wu *et al.* (1999), such strong receptivity has been clearly observed. Sengupta *et al.* (2002) further showed this connection by producing results simultaneously by solving Orr-Sommerfeld equation and two dimensional direct simulation of receptivity. This is discussed further in section 2.7.

2.6.5 General Excitation and Upstream Propagating Mode

Consider the following flow field over a flat plate that is excited simultaneously at the wall $y = 0$ and at the free stream ($y = Y$) as shown in Fig.2.24, where Y is significantly larger than the boundary layer thickness. At the wall, a time-periodic blowing-suction device is placed at $x = x_0$ defined in a coordinate system fixed at the leading edge of the plate. The circular frequency of excitation of the wall device is ω_0 such that the transverse velocity oscillation at the wall is set up as,

$$u = 0 \qquad v = v_w \delta(x - x_0) e^{-i\omega_0 t} \tag{2.6.91}$$

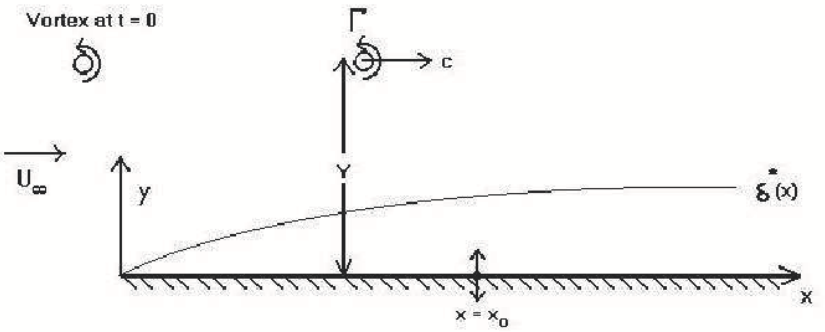

Figure 2.24 General excitation on flat plate boundary layer-simultaneous time-periodic excitation at the wall and a convecting vortex at constant speed in the freestream.

The line vortex of strength Γ convects in the free stream with a constant speed c, and at a constant height Y over the flat plate. Let the instantaneous location of this irrotational vortex be given by $\bar{x}$ from the leading edge.

The corresponding stream function at any field point (x, y), created by this localized line vortex at Y is given by,

$$\psi_\infty = \frac{\Gamma}{4\pi} \; In \; \frac{(x-\bar{x})^2 + (y+Y)^2}{(x-\bar{x})^2 + (y-Y)^2} \tag{2.6.92}$$

where Γ is the strength of the potential line-vortex located instantaneously at $\bar{x} = x_{v_0} - ct$, with x_{v_0} as the initial location of the vortex. The denominator accounts for the image system below the wall created by the reflection of the vortex in the freestream. If one defines the full time-dependent perturbation stream function by,

$$\psi(x, y, t) = \frac{1}{(2\pi)^2} \int\int_{Br} \phi(y, \alpha, \omega) e^{i(\alpha x - \omega t)} d\alpha \;\; d\omega \tag{2.6.93}$$

then one can write down the Laplace-Fourier transform of it, in terms of all the four fundamental solutions as

$$\phi(\alpha, y, \omega) = C_1\phi_1 + C_2\phi_2 + C_3\phi_3 + C_4\phi_4 \tag{2.6.94}$$

Note that one has to retain all the four modes for this general excitation case. To satisfy the first condition of (2.6.91), one must have the following satisfied,

$$C_1\phi'_{10} + C_2\phi'_{20} + C_3\phi'_{30} + C_4\phi'_{40} = 0 \tag{2.6.95}$$

with a prime indicating a derivative with respect to y. Subscript '0' refers to the condition at the wall. For the wall-normal velocity boundary condition of (2.6.91), one can write it using the "time-Shift" theorem of Fourier-Laplace transform as,

$$v_w \delta(x - x_0) e^{-i\omega_0 t} = \frac{1}{(2\pi)^2} \int\int_{Br} v_w e^{i[\alpha(x-x_0) - \omega t]} \;\; \delta(\omega - \omega_0) \; d\alpha \; d\omega \tag{2.6.96}$$

Therefore,

$$C_1\phi_{10} + C_2\phi_{20} + C_3\phi_{30} + C_4\phi_{40} = \frac{v_w}{i\alpha} e^{-i\alpha x_0} \;\; \delta(\omega - \omega_0) \tag{2.6.97}$$

In the same way, one can convert the implied freestream condition of (2.6.92) as

$$C_1\phi'_{1\infty} + C_2\phi'_{2\infty} + C_3\phi'_{3\infty} + C_4\phi'_{4\infty} = B(\alpha, \omega) \tag{2.6.98}$$

and

$$C_1\phi_{1\infty} + C_2\phi_{2\infty} + C_3\phi_{3\infty} + C_4\phi_{4\infty} = D(\alpha, \omega) \tag{2.6.99}$$

Specific type of free stream condition can be represented by finding the appropriate functions, $B(\alpha,\omega)$ and $D(\alpha,\omega)$ defining the tangential and normal velocity components. The additional subscript '(∞)' refers to the conditions being evaluated at the free stream ($y = Y$). Now one can solve for the constants C_1 to C_4 by simultaneously solving (2.6.94) and (2.6.96) - (2.6.98). All these can also be written as the following linear algebraic equation,

$$[\Phi]\{C_i\} = \{f_i\} \tag{2.6.100}$$

where, $\{f_i\} = |0 \;\; \frac{v_w}{2\pi i\alpha} \;\; e^{-i\alpha x_0} \;\; \delta(\omega-\omega_0) \;\; B(\alpha,\omega) \;\; D(\alpha,\omega)|^T$ is the forcing as applied through the boundary conditions. Thus, one can obtain the Fourier- Laplace transform with the constants C_i obtained from,

$$\{C_i\} = [\Phi]^{-1}\{f_i\} \tag{2.6.101}$$

where,

$$\Phi = \begin{bmatrix} \phi'_{10} & \phi'_{20} & \phi'_{30} & \phi'_{40} \\ \phi_{10} & \phi_{20} & \phi_{30} & \phi_{40} \\ -\alpha e^{-\alpha Y} & \alpha e^{\alpha Y} & -Qe^{-QY} & Qe^{QY} \\ e^{-\alpha Y} & e^{\alpha Y} & e^{-QY} & e^{QY} \end{bmatrix}$$

Where, $Q^2 = \alpha^2 + i\alpha Re(1-c)$ and $(\phi_{i\infty},\ \phi'_{i\infty})$'s are obtained from the properties of OSE given in section 2.4. The constants obtained from (2.6.100) can be used in (2.6.86) to obtain the perturbation stream function for this excitation. However, it is also possible to obtain the eigenvalues by calculating them from the characteristic determinant of the corresponding stability problem obtained from,

$$Det \;\; [\Phi] = 0 \tag{2.6.102}$$

This locates the poles of the transfer function obtained from (2.6.93) and (2.6.100). One feature emerges from Eqn. (2.6.101) is that for large Y i.e. when the convecting vortices are far away from the plate, then two sets of terms in the third and fourth rows are sub-dominant in $[\Phi]$. This equation also additionally holds the promise that one can find eigenvalues in the left-half of the complex wave number plane. It is noted that researchers have not been successful in establishing the existence of such modes; see for example the figures in Ashpis & Reshotko (1990) and Schmid & Henningson (2000) where the authors plot the so-called integration contours in the $\alpha-$ plane, indicating unknown eigenvalues on the left-half of plane with question marks. However, this has been shown in Sengupta & Nair (1997) for Blasius boundary layer. This is discussed next.

Let us show a way of locating eigenvalues on the left-half of $\alpha-$ plane from instability analysis point of view. Let us explain the way eigenvalues are located for which $Real\ (\alpha) < 0$ and $Real(Q) > 0$ and $Q^2 = \alpha^2 + i\alpha\ Re(1 - \frac{\omega_0}{\alpha}) = p + iq$. Now as $Y \to \infty$, $\phi_2 (= e^{\alpha y})$ and $\phi_3 (= e^{-Qy})$ are the modes that decay with height in the free-stream. Applied boundary conditions in the free stream are supported then by ϕ_1 and ϕ_4.

Therefore, $Det[\Phi] = 0$ implies the following determinant to be equal to zero.

$$Det[\Phi] = \begin{bmatrix} \phi'_{10} & \phi'_{20} & \phi'_{30} & \phi'_{40} \\ \phi_{10} & \phi_{20} & \phi_{30} & \phi_{40} \\ -\alpha e^{-\alpha Y} & 0 & 0 & Qe^{QY} \\ e^{-\alpha Y} & 0 & 0 & e^{QY} \end{bmatrix}$$

This implies that the following provides the dispersion relation,

$$-[\alpha + Q]\ \ e^{(Q-\alpha)Y}[\phi'_{20}\phi_{30} - \phi_{20}\phi'_{30}] = 0 \tag{2.6.103}$$

Thus, the characteristic determinant obtained from Eqn. (2.6.102) for the eigenvalues in the left-half plane are obtained by the decaying modes ϕ_2 and ϕ_3 only- as noted from (2.6.103). Thus, for the general case of excitation while one needs to retain all the four components of the fundamental solutions of OSE, it is only the decaying modes that determines the dispersion relation. It therefore establishes that the general case of excitation supports modes both in the left-half and the right-half planes simultaneously. The modes on the left-half plane indicate solution components whose phase 'move' upstream. However, whether such modes would actually travel upstream or not would be dictated by the group velocity of that mode. This possibility was investigated in Sengupta & Nair (1997) to detect upstream propagating modes for Blasius profile. Indirect evidence of upstream propagating modes have been reported in Wu *et al.* (1999), where the authors talked about upstream-facing turbulent spots from Navier-Stokes simulation of flow past a plate in the presence of convecting vortices outside the shear layer, affecting the flow that enters the computational domain through the inflow.

However for Blasius boundary layer, these upstream propagating waves are strongly decaying and thus do not give rise to linear instability (see Sengupta & Nair, 1997). In anticipation of possibilities, one notes that for mean flows with adverse pressure gradient upstream propagating modes can become unstable. These upstream propagating modes were discovered serendipitously, as recounted below.

We have noted so far that when Blasius boundary layer is excited by two-dimensional moderate frequency sources one notices TS wave. However at very low frequencies of excitation, TS waves are not seen and instead the whole boundary layer executes a heaving motion; which is now known as the Klebanoff mode of motion. Such mode of motion was also seen experimentally by Gaster *et al.* (1994) when a diaphragm was vibrated at a frequency of 2 Hz on a flat plate with a two-dimensional Blasius boundary layer forming over it. TS waves were not seen as a consequence of this excitation. The mean flow was described adequately by Blasius profile. This prompted Gaster *et al.* (1994) to comment that a proper mathematical account of these disturbances was not known till then. This was provided subsequently in Sengupta *et al.* (1997). To understand the physical nature of Klebanoff mode, first of all we would investigate as to what happens to the disturbance field when the frequency of wall excitation decreases for the Blasius profile, following the results of Sengupta & Nair (1997).

It is worthwhile mentioning that similar experiments were performed earlier by Taylor (1939) and Klebanoff (1971). Klebanoff called this the *breathing mode of motion*. Apart from the fact that TS waves are not seen experimentally, corresponding two-dimensional linear instability studies also do not reveal the presence of any eigen-solutions (TS waves) that decay with height up to the edge of the shear layer. As observed experimentally, the disturbance field is three-dimensional, but it propagates predominantly in the streamwise direction.

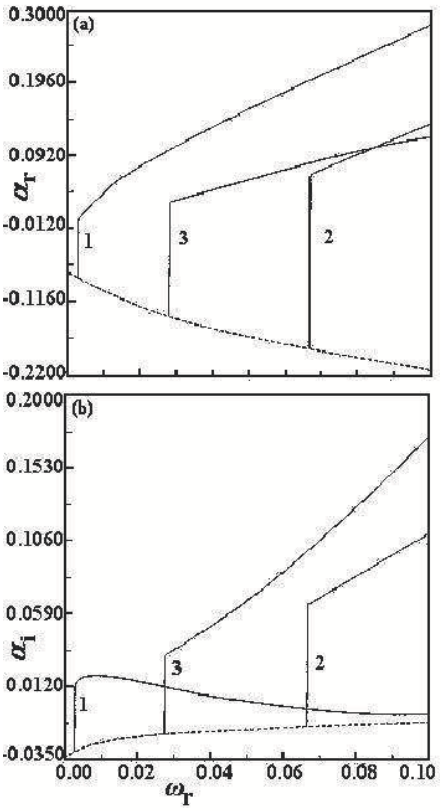

2.25 Variation of α_r and α_i with ω_r for Blasius boundary layer at $Re = 1000$ Note the downstream propagating modes (solid lines) and the upstream propagating mode (dotted line). Downstream propagating modes disappear with ω_r decreasing.

To show the relative roles of various two-dimensional modes at all frequencies, the real and imaginary part of the wave numbers (α_r, α_i) are plotted in Fig. 2.25 as a function of non-dimensional circular frequency for Re = 1000. The three downstream propagating modes that are present at this Reynolds number for moderate frequencies are marked by numerals and are tracked in Fig. 2.25 for their variation with circular frequency. All these two-dimensional modes disappear abruptly one by one, as the frequency is decreased- as noted in Fig. 2.25. Values of circular frequencies at which

these three modes exhibit the above disappearance are listed in Table 2.2. Also shown in the second column are values of ω_0 for a Reynolds number of 1196 that corresponds to the experiments of Gaster *et al.* (1994).

Table 2.2: Values of ω_0 for which 2D modes of Blasius boundary layer disappear

Mode Number	For $Re = 1000$	For $Re = 1196$
1	0.0026	0.0022
2	0.0663	0.0563
3	0.0276	0.0227

If a fluid dynamical system is excited below the lowest of the three values of ω_0 in the above table, then the compound matrix method (Drazin & Reid, 1981, Sengupta *et al.*, 1994 and Allen & Bridges, 2002) detects an eigenvalue that is shown in Fig. 2.25 by a dotted line with its corresponding location on the left-half of the $\alpha-$ plane. It is to be emphasized that finding the eigenvalues on the left-half of the $\alpha-$ plane is possible by compound matrix method due to its unique features and it has not been reported by any other formulations and methods - say the collocation method given in Schmid & Henningson (2000) or the method based on orthonormalization given in Scott & Watts (1977). From Table 2.2 for Re = 1000, this threshold value is given by $\omega_0 = 0.0026$ and for Re = 1196, this value is slightly lower at $\omega_0 = 0.0022$ and any excitation below this critical circular frequency shows the presence of only a single upstream propagating mode noted by the dotted line in Fig. 2.25.

There are certain interesting features of this new mode for which both the values of α_r and α_i are negative. For TS waves, α_r is always positive i.e. they are found in the right-half of the wave number plane. This new upstream propagating mode is in the left-half plane and one would be interested to find out the direction of propagation of such waves- by finding numerically the group velocity of such disturbances from $V_g = \frac{\partial \omega}{\partial \alpha_r}$. One can readily testify that for the TS mode the group velocity is positive, showing the TS mode to propagate downstream. For this new mode, the corresponding variation of phase speed and group velocity with ω_r are calculated numerically and shown in Fig. 2.26. This testify that the new mode

travels upstream (as indicated by the negative value of the group velocity shown for this mode by the dotted line).

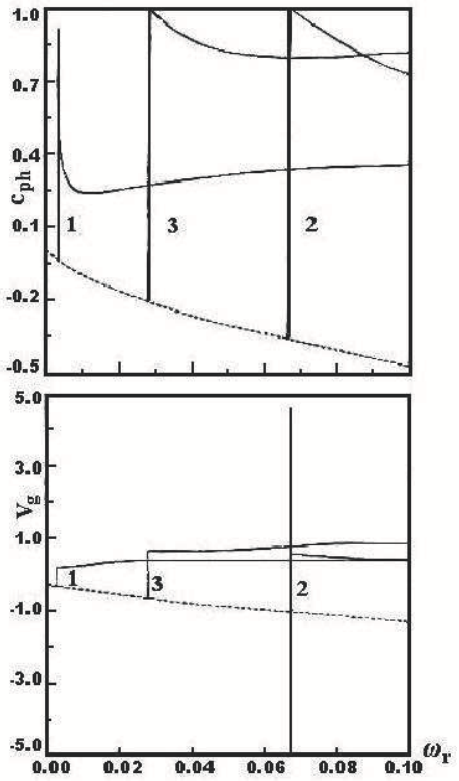

Figure 2.26 Variation of phase speed (top) and group velocity (bottom) of the modes shown in Fig. 2.25, with ω_0 for the Blasius boundary layer at Re = 1000

For the TS mode, a negative value of α_i implies the corresponding wave to be unstable. However for this new mode, the disturbance travels upstream and a high negative value of α_i imply that this is a highly damped mode. One also notices that upon increasing the frequency above the critical value, starting with the upstream propagating mode- it is followed when the circular frequency is increased, even at higher ω_r, when the downstream

propagating modes are restored in the stability analysis. Thus, for a given Reynolds numbers at moderate frequencies, both types of modes are likely to be present. The upstream propagating modes also has the interesting property that their amplitude increases with y i.e. this mode will be able to support any excitation at the free-stream. Henceforth, we will distinguish between these two classes of modes as the *wall-mode* and the *freestream-mode*. The *freestream-mode* can support disturbances due to freestream turbulence or convected vortices in the freestream. There are also other interesting variations of properties of the upstream propagating modes with Reynolds number and these are demonstrated in Fig. 2.27, where $\alpha_r, \alpha_i, c_{ph}$ and V_g are plotted as a function of ω_r for different Reynolds numbers. The chosen ω_r varies over a large range and so does the Reynolds numbers.

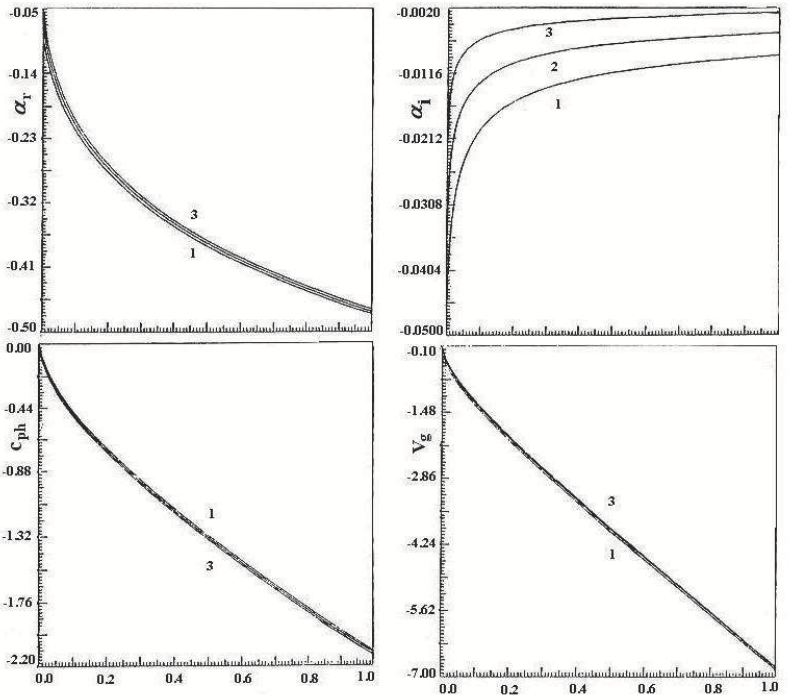

Figure 2.27 Variation of wave properties of upstream propagating mode with ω_r for the Reynolds numbers: (1) Re = 400; (2) Re = 1000 and (3) Re = 4000

For the wide range of ω_r and Re in Fig. 2.27, all the properties seem to be a weak function of Reynolds number except for the value of α_i. The imaginary part of the wave number determines two aspects of the disturbance field in the boundary layer: (a) the extent of the upstream region over which disturbances can be found and (b) the disturbance flow structure in the wall normal direction within the boundary layer. As the magnitude of α_i reduces with increasing Reynolds number for a fixed ω_r, the region of upstream effect will increase with the excitation source convecting downstream in the freestream. As propagating downstream in a growing boundary layer is equivalent to increasing Reynolds number, for sufficiently high Reynolds numbers this will create disturbances that will affect the boundary layer over a larger portion of the flow field with dominant high frequency component. This result establishes the fact that the upstream propagating mode is always damped for the Blasius boundary layer and would not be responsible for linear instability. There is another aspect that has to be pointed out from Fig. 2.27 that when circular frequency is reduced, the modes disappear when the phase speed of eigen-solution reaches the free stream speed ($c = U_\infty$).

2.6.6 Low frequency freestream excitation and the Klebanoff mode

Low frequency excitation of a zero pressure gradient shear layer behaves qualitatively differently, as has been discussed before with respect to the experimental results of Taylor (1939) and Gaster *et al.* (1994). In these experiments, the flow field was created by a shallow oscillating bump inside a zero pressure gradient boundary layer, with the oscillation frequency being very low. For example, in Gaster *et al.*(1994) the oscillation frequency was only 2 Hz and inside the shear layer no waves were seen, instead the whole boundary layer executed a heaving motion. Such low frequency fluctuations were also noticed by Klebanoff (1971) earlier, which he called as the *breathing mode* and now it is known as *Klebanoff mode*.

There are two noticeable features of the experiments reported by Gaster *et al.* (1994). Firstly, the mean flow field is adequately represented by the Blasius profile and for the parameter ranges, two- dimensional instability studies did not reveal the presence of any eigen-solutions that decayed with height, as one approached the edge of the shear layer. Secondly, the disturbance field was three-dimensional, but this propagated predominantly in the streamwise direction. It is easy to see that if the disturbance field has very large wavelengths, then the experimental results will only indicate a heaving motion for relatively low to moderate length test-sections

of tunnels (as was the case for these two experimental results in Taylor (1939) and Gaster *et al.* (1994)). In Gaster *et al.* (1994), the measurement stations were located at 70 and 105 boundary layer thicknesses aft of the shallow bump. The most interesting aspect of the *Klebanoff mode* of motion is that although the mean flow is two-dimensional the flow does not support a two-dimensional disturbance field. This led Gaster *et al.* (1994) to comment that a *proper mathematical account of these disturbances has not yet appeared*. Subsequently Sengupta *et al.* (1997) provided a rational explanation of the same phenomenon and it is the subject of the present discussion.

In this reference, as the flow field was shown not to support any two-dimensional disturbances, three-dimensional disturbances were sought in the analysis. The wall-normal component of the disturbance field is therefore represented as,

$$v'(x,y,z,t) = \frac{1}{4\pi^2}\int\int_{Br} \phi(\alpha,y,\beta,\omega_0)\; e^{i(\alpha x+\beta z-\omega_0 t)} d\alpha \;\; d\beta \qquad (2.6.104)$$

with α and β as the streamwise and spanwise wave numbers, respectively. One is discussing once again the associated signal problem only with the excitation frequency as ω_0. However, in any experiments conducted in a closed tunnel, the spanwise wave number will have a lower cut-off β_0, determined by the spanwise extent of the tunnel i.e. $\beta_0 = 2\pi/\lambda_z$, where the spanwise wavelength (λ_z) is twice the tunnel width. For such cases, one can rewrite the disturbance field as,

$$v'(x,y,z,t) = \frac{1}{2\pi}\sum_{n=1}^{\infty}\int_{Br} \phi(\alpha,y,\beta_0,\omega_0)\; e^{i(\alpha x+n\beta_0 z-\omega_0 t)} d\alpha \qquad (2.6.105)$$

The summation is over all the spanwise modes. One can use the above ansatz in three-dimensional Navier-Stokes equation and linearize the resultant equations after making a parallel flow approximation to get the following Orr-Sommerfeld equation for the Fourier- Laplace transform ϕ of v' as,

$$\begin{aligned}&\phi^{iv} - 2(\alpha^2+n^2\beta_0^2)\phi'' + (\alpha^2+n^2\beta_0^2)^2\phi \\ &= iRe\{(\alpha U + n\beta_0 W - \omega_0)[\phi'' - (\alpha^2+n^2\beta_0^2)^2\phi - [\alpha U'' + n\beta_0 W'']\phi]\}\end{aligned} \qquad (2.6.106)$$

In Eqn. (2.6.106), U(y) and W(y) are the parallel mean flow and Re is the Reynolds number based on the displacement thickness of the boundary layer and primes indicate derivatives with respect to y.

To explain some features of the experiments in Gaster *et al.* (1994), some details of the experimental conditions are recounted first. A flat plate was mounted in the test-section of a low disturbance wind tunnel which is 3.5m long and 0.91m by 0.91m in cross section. Three-dimensional velocity field was created by a circular bump of 20mm diameter which was located 400mm from the leading edge of the plate. At the location of the bump, the undisturbed boundary layer had a thickness of $\delta^* = 0.99$mm. Based on this thickness and free stream speed of 18.10 m/s the Reynolds number is found to be 1196. The circular bump was oscillated at a frequency of 2Hz, which makes the non-dimensional circular frequency $\omega_0 = 6.248 \times 10^{-4}$. The span of the tunnel test-section was 920 times δ^*(approx.) and thus the maximum spanwise wavelength of disturbances that can be supported is twice this dimension. This is the rationale for fixing the lower limit of spanwise wave number β_0 and the corresponding value is 3.41777×10^{-3}. It has been noted in Gaster *et al.* (1994), that most of the disturbance energy is carried by only the first ten modes and this corresponds to $n\beta_0 = 0.7854$.

For the above experimental conditions, it is apparent from Figs. 2.24 and 2.25 that the two-dimensional modes disappear as the value of ω_0 is lower than the critical value ($\omega_0 = 6.248 \times 10^{-4}$) given in the last column of Table 2.2 for $Re = 1196$. This was taken as a cue to investigate if there are three-dimensional modes present for such low frequency excitation in Sengupta *et al.* (1997). The spatial eigenvalues were located by the grid-search method of Mack (1976). Once the eigenvalues were located, the streamwise and spanwise components of the group velocity were obtained numerically using the following,

$$\vec{V_g} = (\frac{\partial \omega}{\partial \alpha_r} \ , \ \frac{\partial \omega}{\partial \beta_r}) \tag{2.6.107}$$

Numerical evaluation of the components of the group velocity required three eigenvalue evaluations. The wave number (α_r), damping rate (α_i), phase speed (c) and the $x-$ and $z-$ components of group velocity are shown in Figs. 2.28 and 2.29 for the first five modes, for different spanwise wave number. It is clearly evident that all the excited modes are damped. Far away from the exciter, only the effects of the least-damped mode (as indicated by the fourth and fifth modes in Fig. 2.28) will be felt. Also the least damped modes have wavelengths those are of the order of few thousand times the displacement thickness, δ^*. To detect such large wavelength disturbances, the test section of the tunnel in the experiments has to be long enough to accommodate at least a few wavelengths. In the experiments of Gaster *et al.* (1994), measurements were made only up to $500\delta^*$ downstream of the exciter and hence it appeared that the whole boundary layer was heaving. From Fig. 2.29, it is also clearly evident that the direction

of propagation of the fourth and fifth modes was predominantly in the $x-$ direction only, since the $z-$ component of the group velocity is negligibly small as compared to the $x-$ component.

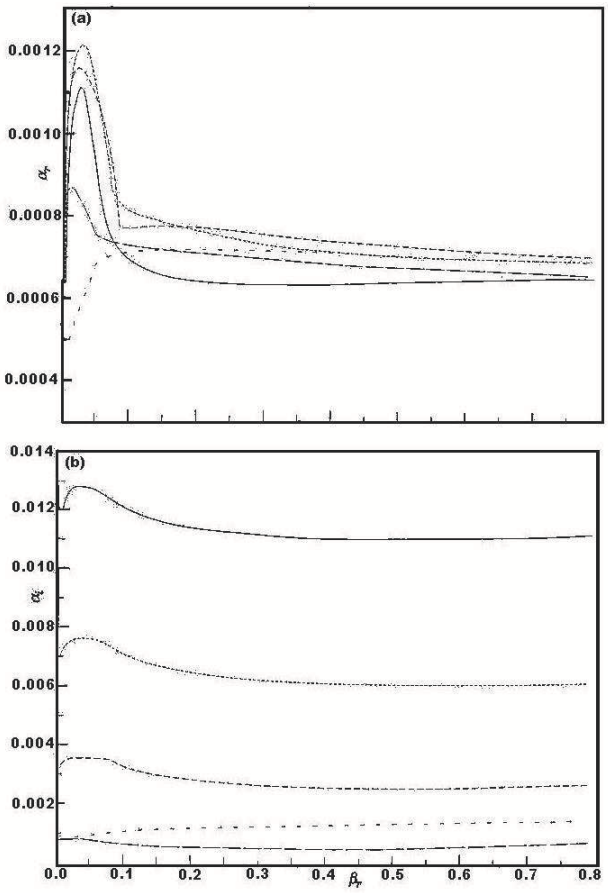

Figure 2.28 Variation of (a) α_r and (b) α_i of the first five modes with spanwise wave number (β_r) for the Klebanoff mode problem. Mode 1: solid line; Mode 2: sparse dotted line; Mode 3: short-chain line; Mode 4: dense dotted lines and Mode 5: long-chain line.

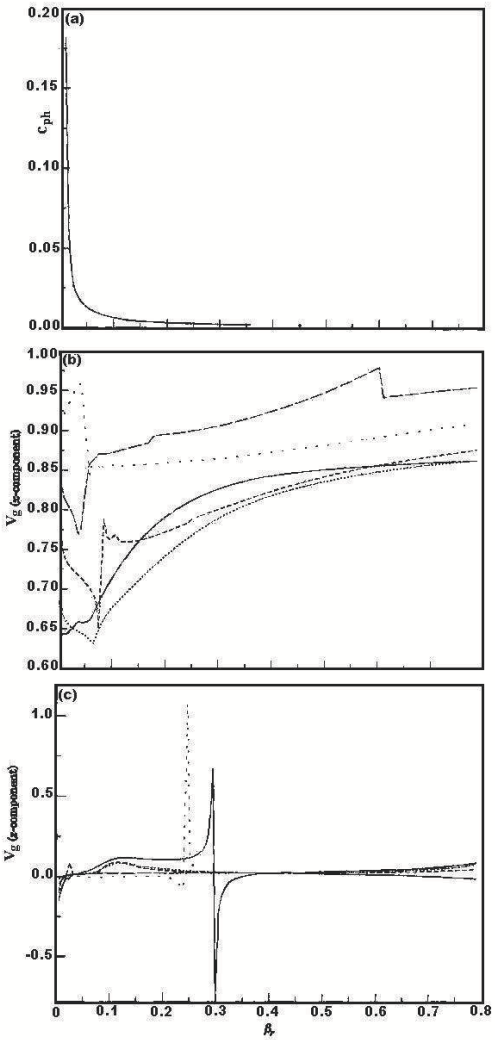

Figure 2.29 (a) Phase speed of first five modes as functions of (β_r); (b) Streamwise component of group velocity of first five modes as functions of (β_r); (c) spanwise component of group velocity of first five modes as functions of (β_r)

In a more general case, if the input represent wide-band disturbances, then the low frequency components will cause the shear layer to heave up and down as the Klebanoff mode of motion. In many experiments involving FST, researchers have reported such heaving motion. This has led researchers to identify response to FST with Klebanoff mode erroneously.

2.7 Direct Simulation of Receptivity to Freestream Excitation:

In general, transition problems are governed by full Navier- Stokes equation and could be solved as receptivity problems by direct simulation, with well defined excitation field. However, unlike stability problems, receptivity problems have to be posed as initial-boundary value problems. Depending upon the nature of the equilibrium flow, various assumptions are made, including linearization to arrive at different receptivity models. For example, in applying asymptotic theory, Goldstein (1983) and Goldstein *et al.* (1983) have shown that the Navier-Stokes equation can be approximated by unsteady boundary-layer equation at the leading edge of a flat plate to study receptivity to acoustic waves. Murdock (1980) numerically solved the incompressible Navier-Stokes equation for flow over a flat plate in a domain excluding the leading edge. The inflow boundary condition was obtained from the solution of unsteady boundary layer equation. Similarly, Lin *et al.* (1995) have modeled the distributed receptivity to freestream vortical disturbances by solving *Parabolized Stability Equation* (PSE) for the Blasius boundary layer over a flat plate with small surface waviness. Lin *et al.* (1992) numerically solved the full Navier-Stokes equations to study the role of discontinuity in curvature near the leading edge of a flat plate and found that the TS wave amplitudes were roughly halved when the curvature discontinuity was removed. Buter & Reed (1993) have studied the receptivity to freestream vorticity by boundary layer forming over a flat plate with an elliptic leading edge, by numerically solving Navier-Stokes equation in stream function - vorticity formulation to track the formation of TS waves. In all the cases considered, the first clear appearance of TS waves occurred at a location aft of the location where the pressure gradient is maximum. The receptivity increases with the magnitude of the pressure gradient maximum. Smoothing the discontinuity in curvature at the juncture of the elliptical leading edge and the flat plate shifted the pressure gradient maximum forward and increased its magnitude, resulting in a stronger TS response. This affirmed the importance of pressure gradient and showed that the continuous changes in surface curvature provide a receptivity source- as the case might be for flow past airfoils.

In section 2.6.5, we have seen how a general excitation field can give

rise to both downstream and upstream propagating disturbances, with the dispersion relation given by Eqn. (2.6.103). Sengupta *et al.* (1999) have demonstrated that there is a direct way of exciting TS modes by freestream excitation while solving OSE- despite the contrary observations in the literature. This is explained next, where a train of periodic vortices is allowed to convect over a zero pressure gradient shear layer. The physical arrangement of the problem is shown in Fig. 2.30. For this problem, results were also obtained by solving the Navier- Stokes equation, and the computational domain is also marked in the figure. An infinite array of vortices is seen to convect over a flat plate in the free stream. The presence of the wall gives rise to the image vortex system, as indicated also in the figure. The vortices of individual strength Γ are at a spacing of a and are convecting at a constant height of $b/2$ over the plate; the height is significantly higher than the shear layer thickness and thus the vortices are always in the inviscid part of the flow.

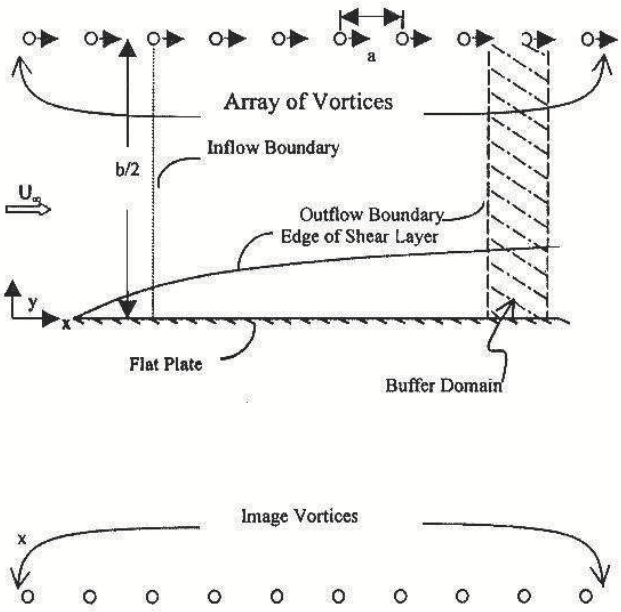

Figure 2.30 Physical arrangement for the flat plate receptivity problem excited by a periodic array of convecting vortices in the free stream.

If these vortices are considered as potential vortices, then the induced perturbation velocity in the inviscid part of the flow is given by,

$$u_\infty = \frac{\Gamma}{2aD}[\sin^2\frac{\pi\bar{x}}{a}\cos h\frac{2\pi y}{a} - \sin h\frac{\pi}{a}(y-\frac{b}{2})\sin h\frac{\pi}{a}(y+\frac{b}{2})]\sin h\frac{\pi b}{a} \quad (2.7.1)$$

$$v_\infty = \frac{\Gamma}{4aD}\sin h\frac{\pi b}{a}\sin\frac{2\pi\bar{x}}{a}\sin h\frac{2\pi y}{a} \quad (2.7.2)$$

where, $\bar{x} = x - ct$ with c as the convection speed of the vortices and

$$D = [\sin^2\frac{\pi\bar{x}}{a}\cos h\frac{2\pi y}{a} - \sin h\frac{\pi}{a}(y-\frac{b}{2})\sin h\frac{\pi}{a}(y+\frac{b}{2})]^2 + \frac{1}{4}\sin^2\frac{2\pi\bar{x}}{a}\sin h\frac{2\pi y}{a}$$

If all the lengths are non-dimensionalized by the displacement thickness and the velocity by U_∞, then the periodic vortices impose a time scale on the flow given by $\omega_0 = 2\pi c/a$ The periodicity of the vortices excites the shear layer at circular frequencies $\omega_0, 2\omega_0, 3\omega_0$.....*etc.* Thus, the disturbance stream function can be expressed as,

$$\psi(x,y,t) = \frac{1}{2\pi}\sum_{n=1}^{\infty}\int_{Br}\phi(\alpha,y,n\omega_0)\, e^{i(\alpha x - n\omega_0 t)}d\alpha \quad (2.7.3)$$

It has already been explained that the eigenvalues near $\alpha = 0$ gives rise to asymptotic solution, while the local solution is contributed by the point at infinity in the spectral plane ($\alpha \to \infty$) (Sengupta & Rao, 2006). Also, for small values of Γ and large values of b, the receptivity problem can be solved by linearizing the Navier -Stokes equation.

The imposed Cartesian velocity components u_∞ and v_∞ are plotted in Fig. 2.31 for the indicated parameters, over a single vortex pair spacing given by $a = 100\pi\delta^*$ The input disturbances are shown for a single period with $Y = 18\delta^*$ and these are calculated at $y = 16\delta^*$.

It is to be noted that the values of u_∞ and v_∞ obtained by an inviscid analysis are used here to calculate the impressed pressure over the shear layer. If Γ is considered to be small, then the impressed pressure gradient is going to be negligibly small and not cause flow separation. In the absence of separation, boundary layer assumption holds and the impressed pressure remains the same across the shear layer and is the reason that the analysis results using inviscid pressure distribution provide vital clue to the receptivity route.

In Fig. 2.32, the bilateral Laplace transform, ϕ_∞ and its normal derivative, ϕ'_∞ have been shown that correspond to the imposed velocity boundary conditions of Fig.2.31. It is clearly evident that ϕ_∞ is much larger than ϕ'_∞ and this information is used here to compare different types of free stream excitations in the next subsection.

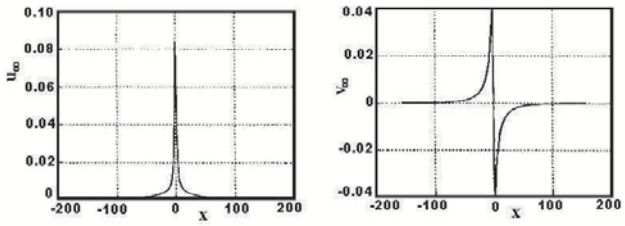

Figure 2.31 Imposed velocity perturbation by a periodically passing train of vortices in the free stream convecting with U_∞. Shown are the velocity components at $y = 16\delta^*$ when the array is convecting at $Y = 18\delta^*$ with vortices at a gap of $a = 100\pi\delta^*$

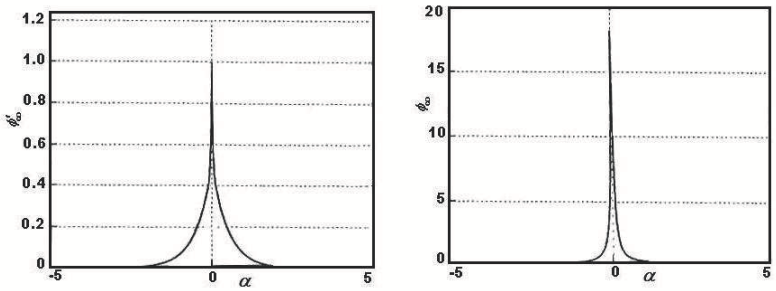

Figure 2.32 The bilateral Laplace transform of imposed velocity disturbance components shown in Fig. 2.30

2.7.1 Coupling Between Wall- and Freestream-Modes

The solution of Orr- Sommerfeld equation has four fundamental modes as expressed below,

$$\phi = C_1\phi_1 + C_2\phi_2 + C_3\phi_3 + C_4\phi_4 \tag{2.7.4}$$

These four fundamental modes have already been defined in section 2.6, whose asymptotic values in the freestream are given by: $\phi_{1\infty} \sim e^{-\alpha y}$; $\phi_{2\infty} \sim e^{\alpha y}$; $\phi_{3\infty} \sim e^{-Qy}$; $\phi_{4\infty} \sim e^{Qy}$, where $|Q| = [\alpha^2 + i\alpha Re(1-c)]^{1/2}$. The first and third modes decay, while the second and fourth modes increase with y, whenever real part of α and $\sqrt{Q^2}$ are positive. The decaying modes are

required for pure wall excitation and we have formally defined these as the *wall- mode* and notify as,

$$\Phi_I = C_1\phi_1 + C_3\phi_3 \tag{2.7.5}$$

Similarly the *freestream-mode* is defined as,

$$\Phi_{II} = C_2\phi_2 + C_4\phi_4 \tag{2.7.6}$$

Φ_{II} grows with y to match with the applied disturbance at the free stream. Now for a receptivity problem, where the shear layer is excited at the free stream one can fix the values of C_2 and C_4 by matching u_∞ and v_∞ or ϕ_∞ and ϕ'_∞. The far field boundary for the problem is considered far out enough so that $\phi_{1\infty}$ and $\phi_{3\infty}$ are negligibly small and the disturbance solution is solely due to the *freestream- mode*. Thus, fixing of the free stream boundary condition leaves satisfying the homogeneous boundary conditions at the wall. However, there are two qualitatively different ways the coupling will be achieved if the convected vortices move at free stream speed or at a speed different from the free stream speed.

Pure Convection Problem:

When the convected vortices move at the free stream speed, notice that the fundamental solutions coalesces i.e. $\phi_{1\infty} = \phi_{3\infty}$ and $\phi_{2\infty} = \phi_{4\infty}$. Thus, to satisfy the free stream boundary conditions we fix C_2 and C_4 from,

$$\Phi_{II\infty} = \phi_\infty = C_2 e^{\alpha Y} + C_4 Y e^{\alpha Y} \tag{2.7.7a}$$

and

$$\Phi'_{II\infty} = \phi'_\infty = \alpha C_2 e^{\alpha Y} + C_4(1+\alpha Y)e^{\alpha Y} \tag{2.7.7b}$$

This occurs, as $\phi_{I\infty} = \phi'_{I\infty} \equiv 0$ as $Y \to \infty$. The solution of these provides $C_2 = [(1+\alpha Y)\phi_\infty - Y\phi'_\infty]e^{-\alpha Y}$ and $C_4 = [\phi'_\infty - \alpha\phi_\infty]e^{-\alpha Y}$. Now to satisfy the homogenous boundary conditions at the wall, one must have $\phi(y=0) = 0 = \Phi_{I0} + \Phi_{II0}$. Thus, we call the wall boundary condition for the *wall-mode* as ϕ_{PC} that is given by,

$$\begin{aligned}\phi_{PC} = \Phi_{I0} = -\Phi_{II0} = -\, e^{-\alpha Y}[\{\phi_\infty(1+\alpha Y) - Y\phi'_\infty\}\bar{\phi}_{20} \\ + \{\phi'_\infty - \alpha\phi_\infty\}\bar{\phi}_{40}]\end{aligned} \tag{2.7.8}$$

where the fundamental solutions in this case have been written with an overbar. Similarly, one can write down an expression for Φ'_{I0} providing two equations to solve for the other two unknowns, C_1 and C_3 from

$$C_1\bar{\phi}_{10} + C_3\bar{\phi}_{30} = -(C_2\bar{\phi}_{20} + C_4\bar{\phi}_{40})$$

$$C_1\bar{\phi'}_{10} + C_3\bar{\phi'}_{30} = -(C_2\bar{\phi'}_{20} + C_4\bar{\phi'}_{40})$$

Solution of these two equations provides: $C_1 = (r_1\bar{\phi'}_{10} - r_2\bar{\phi}_{10})/D$ and $C_3 = (r_2\bar{\phi}_{30} - r_1\bar{\phi'}_{30})/D)$ where $D = (\bar{\phi'}_{10}\bar{\phi}_{30} - \bar{\phi}_{10}\bar{\phi'}_{30})$; $r_1 = e^{-\alpha Y}[\bar{\phi}_{20}\{\phi'_\infty Y - (1+\alpha Y)\phi_\infty\} + \bar{\phi}_{40}(\alpha\phi_\infty - \phi'_\infty)]$ and $r_2 = e^{-\alpha Y}[\bar{\phi'}_{20}\{\phi'_\infty Y - (1+\alpha Y)\phi_\infty\} + \bar{\phi'}_{40}(\alpha\phi_\infty - \phi'_\infty)]$. The non-zero C_1 and C_3 obtained in terms of C_2 and C_4 provides the coupling for this case.

Bypass problem:

If the convected vortices do not move at the free-stream speed, then the modes do not coalesce as in the previous case and one can simply calculate the wall boundary condition for the *wall-mode* and call it as ϕ_{BP} to distinguish it from the previous case. Thus,

$$\phi_{BP} = \Phi_{I0} = \frac{1}{p-\alpha}[e^{-\alpha Y}(\phi'_\infty - p\phi_\infty)\phi_{20} - e^{-pY}(\phi'_\infty - \alpha\phi_\infty)\phi_{40}] \quad (2.7.9)$$

where $p = Real(\sqrt{Q^2})$. Thus, Eqns. (2.7.8) and (2.7.9) represent the equivalent *wall-mode* amplitudes calculated at the wall for pure freestream excitation problems, in pure convection and bypass mode, when real part of α and p are positive. For transition problems, usually $|p| >> |\alpha|$. Also, note for the case of freestream vortical disturbances, $\phi_\infty > \phi'_\infty$, as shown in Fig. 2.31 and then

$$\frac{\phi_{PC}}{\phi_{BP}} = -(p-\alpha)\{\frac{\bar{\phi}_{20}[\phi_\infty(1+\alpha Y) - Y\phi'_\infty] + \bar{\phi}_{40}[\phi'_\infty - \alpha\phi_\infty]}{(\phi'_\infty - p\phi_\infty)\phi_{20}}\} \quad (2.7.10)$$

This can be further simplified to

$$\frac{\phi_{PC}}{\phi_{BP}} = \{\frac{\bar{\phi}_{20}}{\phi_{20}}\}[1 + \alpha Y - Y\frac{\phi'_\infty}{\phi_\infty}] \quad (2.7.11)$$

Hence, it is apparent that for the same level of excitation at the free stream, the above ratio indicates that the pure convection of vortices will be a far weaker mechanism for creating disturbances inside the shear layer as compared to the case when $c = \frac{\omega_0}{\alpha} \neq 1$.

The above analysis is for spatial stability problem associated with freestream excitation, where a time scale is imposed. Next, we consider the same case with explicit time scales imposed on the flow - the case of train of convective vortices, posed as the receptivity problem.

2.7.2 Receptivity to Train of Convected Vortices in Freestream

The above distinction between the cases of pure convection at the free stream speed and the bypass route where the train of vortices traveling at speeds lower than the freestream speed can also be demonstrated by solving the Orr-Sommerfeld and the Navier- Stokes equations, as was shown in Sengupta *et al.* (2002). For the shown results, the spacing between successive vortices was taken as $a = 100\pi\delta^*$ with $Y = 20\delta^*$ and Re = 1000. The Orr-Sommerfeld equation has been solved for the boundary conditions displayed in Fig. 2.32 by Chebyshev collocation method with the weighting coefficients developed using the Generalized Differential Quadrature (GDQ) method of Shu & Chew (1998).

For the pure convection case i.e. when $c = U_\infty$, the excited modes are those for which the following dispersion relation must be satisfied: $\alpha_n = n\omega_0$. The cause for the severely damped solution (not shown) can be ascribed to the stability property of the basic profile. This has been shown in Fig. 2.33. In this figure, the neutral curve is re-plotted along with $c = const.$ loci in the $(Re - \omega_0)$-plane. The very existence of the $c = U_\infty$ line (in the figure shown as the non-dimensional value of c = 1), far removed from the neutral curve in the stable zone, implies that such a convecting mode would decay very rapidly. Similarly the upstream propagating modes corresponding to $\omega_0 = 0.02$ are also highly damped. Figure 2.33 also indicates the possibility by which wavy or oscillatory disturbances can be generated. Of particular significance are the properties of the upstream and downstream modes with $c < U\infty$. The real phase speed c indicates the speed at which a freestream disturbance convects, and for a vortex train that does not disperse; this would be the speed of the individual vortices. Figure 2.33 clearly indicates that instability can be very effectively triggered if the convection speed of the vortices lies within the narrow range of $0.26U_\infty$ to $0.32U_\infty$ that in this case correspond to n = 13 to 16.

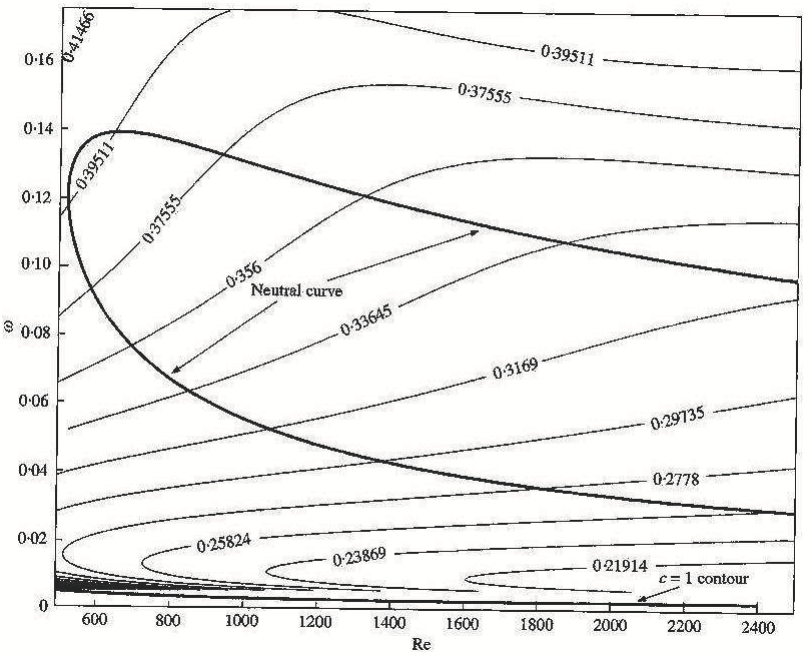

Figure 2.33 Stability diagram for a flat plate boundary layer showing the neutral curve superposed over c = const. disturbance propagation contours shown by thin lines. Note that the line c = 1 corresponds to the case of pure convection of vortices.

Convecting free-stream disturbances within this speed range are likely to trigger strong sustained instability, because of the high amplification rate that such modes would experience. Also for $c > 0.4U_\infty$, the convecting disturbances would create damped wave packets.

For convected vortical disturbance field in the freestream, the growth process is also qualitatively different as compared to the growth of disturbances that are created at the wall or inside the shear layer- as reported in Schubauer & Skramstad (1947). For monochromatic wall excitation, the real frequency of the disturbance field is held fixed and the phase speed adjusts itself continually to the local stability property of the shear layer. Contrarily, for the disturbance field generated by convecting vortices, it is the phase speed or group velocity that is an invariant of the input distur-

bance field; while the corresponding real frequency will continuously vary, satisfying the dispersion relation: $\alpha c = n\omega_0$. In other words, for freestream excitation, the disturbance will follow a path of constant phase speed, while for localized wall excitation, this path will be along a straight line in the $(Re - \omega_0)$ plane with a slope that denotes the physical frequency. Hence, if the convection speed of the vortex train is chosen to be between $0.26U_\infty$ to $0.32U_\infty$, then the created disturbance field inside the shear layer will experience a very high sustained growth, as the $c = constant$ lines remain closer to α_i maximum region over a longer streamwise stretch, as shown in Fig. 2.33. Moreover, the figure also indicates that the rate of growth will be much higher than that for disturbances that are excited from inside the shear layer at a constant physical frequency. There is a clear experimental evidence of the presented analysis here with the results reported in Kendall (1987). In that experiment, Kendall (1987) made a circular cylinder to rotate in a circular trajectory above a flat plate. During the motion of the cylinder in its trajectory, the equivalent ejected disturbances over the flat plate were much more complicated, because the strength, location and migration speed of the vortices are, however, not controlled as compared to the model problem discussed above. Despite these differences, figure 3 of Kendall (1987) clearly showed that a rotation speed that corresponded to $c = 0.3U_\infty$ showed maximum receptivity as compared to $c = 0.23U_\infty$ and $c = 0.5U_\infty$. The hot-wire oscillograms corresponding to the circumferential speed $c = 0.3U_\infty$ of the rotor indicated the presence of very large amplitude wave packets.

One notes here that the freestream convecting vortical excitation is not monochromatic. This is the fundamental difference between free stream excitation by convecting vortices and the vibrating ribbon excitation at a fixed frequency given in Schubauer & Skramstad (1947). If nonlinearity is important and one solves the full Navier- Stokes equation for the disturbance quantities, then the wave packets can grow as they propagate downstream, while the growing disturbance within the packet can saturate in amplitude. Therefore, the solution of the Navier- Stokes equation will provide vital information about the role of nonlinearity for this problem, apart from including the effects of growth of the shear layer.

A direct simulation of the flow field was also attempted in Sengupta *et al.* (2002), where the following stream function- vorticity formulation of Navier- Stokes equation was used,

$$\frac{\partial^2 \psi}{\partial x^2} + \frac{\partial^2 \psi}{\partial y^2} = -\omega \tag{2.7.12}$$

$$\frac{\partial \omega}{\partial t} + \frac{\partial}{\partial x}(u\omega + u_b\omega + u\omega_b) + \frac{\partial}{\partial y}(v\omega + v_b\omega + v\omega_b) = \frac{1}{Re_1}[\frac{\partial^2 \omega}{\partial x^2}\frac{\partial^2 \omega}{\partial y^2}] \quad (2.7.13)$$

where u_b, v_b, and ω_b are the undisturbed base flow quantities for the flat-plate boundary layer flow as given by the Blasius similarity solution. Re_1 is the Reynolds number based on the free stream velocity, the displacement thickness at the inflow and ν, the kinematic viscosity.

To resolve the flow gradient near the wall, the above equations were solved in a stretched co-ordinate system (in the wall-normal direction) via the transformations

$$x = \xi$$

$$y = \frac{y_{max}\sigma\eta}{\eta_{max}\sigma + y_{max}(\eta_{max} - \eta)} \quad (2.7.14)$$

where y_{max} is the height of the domain in the physical plane and η_{max} is the corresponding height in the computational plane; σ is a control parameter that clusters the grid points close to the wall.

At the inflow boundary and on top of the computational domain, analytic solution for the disturbance velocity was used in accordance with Eqn. (2.7.1) and (2.7.2). On the flat plate, the no-slip condition simultaneously provides a Dirichlet boundary condition for the stream function and the wall vorticity at every instant of time.

In order to eliminate the reflection of waves from the outflow boundary, the buffer domain technique developed by Liu & Liu (1994) was used in these simulations. The buffer domain, as indicated in Fig. 2.30, is a narrow strip of the computational domain adjacent to the outflow boundary. A continuous buffer function $b(\xi)$ was introduced (in Eqns. (2.7.15) and (2.7.16)); which has a value of one in the main computational domain that decreased monotonically in the buffer domain to zero at the outflow boundary. To treat growing or unstable modes, a second buffer function $b_{Re}(\xi)$ was used (in Eqn. (2.7.16)) to gradually reduce the Reynolds number in the buffer domain to a value below the critical Reynolds number. The used buffer functions $b(\xi)$ and $b_{Re}(\xi)$ are as given in Liu & Liu (1994).

The transformed equations that were actually solved are given by,

$$b\frac{\partial^2 \psi}{\partial \xi^2} + \frac{\partial^2 \psi}{\partial \eta^2}\frac{1}{y_\eta^2} + \eta_{yy}\frac{\partial \psi}{\partial \eta} = -\omega \quad (2.7.15)$$

$$\frac{\partial \omega}{\partial t} + \frac{\partial}{\partial \xi}(u\omega + u_b\omega + u\omega_b) + \frac{1}{y_\eta}\frac{\partial}{\partial \eta}(v\omega + v_b\omega + v\omega_b)$$
$$= \frac{b_{Re}}{Re_1}(b\frac{\partial^2 \omega}{\partial \xi^2} + \frac{\partial^2 \omega}{\partial \eta^2}\frac{1}{y_\eta^2} + \eta_{yy}\frac{\partial \omega}{\partial \eta}) \tag{2.7.16}$$

At the outflow of the domain, the traditional extrapolation based on $\frac{\partial^2 \psi}{\partial \xi^2} = \frac{\partial^2 \omega}{\partial \xi^2} = 0$ was applied for stream function and vorticity transport equations. Equations (2.7.15) and (2.7.16) have been solved in Sengupta *et al.* (2002) first for the case of $c = U_\infty$, in a domain for which Reynolds number varies from 165 to 1900. The results are shown in Fig. 2.34 at different indicated times.

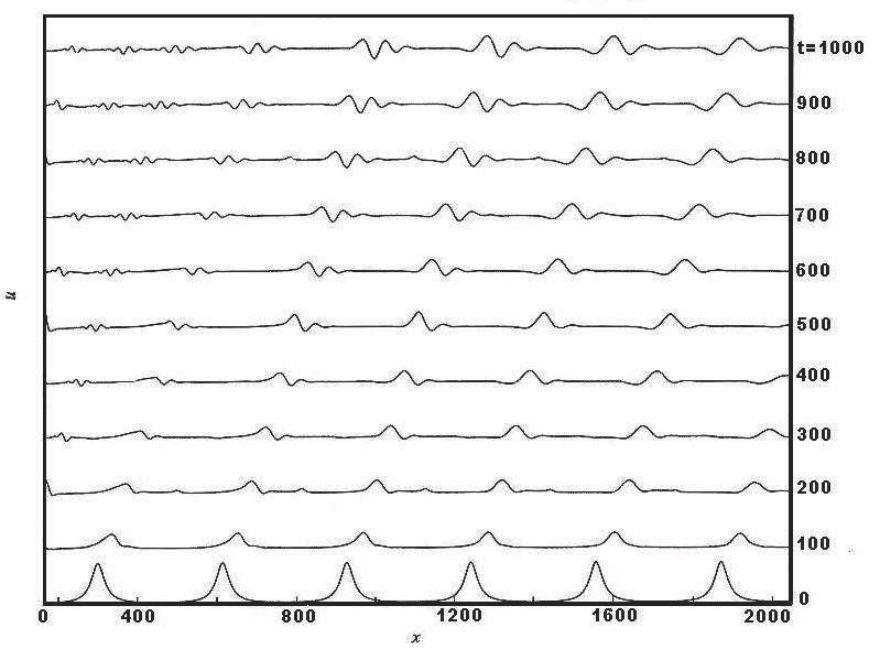

Figure 2.34 Streamwise disturbance velocity component plotted at a height $y = 0.3\delta^*$ for the pure convection case ($c = U_\infty$) at the indicated times, when solution is obtained by solving the Navier-Stokes equation for the problem shown in Fig.2.30

The abscissa is actually the Reynolds number based on local displacement thickness. In this case, only the local solution is predominant at early times. This component also disperses and decays, as can be seen from the solution at t = 100. The observed single peak at $t = 0$ that is due to the local solution disperses into multiple peaks- as can be noted for all subsequent times. This dispersion of solution is due to the presence of upstream propagating modes and the presence of multiple harmonics for the downstream propagating modes. The adjective upstream here is to be understood with respect to the local condition of the disturbance field. More details about this dispersion mechanism and tracking of the upstream propagating modes were first discussed in Sengupta *et al.* (1999) and will be discussed again in the next subsection.

Next the case for $c = 0.3U_\infty$ was investigated by solving the Navier-Stokes equation with the same formulation. As per the previous discussion based on stability properties of Blasius profile depicted in Fig. 2.33 and the experimental observation of Kendall (1987), one would expect to see a rapid growth of disturbances. The domain is the same that was considered for the previous case in Fig. 2.34 and the other domain and excitation field data are also the same. The results for this case are as shown in Figs. 2.35(a) and 2.35(b) for the locations at $y = 0.3\delta^*$ and $1.5\delta^*$, respectively. Here, it is apparent that with time the shear layer displays supporting growing disturbances as it convects downstream. At early times up to t = 400, once again one notices the splitting of the full solution into upstream and downstream propagating components. While these results are for two-dimensional flows, similar computations have been performed in Wu et al. (1999) in a 3D box where freestream vortices were directed towards the base by the imposition of a constant downward velocity at the inflow. The resultant trajectory of the vortex-induced disturbance is intuitively expected to lie in the south-east direction if the mean flow is from west to east. However, induced disturbances in Wu *et al.* (1999), moved down and in upstream direction instead, clearly indicating that the free stream excitation causes a disturbance field that propagates upstream, as predicted here by the displayed two-dimensional calculations. The existence of common features among the results from three-dimensional DNS, two-dimensional simulation and the solution of linearized Navier- Stokes equation points to the common mechanism that is seen in all the cases.

2.7.3 Further Explanation of Freestream Periodic Excitation:

For the physical problem described in Fig. 2.30 and its solution in Figs. 2.34 and 2.35 for $c = U_\infty$ and $c = 0.3U_\infty$, respectively, brings out some interesting features of the response field due to periodic freestream excitations. We have already noted that for such excitations one would get both downstream and upstream propagating disturbances, whose properties are as shown in Figs. 2.25 to 2.27. However, the upstream propagating mode will dominate for the case of $c = U_\infty$, as the downstream propagating mode corresponding to $c = U\infty$ are highly attenuated- as seen from Fig. 2.34. The upstream propagating part will be less attenuated, as shown in Fig. 2.27 for the variation of α_i with increasing Reynolds number. The downstream mode is always excited for any freestream excitation that is introduced via the coupling mechanism described in section 2.7.1. Thus, the response consists predominantly of upstream propagating modes as it convects downstream.

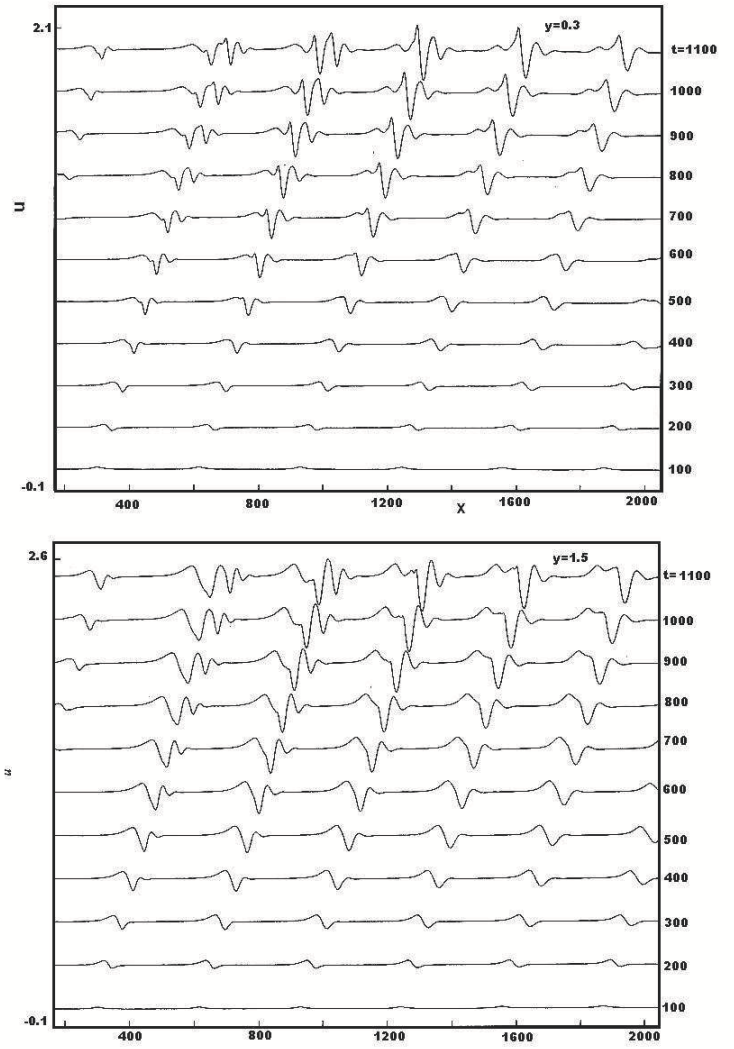

Figure 2.35 Streamwise velocity component plotted for the case $(c = 0.3U\infty)$ **at the indicated times obtained by solving the Navier-Stokes equation for the problem shown in Fig. 2.29 for the height: (a)** $y = 0.3\delta^*$ **and (b)** $y = 1.5\delta^*$**.**

The upstream propagating mode properties are indicated by the dotted line in Fig. 2.25 and this component of the solution can be seen in the solution shown in Figs. 2.34 and 2.35. Here, we demonstrate these aspects further with respect to the case shown in Fig. 2.34, for which the freestream vortices travel with the freestream speed, $c = U\infty$, for the pure convection problem. In Fig. 2.30, the gap between successive vortices has been taken as $a = 100\pi$ and that corresponds to a time scale given by $\omega_0 = \frac{2\pi c}{a} = 0.02$. Thus, the given excitation creates a multi-periodic response field with $n\omega_0$ (for $n = 1, 2, 3, ...$) as the frequencies in Eqn. (2.7.3).

For the fundamental frequency ω_0 of the problem in Fig. 2.34, one notices the propagation speed of disturbance energy to be given by $V_{g0} \approx -0.5U_\infty$ (from Figs. 2.27 and 2.36), while for the next few harmonics the group velocity increases with circular frequency. In Fig. 2.36, we show the variation of group velocity with circular frequency varying in the range of $0 \leq \omega \leq 0.2$ for different Reynolds numbers.

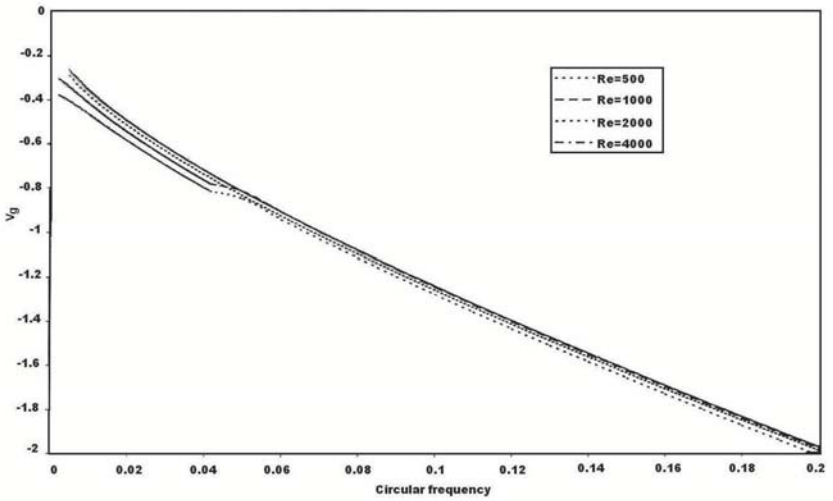

Figure 2.36 Variation of group velocity with circular frequency for the indicated Reynolds number for the upstream propagating mode.

This figure shows the value to increase in magnitude from $0.5U_\infty$ to $0.8U_\infty$ for the first and second harmonic, respectively. For higher harmonics, this further increases almost linearly. The initial solution created by the

freestream vortices inside the shear layer appear as wave-packets. At early times, the packets retain their coherence due to small dispersion of various harmonics. However, the freestream vortices convect at a speed given by $c = U_\infty$ and the vanishingly small downstream propagating disturbance field inside the shear layer convects with c. The upstream component would travel with respect to the downstream component with the group velocity $V_{g0} = -0.5U_\infty$. We note that the higher harmonics would be less damped as compared to the fundamental mode depending furthermore upon the Reynolds number - as shown in Figs. 2.25 and 2.27. The higher harmonics would dominate at later times, due to the reason that they have lower damping and as the packets move downstream the Reynolds number also increases for which the damping rate decays even further. This would therefore create a dispersion of the disturbance field. Effects of such dispersion would be equivalent to creating newer length scales. This is a completely new mechanism for the creation of different length scales (specifically the smaller length scales) that has been overlooked before for transitional and turbulent flows.

To understand the creation of new length scales by the dispersive effect, it is explained clearly with an additional figure and a table. In Fig. 2.37, the disturbance stream function is shown at two heights ($y = 0.3\delta^*$ and $1.0\delta^*$) at four distinct time instants- as indicated in the figure for the case of $c = U_\infty$.

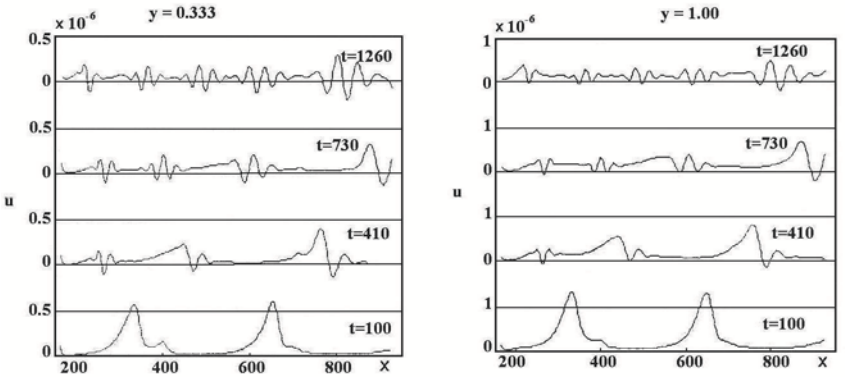

Figure 2.37 The disturbance stream function at the two indicated heights as functions of streamwise distance for the indicated times- for the pure convection case

Comparison of the disturbance fields at these two heights clearly demonstrate a strong coherence of the data, while the disturbance increases with height- once again attesting to the properties explained before for the freestream mode. The dispersion of the solution field can be explained by looking at this figure and the Table 2.3.

Table 2.3: Position of response field with respect to freestream vortices and their time of entry in the computational domain

Vortex Number →

$Time \downarrow$	1	2	3	4	5	6
$t = 0$	-960	-645	-330	-15	300	615
$t = 100$	-860	-545	-230	85	400	715
				(35)	(350)	(665)
$t = 410$	-550	-235	80	395	710	1025
				(270)	(505)	(820)
				$t_1 = 165*$		
$t = 720$	-230	85	400	715	1030	1345
			(280)	(450)	(665)	(980)
		$t_1 = 810*$	$t_1 = 490*$			
$t = 1260$	300	615	930	1245	1560	1875
	(230)	(390)	(550)	(695)	(945)	(1260)
	$t_1 = 1120*$					

In the table, the initial condition ($t = 0$) identifies the packets at a non-dimensional distance of 100π -with packets identified by their location outside the computational domain and those entering the domain at later times indicated by asterisks. Due to higher damping rate of both upstream and downstream modes, solution at very early times consists of only the local solution- as discussed with respect to the results in Fig. 2.19. We note six disturbance packets at $t = 0$, exactly at the same streamwise locations exactly below the freestream vortices. Subsequently at $t = 100$, two clusters would have been noted at $x = 400$ and at $x = 715$, if the disturbance field would have moved with $c = U_\infty$. One notes two smaller peaks at these two locations at $t = 100$. However, the major peaks are at the locations indicated by the quantities within parentheses in Table 2.3. These are exactly at those locations, if one calculated the disturbance clusters to move with the group velocity $V_{g0} = 0.5U_\infty$ with respect to the corresponding source i.e. the free stream vortices. This is verified for the clusters' location at

$t = 100$ and 410, from the Table 2.3 and Fig. 2.37. At later times, the higher harmonics moves further upstream due to their higher propagation speeds and lower damping rates showing visible dispersion. This is evident from the results shown in the figure and the table at $t = 730$ and 1260. Thus, one notes that pure convection of vortices in the free stream causes dispersed disturbance field inside the shear layer that grows with height and those are not Tollmien-Schlichting waves. Moreover, the damped disturbances are multi-periodic. It has been shown in Sengupta *et al.* (2006, 2006a) that such damped modes can also interfere to form spatio-temporal growing wave-fronts. While such a mechanism has been found in these references for two-dimensional disturbance fields, other authors have talked about spatio-temporal algebraically growing modes for three-dimensional flows only. This has been termed as bypass transition by some authors; see e.g. Breuer & Kuraishi (1993), Morkovin (1969, 1991) and other references in Sengupta *et al.* (2006, 2006a). We will come back to the discussion of spatio-temporal growing wave-fronts in chapter 4, where we will contrast the two mechanisms of disturbance growth. There can still remain a large number of other mechanisms that qualify as bypass transition. Some of these mechanisms of bypass transition are discussed in the next chapter- with special emphasis on vortex-induced instability caused by aperiodic freestream excitation.

Chapter 3

BYPASS TRANSITION

Prof. Tapan K. Sengupta
HPCL, Aerospace Engineering
I.I.T. Kanpur

3.1 Introduction

In this chapter we focus mainly upon the problem of vortex- induced instability that creates large perturbations without the appearance of Tollmien-Schlichting waves. Interaction of a shear layer with a finite-core vortex leading to unsteady separation in a boundary layer was noted by Doligalski *et al.* (1994) *as one of the most important unsolved problems of fluid dynamics*. Such unsteady separation is present in (i) Flow past surface-mounted obstacles; (ii) Dynamic stall and blade vortex interaction (BVI); (iii) Impulsive motion of bluff bodies; (iv) Near-wall turbulence and (v) Bypass transition triggered by aperiodic convecting vortices. In this chapter, we will focus on the last topic only, as an example of a physical mechanism during bypass transition. The same mechanism is also present in the other examples mentioned above. Unsteady flow separation has been discussed also in Degani *et al.* (1998) and other references contained therein. Brinckman & Walker (2001) have studied near-wall eddy formation in turbulent boundary layers. In this last work, a late stage of transition whose origin is completely different from one created by linear instability, was studied in a quasi two-dimensional framework. Smith *et al.* (1991) and Robinson (1991) have also discussed the formation of hairpin vortices in near-wall turbulence sites. In another set of studies, Peridier et al. (1991, 1991a) considered the scenario where a vortex placed above a plane wall caused the vortex to migrate and at the same time a thin unsteady boundary layer formed over the wall. Thus, the problem considered in this chapter has many variations- but we will only consider the case where primary instability is triggered by a convecting vortex over a wall-bounded shear layer, as described in Sengupta *et al.* (2003), Sengupta & Dipankar (2005) and Lim et al. (2004).

3.2 Transition via Growing Waves and Bypass Transition:

In the previous chapter, we have noted that a train of periodic convecting vortices in the freestream produce Tollmien-Schlichting waves whose dynamics is different than those produced by wall excitation or that was observed in the vibrating ribbon experiment of Schubauer & Skramstad (1947). There are few reasons for the qualitative differences between freestream and wall excitations. In the previous chapter, we have identified *wall* and *freestream-mode* as the two different types of ensuing motion seen for these two types of excitation. Firstly, in vibrating ribbon experiment monochromatic TS waves are created by constant frequency excitation at or very near the wall. For freestream excitation, the response field is multi-periodic in time, as expressed in Eqn. (2.7.3) and shown in the numerical results in Figs. 2.34, 2.35 and 2.37. The excitation is essentially broad-band. Secondly, the freestream excitation can create both downstream and upstream propagating disturbance fields. Finally, in contrast to the vibrating ribbon case, in freestream excitation one can create disturbance wave-packet that remains within the unstable range over a longer stretch, and also suffer much higher growth rates (as can be reasoned easily from Fig. 2.33).

In contrast, for the case of periodic train of vortices convecting in the freestream at a constant speed, one follows the $c = constant$ line in Fig. 2.33. As a consequence the growth rate for wave in vibrating ribbon experiment initially grows monotonically up to a maximum and thereafter it falls off to zero again. Before and after this phase, disturbances actually decay while propagating- according to the linear stability analysis. For freestream excitation case, disturbances are wave-packets that experience explosive growth if the excitation field has convection speed in the range $0.26U_\infty$ to $0.32U_\infty$, as shown clearly in Fig. 2.33.

The most important difference between wall excitation and free stream excitation is the direction of propagation of the disturbance field with respect to the local mean flow. For low amplitude wall excitation, disturbances propagate downstream only for unseparated flows. In contrast, when the shear layer is excited by train of vortices in the freestream, then a part of the disturbance field travels upstream- in addition to the downstream propagating *wall mode*. While these observations are for two-dimensional flow field, it is noted that very low-frequency wall disturbances create only three-dimensional disturbances -the Klebanoff mode. Thus, when a shear layer is excited by periodic freestream sources, the resultant flow field is a mixture of two- and three-dimensional disturbances and their mutual interaction as they travel upstream and downstream with respect to the excitation source. These elements were noted in the Direct Numerical Simulation (DNS) results of Wu *et al* (1999) and Jacobs & Durbin (2001). In the former, the

periodic freestream excitation is by a periodic wake and in the latter by *synthetic free stream turbulence* characterized by superposition of spanwise and temporal Fourier modes, times vertical *Orr-Sommerfeld modes* -the so-called continuous spectrum. In both the cases, the *transition precursors of long backward jets* are noted in the outer part of the shear layer that propagate downstream to form turbulent spots and very long *elongated streaks of velocity fluctuations*. The latter are the three-dimensional Klebanoff modes, while the former are associated with the upstream propagating modes of the two-dimensional component of the disturbance field. While the DNS produces results for the imposed disturbance field, still it does not provide a clear picture of the physical mechanisms involved. But, the shear layer properties of different modes and the simulations in Sengupta *et al.* (1999) and Sengupta *et al.* (2002) provide vital clues to freestream excitation problems by periodic vortices that also validate the observations of the control-experiments of Kendall (1987).

Rapid transition caused by periodic train of vortices follow a maximum growth path when the convection speed is within $0.26U_\infty$ and $0.33U_\infty$, if Re_{cr} is restricted to a maximum of 1900 at the outflow. The instability is still by TS wave generated packets, if the applied perturbation is small. This route of instability is not the bypass transition. However, when the free stream turbulence intensity exceeds 1%, it has been observed experimentally that transition occurs rapidly, bypassing the TS route. It is noted in Jacobs & Durbin (2001) that *inertial-time-scale processes apparently come into play, but their origin and nature are not at present known.* These large amplitude perturbations are noted to cause bypass transition and Jacobs & Durbin (2001) have stated that bypass transition is *stochastic by nature, and so lies within the province of statistical fluid dynamics.* Progress has been limited in understanding bypass transition due to lack of definitive controlled experimental observation and data in identifying physical mechanism(s) in the spirit of the experiment of Schubauer and Skramstad (1947). Design of control-experiments to identify unit-processes have been advocated by Smith (1993) for transitional and turbulent flows, who notes that one must excite the fluid dynamic system with non-negligible input, while reducing the background disturbances to minimum, such that the causality of inputs can be unambiguously established, the same way in the classical experiments of Schubauer & Skramstad (1947).

Such an experiment was performed and reported in Chattopadhyay (2001), Sengupta *et al.* (2001) and later in Lim *et al.* (2004). In this experiment, the focus was to excite a sub-critical violent instability of the shear layer by a steadily convecting single vortex. Thus, no specific time scale was enforced for the disturbance field. In the experiment, violent breakdown during by-

pass transition was shown to be initiated by a two-dimensional mechanism and the resultant broadband energy spectrum of the corresponding turbulent flow is excited at the receptivity stage itself by the primary instability. The experiment was conducted in a water tunnel using dye visualization technique where the bypass transition was triggered by controlled motion of a captive vortex in the streamwise direction, at a speed different from the free stream speed. This is discussed in the next section.

3.3 Visualization Study of Vortex-Induced Instability as Bypass Transition

In this experiment, stability of a laminar boundary layer is examined when the sub-critical flow (with respect to critical Reynolds number at which growing TS wave first makes its appearance) is affected by convecting a single vortex outside the shear layer. Experiments on vortex-induced instability are challenging, as it is difficult to control and quantify strength and propagation speed of vortical disturbances. This experiment was designed to achieve complete control over these parameters, by rotating a cylinder at high rotation rate to create a stable captive vortex of constant strength and by constraining it to translate at a fixed height with constant convection speed. It is to be emphasized that shed vortices in the wake of the rotating cylinder, if there are any at all, have strengths an order of magnitude lower than that of the captive vortex created due to rotation by Robins-Magnus effect. The role of captive translating vortex with a finite-core size is to destabilize the shear layer by creating a longitudinal disturbance pressure gradient. This was also the scenario proposed in Monin & Yaglom (1971), where the process was thought to arise due to constant buffeting by convected vortices associated with free stream turbulence. In the book, the authors were attempting to explain a similar scenario proposed by Taylor (1936).

Present experiment was conducted in the re-circulating water channel in National University of Singapore. Fig. 3.1 shows a schematic of the experimental set-up. The test section measured $400mm \times 400mm$ in cross section and 1800mm long, made of transparent plexiglass. The flow before entering the test-section passes through a honeycomb, three fine screens and a 4:1 contraction section. The flow velocity in the test section is controlled by a variable-speed A.C. motor driving a centrifugal pump on the return leg of the flow circuit.

The boundary layer under investigation was allowed to form over $1100mm$ long flat plate held vertically on its edge, on the base of the test section. The plate had a rounded leading edge and an adjustable trailing edge flap

that was used to create a stable boundary layer in the absence of excitation. The single captive vortex is created by rotating a circular cylinder of diameter d ($= 15mm$), whose axis was parallel and along the spanwise direction of the plate. The cylinder was attached to a stepper motor whose rotation rate was controlled and varied from 2.5 to 6 revolutions per second in either clockwise or anticlockwise direction on demand. The distance between the flat plate and the rotating cylinder was kept in most of the cases equal to $90mm$, but was also varied between 60 and $120mm$ for some other cases. For the purpose of visualization, dye was released from six dye-ports located $88mm$ downstream from the leading edge of the plate.

Fig. 3.1 shows the schematic of the experimental setup. In Fig. 3.1(a), the side view showing a rotating cylinder translating over a flat plate is shown. In Fig. 3.1(b), the same setup is viewed from the top of the tunnel. H is the adjustable distance of the cylinder from the plate; U_∞ is the oncoming flow speed; c indicates the translational speed of the cylinder and Ω is the angular velocity of the cylinder. The distance of cylinder from the leading edge of the plate is indicated by x. This arrangement creates a captive vortex (at the center of the cylinder) that can be made to travel at pre-determined speed. Reynolds number of the rotating cylinder was 2975 based on the diameter and the free stream speed of U_∞. The displacement thickness (δ^*), at the location of dye port was calculated as $3.27mm$ and thus, the distance between the cylinder and plate is equivalent to 27.52 δ^*. Therefore, the disturbance source was by design kept significantly outside the shear layer to mimic the unit process of free stream turbulence effects. The cylinder was constrained to travel at the fixed height (H) over the flat plate and the translational speed c, was also controlled. All of these parameters were used to control the events in a reproducible fashion.

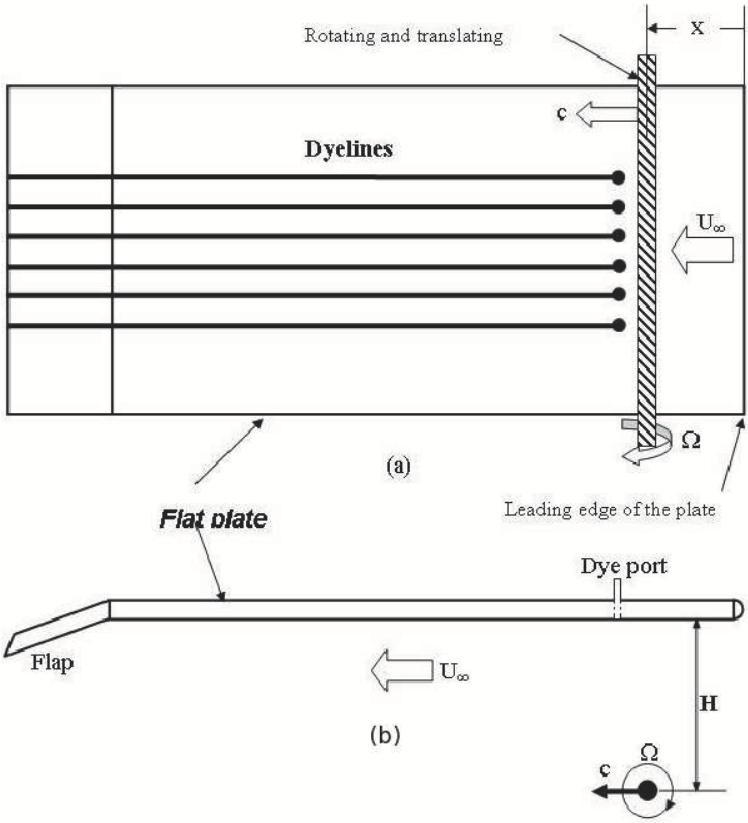

Figure 3.1 Schematic of the experimental setup. (a) Side view showing a rotating cylinder translating over a flat plate. (b) Same setup as viewed from the top of the tunnel. H= adjustable distance of the cylinder from the plate, U_∞ = flow speed, c= translational speed of the cylinder, and Ω= angular velocity of the cylinder. x= distance of cylinder from the leading edge of the plate. This arrangement creates a captive vortex (at the center of the cylinder) that can be made to travel at predetermined speed.

Eight significant cases were reported in Lim *et al.* (2004) (as given in Table 3.1). The first two cases correspond to the condition when the cylinder

rotates in the counter-clockwise direction and translates slower than the free stream speed. However, the translation speed of the cylinder in Case 2 is almost double than that of Case 1. For Case 3 the cylinder was not rotated and this was a case where the shear layer on the flat plate would have been perturbed by the shed vortices that are significantly weaker and periodic. This case also demonstrated the importance of controlled over uncontrolled disturbances in the freestream. The shed vortices behind a non-rotating cylinder travel at unknown non-uniform speed and whose heights also keep changing, and that cannot be controlled. For Cases 4 and 5, the cylinder rotates in the opposite direction to that of Cases 1 and 2.

Table 3.1

	c/U_∞	$\Omega(rps)$	H/δ^*	$U_s/(U_\infty - c)$
Case 1	0.386	+5	27.52	2.360
Case 2	0.772	+5	27.52	6.364
Case 3	0.386	0	27.52	0
Case 4	0.386	-5	27.52	2.360
Case 5	0.237	-5	27.52	2.324
Case 6	0.386	+5	18.35	2.360
Case 7	0.386	+5	24.45	2.360
Case 8	0.386	+5	36.70	2.360

In Cases 6 to 8, rotation and translation velocities of the cylinder are the same, but the cylinder is located at different distances above the boundary layer. The last column of the table shows the ratio of surface speed ($U_s = \Omega d/2$) to the relative free stream speed, $(U_\infty - c)$. Except for Case 3 where the cylinder is not rotating, the values given in the last column for all other cases are greater than 2. This parameter value is known to cause limited or no Karman vortex shedding, as noted experimentally in Tokumaru & Dimotakis (1993) and Diaz *et al.* (1983).

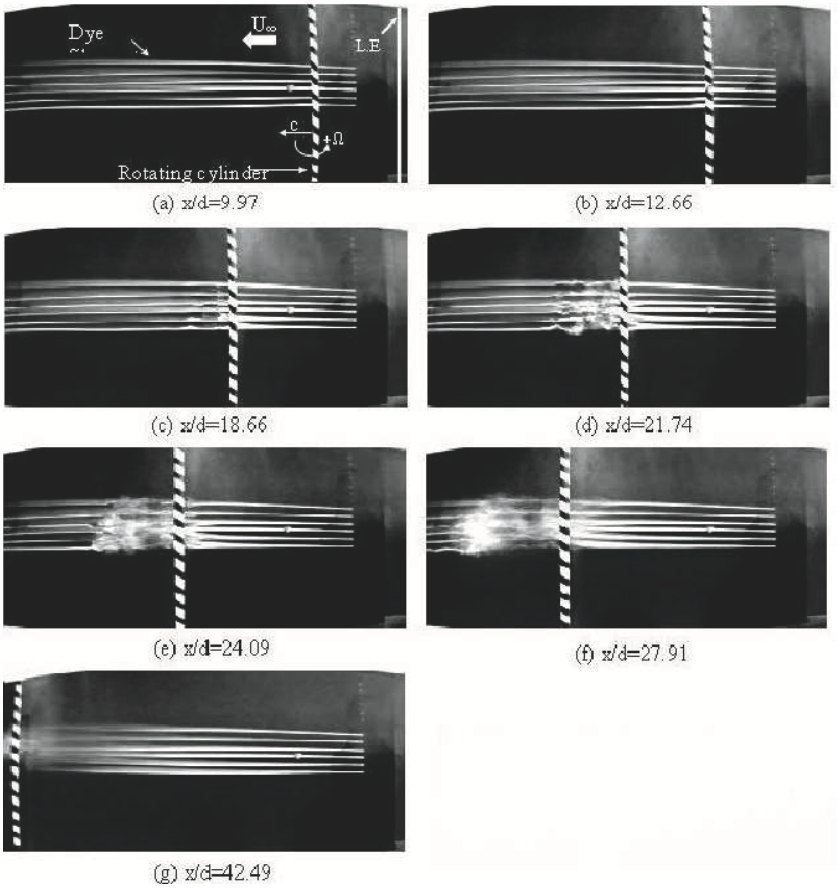

Figure 3.2 Case 1, c=0.386, H/δ^*= 27.52, $\Omega = +5$. Note: is x is measured from the leading edge of the plate and d is the diameter of the cylinder.

In Fig. 3.2, flow visualization sequences for the Case 1 are shown that indicate vortex-induced instability as localized increase in mixing, diffusion and irregularity of the dye filaments. The dye filaments were initially parallel, implying two-dimensionality of the primary flow. As the vortex moved in the flow direction from right to left, each dye filament splits into two, with one part lifting off with little or no spanwise spreading at the early stages and the other part staying in its course. The direct consequence of this is in

the incipient formation of disturbance packets those keep lengthening due to higher *front speed*. The disturbance starts off ahead of the cylinder, and as time progresses it grows while convecting faster than the cylinder and hence affecting a larger part of the flow with time. The violent breakdown of dye filaments indicates strong unsteadiness due to an instability caused by the translating vortex ($c = 0.386U_\infty$).

In contrast, when the translation speed of the cylinder was increased to ($c = 0.772U_\infty$) (Case 2), there was no violent breakdown of the flow, as shown in Fig. 3.3. This indicates that the boundary layer is insensitive to the vortex convecting at higher speeds. For the range of translation speed investigated, it was found that slower the translation speed of the vortex, greater was the effect on boundary layer stability, when other parameters were kept the same.

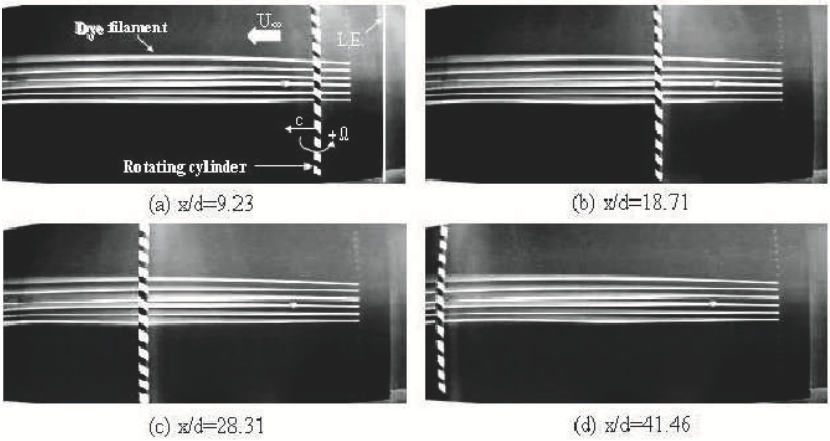

Figure 3.3 Case 2, c=0.772, H/δ^*= 27.52, $\Omega = +5$.

To explain the above aspect of results, note that a rotating and translating cylinder of diameter d induces a disturbance stream function (Ψ) in the inviscid irrotational part of the flow field that is given in Robertson (1969) by,

$$\Psi = (U_\infty - c)[2y - \frac{(y-H)(d/2)^2}{\bar{x}^2 + (y-H)^2} - \frac{(y+H)(d/2)^2}{\bar{x}^2 + (y+H)^2}] + \frac{\Gamma}{4\pi} Ln \frac{\bar{x}^2 + (y+H)^2}{\bar{x}^2 + (y-H)^2} \tag{3.3.1}$$

with $\bar{x} = x - x_v$; where $x_v(= x_0 - ct)$ is the current location of the convecting vortex with x_0 as the location of it at $t = 0$ and Γ is the circulation of the vortex. This expression takes into account of the image system due to the presence of the wall. Equation (3.3.1) is an expression that is the cause for the fluid dynamical system to be destabilized inside the shear layer in a receptivity scenario. The imposed disturbance, as given in (3.3.1) consists of two parts: (i) the displacement effect of the finite-core vortex given by the first term with c, d and H as the defining parameters and (ii) the circulatory effect of Biot-Savart interaction given by the last term, that depends upon c, H and Γ. In Fig. 3.4, these effects are shown separately for the parameters given by $H = 6d$, that is also equal to $27.52\delta^*$- as mentioned earlier.

In Fig. 3.4(a), the disturbance stream function induced by a positive spanwise vortex is shown which establishes that the circulation effect predominates over displacement effect for the large value of H chosen. The disturbance stream function is evaluated when the vortex is located at $x_v = 5$. In Fig. 3.4(b), the imposed pressure gradient is shown as a function of x for two values of non-dimensional c, for the same case. It is seen that the imposed pressure gradient does not vary appreciably with c and the adverse pressure gradient for both the cases occur at the same downstream location, while there is a stabilizing favourable pressure gradient upstream of the freestream vortex, whose location is indicated by the vertical dotted line. Thus, the adverse pressure gradient is mostly determined by the circulation effect and the induced adverse pressure gradient that can destabilize the flow remains constant for same Γ, when c is varied. This might seem counter-intuitive, as one notices that the Cases 1 and 2 indicate different receptivity. The difference is understood, when one looks at Fig. 3.4(c), where the induced pressure gradient is plotted as a function of time at $x = 5$. For this figure the vortex is moved from $x_o = 1$ at $t = 0$ to $t = 30$. For the three values of non-dimensional c considered in this figure, for the stationary vortex case ($c = 0$) the induced pressure gradient remains the same at all time. However, for $c \neq 0$ cases, higher the value of c, the shear layer experiences larger adverse pressure gradient- but, for a shorter duration and subsequently it becomes favourable in comparison to cases with smaller c.

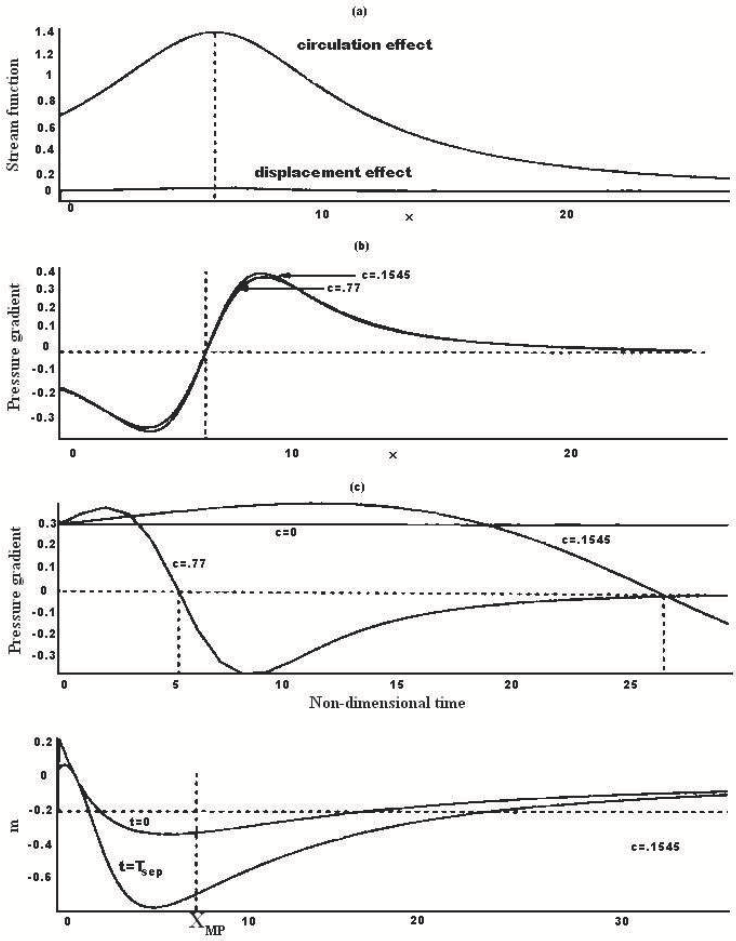

Figure 3.4 (a) Disturbance stream function as a function of x caused by circulatory and displacement effects at y = 1.92, when the freestream vortex is at $x_c = 5; H = 6$ and c = 0.1545; (b) Pressure gradient at the same height for the case of (a); (c) Pressure gradient as a function of time at x = 5 and same height when the vortex is started from $x_c = 1$ and (d) variation of Falkner-Skan parameter m with x for the indicated time instants.

In comparison, for the case of $c = 0.1545$ the adverse pressure gradient experienced is larger as compared to $c = 0$ case and that is also experienced over longer time duration. In Fig. 3.4(d), the Falkner-Skan pressure gradient parameter, $m = \frac{x}{U_e}\frac{dU_e}{dx}$ is shown as a function of x for the two indicated time instants, for $c = 0.1545$. Apart from the initial time instant $t = 0$, another large time is considered for plotting m in this figure. The latter time is when the Navier-Stokes solution indicates unsteady separation at $x_{MP} = 6.4$ at $t = 23$ (as shown in Sengupta *et al.* (2003)). The horizontal dotted line in the figure is drawn at $m = -0.19884$, for which the similarity flow suffers steady separation. This figure clearly shows that the considered cases represent truly unsteady flow that can sustain much larger adverse pressure gradient for a long time before it shows unsteady separation, as compared to steady flows.

In Fig. 3.5, visualization sequences are shown for the Case 3. In this case of non-rotating translating cylinder, no violent instability was seen to occur for two reasons. Firstly the imposed disturbance field, as given by Eqn. (3.3.1) has no captive vortex (*i.e.*$\Gamma \equiv 0$) as the cylinder does not rotate while translating. Secondly, if there are shed vortices present, they will be very weak and Benàrd- Karman vortex street is seen to affect the flow weakly far downstream of the translating cylinder - only at earlier times.

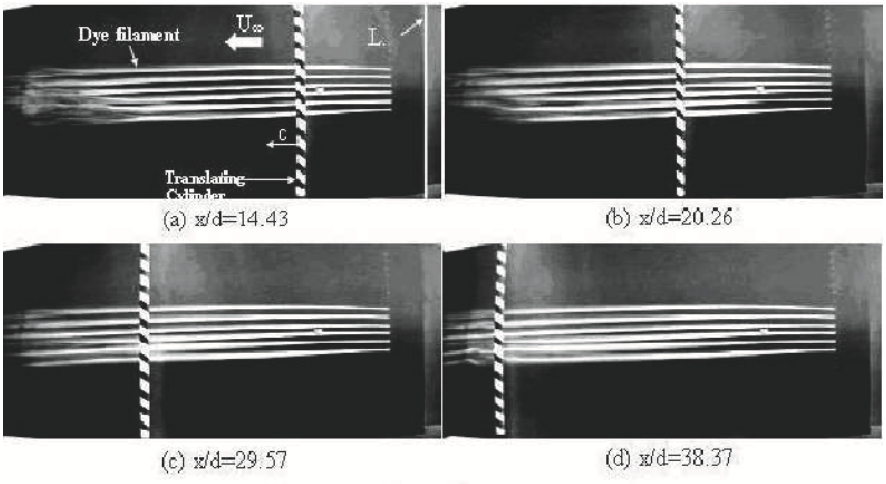

Figure 3.5 Case 3, c=0.386, H/δ^*= 27.52, $\Omega = 0$

Fig. 3.6 shows results for the Case 5, when the cylinder rotates in opposite direction with same rotation rate and translates with a speed $c = 0.237$. In this case, very weak transition was noted at later times, as opposed to the counter-rotating vortex cases.

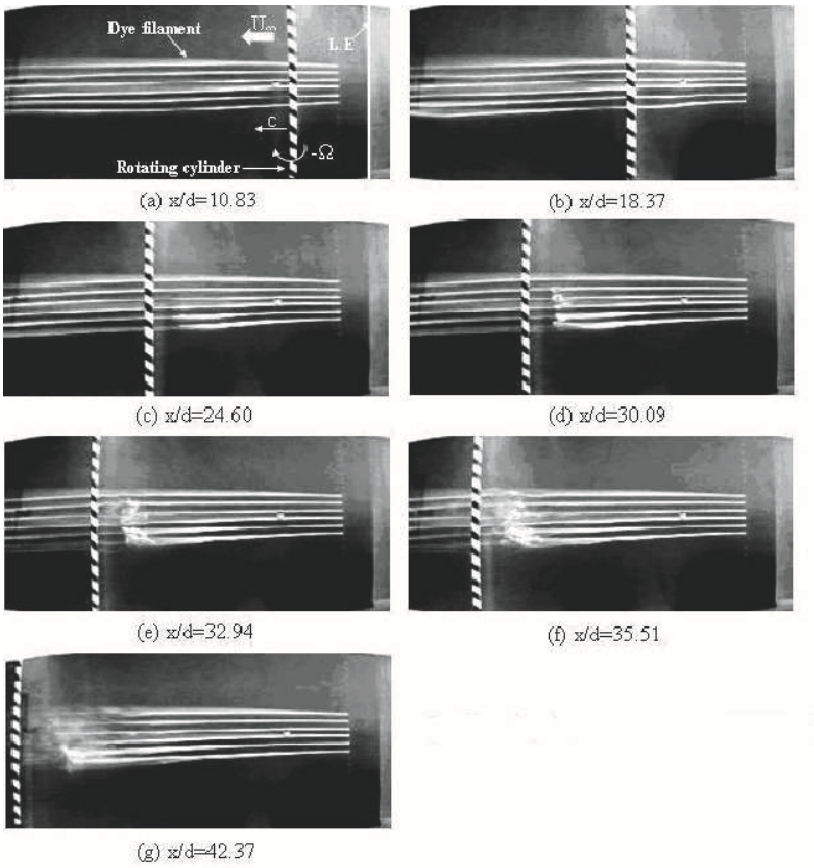

Figure 3.6 Case 5, c= 0.237, H/δ^***= 27.52,** $\Omega = -5$

For the Cases 4 and 5, the main distinguishing features are: 1) The disturbances trail behind the freestream vortex and 2) The disturbance growth is far lower than that for the Cases 1 and 2. The first reason can be sought in terms of the input adverse pressure gradient on the shear layer. In

the case of clockwise rotation, the adverse pressure gradient trailed behind the cylinder, while in the case of counter-clockwise rotation the adverse pressure gradient is created ahead of the cylinder. This is explained in Fig. 3.7 that show sketches of streamline patterns in the inviscid part of the flow that would be created by a rotating and translating cylinder for both the clockwise and the counter-clockwise rotation cases.

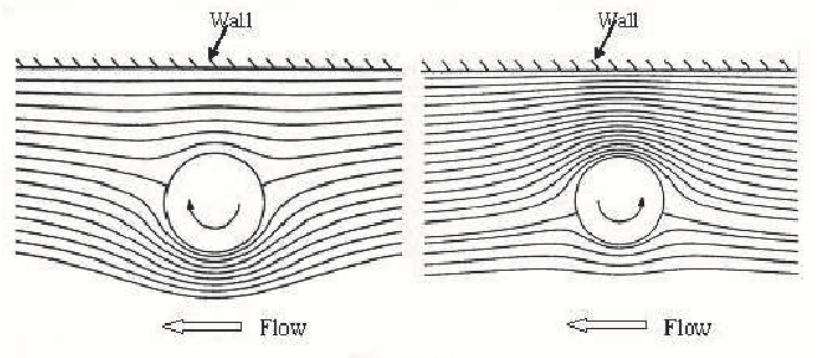

Figure 3.7 Sketches showing ideal streamline patterns created by a rotating and translating cylinder for both clockwise and counter-clockwise rotation. In the real situation, they are slightly more complicated.

Streamline curvature in each case is an indicator of the imposed pressure gradient. For the counter-clockwise rotating cases, streamline divergence ahead of the cylinder is more pronounced than that is behind the cylinder for the clockwise rotating cylinder cases. This explains as to why the counter-rotating vortex will create a stronger effect than the clockwise rotating vortex. This is consistent with the computational and experimental results reported in Sengupta *et al.* (2001), Sengupta *et al.* (2003) and Chattopadhyay (2001). In closing this section, we note that the displayed evidence is for an instability of wall-bounded shear layer at a streamwise location where theoretical investigation reveals that there would not be instability leading to the formation of TS waves. For this reason, in Lim *et al.* (2004) this is referred to as subcritical instability. There is a very good reason for the receptivity experiment to have been conducted for a sub-critical condition. For super-critical conditions, the instability can be triggered by residual background disturbances, that is difficult to measure and categorize. Also, at higher Reynolds numbers, the transfer function of

the dynamical system is very receptive to trace magnitude of disturbances. In contrast, for sub-critical condition the transfer function is not receptive to small amplitude disturbances and one needs definitive stronger input to destabilize the shear layer. Thus, at sub-critical conditions one has more control in studying the receptivity problem with the help of carefully designed experiments.

3.4 Computations of Vortex-Induced Instability as A Precursor to Bypass Transition

For the subcritical instability of the zero pressure gradient boundary layer shown in the experimental results of the previous section, the mean flow was given by the Blasius boundary layer that was destabilized by a convecting captive vortex. In Chattopadhyay (2001), Sengupta *et al.* (2001, 2003) the early stages of the bypass transition was computed by solving the full Navier-Stokes equation in two-dimensions.

The two-dimensional Navier-Stokes equation is solved in stream function-vorticity formulation, as reported variously in Sengupta *et al.* (2001, 2003), Sengupta & Dipankar (2005). Brinckman & Walker (2001) also simulated the burst sequence of turbulent boundary layer excited by streamwise vortices (in x- direction) using the same formulation for which a stream function was defined in the $(y-z)$ -plane only. To resolve various small scale events inside the shear layer, the vorticity transport equation (VTE) and the stream function equation (SFE) are solved in the transformed $(\xi-\eta)-$ plane given by,

$$h_i h_2 \frac{\partial \omega}{\partial t} + h_2 u \frac{\partial \omega}{\partial \xi} + h_1 v \frac{\partial \omega}{\partial \eta} = \frac{1}{Re}\left[\frac{\partial}{\partial \xi}\left(\frac{h_2}{h_1}\frac{\partial \omega}{\partial \xi}\right) + \frac{\partial}{\partial \eta}\left(\frac{h_1}{h_2}\frac{\partial \omega}{\partial \eta}\right)\right] \quad (3.4.1)$$

And

$$\frac{\partial}{\partial \xi}\left[\frac{h_2}{h_1}\frac{\partial \psi}{\partial \xi}\right] + \frac{\partial}{\partial \eta}\left[\frac{h_1}{h_2}\frac{\partial \psi}{\partial \eta}\right] = -h_1 h_2 \omega \quad (3.4.2)$$

Where h_1 and h_2 are the scale factors of transformation defined by

$$h_1^2 = \left(\frac{\partial x}{\partial \xi}\right)^2 + \left(\frac{\partial y}{\partial \xi}\right)^2 \ \textit{and} \ \ h_2^2 = \left(\frac{\partial x}{\partial \eta}\right)^2 + \left(\frac{\partial y}{\partial \eta}\right)^2 \quad (3.4.3)$$

The above equations are solved in a domain: $-1 \le x \le 25$ *and* $0 \le y \le 1.92$, with all lengths non-dimensionalized by the core size of the convecting vortex that is in this case identified with the diameter of the convecting cylinder. A uniform grid spacing of $\triangle x = 0.04$, is used in the streamwise

direction and a stretched grid is used in the wall-normal direction with the wall resolution given by, $\triangle y = 0.000780$. This grid has been used along with the high accuracy compact schemes of Sengupta *et al.* (2003a, 2006b) for resolving the nonlinear convection terms. From the visual experimental observation, one cannot obtain the strength of captive convecting vortex and in the computation this has been treated as a parameter. For the shown results in Fig. 3.8, a value of $\Gamma = 9.1$ has been taken.

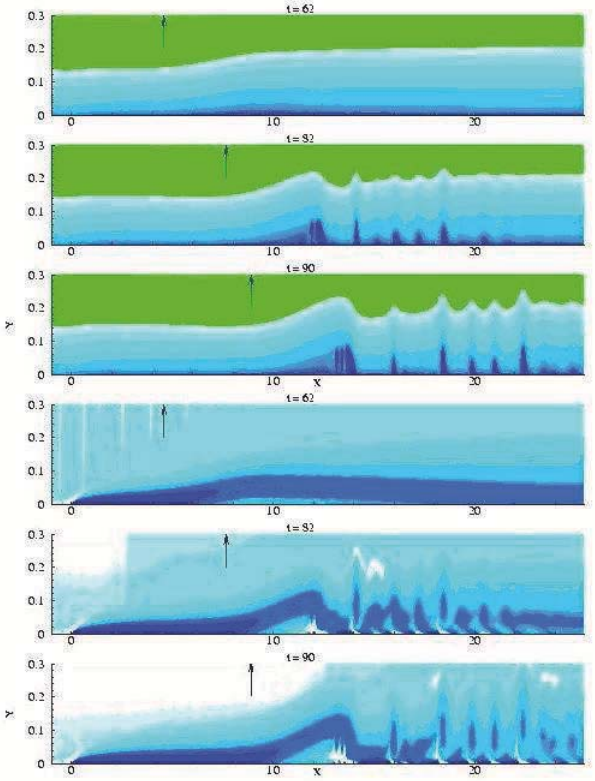

Figure 3.8 Stream function (top three panels) and vorticity contours plotted at the indicated times. Same contour values are plotted for each quantity. Arrowheads at the top of each frame indicate the instantaneous streamwise location of the freestream vortex.

The Reynolds number based on displacement thickness of the undisturbed flow at the outflow of the computational domain is 472. Thus, the flow is fully sub-critical in the computational domain (with respect to linear stability theory criticality).

At the inflow and at the top of the computational domain one calculates the flow variables, as induced by the freestream vortex via Biot-Savart interaction rule. At the outflow, fully developed condition is applied for the wall-normal component of the velocity ($\frac{\partial v}{\partial \xi} = 0$) and using the same in SFE, one can obtain the vorticity boundary condition at the outflow from Equation (3.4.2). At the top frame of Fig. 3.8, one sees incipient unsteady separation on the wall. In subsequent frames, one notices secondary and tertiary events induced by the primary instability. In these computed cases, one does not notice TS waves and the vortices formed on the wall are essentially due to unsteady separation that is initiated by the freestream convecting vortex. These ensemble of events have been noted as the vortex-induced instability or bypass transition in Sengupta *et al.* (2001, 2003), Sengupta & Dey (2004) and in Sengupta & Dipankar (2005).

3.5 The Instability Mechanism in Vortex-Induced Instability

The mechanism at play during vortex-induced instability has been explained in Sengupta *et al.* (2001, 2003) and the present discussion is based on these sources. The experimental and computational results clearly reveal the existence of a receptivity mechanism inside the shear layer that induces instability as a consequence of single vortex migrating in the freestream at a uniform speed convecting at a constant height. To understand the instability in flows, one must understand the growth of disturbance mechanical energy. It was Landahl & Mollo-Christensen (1992), who emphasized the fact that in understanding transition and turbulence, one must consider the growth of total mechanical energy and not just simply the disturbance kinetic energy. This prompted Sengupta *et al.* (2001, 2003) to develop an equation for the total mechanical energy from the Navier-Stokes equation without making any assumption on the nature of the equilibrium and disturbance flow field. Such restrictions are imposed in all linear viscous instability mechanism studied in Chapter 2. For incompressible flows this disturbance equation energy equation is obtained by taking the divergence of the rotational form of the Navier-Stokes equation and is given by,

$$\bigtriangledown^2 E = \vec{\omega} \bullet \vec{\omega} - \vec{V} \bullet (\bigtriangledown \times \vec{\omega}) \tag{3.5.1}$$

Where $E = \frac{p}{\rho} + \frac{V \bullet V}{2}$, is the total mechanical energy. The solid dots in these equations represent vector dot product. The instability is related to

the rotationality of the flow and Sengupta *et al.* (2003) have shown that the instability associated with the growth of disturbance energy is driven by the right hand side of Equation (3.5.2). This is based on the observation in Sommerfeld (1949) that a negative right hand side indicates a source of energy while a positive quantity represents a sink. If one divides E into a mean and a disturbance part via , $E = E_m + \varepsilon E_d$ and substitute it in Eqn. (3.5.1), one gets the equation for the disturbance energy given by,

$$\bigtriangledown^2 E_d = 2\vec{\omega}_m \bullet \vec{\omega}_d + \vec{\omega}_d \bullet \vec{\omega}_d - \vec{V}_m \bullet \bigtriangledown \times \vec{\omega}_d - \vec{V}_d \bullet \bigtriangledown \times \vec{\omega}_m - \vec{V}_d \bullet \bigtriangledown \times \vec{\omega}_d \quad (3.5.2)$$

This equation can be used to describe the onset of instability, when a suitable mean flow is defined. We note that this equation is very generic for all incompressible flows (steady or unsteady flows), as it is based on full Navier-Stokes equation without making any assumptions. In Sengupta *et al.* (2006a) this equation has been used to explain the classical linear instability theory for parallel flows showing exactly identical TS waves obtained from Orr-Sommerfeld equation. In section 4.3, this is fully explained with the development of the actual equations and results. For the computational data, a mean flow was taken at t = 20 as representative undisturbed flow and the right hand side of (3.5.2) was calculated and plotted as shown in Fig. 3.9- at some representative times.

In the figure, regions with darker shades of blue indicate the presence of disturbance energy sources. At early times, one notes two sites from where instability originates. They are at the leading edge of the plate and a location more than $5D$ from the leading edge of the plate. It is seen that the leading-edge instability is weaker of the two and the disturbance energy sources remain outside the shear layer that originate from the leading edge. The other site grows stronger with time and little before $t = 80$, it becomes strong enough to create an eruption from the wall - somewhat reminiscent of burst sequence in fully developed turbulent flows that causes a *connection between the two sites* via the eruption and spike formation from the wall. In stream function and vorticity contour plots of Fig. 3.8 the spikes are also evident, in the form of secondary and tertiary bubble formations. It is therefore, necessary to include the leading edge in such computing exercises; otherwise one would compute unimpeded spike stage from a location downstream of the leading edge, as reported earlier in Peridier et al. (1991) and Obabko & Cassel (2002). We must also point out another aspect of this present energy-based instability theory developed around Eqns. (3.5.1) and (3.5.2). This is to be noted that the corresponding homogeneous equation would indicate intrinsic instabilities, if there are any. However, this being a simple Laplacian operator, there are no intrinsic instability identified for it so far and the noted instability is driven by interaction of velocity and

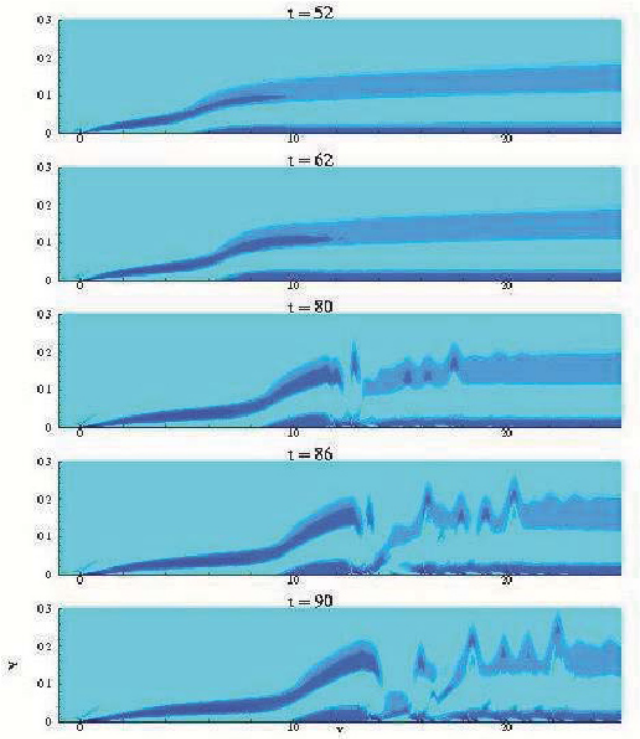

Figure 3.9 Contours of the right hand side of the disturbance energy equation (3.5). The negative contours are shown by darker blue colour in the figure, those indicating the energy source for disturbance quantities.

vorticity field acting as source terms on the right hand side of (3.5.1) and (3.5.2). The major issue is about how the energy is initially exchanged from the mean to the disturbance field and this is clearly brought out by the first term on the right hand side of (3.5.2) that indicates the interaction between mean and disturbance vorticity field.

It is noted that during later stages of bypass transition caused by convecting vortex in the freestream, large coherent vortices are formed inside the shear layer. Such coherent structures have been characterized by Proper orthogonal Decomposition (POD) - a method that was originally developed

by Kosambi (1943) and later used in fluid dynamics by Sirovich (1987) and Holmes et al. (1996). For the present bypass transition problem, POD analysis results have been shown in Sengupta *et al.* (2003) and Sengupta & Dey (2004). In these references, the method of snapshot due to Sirovich (1987) and a local analysis method are used. For the method of snapshot, 21 frames have been used in a time-span of 10 to perform POD. In Fig. 3.10, the eigenvalue and leading eigen-modes are shown for the vorticity data.

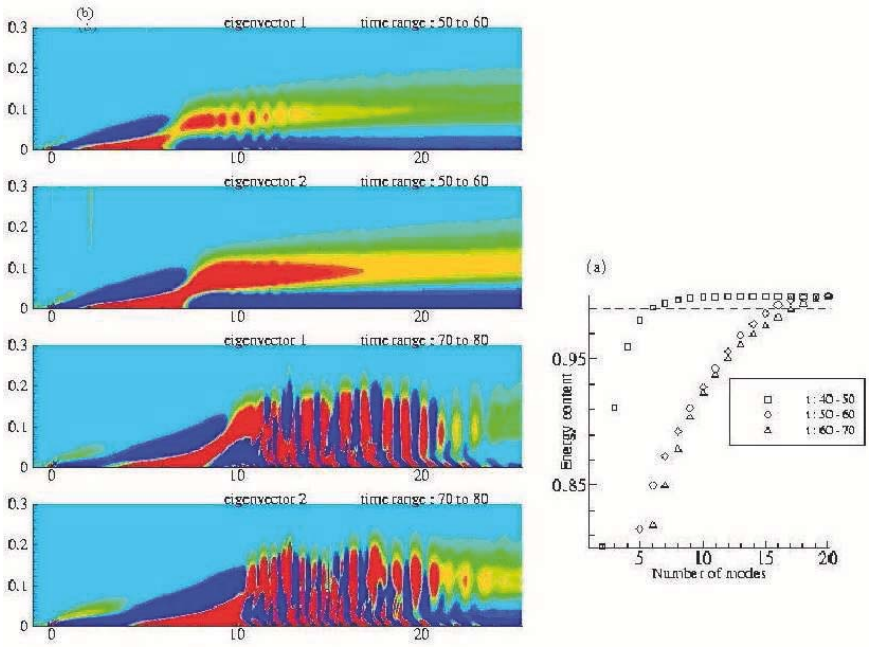

Figure 3.10 Sum of a specific number of eigenvalues divided by their total sum, indicating disturbance enstrophy content. The dotted line indicates 99% level. (b) The first two eigenvectors of disturbance vorticity during the indicated time ranges

The eigenvalues in Fig. 3.10 represent the fraction of the total enstrophy contained by a specific number of leading eigenmodes and these are shown on the right of the figure. The fractional enstrophy content is given by the sum of the leading eigenvalues divided by their total sum. One notices that the largest eigenvalue is well separated from other eigenvalues. Also, up

till around $t = 50$, five eigenmodes capture 99% of the total disturbance enstrophy. This number increases to 14 during $t = 80$ to 90. Thus, POD analysis provides a very good basis for reduced order modeling (ROM) of fluid dynamical systems during bypass transition - as have been discussed in Sengupta & Dey (2004).

The proto-typical vortex-induced instability described in this chapter so far, also makes its appearance in other flows. In the following, we describe a special flow that depends on this mechanism to trigger instability that otherwise have remained unexplained before.

3.6 Instability on The Attachment-Line of Swept Wings

The leading edge of a swept-back wing in contact with the fuselage is noted to experience abrupt flow transition due to the convection of continuous turbulent puffs along the attachment-line plane whenever the Reynolds number based on momentum thickness Re_θ is greater than 100 or $Re_{\delta^*} \geq 245$, a fact noted in Poll (1979) and Arnal (1986); whereas various investigations based on linear and weakly nonlinear theories have shown the lowest critical Reynolds number as $Re_{\delta^*} = 535$, indicating the actual transition to be a sub-critical phenomenon. This is pointed out in Sengupta & Dipankar (2005), who put forward the viewpoint that flow rapidly turning to turbulent stage right at the leading edge is due to vortex-induced instability described in the previous sections of this chapter. Otherwise, it is well known that the attachment-line boundary layer is very stable and the critical Reynolds number is orders of magnitude larger as compared to zero pressure gradient boundary layer. There were two major issues that remain unanswered and were pointed out in Theofilis *et al.* (2003). The first is related to the sub-critical instability and second issue is that of relating the instability at the attachment-line to the events downstream in the chordwise direction. The first issue was tackled in Sengupta *et al.* (2004) and in Sengupta & Dipankar (2005) and the second issue follows from the first as self-explanatory, if the flow becomes turbulent at the leading edge itself- as it is stated in these references.

It has been demonstrated that attachment-line boundary layer supports instability waves, the kind predicted in linear theory (shown by very careful experiments in Pfenninger & Bacon 1969; Poll 1979; Arnal, Coustols & Jullien 1984; Hall, Malik & Poll 1984; Poll, Danks & Yardley 1996). However, they do not cause transition occurring at the attachment-line, as no linear or nonlinear theories have explained transition at the attachment-line. In the literature, this premature transition is referred to as the Leading Edge Contamination (LEC) problem. In Sengupta *et al.* (2004) and in Sengupta

& Dipankar (2005), LEC was posed as a vortex-induced instability problem, where the freestream convecting vortex in the attachment-line plane is created at the wing-body junction, as has been suggested in Arnal (1986) that *the leading edge is contaminated by large turbulent structures coming from the wall at which the wing is fixed.* According to Arnal, the flow undergoes transition right at the leading edge via bypass mechanism. Gaster (1965a) specifically noted that vortices associated with junction flow are fed into the attachment-line boundary layer. The mean flow field and co-ordinate systems for flow past a swept-back wing is schematically shown in Fig. 3.11. On the attachment-line plane itself, the flow is essentially two-dimensional as noted by Prandtl (1946) and Crabtree *et al* (1963).

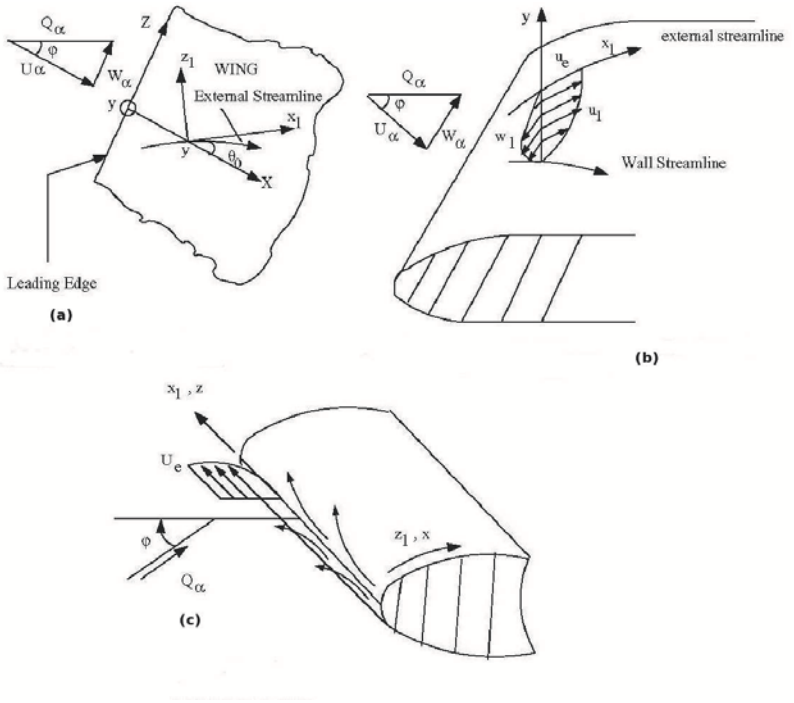

Figure 3.11 Flow profiles and schematic of co-ordinate systems for flow past a swept-back wing. (a) Notation and co-ordinate system; (b) Streamwise and cross-flow mean velocity profiles and (c) Attachment-line flow

In all early experiments including the one by Poll (1979), existence of attachment-line vortical structures is well established. It is thus natural to investigate the sub-critical instability by looking at the role of convecting vortical structures in explaining LEC from the solution of two-dimensional Navier-Stokes equation in the attachment-line plane itself, similar to the vortex-induced instability problem studied in Lim *et al.* (2004) and Sengupta *et al.* (2003) for zero pressure gradient flow.

Navier-Stokes equations have been solved in Sengupta & Dipankar (2005) using a (501X101) grid with 501 points in the streamwise direction distributed uniformly. In Fig. 3.12, computational results are shown for the case of a counter-clockwise circulating vortex convecting at a speed of $0.2U_\infty$ at a height of $30\delta^*$ of the attachment-line boundary layer. This height is more than that was considered for the Blasius boundary layer in Sengupta *et al.* (2003) and thus, establishes enhanced receptivity of attachment-line boundary layer as compared to zero-pressure gradient boundary layer.

In the figure, the first frame corresponds to an early time when the convecting vortex is to the left and out of the computational domain and its influence is seen as an upwelling of the shear layer near the inflow of the domain. By $t = 748$, the convecting vortex appears over the computational domain and very intense sequence of instabilities are seen over the attachment-line. At $t = 2001$, the convecting vortex is located around $x = 460$ and the leading coherent structures are out of the domain. As explained before, the shear layer aft of the convecting vortex is always stabilized due to the impressed favourable pressure gradient- to the extent that the shear layer thins down and this is clearly evident in the frames at $t = 1500$ and 2001. It has been shown in Sengupta & Dipankar (2005) that for a particular case with $\Gamma/\upsilon = 211.063$ and the non-dimensional core size of the vortex (with respect to δ^* of the shear layer at inflow) as 6, the first bubble occurs at a location where the Reynolds number based on displacement thickness was $Re_{\delta^*} = 190$ If the appearance of first bubble is taken as an indication of flow criticality, then this is a case of sub-critical instability. Once the first bubble forms on the wall, a succession of other follows due to local strong adverse pressure gradient being created ahead of the primary bubble. Also, this cascading phenomenon occurs at a very high speed and the flow contaminates very rapidly. As attachment-line shear layer is more stable with respect to linear mechanism, it is of more interest to investigate this bypass mechanism for LEC.

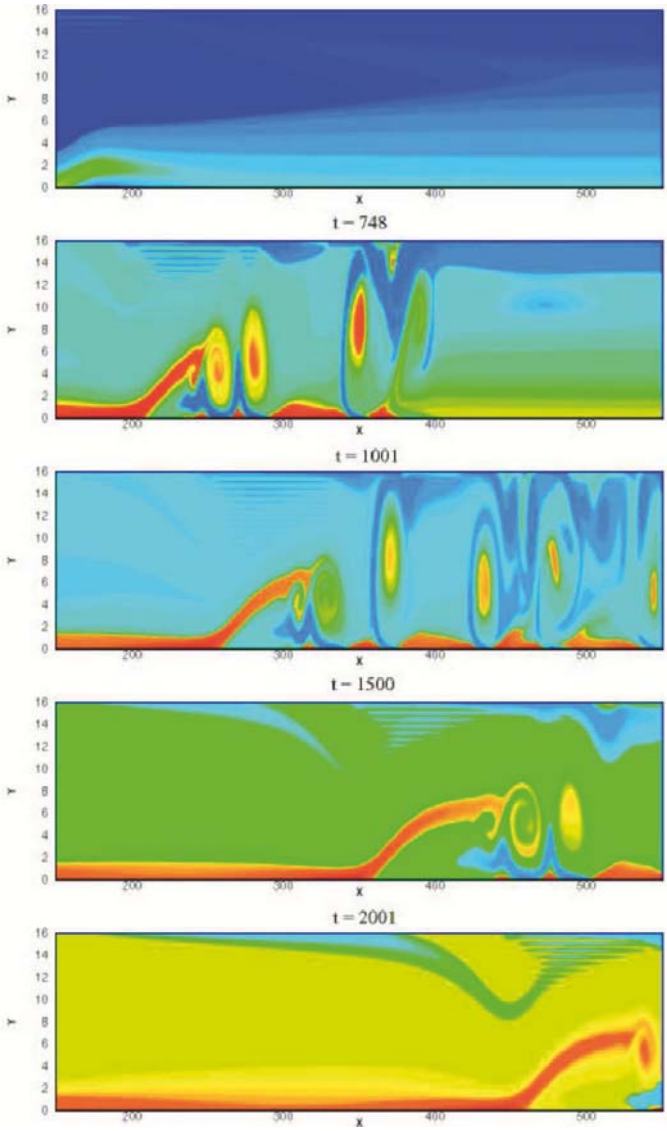

Figure 3.12 Vorticity contours for the case of LEC by a counter-clockwise rotating vortex

It is interesting to note that the instability is only feasible when the speed of the train of convecting vortex is far below the freestream speed- as was explained in the last chapter via Eqn. (2.7.8) to (2.7.11), following the work reported in Sengupta *et al.* (2002). However, when we consider aperiodic vortex convecting in the freestream, then the mechanism of instability is completely different, as there are no imposed time scales. In section 3.3, we have seen the visual signature of such events that we preferred to call the bypass transition. In this mode also, lower speed of convection has higher receptivity, as was explained with the help of Eqn. (3.3.1) and the associated discussion with the help of results shown in Fig. 3.4. For this same reason, present computations for LEC show strong bypass transition as compared to that shown in Obrist & Schmid (2003), where their computations displayed lower (exponential) growth rates for the introduced bubble moving at freestream speed. In Sengupta & Dipankar (2005), this bypass mechanism was explained with respect to the disturbance energy equation (3.5.2). Furthermore, it is worth quoting the following from this reference in explaining the bypass mechanism: *The disturbance energy equation arises by taking the divergence of the Navier-Stokes equation in the rotational form, representing the irrotational component of the disturbance field. The rotational field of the Navier-Stokes equation as governed by the vorticity transport equation yields the Orr-Sommerfeld equation obtained by linearization and making parallel flow approximation. Although Morkovin (1991) suggested that unsteadiness during bypass transition is due to the shear noise term in the Poisson equation for the static pressure.* What is more important for us to realize is that the Poisson equation for disturbance energy actually shows the coupling between the rotational part of the flow field (through velocity and vorticity terms) with the irrotational part (given by the Laplacian on the left hand side). Furthermore, this mechanism is equally valid for both two- and three-dimensional flow fields. Thus, significant unsteadiness with large spectral bandwidth disturbances can be created without the vortex stretching mechanism to explain the excited small-scales in transitional and turbulent flows.

The effects of a clockwise convecting vortex in the freestream is studied for this case too in Sengupta *et al.* (2004) and Sengupta & Dipankar (2005). A typical set of results are shown in the vorticity contour plots shown next in Fig. 3.13. As noted in Lim *et al.* (2004) and Sengupta *et al.* (2003), role of a negative vortex is to create an adverse pressure gradient behind it and hence instability onset is noted upstream of the convecting vortex. It has been noted and explained in Sengupta *et al.* (2001) and also here that there prevails a favourable pressure gradient region ahead of the clockwise convecting vortex. Thus, the cascade of secondary and higher instabilities

seen for the counter-clockwise vortex ahead of it is completely absent here. First and foremost, absence of adverse pressure gradient does not promote disturbance growth at all. Even if there is some disturbance present, the induced favourable pressure gradient attenuates it strongly. This feature of the flow is clearly visible in Fig. 3.13 that shows the existence of virtually a single coherent vortex.

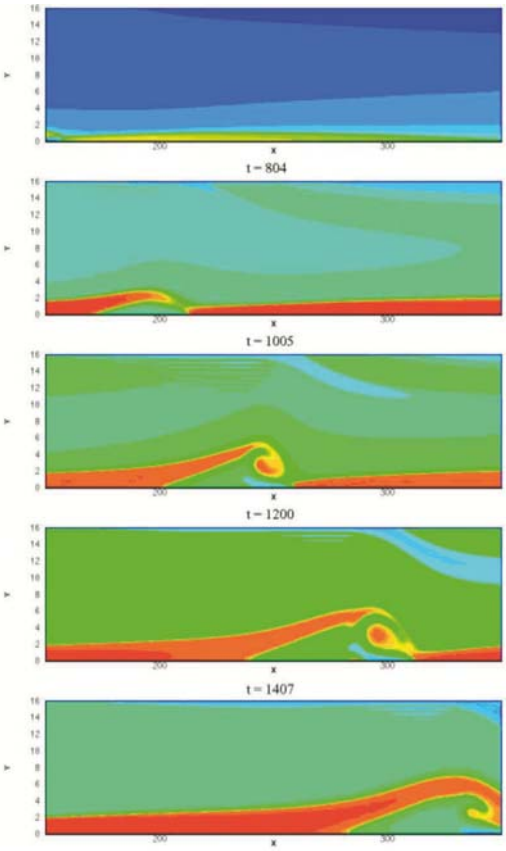

Figure 3.13 Vorticity contours for the case of a convecting negative vortex with strength given by $|\Gamma|/v = 126.638$ and other parameters same as in the previous case. Details of this is available from Sengupta & Dipankar (2005) and Sengupta *et al.* (2004)

We have already commented about the DNS of attachment-line instability study performed in Obrist & Schmid (2003) and explained the reason for their failure to explain LEC due to the wrong choice of convection speed of the vortex. In the following, we also make some general remarks about various such other efforts towards DNS. When full Navier-Stokes equation is solved to reproduce experimentally observed LEC effects, there also appears to be no consensus among reported results. Spalart (1988)'s three-dimensional DNS could not reproduce even the nonlinear equilibrium solution reported in Hall & Malik (1986), but it did produce the correct experimental transitional Reynolds number in Poll (1979)! Spalart (1988) used white noise to trigger instability for spatial DNS, where spanwise periodicity and a buffer domain in the chordwise direction were used additionally. Two-dimensional DNS results, however, produced conflicting results, with Theofilis (1998) predicting the wrong frequency of disturbance as compared to the experimental value of Poll *et al.* (1996). Joslin (1995) in reporting DNS results from a formulation that does not make spanwise periodicity assumption, showed the existence of the sub-critical two-dimensional equilibrium solution of Hall & Malik (1986). Subsequently, Joslin (1996) postulated that interactions of multiple three-dimensional modes lead to observed computational bypass transition. Thus, it appears that these simulations suffered due to multiple reasons, primary ones being: (i) inappropriate modeling of the problem through boundary conditions see e.g. the failure of Spalart (1988) to capture even the mean flow; (ii) inappropriate excitation field- as seems to be the case in all these simulations except Obrist & Schmid (2003) and (iii) inappropriate convection speed of the freestream vortex- as was the case in Obrist & Schmid (2003). Finally, it is also required that the adopted numerical methods must be dispersion relation preserving (DRP)-which most of these methods are not for the chosen numerical methods and the computational parameters, barring the spectral methods.

Chapter 4

SPATIO-TEMPORAL INSTABILITY AND TRANSITION

Prof. Tapan K. Sengupta
HPCL, Aerospace Engineering
I.I.T. Kanpur

4.1 Introduction

Significant advances have been made in the understanding the process of instability and transition where unstable TS waves are created by a viscous instability mechanism for external flows, as is explained in Chapter 2. Classical approaches to instability studies identify an equilibrium state, whose stability is studied by eigenvalue analysis by linearizing the governing equations. Results obtained by this approach match with controlled laboratory experiments for thermal and centrifugal instabilities. But, instabilities dictated by shear force do not match so well, e.g. (i) Couette and pipe flows are found to be linearly stable for all Reynolds numbers, while the former is found to suffer transition in a computational exercise at Re = 350 (see Lundbladh & Johansson, 1991) and the latter found to be unstable experimentally at $Re \geq 1950$ (see Reynolds, 1883), with the exact value dependent upon facilities and background noise level; (ii) plane Poiseuille flow has $Re_{cr} = 5772$, while in the laboratory experiment transition was shown to occur even at Re = 1000 by Davies & White (1928). Interestingly, according to Trefethen *et al.* (1993) the other example for which *"eigenvalue analysis fails include to a lesser degree, Blasius boundary layer flow"*. This is the flow which many cite as the success story of linear stability theory.

One of the features of traditional eigenvalue analysis is that the disturbance field is assumed to grow either in space or in time. This distinction is only for ease of analysis and there are no general proofs or guidelines available that would tell an investigator which growth rate to investigate. Huerre & Monkewitz (1985) have applied the so-called combined spatio-temporal

theory (developed originally to study plasma instabilities- as given in Bers, (1975)) to a family of mixing layers with the goal of determining a general criterion whereby a flows can be analyzed by either the spatial or temporal theory by inspecting the dispersion relation in the complex wave number-frequency plane. We point out that this does not treat the growth as a spatio-temporal one, but simply tells one which of the two theories may be appropriate for its study. In contrast, the spatio-temporal approach based on Bromwich contour integral method of Chapter 2, enables one to truly perform an analysis without any presumption whether to go for spatial or temporal approach. In fact, there must be many cases of instability where both spatial and temporal growths are present simultaneously.

In addition to the above examples, it is also noted that three-dimensional disturbances e.g. surface roughness or localized disturbances can lead directly to turbulence without any observed TS wave growth. Breuer & Kuraishi (1993) mentions that *these kinds of transitions are collectively known as "bypass mechanisms"*. Instead of classifying these as bypass transition (that we discussed in chapter 3), one can describe such instabilities, in terms of transient energy growth of kinetic energy. This kinetic energy approach is distinctly different from the developed theory in Sengupta *et al.* (2001, 2003) of disturbance mechanical energy growth described in Section 3.5. It is to be noted that such transient kinetic energy growth scenario was sought to be explained in the literature only for three-dimensional disturbance field, as the corresponding analysis for two-dimensional flows showed meager growth rate- see Trefethen *et al.* (1993) for a detailed discussion.

It was Landahl (1975) who showed that subject to certain general constraints, three-dimensional disturbances grow algebraically in a mean shear via an inviscid mechanism. This instability is not related to Orr-Sommerfeld equation and is related to the tilting of vorticity by mean shear. However, in later works by Henningson (1988) and Bruer & Haritonidis (1990), it was revealed that the algebraic instability is due to a coupling between the Orr-Sommerfeld and Squire Equations. The latter equation is nothing but the linearized vorticity transport equation for vertical component of vorticity. The above coupling creates an inclined shear layer that intensifies with time. Furthermore, Breuer & Landahl (1990) investigated the corresponding nonlinear growth and found a secondary instability that leads to direct breakdown to turbulence. However, in a subsequent Direct Numerical Simulation, Henningson, Lundbladh & Johansson (1993) reported a bypass transition occurring through a different breakdown mechanism.

The focus of this mechanism of algebraic growth of transient energy is two-fold, as explained in Breuer & Kuraishi (1993). Firstly, the transient energy growth can occur for linearly stable systems by two to three orders

of magnitude at which *nonlinear effects might push the disturbance into turbulence* directly. This has been termed the sub-critical route of bypass transition in Breuer & Kuraishi (1993). Secondly, such transient energy growth in a super critical flow can boost relatively slow TS waves with the former providing the initial algebraic growth that will be followed by the exponential growth of the linear mechanism of TS waves. However, none of these mechanisms have been experimentally verified in a controlled and unambiguous manner till to date.

There is an alternate view-point that treats the transient growth as that is due to non-normal modes. It has been shown in Schmid & Henningson (2001) that the regular and adjoint solutions of OSE are orthogonal, however Orr-Sommerfeld eigenfunctions are not orthogonal to each other. This leads to the sensitivity of the eigenvalues to perturbations to the underlying stability operator that has been shown for channel flow. It has been pointed out that the *non-normality of the Orr-Sommerfeld operator not only has consequences for the sensitivity of the spectrum, but it also influences the dynamics of disturbances governed by the linearized Navier-Stokes equations*. The resultant transient growth has also been noted in Schmid (2000). Note the Fig. 4.6 of Schmid & Henningson (2001) records transient growth for Blasius boundary layer at Re = 1000 to be thousand-folds for three-dimensional disturbance fields. However, for two-dimensional disturbance fields, corresponding maximum transient growth rates are very small. This aspect has been clearly stated in Trefethen *et al.* (1993) as the *essential feature of this non modal amplification is that it applies to three-dimensional (3D) perturbation of the laminar flow field ... When only 2D perturbations are considered, some amplification can still occur, but it is far weaker*. Apart from these, there are other asymptotic stability studies involving algebraic or transient growth of three-dimensional disturbance fields, as in Zuccher *et al.* (2006).

4.2 Transient Energy Growth

Above discussion clearly reveals that even linearized Navier-Stokes equation supports transient energy growth outside the context of classical eigenvalues, albeit that is true only for three-dimensional disturbance field. In the following, we recount a totally different route of spatio-temporal growth via the linearized receptivity analysis as was originally reported in Sengupta *et al.* (1994) for a full time dependent problem of Blasius boundary layer. Same approach of using Bromwich contour integral method has been reported in Sengupta *et al.* (2006, 2006a) and in Sengupta & Rao (2006). In these papers, a curious property of shear layer has been reported. It is

shown that one needs to perform a full time dependent receptivity analysis, rather than the spatial stability analysis, which is the practice for wall-bounded unseparated flows. It is shown that for spatially stable systems multiple stable modes can interact to give rise to spatio-temporally growing wave-packets and this is explained in this chapter. In essence, this raises the question on validity of normal mode analysis that is the mainstay of all eigenvalue analysis. In the presence of multi-mode interactions, it is natural to adopt the receptivity analysis using the Bromwich contour integral method described in Sengupta *et al.* (1994) and Sengupta & Rao (2006). The most important aspect of this work is that one does not require to impose any restrictions on the dimensionality of the problem in explaining large spatio-temporal growth. Sengupta *et al.* (2006, 2006a) explained the transient energy growth from the mechanical energy perspective that was developed in explaining bypass transition. Not only that, the equivalence of viscous instability theory (when TS waves are generated) with energy-based approach was shown in these papers.

Instead of studying stability using mass and momentum conservation, alternate approaches based on energy consideration had been initiated early, leading to the well known Reynolds-Orr equation, as described originally in Orr (1907). This has been further explained in Lin (1955), Stuart (1963) and Schmid & Henningson (2001). This equation deals with the evolution of the disturbances in terms of the kinetic energy. If one writes the Navier-Stokes equation in the indicial notation and take a dot product of it with the velocity vector, one gets the following equation,

$$u_i\frac{\partial u_i}{\partial t} = -u_iu_j\frac{\partial U_i}{\partial x_j} - \frac{1}{Re}\frac{\partial u_i}{\partial x_j}\frac{\partial u_i}{\partial x_j} + \frac{\partial}{\partial x_j}[-\frac{u_iu_i}{2}U_j - \frac{u_iu_iu_j}{2} - u_ip\delta_{ij} + \frac{u_i}{Re}\frac{\partial u_i}{\partial x_j}] \tag{4.2.1}$$

If one defines the kinetic energy of the full domain as $E_v = 1/2\int_v u_iu_idV$, then the above can be integrated over the whole domain to give rise to the Reynolds-Orr equation as,

$$\frac{dE_v}{dt} = -\int_v u_iu_j\frac{\partial U_i}{\partial x_j}dV - \frac{1}{Re}\int_v \frac{\partial u_i}{\partial x_j}\frac{\partial u_i}{\partial x_j}dV \tag{4.2.2}$$

However, this equation is derived subject to the assumption that the disturbance field is localized and/ or spatially periodic. This assumption removes any contribution coming from the nonlinear convection terms. Lin (1955) and Stuart (1963) point out that various estimates of critical Reynolds number obtained by this approach are erroneously too low due

to the above mentioned assumption that leads to the elimination of nonlinear terms appearing in the divergence form of the equations of motion. In contrast, the disturbance mechanical energy concept of Eqns. (3.5.1) and (3.5.2) retain the nonlinear term contributions, those are central to any instability studies. This energy-based receptivity analysis is all-inclusive as it is based on full Navier-Stokes equation without any assumption.

4.3 Energy-Based Receptivity Analysis

Explanation of this mechanism is presented here from the solution obtained by Bromwich contour integral method of Sengupta *et al.* (1994) and Sengupta & Rao (2006) for two-dimensional disturbances in two-dimensional mean flows, with the disturbance stream function given in Eqn. (2.6.86),

$$\psi(x,y,t) = \frac{1}{(2\pi)^2}\int\int_{Br} \phi(y,\alpha,\omega)e^{i(\alpha x-\omega t)}d\alpha\ d\omega \tag{4.3.1}$$

The Blasius boundary layer problem was solved in all these references for a parallel mean flow at Re = 1000 excited at the wall. In terms of the wall modes ϕ_1 and ϕ_3, the disturbance stream function can also be written down as,

$$\psi(x,y,t) = \frac{1}{(2\pi)^2}\int\int_{Br} \frac{\phi_1(\alpha,y,\omega)\phi'_{30} - \phi'_{10}\phi_3(\alpha,y,\omega)}{\phi_{10}\phi'_{30} - \phi_{30}\phi'_{10}} BC_w\ e^{i(\alpha x-\omega t)}d\alpha d\omega \tag{4.3.2}$$

Where BC_w was defined in Eqn. (2.6.88b) for the harmonic excitation at the wall shown in Fig. 4.1 (at y =0): $u = 0\ \psi(x,0,t) = U(t)\delta(x)e^{-i\omega_0 t}$. U (t) is the Heaviside function that represents the finite start-up of the exciter placed at the origin of the co-ordinate system.

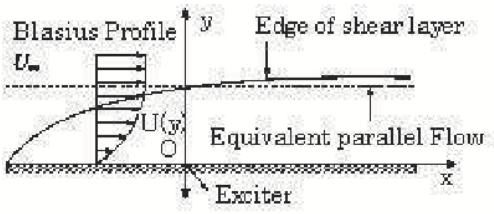

Figure 4.1 Harmonic excitation of a parallel boundary layer corresponding to the location of the exciter

The governing equation for the Fourier-Laplace transform is given by the following Orr-Sommerfeld equation,

$$\phi^{iv} - 2\alpha^2\phi'' + \alpha^4\phi = iRe\{(\alpha U - \omega)[\phi'' - \alpha^2\phi] - \alpha U''\phi\} \tag{4.3.3}$$

To understand the spatio-temporal growth of waves, few cases were considered in Sengupta *et al.* (2006), marked as A, B, C and D in Fig. 4.2, with respect to the neutral curve shown in the $(Re - \omega_0)$-plane for the leading eigenmode.

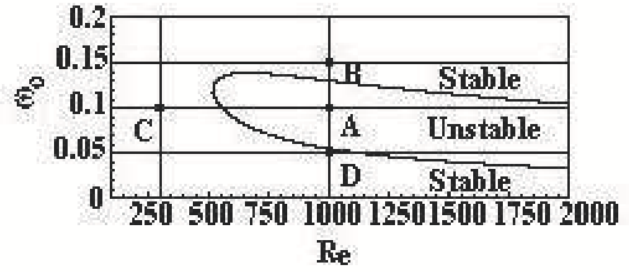

Figure 4.2 Neutral curve for the Blasius boundary layer identifying stable and unstable regions. The marked points are further investigated.

The Bromwich contour for point A was chosen in the α -plane on a line extending from -20 to +20 that is below and parallel to the α_{real} axis at a distance of 0.009 and in the ω-plane it extended from -1 to +1, above and parallel to the ω_{real} axis at a distance of 0.02. For the other points, the Bromwich contour in the α- plane is located at a distance of 0.001 below the α_{real} axis. The choice of the Bromwich contour in the α- plane was such that all the downstream propagating eigenvalues lie above it. Orr-Sommerfeld equation was solved along these contours with 8192 equidistant points in the α- plane and 512 points in the ω-plane. Orr-Sommerfeld equation was solved taking equidistant 2400 points across the shear layer in the range $0 \leq y \leq 6.97$. Spatial stability analysis produced waves for the four points of Fig. 4.2 with the properties shown in Table 4.1.

Table 4.1: Wave properties of the selected points in Figure 4.2

Mode	α_r	α_i	V_g	V_s	V_e
$A1$	0.279826	0.007287	0.4202	0.42	0.42
$A2$	0.138037	0.109912	0.4174	....	....
$A3$	0.122020	0.173933	0.8534	....	....
$B1$	0.394003	0.010493	0.4267	0.352	0.352
$B2$	0.272870	0.167558	0.2912		
$B3$	0.189425	0.322635	0.1159		
$C1$	0.246666	0.013668	0.5026	0.50	0.50
$D1$	0.160767	0.001520	0.3908	0.33	0.33
$D2$	0.062141	0.069659	0.2762		

For the point A, receptivity analysis produced streamwise perturbation velocity (u) that is shown in the bottom frame of Figure 4.3 at $t = 801.1$. In this figure, top two frames show solutions for the case of point B at the indicated times. Results obtained for point A are indistinguishable from the growing asymptotic solution obtained by treating this as a signal problem. Comparison of results by this two approaches were made in Sengupta *et al.* (1994), as shown in Figure 2.23.

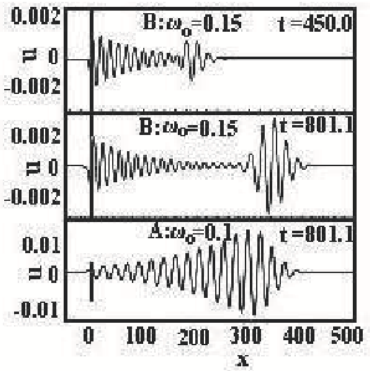

Figure 4.3 Streamwise disturbance velocity component plotted as function of x at indicated times for Re = 1000 at y = 0.278

Both the type of receptivity analyses (signal problem and full time dependent problem) provide the local solution in the neighbourhood of the exciter, but a forerunner- preceding the asymptotic solution is present only for the full time analysis. For spatially unstable system one cannot see a clear demarcation line between the asymptotic solution from the forerunner- with one merging smoothly into the other.

For the point A, the receptivity solution is dominated by the leading eigenmode, without any effects coming from the second and the third modes of Table 4.1. In contrast, for the point B the asymptotic solution is due to the first mode of Table 4.1 (in terms of wavelength and decay rate) and the growing wave-front corresponds to the second mode, in terms of the wavelength. Effects of the third mode are not seen to contribute to the overall solution for the point B. It is noted that the leading edge of the asymptotic solution continues to decay at the same rate predicted by spatial stability analysis, while the forerunner continues to grow spatio-temporally, although the spatial theory identifies this as a damped mode.

The necessary condition for the creation of a forerunner is found by looking at the receptivity solutions for points C and D, with the former having a single stable mode and latter with two damped modes. Results are shown in Fig. 4.4 for the streamwise perturbation velocity, at the indicated large time.

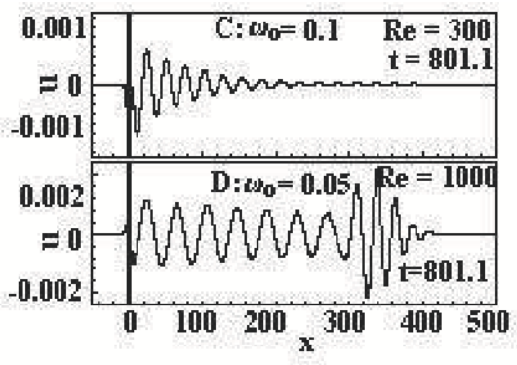

Figure 4.4 Streamwise velocity plotted as a function of x at indicated times for Re = 300 and 1000 for the indicated circular frequencies. Results are shown for non-dimensional height y = 0.278, over the plate.

The essential difference between these and the cases shown in Fig. 4.3 is that the latter have three modes, while C possesses a single mode and D possesses two modes. The frontrunner in Fig. 4.3 is due to interactions of multiple stable modes. In the absence of multiple modes- as for the point C- no such forerunner is seen in Fig. 4.4. Again for the point D, there are only two stable modes that create spatio-temporally growing wave front. Thus, for fluid dynamic systems presence of a minimum of two stable modes is necessary to produce a spatio-temporally growing wave front, when the least stable mode is spatially damped.

There is an alternate possibility for the results shown in Table 4.1 and Figs. 4.3 and 4.4. The spatio-temporal front for the case B has wavelength of B2 in Table 4.1. However, a superposition of all the spatio-temporal fronts (in terms of wave length and propagation speed) show identical properties including that is shown for the spatially unstable point A in Fig. 4.3. This raises the possibility that the forerunner is a wave-packet centered around one of the unstable wave number corresponding to the fixed Reynolds number of $Re = 1000$ for all the three points A, B and D. However, this possibility needs to be further probed by looking at multi-modal solutions at other Reynolds numbers in fixing the propagation properties of the wave-packet defining the forerunner. There is a band of circular frequencies those are unstable for all $Re > Re_{cr}$. In Figs. 4.8 and 4.9, we have shown results for cases those are excited by band-limited excitation around a mean unstable frequencies that also helps in understanding the complex interactions of multiple modes for evolving wave fields. Also, we will append additional discussions at the end of this chapter to discuss the origin of spatio-temporal fronts.

There is now enough evidence to suggest that the growth of the forerunner is due to competing groups associated with multiple modes, reinforcing each other at the front. Such forerunners have been shown to exist in electrodynamics problems in Brillouin (1960). The propagation speed of signal has been variously described as the group velocity by Rayleigh, signal velocity by Sommerfeld and also the velocity of energy transfer by Brillouin. Furthermore, Brillouin (1960) has noted that the three definitions are identical for non-dissipative systems. The forerunner is very weak and difficult to trace for electromagnetic waves in stable systems, and it can attain high amplitudes only when the group velocity attains a minimum. In dissipative systems, these velocities can differ considerably and in fluid dynamical systems, both stable and unstable modes exist side by side. Group velocity (V_g) for the presented problem here is also given in Table 4.1, obtained from an eigenvalue analysis. From Figs. 4.3 and 4.4, one can directly estimate the signal speed (V_s) by tracking the crests and these information is also

given in Table 4.1. An estimate of energy propagation speed (V_e) can also be obtained from the equation for the disturbance energy given in Eqn. (3.5.2). If one represents (E_d), in terms of its Fourier-Laplace transform as: $E_d(x,y,t) = \frac{1}{(2\pi)^2}\int\int_{Br}\hat{E}_d(y,\alpha,\omega)e^{i(\alpha x-\omega t)}d\alpha\, d\omega$, then the governing equation for $\hat{E}_d$ is given by,

$$\hat{E}_d'' - \alpha^2\hat{E}_d = \phi'''U + 2\phi''U' + \phi'(U'' - \alpha^2 U) - 2\alpha^2\phi U'' \qquad (4.3.4)$$

Equation (4.3.4) was solved in Sengupta *et al.* (2006) as a function of α and ω and the solution was reconstructed as a function of x and t by performing Bromwich integrals successively. Results for E_d are shown as a function of x for the points A and B in Fig. 4.5.

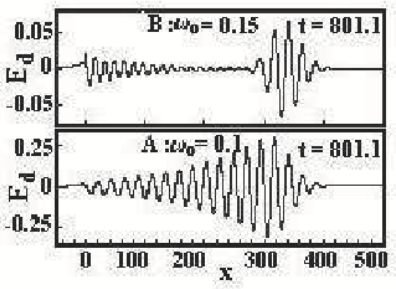

Figure 4.5 Disturbance energy E_d plotted as a function of x at indicated times for Re = 1000 at y = 0.278

Here, the plot shows the variation of E_d to be smoother than u. Once again, for the point A there is no detached forerunner from the asymptotic solution, while the point B displays the same detached forerunner as before. The rate at which E_d propagates can be estimated roughly from the figures. This is shown in Table 4.1 as V_e. We note that the system dynamics is determined by the least stable mode (A1) for the spatially unstable case, with all the three definitions of propagation speed producing identical results. In contrast, for stable systems with multiple modes, the forerunner has identical V_e and V_s which lies between the group velocity values of the leading two modes. Again, for the stable systems with a single mode, all the three definitions produce the same value. Thus, for all systems the signal speed and energy propagation speed are the same. This also shows the importance of the energy based receptivity theory developed in Chapter 3.

The appearance and propagation of a forerunner is not a transient phenomenon, and this was also further demonstrated by performing direct simulation of the 2D Navier-Stokes equation following the formulation and numerical method given in Sengupta *et al.* (2004a) for wall-excitation by simultaneous blowing and suction strip. The use of this type of excitation field for instability study was originally reported in Fasel & Konzelmann (1990). Results from the solution of Navier-Stokes equation are shown in Fig. 4.6 at $t = 150$ and 300 respectively, that clearly identify the forerunner. This verification additionally shows that the receptivity solutions obtained earlier by linearized analysis remains valid, when the shear layer is not considered parallel and growth of it is also included.

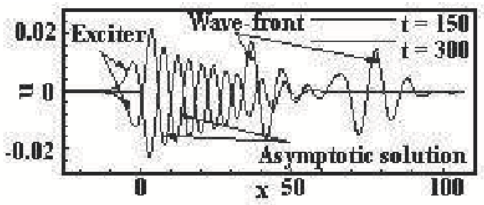

Figure 4.6 Direct numerical simulation of 2D Navier-Stokes equation for simultaneous blowing-suction excitation at the wall for Re = 1000 and $\omega_0 = 0.14$

Further properties of spatio-temporally growing wave-front were studied in Sengupta *et al.* (2006a). It was investigated by exciting the Blasius boundary layer at a frequency that corresponds to the point on branch II of the neutral curve at $\omega_0 = 0.1307$ for Re = 1000. Computed streamwise perturbation velocity at different time instants are shown in Fig. 4.7.

Here, the asymptotic solution is a neutrally stable solution in Fig. 4.7- as one would expect. However, one also notices a constantly growing wave-front ahead of the asymptotic solution. For this case also, there are three modes with the leading mode neutrally stable and the other two modes are highly stable, given by: $\alpha_1 = (0.3498239, 0.0)$; $\alpha_2 = (0.2149177, 0.1454643)$ and $\alpha_3 = (0.1604025, 0.2593028)$.

To emphasize the role of mode interactions, another case was considered in Sengupta *et al.* (2006a) where the Blasius boundary layer was excited by a wide-band excitation given by, $0.08 \leq \omega_0 \leq 0.12$. If the response field for an excitation at ω_0 is given by,

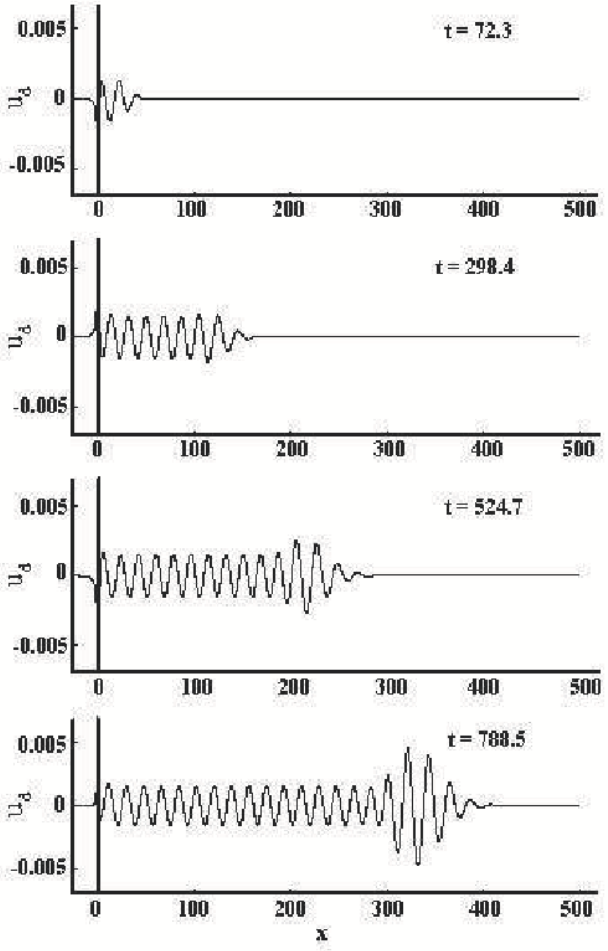

Figure 4.7 Streamwise disturbance velocity component plotted as a function of x at indicated times for Re = 1000 for $\omega_0 = 0.1307$ Results are shown for the non-dimensional height of y = 0.278

$$\psi(x,y,t;\omega_0) = \frac{1}{(2\pi)^2}\int\int_{Br} \frac{\phi_1(\alpha,y,\omega)\phi'_{30} - \phi'_{10}\phi_3(\alpha,y,\omega)}{i(\phi_{10}\phi'_{30} - \phi_{30}\phi'_{10})(\omega-\omega_0)}\, e^{i(\alpha x-\omega t)} d\alpha\, d\omega \tag{4.3.5}$$

Then the solution for the banded excitation case is obtained from the convolution of the above given by,

$$\psi(x, y, t, \omega_1, \omega_2) = \int_{\omega_1}^{\omega_2} \psi(x, y, t, \omega_0)\, d\omega_0 \tag{4.3.6}$$

Where ω_1 and ω_2 defines the bandwidth of the excitation. The chosen bandwidth was such that the fundamental mode remained unstable for all the frequencies. Thus, for the banded excitation each unstable mode will interact with other to create wave-packets. Presented results in Sengupta *et al.* (2006a) for the banded excitation case is reproduced in Fig. 4.8 for the indicated time instants.

From the figure one notices that up to some early times ($t = 110$), effects of the banded excitation is not perceptible, as the evanescent waves are dominated by the local solution. However at later times, this is not the case (seen at $t = 185.4$) as one can see the presence of multiple frequencies behind the leading wave-front. There appears to be significant cancellations among different unstable waves at the back of the wave-front. As a result of such cancellations, one notices attenuated multiple packets traveling downstream, except the leading wave-front that continues to grow. This is an example of multiple unstable waves annihilating each other (including the local solution), while leaving the growing wave-front.

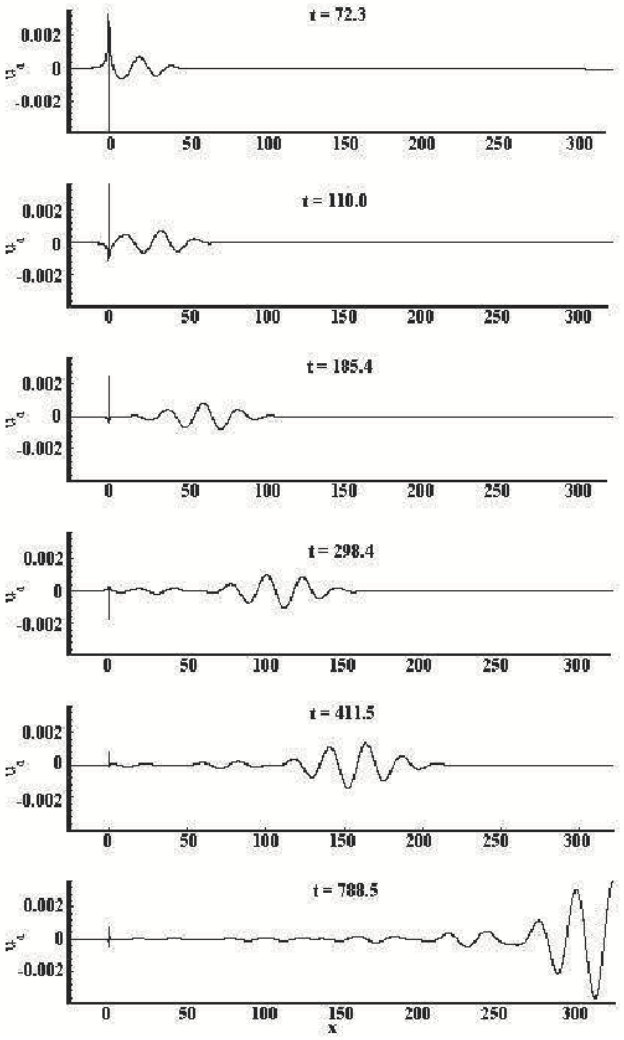

Figure 4.8 Streamwise disturbance velocity plotted as a function of x at indicated times for banded excitation centered around $\omega_0 = 0.1, \triangle\omega = \pm 0.02$ for Re = 1000 and y = 0.278

The feature of signal cancellation for unstable wave systems can be better understood, if one looks at some representative harmonic components

of the response field. In Fig. 4.9(a), the streamwise disturbance velocity component of various circular frequencies as a function of space is shown for $t = 411.5$.

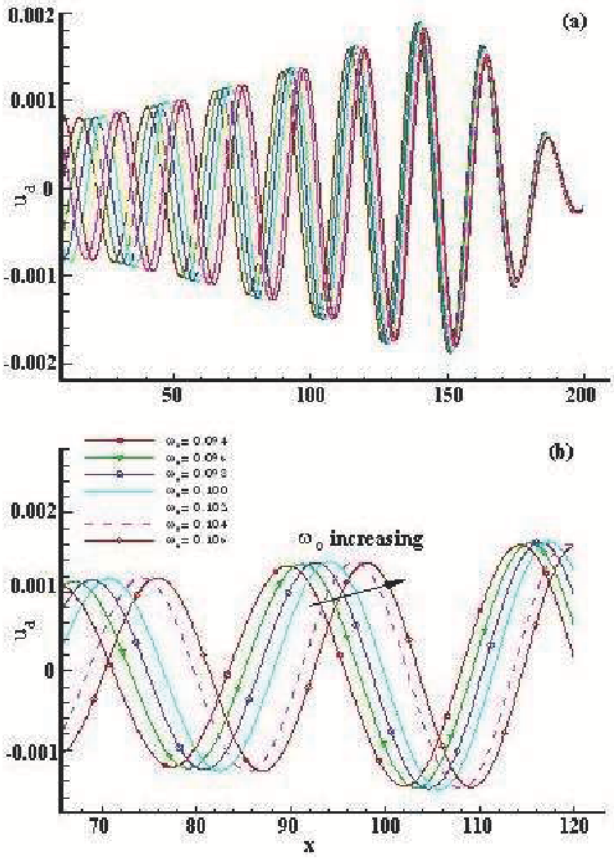

Figure 4.9 (a) Streamwise disturbance velocity plotted as a function of x at t = 411.5 for different ω_0 with Re = 1000 and results shown at y = 0.278. (b) Enlarged view of (a) for selected frequencies.

Here, only seven distinct circular frequency solutions are shown for ease of explanation. Significant phase shifts among these solutions for $x \leq 120$ are responsible for mutual cancellations within the signal. The zoomed part

shown in Fig. 4.9(b) show more phase shift among the displayed components at the left of the frame, resulting in cancellation of these components in antiphase. In contrast, there is lesser phase shift among the signal components seen in the left of the frame in Fig. 4.9(a). This will lead to reinforcing of the components in this part of the domain.

Further understanding of the role played by different stable modes, when significant transient growth is present, was studied in Sengupta & Rao (2006). Two specific cases of $\omega_0 = 0.05$ and 0.15 considered in Table 4.1, are compared. The complex wave numbers are re-listed again in Table 4.2.

Table 4.2: The wave properties of the indicated circular frequency disturbances.

ω_0	α_r	α_i
0.05 (D)	1)0.0621413	0.0696594
	2)0.1607670	0.0015206
0.15 (B)	3)0.1894256	0.3226357
	4)0.27228701	0.1675585
	5)0.3940036	0.0104936

For these excitation parameters, existing spatial modes are all damped: One set corresponding to the lower frequency (identified as 1 and 2 in Table 4.2) are below the neutral curve and the other set (B) corresponding to the higher frequency (identified as 3, 4 and 5 in the table) are above the neutral curve. In Fig. 4.10, the computed disturbance velocity in streamwise direction, obtained by Bromwich contour integral method is shown for the case of B ($\omega_0 = 0.15$).

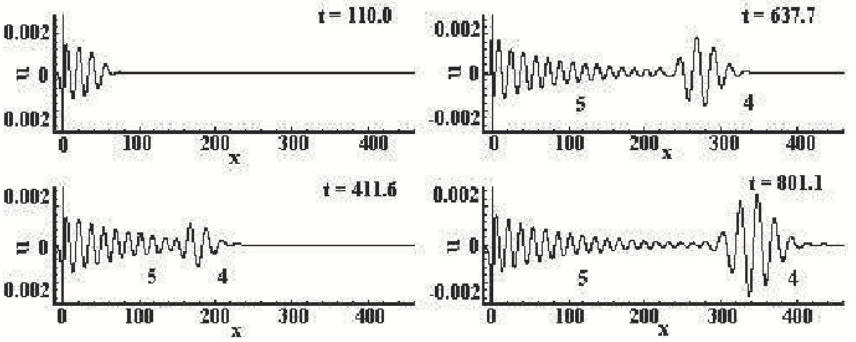

Figure 4.10 Streamwise disturbance velocity plotted as a function of x at different times for Re = 1000, $\omega_0 = 0.15$ with results shown for $y = 0.278$.

The solutions at the indicated time instants show: (i) the near-field given by the local solution and the far field consisting of (ii) a decaying wave and (iii) a spatio-temporally growing wave-front. The Fourier-Laplace transform of the solution at $t = 801.1$ is shown in Fig. 4.11 with vertical lines indicating the location of the three modes. This result indicate that the displayed decaying wave corresponds to Mode 5 and the growing wave-front is centered around Mode 4 of Table 4.2. Effects of Mode 3 is not visible due to its extremely large damping rate.

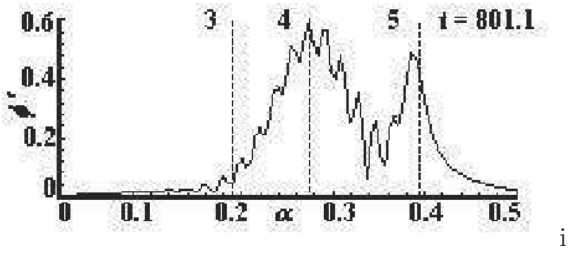

Figure 4.11 Fourier transform (FFT) of streamwise velocity data of Fig. 7.10, shown as a function of wave-number for the point B.

In Fig. 4.12, the computed disturbance velocity in streamwise direction, obtained by Bromwich contour integral method is shown for the case of the

point D ($\omega_0 = 0.05$). The results at the indicated time instants show similar structures of near- and far-field of the disturbance- as was the case for point B.

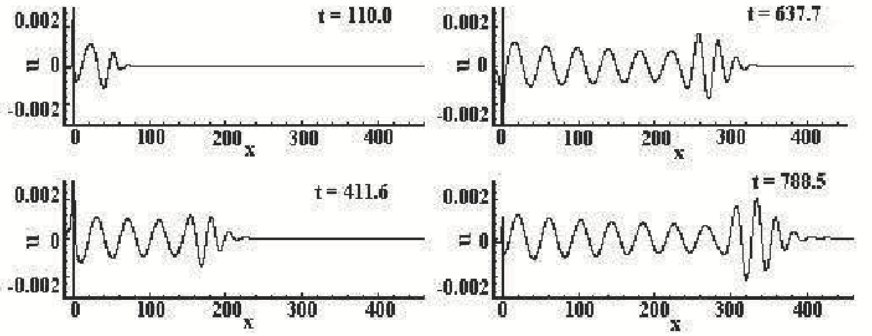

Figure 4.12 Streamwise disturbance velocity plotted as a function of x at different times for ($\omega_0 = 0.05$), Re = 1000 and results shown for y = 0.278

In Fig. 4.13, the Fourier-Laplace transform of the solution at $t = 788.5$ is shown. In this case, the asymptotic decaying signal corresponds to Mode 2, while the effect of Mode 1 is not visible here, due to its high decay rate. The growing wave-front corresponds to the packet to the right of Mode 2.

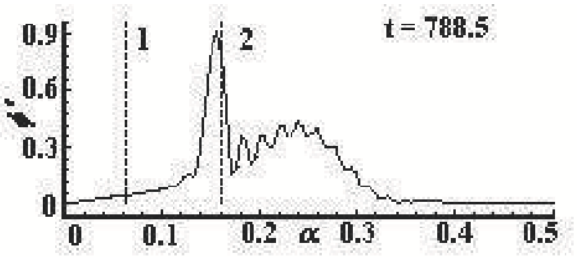

Figure 4.13 Fourier transform (FFT) of data shown in Fig. 4.11, shown as function of wave number for the point D.

In summarizing the discussion on the spatio-temporal growth shown here to occur for viscous flows, we note that this is in sharp contrast to what has been written either about algebraic growth by Landahl (1975) and Zuccher *et al.* (2006) or the non-normal modes discussed in Trefethen *et al.* (1993) and Schmid (2000)- for more than one reasons. All these works are premised on the basis of inadequacy of Orr-Sommerfeld equation and are valid for three-dimensional disturbance field only. In Sengupta *et al.* (2006, 2006a) and Sengupta & Rao (2006), the spatio-temporal growth is due to the mutual interaction of multiple modes and is equally valid for both two- and three-dimensional flows. The only commonality of these two approaches lie in noting fact that such growth is obtained for systems exhibiting spatial stability. Also, we note the spatio-temporal growth recorded here are not transient in nature, while most of the other work report about transient energy growth.

There is also the distinction between the two approaches in the way the mechanism occurs. As stated in Breuer & Kuraishi (1993), firstly, the transient energy growth can occur for sub-critical systems by two to three orders of magnitude at which *nonlinear effects might push the disturbance into turbulence*. Secondly, in super critical flows transient growth can boost existing TS waves with the initial algebraic growth followed by the exponential growth of TS waves. Neither of these two mechanisms for transient growth has been demonstrated experimentally yet. In contrast, the spatio-temporal growth shown in Sengupta *et al.* (2006, 2006a) and Sengupta & Rao (2006) are similar to what is seen in ocean surface due to localized disturbances in the sea-bed. Although the governing equations and flow topology of the equilibrium flow may not bear exact resemblance.

Chapter 5

LANDAU EQUATION AND MULTIPLE HOPF-BIFURCATION

Prof. Tapan K. Sengupta
HPCL, Aerospace Engineering
I.I.T. Kanpur

5.1 Landau's Equation and Its Application for Flow Past a Cylinder

The linear theory of stability of a steady basic flow generally gives a spectrum of independent modes with velocity perturbation of the form,

$$u'(\vec{X},t) = \sum_{j=1}^{\infty} A_j(t) f_j(\vec{X}) + A_j^*(t) f_j^*(\vec{X}) \tag{5.1.1}$$

where the quantities with asterisks denote complex conjugate. In the linear stability theory, we generally focus upon one mode at a time- the so-called normal mode analysis. If the complex amplitude of any one of the mode that grows with time is given by,

$$A_j(t) = Const.e^{s_j t} \tag{5.1.2}$$

then it is easy to see that the evolution equation for the amplitude of this mode is given by,

$$\frac{dA_j}{dt} = s_j A_j \tag{5.1.3}$$

In the linear theory, the natural choice of f_j in (5.1.1) is the set of eigenfunctions. If one relaxes the linearity approximation and use Galerkin method, then the complex amplitude equation can be written as,

$$\frac{dA_j}{dt} = s_j A_j + N_j(A_k) \tag{5.1.4}$$

where $N_j(A_k)$ provides the nonlinear action of all other modes on the j^{th} mode- including the self-interaction. In extending the linear theory, Landau suggested that

$$N_j(A_k) = A_j|A_k|^2 \tag{5.1.5}$$

If there is only a single dominant mode, then the nonlinear action will be restricted to self-interaction only. In such a case, the above equation can be written down as

$$\frac{dA}{dt} = sA - \frac{l}{2}A|A|^2 \tag{5.1.6}$$

where $s = \sigma_r + i\omega$ and $l = l_r + il_i$. Substitution of these and some algebraic manipulation gives for the real part of the equation as,

$$\frac{d|A|^2}{dt} = 2\sigma_r|A|^2 - l_r|A|^4 \tag{5.1.7}$$

where $A = |A|e^{i\theta}$ and the imaginary part of the Landau equation is given by

$$\frac{d\theta}{dt} = \omega - \frac{l_i}{2}|A|^2 \tag{5.1.8}$$

For different systems, we have different signs of the real and imaginary part of Landau coefficient l. Here, we will keep our attention focused to flow past a circular cylinder, that works as a prototypical model for bluff-body flow instability. This instability begins as a linear temporal instability and its first appearance with respect to the Reynolds number is referred to as Hopf bifurcation. Thus, the Reynolds number at which the first bifurcation occurs is given by Re_{cr}. Thus, above Re_{cr} : the value of $\sigma_r > 0$ signifies linear instability. One of the most important aspect of this linear instability is the subsequent non-linear saturation that can be adequately explained by the Landau's equation, if only l_r is positive. We will focus upon this type of flow only in the next.

We also note from Eqn. (5.1.7) that an equilibrium amplitude is achieved after the nonlinear saturation and this is given by,

$$|A_{eq}| = \sqrt{2\sigma_r/l_r} \tag{5.1.9}$$

Similarly, one can also obtain the equilibrium Strouhal number after the nonlinear saturation from Eqn. (5.1.8). In the following, we discuss specifically about the flow past a circular cylinder.

5.2 Instability of Flow Past a Cylinder

Vortex shedding behind a circular cylinder is explained theoretically as a Hopf bifurcation which is a consequence of linear temporal instability of the flow. In this point of view, the above temporal instability is moderated by nonlinearity of the system, that is quite adequately explained by Landau equation, as given in Landau (1944) and Drazin & Reid (1981). Earlier numerical investigations by Zebib (1987), Jackson (1987) and Morzynski & Thiele (1993) have identified the onset of vortex shedding to be at a critical Reynolds number (Re_{cr}) between 45 and 46.

However, different values of critical Reynolds number Re_{cr} for flow past a circular cylinder reported by various investigators show lack of unanimity in defining an universal number. For example, Batchelor (1988) conjectured it to be between 30 and 40; Landau & Lifshitz (1959) quoted it as 34. Experimentally, different investigations obtained different Re_{cr}: Kovasznay (1949) obtained it as 40; Strykowski & Sreenivasan (1990) found it to be between 45 and 46; Roshko (1954) reported a value of 50; Kiya *et al.* (1982) have reported it to be 52; Tordella & Cancelli (1991) have reported it as 53 and Homann (1936) has reported it to be 65.2, a maximum value so far.

Theoretically, flow criticality is related to the onset of global linear instability, performed numerically by Jackson (1987), Zebib (1987), Morzynski & Thiele (1993), who all have reported : $45 < Re_{cr} < 46$. For steady flows, we will identify this critical Reynolds number as Re_{cr_1}, for the ease of future discussion. Similarly, we will identify the critical Reynolds number value indicated in Homann's experiment as Re_{cr_2}. Hopf bifurcation describes the passage of a dynamical system from a steady state to a periodic state as a typical bifurcation parameter is varied, that in this case is the Reynolds number (Golubitsky & Schaefer (1984)). The results of the numerical investigations mentioned above, relate to study of the flow system unimpeded by noise or perturbations- barring numerical errors.

For flow instability problems, dispersion error is a major source of numerical error that can significantly alter the flow dynamics. Even spurious dispersion can lead to wrong spatio-temporal dynamics. This source of error has been overlooked so far, except in Sengupta, Ganeriwal & De (2003) and Sengupta, Sircar & Dipankar (2006). The importance of preserving physical dispersion of a system in a numerical sense is appreciated, while investigating flow control problems. Vortex shedding for the flow past a cylinder was controlled in Strykowski & Sreenivasan (1990) for $Re \leq 120$ and for this nominal two dimensional flow, only computational results are given in Strykowski & Sreenivasan (1990) and Dipankar, Sengupta & Talla (2007). In Strykowski & Sreenivasan (1990) an accurate Galerkin method was used for an approximate geometry while the exact problem was solved

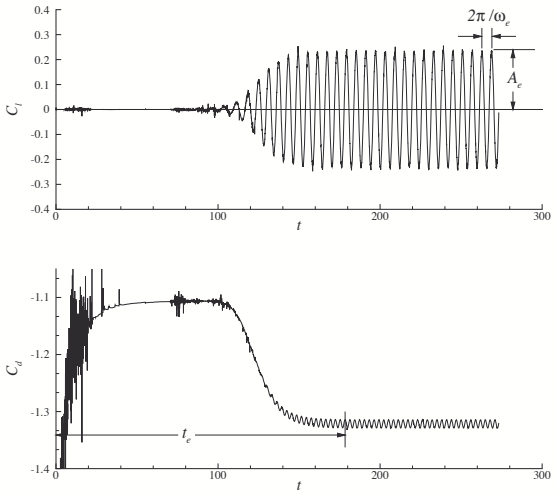

Figure 5.1 Schematic showing the time history of lift and drags coefficients for flow past a circular cylinder at Re = 100.

in Dipankar, Sengupta & Talla (2007) by a very accurate dispersion relation preservation (DRP) method, the same being used here. This has clearly demonstrated the need to use DRP methods in studying instability problems. Flow past a circular cylinder is a typical example that also displays nonlinear saturation of such instabilities.

5.3 Nonlinear Instability and Amplitude Equation

Terminology used here is as given in Fig. 5.1, showing the variation of computed lift coefficient C_l, with time for an impulsive start of the flow past a cylinder. It is noted that the amplitude of the lift variation always attains the same value (not shown here) and the corresponding time period is given by $T = 2\pi/\omega_e$, irrespective of the method used for the computation, provided the same grid is used for these calculations.

Below Re_{cr1}, the real part σ_r is negative i.e. the small disturbances damp, while above Re_{cr1} the flow becomes temporally unstable in the linear sense that would amplify the velocity and vorticity field, that can be traced from the lift variation itself. Presence of the nonlinear term does not allow uninhibited growth of such disturbances. Passage of σ_r from negative to

positive value across Re_{cr1} heralds a qualitative change of the equilibrium flow and this transition is referred to as the Hopf bifurcation.

Landau did not address the issue of phase angle (see Landau (1944)), it was later derived by treating the landau coefficient l, as a complex quantity-as given in the last section. Despite the nonlinearity of Eqn. (5.1.7), it is readily integrable to provide

$$|A|^2 = \frac{A_0^2}{(A_0/A_e)^2 + [1 - (\frac{A_0}{A_e})^2]e^{-2\sigma_r t}} \tag{5.3.1}$$

where A_0 is the value of A at t=0 and A_e as defined before. Approach of A to A_e with $t \to \infty$ indicates the independence of A_e on A_0, as also noted by the independence of computational methods.

While lots of attention have been paid on the real part of Landau's equation, the imaginary part has not been analyzed in great detail. As A approaches its asymptotic value A_e, the circular frequency $(\frac{d\theta}{dt})$ also reaches its asymptotic value, ω_e. Thus, the Strouhal number is found to be amplitude dependent and is given by,

$$\omega_e = \omega - \sigma_r \frac{l_i}{l_r} \tag{5.3.2}$$

Instead of using this equation, in the literature, there are few models proposed by which the frequency or Strouhal number of the shedding is fixed. Koch (1985) proposed a resonance model that fixes it for a particular location in the wake by a local linear stability analysis. Upstream of this location, flow is absolutely unstable and downstream, the flow displays convective instability. Nishioka & Sato (1973) proposed that the frequency selection is based on maximum spatial growth rate in the wake. The vortex shedding phenomenon starts via a linear instability and the limit cycle-like oscillations result from nonlinear super critical stability of the flow, describable by Eqn. (5.3.1).

The discussion following Eqn. (5.1.8) imply a single Hopf bifurcation when Reynolds number increases beyond Re_{cr}. It is interesting to note that Landau (1944) talked about further instabilities following the nonlinear saturation of the primary instability mode. This is akin to Floquet analysis of the resulting time periodic system (Bender & Orszag (1978)). The possibility of multiple bifurcation was also mentioned in Drazin & Reid (1981) who stated that *in more complete models of hydrodynamic stability we shall see that there may be further bifurcations from the solution* $|A| = 0$*, e.g. where the next least stable mode of the basic flow becomes unstable, and from the solution* $|A| = A_e$. To the knowledge of the present authors, no theoretical analysis exist that showed multiple bifurcation before for this flow. Here,

this is shown using the numerical simulation results following the method of Dipankar, Sengupta & Talla (2007).

5.4 Numerical Simulation of Flow Past a Circular Cylinder

In the numerical simulation, two dimensional Navier-Stokes equation in stream function- vorticity formulation is solved. While solving the vorticity transport equation, the non- linear convection terms are discretized using high accuracy DRP method of Sengupta, Ganeriwal & De (2003) and Sengupta, Sircar & Dipankar (2006) that provides near-spectral accuracy in the azimuthal periodic direction. A similar accuracy is attained at all interior points in the radial direction, except at the boundary points. Because of these, a (150×400) grid has been used in all the calculations reported here with 150 points in the azimuthal direction. The loads have been calculated by solving the Poisson equation for total pressure. Lift, drag and out of plane moment have been obtained from these results. From the detailed time variation of the drag history, as shown in Fig. 5.1, we estimated the non- dimensional time t_e, at which asymptotic value of C_d is reached and plotted its variation with Reynolds number in Fig. 5.2.

It is readily evident that this time t_e, reduces rapidly as the Reynolds number increases beyond Re_{cr2}. Also as one approaches Re_{cr1} from above, t_e increases in almost an unbounded manner. We emphasize that the periodic variation of lift was obtained without any artificial excitation, as has been done in many previous investigations. This figure qualitatively displays the fact that the instability and its supercritical saturation changes when the Reynolds number transits through Re_{cr2}.

To understand better the qualitative and quantitative changes as the flow transits through Re_{cr1} and Re_{cr2}, in Fig. 5.3, we have plotted the computed asymptotic amplitude A_e, for different Reynolds numbers, shown by discrete symbols. In Drazin & Reid (1981), σ_r is approximated to $k(Re - Re_{cr1})$ and thus Eqn. (5.1.9) becomes,

$$A_e \sim \{2k(Re - Re_{cr1})/l_r\}^{1/2} \tag{5.4.1}$$

Here, A_e varies qualitatively as, $\epsilon^{1/2}$, where $\epsilon = Re - Re_{cr}$. We have drawn three continuous lines (to represent different segments of Fig. 5.3) that can be parametrically represented as

$$Ae = [k_1\epsilon + k_2\epsilon^2 + k_3\epsilon^3 + k_4\epsilon^4]^{1/2} \tag{5.4.2}$$

The solution as given by Eqn. (5.4.1), contains only the first term of Eqn. (5.4.2). Also note that in describing this variation, the Re_{cr} used

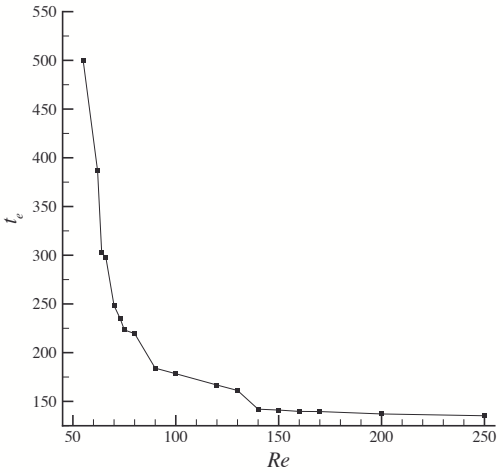

Figure 5.2 Non dimensional time at amplitude saturation vs Reynolds number.

in ϵ corresponds to three different values indicated in the last column of Table-5.1 and marked in Fig. 5.3.

Table 5.1: Coefficients used in the saturation amplitude equation (Eq.(5.4.2))

Rey No. range	$k_1 \times 10^4$	$k_2 \times 10^6$	$k_3 \times 10^8$	$k_4 \times 10^9$	Re_{cr}
51.934 to 80	7.69	92.6	−674	136	51.934
80 to 133	24.4	−51.0	105	−7.2	63.868
133 to 250	25.7	−9.58	7.6	−0.21	84.6154

In turn, these three critical Reynolds number values along with the $k_i s$ (shown in Eqn. (5.4.2)) have been obtained by using direct simulation data in Eqn. (5.4.2) for different Reynolds numbers, in the appropriate range. It is noted that the $k_i s$ have values in the same range for these three Reynolds number intervals, except k_1. In the second interval, k_1 increases roughly by a factor of 18 and is compatible with Fig. 5.3. As the previous linear stability results from Jackson (1987), Zebib (1987) and Morzynski & Thiele

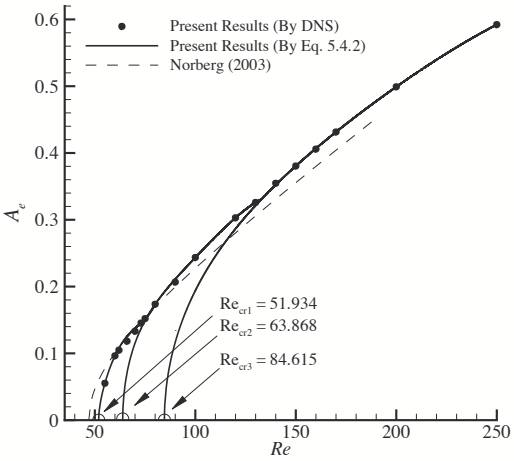

Figure 5.3 Variation of Saturation amplitude of lift coefficient with Reynolds number.

(1993) indicate a smooth variation of σ_r across Re_{cr1} as well as Re_{cr2}, it is therefore correct to state that the discontinuous changes observed in the amplitude curve are due to rapid changes associated with decreasing value of the Landau coefficient. Thus, the qualitative change across critical Reynolds numbers may be attributed due to change in the non-linear property of the fluid dynamical system. It is also noted that k_2, k_3 and k_4 are orders of magnitude different from k_1 and are unimportant near respective Re_{cr} and only helps in explaining smooth transition from one interval of Reynolds number to the other.

It is noted that k_4 is comparatively dominant in the first interval, while k_3 reduces by nearly two decimal places from the first to third interval. As these extra terms are needed near the overlap region of the intervals, their presence indicate an interaction of the higher order modes of the system, before transiting to the next interval. Fig. 5.3 indicates that the first Hopf bifurcation occurs at $Re_{cr1} = 51.934$. Difference between this value and the other values given by Jackson (1987), Zebib (1987) and Morzynski & Thiele (1993) is essentially due to different error sources of different methods accumulating to trigger vortex shedding in the wake. An accurate method

that is less affected by the dispersion and numerical dissipation will indicate a higher Re_{cr1}, without significant difference. However, if the error in computation or disturbance in an experiment can be damped, as in the experiments of Homann (1936), then the first criticality can be completely bypassed. The high viscosity of the working fluid in the experiment works like a source of dissipation in the wake (as shown in Strykowski & Sreenivasan (1990) experimentally and in Dipankar, Sengupta & Talla (2007) computationally) by a small control cylinder.

It is also possible that one can re-interpret the Landau equation and write its amplitude variation by,

$$\frac{d}{dt}|A|^2 = 2\sigma_r|A|^2 - l'_r|A|^4 \tag{5.4.3}$$

Where,

$$l'_r = \frac{l_r}{1 + \frac{k_2}{k_1}\epsilon + \frac{k_3}{k_1}\epsilon^2 + \frac{k_4}{k_1}\epsilon^3} \tag{5.4.4}$$

In Eqn. (5.4.4), the Landau coefficient l'_r is truly a constant independent of Re; its dependence on Reynolds number comes from the factor in the denominator through σ. Once again, one would need different values of $k_i s$ for different Reynolds number ranges- as given in Table 5.1.

In Fig. 5.3, computed A_e is also compared with the correlation proposed by Norberg (2003)- based on his experimental results. For his experimental facility, $Re_{cr1} = 47$ and in the range $47 \leq Re \leq 190$ asymptotic amplitude variation (r.m.s.) with Re is given by, $A_e = (\frac{\epsilon}{30} + \frac{\epsilon^2}{90})^{1/2}$. Whereas, in the range $165 \leq Re \leq 230$ this is simply replaced by, $A_e = 0.43$. The main trends appear to be similar with discontinuities indicated in the range $165 \leq Re \leq 190$ in Norberg's correlation, due to change from parallel to oblique shedding in the wake (see Williamson (1989)).

Some investigators have studied the effects of noise on pitchfork and Hopf bifurcation and reported finding changed critical parameters. For example, Juel, Darbyshire & Mullin (1997) reported only 0.2% change in the parameter value towards sub-criticality when measured with respect to Landau model. This is indeed a very small change as compared to experimental value of critical parameter that is more than 50% for the flow past a cylinder. The estimates in Juel, Darbyshire & Mullin (1997) are with respect to white noise, that is hardly typical of experimental facilities. Interestingly, Wiesenfeld & McNamara (1986) have reported that near the onset of dynamic instability, any time-periodic system can act to amplify small periodic perturbations, whose details depend solely on the type of bifurcation involved. In a tunnel, presence of such periodic perturbations can not be

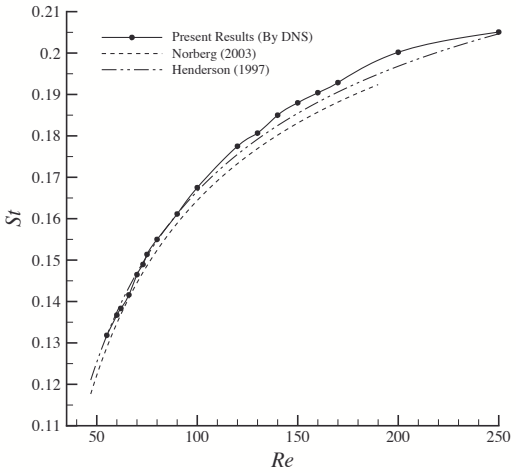

Figure 5.4 Variation of Strouhal number with Reynolds number.

ruled out and that can explain a whole range of Re_{cr} reported experimentally. Based on this discussion, one can conjecture that the appearance of Re_{cr1} and Re_{cr2} are due to the presence of such small periodic perturbations. In Homann's experiment the viscous dissipation of the working fluid could delay vortex shedding, while in Strykowski & Sreenivasan (1990), presence of small control cylinder acted as a source of dissipation that helped in suppression of shedding to higher Reynolds number. Present investigation was restricted up to $Re \simeq 250$, as beyond which flow can not be represented by two dimensional simulation (see Henderson (1997)). Thus, the existence of any other critical Reynolds number beyond Re_{cr3} is of lesser interest.

In Fig. 5.4, the computed Strouhal number is shown plotted against Reynolds number by discrete symbol and solid line. In the same figure, the dotted curve shows the correlation proposed by Norberg (2003) based on experimental data from his facility. The empirical correlations are given by, $St = 0.2663 - \frac{1.019}{\sqrt{Re}}$ for $47 \leq Re \leq 190$ and $St = -0.089 + \frac{22.9}{Re} + 7.8 \times 10^{-4} \times Re$ for $165 \leq Re \leq 260$. Thus, it is very apparent that in the experimental facility of Norberg (2003), the Strouhal number variation is discontinuous or non-unique in the range $165 \leq Re \leq 190$. This is due to the difference between parallel and oblique shedding in the wake, that has also

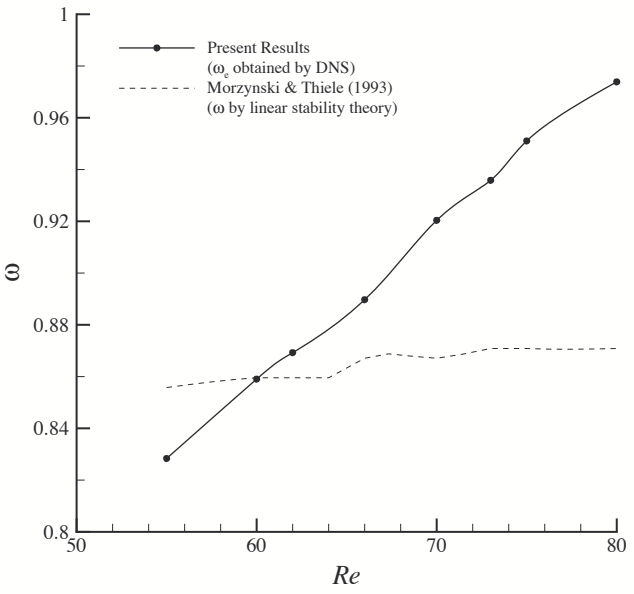

Figure 5.5 Circular frequency of linear instability and its nonlinear supercritical saturation plotted as a function of Reynolds number.

been addressed in Hamache & Gharib (1991) and Williamson (1989). Our calculated Strouhal number displays a distinct slope discontinuity around $Re \simeq 60$, and is consistent with Eq. (4.3.2) that shows the nonlinear effect of the Strouhal number through its dependence on amplitude. It is interesting to note that Tordella & Cancelli (1991) have reported a Strouhal number discontinuity at around $Re \simeq 90$, that was also reported by Tritton (1970).

The nonlinear effects on vortex shedding is also demonstrated in Fig. 5.5, where the present computed Strouhal number is compared with linear global stability results of Morzynski & Thiele (1993). Having obtained ω_e by direct simulation, one can estimate the imaginary part of the Landau coefficient by using Eq. (5.3.2) employing the linear stability results of Morzynski & Thiele (1993). These results for the variation of l_i with Re is shown in Fig. 5.6, in the limited range of Reynolds numbers, for which

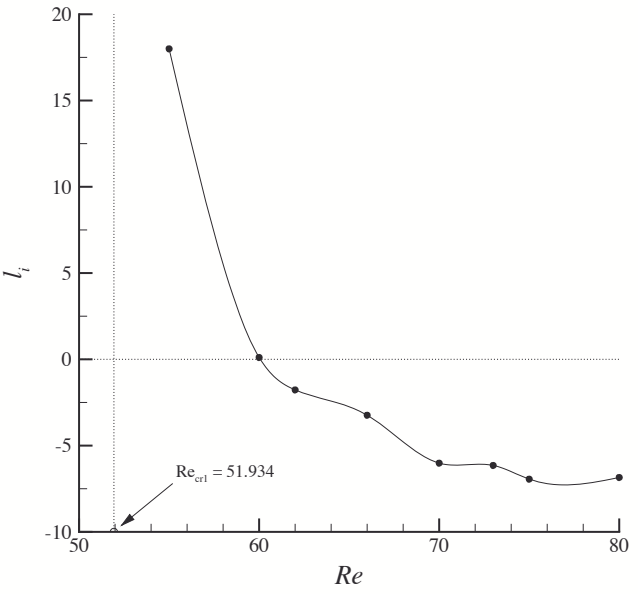

Figure 5.6 Variation of Imaginary part of Landau coefficient with Reynolds number.

linear stability results are available. In following this, we are assuming that the global linear stability analysis would produce identical numbers for σ_r and ω for different methods, domains and grids. However, the qualitative trends for the variation of l_i with Re will essentially be same. In this figure, Re_{cr1} is marked for reference, at which l_i should be infinitely large. It is also noted that for most of the Reynolds number range, $l_i \neq 0$, implying the phase to be always dependent upon the amplitude, as indicated by Eqn. (5.3.2).

Landau's amplitude and phase evolution equations, as obtained by treating Landau's constant as a complex quantity, have been used for the analysis of the direct simulation. These equations are re-interpreted here and modifications proposed in the light of multiple bifurcations. Also, the amplitude and the phase variation with Reynolds numbers obtained by numerical simulation are compared with the correlations proposed by Norberg (2003) based

on his experimental data. Results of linear stability theory by Morzynski & Thiele (1993) are used in obtaining the variation of imaginary part of Landau coefficient. A discontinuity found experimentally at low Reynolds number in the St - Re curve by some investigators can also be explained as the amplitude-dependent behaviour of the phase; while, the discontinuity reported at higher Reynolds number, are due to change of mode of shedding from parallel to oblique mode.

Chapter 6

STABILITY OF MIXED CONVECTION BOUNDARY LAYER

Prof. Tapan K. Sengupta
HPCL, Aerospace Engineering
I.I.T. Kanpur

6.1 Introduction

The spatial stability properties of a mixed convection boundary layer developing over a heated horizontal plate is studied here under linear and quasi-parallel flow assumption. The main aim of the present work is to find out if there is a critical buoyancy parameter that would indicate the importance of heat transfer in destabilizing mixed convection boundary layers, when the buoyancy effect is given by Boussinesq approximation. The undisturbed flow used here is that given by the similarity solution of Schneider (1979), that imply the wall temperature to vary as the inverse square root of the distance from the leading edge of the plate. The stability of this flow has been investigated by using the compound matrix method (CMM)- that allows finding all the modes in the chosen range in the complex wave number plane for spatial stability analysis. Presented neutral curves for mixed convection boundary layer show the existence of two types of disturbances present simultaneously, for large buoyancy parameter. One notices very unstable high frequency mode when the buoyancy parameter exceeds the above mentioned critical value. This unstable thermal mode is in addition to the hydrodynamic mode of isothermal flow given by corresponding similarity profile.

Mixed convection flows are important as they are found in many practical situations- in nature and man-made devices. For problems of the continuum they are as relevant for atmospheric dynamics at planetary scale to that for electronic devices at micro-scale. Mixed convection differs from isothermal flow due to the induced buoyancy effects via heat transfer. It

has been noted by Brewster & Gebhart (1991) that in natural convection and in mixed regime, the instability is due to growth of small disturbances. For natural convection this is a narrow-band phenomenon while for forced convection boundary layers the unstable frequency-band is wider. Buoyancy forces- even when they are small- can not be neglected when the convection velocities are small or the temperature difference between the surface and the ambient is large. A comprehensive review of the heat transfer aspect of mixed convection can be found in Gebhart *et al.* (1988). For some flows the induced body forces are either parallel or anti-parallel to the mean convection direction- as in the case of mixed convection flow past vertical plates.

However, the flow and heat transfer properties are more complicated when mixed convection flows are considered past inclined or horizontal plates. This is due to the fact that the buoyancy forces induce a longitudinal pressure gradient that will directly alter flow and heat transfer rates. This is readily evident by looking at Eqns. (6.2.2) and (6.2.3) describing the mean flow. Additionally, such imposed pressure gradient also alters the instability pattern. For example, Eckert & Soehngen (1951) (as reported in Brewster & Gebhart (1991)) have shown using visualization that transition to turbulence for natural convection problem follows the instability of small disturbances. For natural convection past inclined flat plates, Sparrow & Husar (1969) have reported generation of an array of longitudinal vortices. Lloyd & Sparrow (1970), Zuercher *et al.* (1998) have experimentally investigated instability of flow past inclined plate and reported presence of two modes depending on the inclination angle of the plate. When the inclination angle with respect to the vertical is less than 14^o then the authors reported wave-like instability. Such wavelike instability has also been studied in Chen & Moutsoglu (1979). For inclination angles greater than 17^o- for the natural convection problem- it is noted experimentally that the disturbance field is dominated by vortices and is often termed as vortex instability. This vortex mode of instability is present for both the horizontal and inclined plates. This has been variously studied in Haaland & Sparrow (1973), Wu & Cheng (1976), Shaukatullah & Gebhart (1978), Gilpin *et al.* (1978), Moutsoglu *et al.* (1981) and Wang (1982) among many other such studies. In an alternate view-point Hall & Morris (1992) classify instability of forced-convection boundary layers over horizontal heated plates in terms of the two prototypical instabilities: Rayleigh-Benard type that is usually described for closed convection system heated from below and Tollmien -Schlichting type that is typical of isothermal open flows- as in wall bounded shear layers triggered by viscous instability. Hall & Morris (1992) in their theoretical analysis report the simultaneous presence of both the modes that coalesce in the

small wave number limit.

As the instability in mixed convection flows start off as growing small disturbances, linear stability is often used to analyze such flows. The analysis has been traditionally performed using temporal theory, as in Mucoglu & Chen (1978) for mixed convection flow along an isothermal vertical flat plate. The effect of buoyancy was studied by the temporal theory of a flow perturbed by small buoyancy induced body force. The primary mean flow was obtained by local non-similarity method and they reported for assisting flows the buoyancy force to stabilize the flow. One should, however, note the critique of various non-similar flow descriptions used in instability studies given in Brewster & Gebhart (1991). For an inclined plate the earliest instability study was by Chen & Moutsoglu (1979) and for horizontal isothermal plate by Chen & Mucoglu (1979). The results of these studies indicated that the flow along vertical and inclined plates are more stable when the buoyancy force aids external convection and stability decreased as the inclination angle approached towards the horizontal. It was also noted for horizontal plates the flow to become more unstable when the buoyancy force is directed away from the surface.

However, the experimental studies relate to spatial growth of disturbances as the flow system is always excited by fixed frequency sources. Hence a spatial theory is preferred to study the stability of non-isothermal flows. Despite the distinction between temporal and spatial methods, the neutral curve, however, is identical. Iyer & Kelly (1974) reported results using linear spatial theory under parallel flow approximation for free-convection flow past heated, inclined plates. Tumin (2003) also reports the spatial stability of natural convection flow on inclined plates providing the eigen spectrum.

Here, we will investigate the stability property of mixed convection flow past a heated horizontal plate, to provide the threshold buoyancy parameter that alters the instability property qualitatively. Such a problem is of importance for many engineering applications and in geophysical fluid dynamics. We also note that Steinrück (1994) has shown, for mixed convection over a horizontal plate that is cooled to exhibit non-uniqueness and numerical instabilities for the corresponding boundary layer equation, that would not affect the analysis when the plate is heated.

When Boussinesq approximation is adopted in full conservation equations, it is noted that the effect of buoyancy force appears in terms of Gr/Re^2, where Gr is the Grashof number and Re is the Reynolds number defined in terms of appropriate length, velocity and temperature scales. However, Leal *et al.* (1973) and Sparrow & Minkowycz (1962) have shown that the equivalent buoyancy parameter with the boundary layer assump-

tion changes to $K = Gr/Re^{5/2}$. Experimental investigations by Wang (1982) and Gilpin *et al.* (1978) have also demonstrated that the onset of instability always occurs at the same value of K- underlying the importance of it as the relevant buoyancy parameter. We note that the similarity profile derived by Schneider (1979) is given in terms of the same buoyancy parameter. In defining the mean flow past a horizontal flat plate we use the same in the present study. It will be one of the main aim here to identify a critical value of K beyond which the transport property changes qualitatively for a mixed convection flow past horizontal plate. It is noted by Chen, Sparrow & Mucoglu (1977) that with respect to heat transfer results, significant buoyancy effects are encountered for $K_x \geq 0.05$ and $K_x \leq -0.03$ for aiding and opposing flow past horizontal plate, where $K_x = Gr_x/Re_x^{5/2}$. In studying the stability properties of flow over a heated horizontal plate, present work is kept within this limit given by Chen *et al.* (1977).

As compared to the canonical problem of instability of flow past a plate for isothermal flow, the study becomes involved and complicated when heat transfer effects are introduced. It is known that the viscous action can be destabilizing for isothermal flows, giving rise to Tollmien-Schlichting waves. For flow past a heated horizontal flat plate, buoyancy force is an additional source of destabilization and both these destabilizing effects can enhance instabilities. Such effects have not been studied in great details due to numerical problems. Addition of heat transfer effects necessitates incorporating the energy equation - that requires solving sixth order stability equation, instead of fourth order equations for isothermal flows. In reporting results Chen & Mucoglu (1979) have used Runge-Kutta integration scheme along with the Kaplan filtering technique to avoid numerical difficulties. Tumin (2003) has used both Chebyshev collocation and Runge-Kutta integration schemes to solve the ninth order stability equation. In the collocation method 70 modes were taken and Runge-Kutta method required Gram-Schmidt orthonormalization procedure to maintain linear independence of the components of fundamental solutions.

One of the major obstacle in the study of instability is that the fundamental solutions of the composite system displays variation of variables at totally dissimilar rates, when the independent variable changes. This is the well known problem of *stiffness* and is variously avoided by different techniques for solution. The main three approaches in solving hydrodynamic stability problems are based on (see Drazin & Reid (1981) and Schmid & Henningson (2001) for description): (i) matrix method using spectral or finite difference discretization; (ii) shooting methods using orthogonalization or orthonormalization and (iii) shooting method using Compound Matrix Method (CMM). The Chebyshev collocation method belongs to the first

category, while the Runge-Kutta method with orthonormalization or Kaplan filter belongs to the second category. Bridges & Morris (1984) have noted that *the matrix method leads to the appearance of "spurious" eigenvalues*. For plane Poiseuille flow, Bridges & Morris (1984) reported both stable and unstable spurious eigenvalues with large distinguishable magnitude. According to Allen & Bridges (2003), such spurious eigenvalues are created due to fracturing of the continuous spectrum for problems in infinite domain. Moresco & Healey (2000) have used a QR algorithm based on Chebyshev polynomials for the spatio-temporal study of mixed convection boundary layers developing over a vertical plate. It has also been noted by Allen & Bridges (2003) that orthogonalization/ orthonormalization procedure causes numerical solution to be non-analytic and on infinite domains there is the added problem that asymptotically correct boundary conditions may not preserve analyticity. Kaplan filter-based method also suffers from this source of error. In contrast, CMM does not suffer from any of these problems. Basic ideas behind CMM are given in Allen & Bridges (2002), Ng & Reid (1985) and Drazin & Reid (1981). CMM has been re-developed using exterior algebra in a co-ordinate free context in Allen & Bridges (2002). CMM has been used in Sengupta *et al.* (1994) for receptivity analysis and reporting the eigen-spectrum of Blasius boundary layer. Some improvements to CMM have been suggested in Sengupta (1992) to obtain eigen functions correctly. Allen & Bridges (2003) solved the stability problem of Ekman boundary layer interacting with a compliant surface by solving a sixth order system. Ng & Reid (1985) had developed CMM for general fourth and sixth order systems. For the mixed convection problem over a heated horizontal flat plate investigated here, CMM is used.

The governing equations are given in the next section. The mean flow, whose stability will be studied, is given in the section 6.3. The stability equations and related numerical methods for CMM is given in section 6.4. The results and discussion follow in section 6.5. The chapter closes with some comments and outlook in section 6.6.

6.2 The Governing Equations

We consider the laminar two-dimensional motion of fluid past a hot semi-infinite plate, with the free stream velocity and temperature denoted by, U_∞ and T_∞. We will focus our attention on the top of the plate, for which the temperature is T_w- that is greater than T_∞, while assuming the leading edge of the plate as the stagnation point. Governing equations are written in dimensional form (indicated by the quantities with asterisk), along with the Boussinesq approximation to represent the buoyancy effect,

for the velocity and temperature fields by (Gebhart *et al.* (1988)),

$$\nabla^* \cdot \vec{V^*} = 0 \tag{6.2.1}$$

$$\frac{D\vec{V^*}}{Dt^*} = g_j \beta (T^* - T_\infty) - \frac{1}{\rho}\nabla p^* + \nu \nabla^2 \vec{V^*} \tag{6.2.2}$$

$$\frac{DT^*}{Dt^*} = \alpha \nabla^{*2} T^* + \frac{\nu}{C_p}\phi_v + \frac{q}{\rho C_v} \tag{6.2.3}$$

where $\frac{D}{Dt^*}$ represents the substantive derivative and ϕ_v and q are the viscous dissipation and the heat generation term in the energy equation. $g_j = [0, g, 0]^T$ is the gravity vector; α and ν are the thermal diffusivity and kinematic viscosity respectively; β represents the volumetric thermal expansion coefficient. In our analysis we will neglect the viscous dissipation and the heat source term.

If we introduce a length scale (L), velocity scale (U_∞), temperature scale ($\Delta T = T_w - T_\infty$) and pressure scale ($\rho U_\infty^2$), then the above equations can be represented in non-dimensional form by,

$$\nabla \cdot \vec{V} = 0 \tag{6.2.4}$$

$$\frac{D\vec{V}}{Dt} = \frac{Gr}{Re^2} T - \nabla p + \frac{1}{Re}\nabla^2 \vec{V} \tag{6.2.5}$$

$$\frac{DT}{Dt} = \frac{1}{RePr}\nabla^2 T \tag{6.2.6}$$

where $T = (T - T_\infty)/\Delta T$ and $Gr = \frac{g\beta \Delta T L^3}{\nu^2}$; $Re = \frac{U_\infty L}{\nu}$ and $Pr = \nu/\alpha$. In the momentum conservation equation, the quantity Gr/Re^2 is also known as the Richardson number or Archimedes number. The Grashof number weighs in the relative importance of buoyancy and viscous force terms and in the mixed convection regime the Richardson number/ Archimedes number is of order one.

6.3 Mean Flow Equations

The mean flow equations are obtained by invoking boundary layer approximation to the above conservation equations. For the two-dimensional steady incompressible flow with constant properties and Boussinesq approximation, the non-dimensional equations are written in a Cartesian coordinate system, fixed at the leading edge of the semi-infinite horizontal flat plate as,

$$\frac{\partial u}{\partial x} + \frac{\partial v}{\partial y} = 0 \tag{6.3.1}$$

$$u\frac{\partial u}{\partial x} + v\frac{\partial u}{\partial y} = -\frac{1}{\rho}\frac{\partial p}{\partial x} + \nu\frac{\partial^2 u}{\partial y^2} \tag{6.3.2}$$

$$0 = g\beta(T - T_\infty) - \frac{1}{\rho}\frac{\partial p}{\partial y} \tag{6.3.3}$$

$$u\frac{\partial T}{\partial x} + v\frac{\partial T}{\partial y} = \alpha\frac{\partial^2 T}{\partial y^2} \tag{6.3.4}$$

Following the notations and non-dimensionalization schemes of Schneider (1979), these equations are written as,

$$\frac{\partial U}{\partial X} + \frac{\partial V}{\partial Y} = 0 \tag{6.3.5}$$

$$U\frac{\partial U}{\partial X} + V\frac{\partial U}{\partial Y} = -\frac{\partial P}{\partial X} + \frac{\partial^2 U}{\partial Y^2} \tag{6.3.6}$$

$$0 = K\theta - \frac{\partial P}{\partial Y} \tag{6.3.7}$$

$$U\frac{\partial \theta}{\partial X} + V\frac{\partial \theta}{\partial Y} = \frac{1}{Pr}\frac{\partial^2 \theta}{\partial Y^2} \tag{6.3.8}$$

where $X = x/L$; $Y = y\sqrt{Re}/L$; $U = u/U_\infty$; $V = \sqrt{Re}v/U_\infty$; $\theta = (T - T_\infty)$; and $P = p/(\rho_\infty U_\infty^2)$. Furthermore, in the above equation, $K = Ar/\sqrt{Re}$, which is identical to that defined in the previous section.

These equations are solved subject to boundary conditions at the wall ($Y = 0$ and $X > 0$): $U = V = 0$ and $\theta = \theta_w(X)$; and at the free-stream ($Y \to \infty$): $U = 1$ and $\theta = P = 0$.

In the above set of equations, (6.3.5) is automatically satisfied if we introduce a stream function (ψ). As P indicates an excess pressure over the free-stream value, then (6.3.7) can be integrated to $P = -\int_Y^\infty K\theta dY$. When these are introduced in the x-momentum and the energy equation, one gets

$$\psi_Y\psi_{XY} - \psi_X\psi_{YY} - K\int_Y^\infty \theta_X dY = \psi_{YYY} \tag{6.3.9}$$

$$\psi_Y\theta_X - \psi_X\theta_Y = \frac{1}{Pr}\theta_{YY} \tag{6.3.10}$$

It is shown in Schneider (1979), that the above formulation admits similarity solution, if $\theta_w \propto X^{-1/2}$ and for which a similarity transformations is introduced for the independent variable: $\eta = YX^{-1/2}$ and for the dependent variables via: $\psi = X^{1/2}g(\eta)$ and $\theta = \theta_w\Theta$. These transformation yield the following system of equations,

$$2g''' + gg'' + K\eta\Theta = 0 \tag{6.3.11}$$

$$\frac{2}{Pr}\Theta'' + g\Theta' + g'\Theta = 0 \tag{6.3.12}$$

In these equations a prime indicates a derivative with respect to the independent variable, η. These equations have to be solved subject to the boundary conditions at $\eta = 0$: $g = g' = 0$ and $\Theta = 1$ and as $\eta \to \infty$: $g' = 1$ and $\Theta = 0$. The energy equation can be furthermore integrated analytically once to obtain,

$$\frac{2}{Pr}\Theta' + g\Theta = 0 \tag{6.3.13}$$

Note that the solutions depend on Reynolds number, that is implicitly included in the Y or η co-ordinate itself. The numerical results of these were presented in Schneider (1979) and an interesting feature of it was seen that the wall slope for Θ is equal to zero for all values of K-, implying the solution to be given for adiabatic wall condition.

6.4 Stability Equations and Numerical Method

Here the stability equations for two dimensional plane flows have been derived, by starting from the non-dimensional Eqns. (6.2.4) -(6.2.6) given by,

$$\frac{\partial u}{\partial x} + \frac{\partial v}{\partial y} = 0 \tag{6.4.1}$$

$$\frac{\partial u}{\partial t} + u\frac{\partial u}{\partial x} + v\frac{\partial u}{\partial y} = -\frac{\partial p}{\partial x} + \frac{1}{Re}\left(\frac{\partial^2 u}{\partial x^2} + \frac{\partial^2 u}{\partial y^2}\right) \tag{6.4.2}$$

$$\frac{\partial v}{\partial t} + u\frac{\partial v}{\partial x} + v\frac{\partial v}{\partial y} = \frac{Gr}{Re^2}T - \frac{\partial p}{\partial y} + \frac{1}{Re}\left(\frac{\partial^2 v}{\partial x^2} + \frac{\partial^2 v}{\partial y^2}\right) \tag{6.4.3}$$

$$\frac{\partial T}{\partial t} + u\frac{\partial T}{\partial x} + v\frac{\partial T}{\partial y} = \frac{1}{RePr}\left(\frac{\partial^2 T}{\partial x^2} + \frac{\partial^2 T}{\partial y^2}\right) \tag{6.4.4}$$

For the stability analysis, all the physical variables would be split into the mean part, derived in section 6.3, and a disturbance component indicated by a caret in the following,

$$u(x,y,t) = \bar{U}(x,y) + \epsilon\hat{u}(x,y,t)$$
$$v(x,y,t) = \bar{V}(x,y) + \epsilon\hat{v}(x,y,t)$$
$$p(x,y,t) = \bar{P}(x,y) + \epsilon\hat{p}(x,y,t)$$
$$T(x,y,t) = \bar{T} + \epsilon\hat{T}(x,y,t)$$

The quantities with the over-bar are related to the mean flow solutions of the previous section, via the appropriate transformations. The stability equations are obtained by making the additional parallel flow assumption, $\bar{U} = \bar{U}(y)$, $\bar{V} = 0$ and $\bar{T} = \bar{T}(y)$ so that a normal mode spatial instability analysis is possible by looking for a solution of the linearized equations of the following form:

$$[\hat{u}, \hat{v}, \hat{p}, \hat{T}] = [f(y), \phi(y), \pi(y), h(y)]e^{i(kx-\omega t)} \tag{6.4.5}$$

After substituting (6.4.5) into (6.4.1) to (6.4.4), one can obtain the system of equation governing the disturbance amplitude functions as,

$$ikf + \phi' = 0 \tag{6.4.6}$$

$$i(k\bar{U} - \omega)f + \bar{U}'\phi = -ik\pi + \frac{1}{Re}(f'' - k^2 f) \tag{6.4.7}$$

$$i(k\bar{U} - \omega)\phi = \frac{Gr}{Re^2}h - \pi' + \frac{1}{Re}(\phi'' - k^2\phi) \tag{6.4.8}$$

$$i(k\bar{U} - \omega)h + \bar{T}'\phi = \frac{1}{RePr}(h'' - k^2 h) \tag{6.4.9}$$

In these equations, prime once again denote differentiation with respect to y. One can eliminate π and f from these equations to obtain,

$$i(k\bar{U} - \omega)(k^2\phi - \phi'') + ik\bar{U}''\phi = \frac{Gr}{Re^2}k^2 h - \frac{1}{Re}(\phi^{iv} - 2k^2\phi'' + k^4\phi) \tag{6.4.10}$$

$$i(k\bar{U} - \omega)h + \bar{T}'\phi = \frac{1}{RePr}(h'' - k^2 h) \tag{6.4.11}$$

These are the well-known Orr-Sommerfeld equations for mixed convection flows, that show the disturbance normal velocity and the temperature fields to be coupled, constituting a sixth order differential system. Equations (6.4.10) and (6.4.11) are to be solved subject to the six boundary conditions:

$$at \quad y = 0 : \phi, \phi' = 0 \quad and \quad h = constant \tag{6.4.12}$$

$$as \quad y \to \infty : \qquad \phi, \phi', h \to 0 \tag{6.4.13}$$

The indicated boundary conditions imply the forcing of the system by thermal input on the wall, while the disturbances decay in the far stream, as $y \to \infty$. Equations (6.4.10)-(6.4.11), together with the boundary conditions (6.4.12)-(6.4.13) reveal an interesting phenomenon that the temperature field given by (6.4.11), decouples from the velocity field in the free stream ($y \to \infty$), as $\bar{T}' \approx 0$ there. The characteristic modes at free stream are given by: $\lambda_{5,6} = \mp S$, where $S = [k^2 + iRePr(k - \omega)]^{1/2}$. However, the disturbance momentum equation is not decoupled, as (6.4.10) at the free-stream simplifies (as $\bar{U} = 1$ and all mean flow derivatives are zero) to

$$i(k-\omega)(k^2\phi - \phi'') = \frac{Gr}{Re^2}k^2 h - \frac{1}{Re}(\phi^{iv} - 2k^2\phi'' + k^4\phi) \tag{6.4.14}$$

This equation for the disturbance amplitude of normal component of velocity represents a forced dynamics with the thermal field acting as the forcing. The homogeneous part of the solution is governed by the following characteristics, $\lambda_{1,2} = \mp k$ and $\lambda_{3,4} = \mp Q$ where $Q^2 = k^2 + iRe(k-\omega)$. Out of these six characteristic values, we will discard those modes that grow with y. Let us identify the admissible fundamental solution components by,

$$\phi_1 = e^{-ky}; \phi_3 = e^{-Qy} \quad and \quad \phi_5 = e^{-Sy} \tag{6.4.15}$$

when the real part of k, Q and S are all positive. For this combination of fundamental solutions, the particular solution is of the type $\phi_p = C_n e^{-Sy}$ in the free stream where, $C_n = \frac{k^2 Gr}{Re} / \left[S^4 - 2k^2S^2 + k^4 + iRe(k-\omega)(k^2 - S^2) \right]$.

We will represent the governing stability equations as a set of six first order ordinary differential equations by introducing the vector:

$\mathbf{u}(y,.) = [u_1(y,.), u_2(y,.), u_3(y,.), u_4(y,.), u_5(y,.), u_6(y,.)]^T$.

Where, $u_1 = \phi$, $u_2 = \phi'$, $u_3 = \phi''$, $u_4 = \phi'''$, $u_5 = h$ and $u_6 = h'$. The governing system of equations given by (6.4.10) and (6.4.11) can be written as,

$$\{u_j'\} = [A]\{u_j\} \tag{6.4.16}$$

Thus, u is defined by $u \in \mathbb{C}^6$ and where the matrix A is written as,

$$A = \begin{bmatrix} 0 & 1 & 0 & 0 & 0 & 0 \\ 0 & 0 & 1 & 0 & 0 & 0 \\ 0 & 0 & 0 & 1 & 0 & 0 \\ -a & 0 & b & 0 & c & 0 \\ 0 & 0 & 0 & 0 & 0 & 1 \\ e & 0 & 0 & 0 & d & 0 \end{bmatrix}$$

with, $a = k^4 + iRek\bar{U}'' + iRek^2(k\bar{U} - \omega)$; $b = 2k^2 + iRe(k\bar{U} - \omega)$; $c = k^2Gr/Re$; $d = k^2 + iRePr(k\bar{U} - \omega)$ and $e = RePr\bar{T}'$.

The problem is to integrate (6.4.16) on $\mathbb{C}^6$ that are defined on an interval $y \in [0, \infty]$ with three boundary conditions at $y = 0$ -as defined by (6.4.12) and three asymptotic boundary conditions applied at $y = Y_\infty$ for some $Y_\infty > 0$- as defined by (6.4.13). The integration of (6.4.16) subject to boundary conditions (6.4.12) and (6.4.13) is not straightforward - due to the *stiffness* problem discussed in the introduction. For the purpose of removing the *stiffness* of the problem and integrate the ODEs we will employ the CMM- as described next.

6.4.1 Compound Matrix Method For The 6^{th} Order System

The general methods for 4^{th} and 6^{th} order system are as given in Ng & Reid (1985) and the specific formulation presented here is for the 6^{th} order system for mixed convection flow. Allen & Bridges (2002) have listed other references where the compound matrices have been used to integrate stiff linear system without requiring any orthogonalization process. To our knowledge, CMM has not been used for the study of stability of mixed convection flow before- Allen & Bridges (2003) have used it for the 6^{th} order system defining a problem of hydrodynamic stability and the present study is similar in mathematical scope.

While the general method can be found in Ng & Reid (1985) and Allen & Bridges (2002, 2003), only the essential details are given here for the mixed convection instability problem. In this method an induced system is constructed, determined by the set of asymptotic boundary conditions at $y = Y_\infty$ that in turn is governed by the analytic nature of solution at $y \to \infty$. This procedure converts the original boundary value problem into an initial value problem, while removing the stiffness of the differential system. For the sixth order system, this is equivalent to projecting the solution on a subspace of $\mathbb{C}^6$, with the help of three decaying boundary conditions for $y \to Y_\infty$, following the notations of Allen & Bridges (2003)- into $\Lambda^3(\mathbb{C}^6)$. Similarly, the boundary conditions at $y = 0$ defines a second three dimensional subspace of $\mathbb{C}^6$. The problem is thus reduced to linking

these two three-dimensional subspaces satisfying (6.4.16). Any subspace spanned by three linearly independent vectors $\{\phi_1, \phi_3, \phi_5\}$ (as defined in (6.4.15)), is represented notationally as a point $\phi_1 \Lambda \phi_3 \Lambda \phi_5$, in the vector space $\Lambda^3(\mathbb{C}^6)$, where Λ is the wedge product (Allen & Bridges (2003)).

Let us introduce the following basis $e_1 = [\phi_1, \phi_3, \phi_5]$; $e_2 = [\phi_1', \phi_3', \phi_5']$; $e_3 = [\phi_1'', \phi_3'', \phi_5'']$; $e_4 = [\phi_1''', \phi_3''', \phi_5''']$; $e_5 = [\phi_1^{iv}, \phi_3^{iv}, \phi_5^{iv}]$ and $e_6 = [\phi_1^{v}, \phi_3^{v}, \phi_5^{v}]$ in $\mathbb{C}^6$, then all the elements of $e_i \Lambda e_j \Lambda e_k$ form the basis for $\Lambda^3(\mathbb{C}^6)$ with the dimension $\frac{6!}{3!3!} = 20$. The solution matrix $[\phi_1 \phi_3 \phi_5]$, thus has twenty (3×3) minors- that are also called the second compound (Ng & Reid (1985)) denoted by,

$$y_{ijk} = [e_i e_j e_k]^T \tag{6.4.17}$$

where $i = 1, 2, 3, 4$; $j = i + 1, ...5$ and $k = j + 1...6$.

If we let $\mathbf{y} = [y_{123}, y_{124}, y_{125}, ...y_{456}]^T$, then by direct calculation it can be shown that $\mathbf{y}$ satisfy the following set of linear coupled first order equation given by

$$y' = B(y)y \tag{6.4.18}$$

where the B matrix elements are given in Ng & Reid (1985) and Allen & Bridges (2003) for sixth order systems. By listing down the compound matrix variables in a lexicographic fashion i.e. $y_1 \equiv y_{123}$; $y_2 \equiv y_{124}$ .....$y_{20} \equiv y_{456}$, one can obtain the induced system equations as

$$y_1' = y_2 \tag{6.4.19}$$

$$y_2' = by_1 + cy_3 + y_5 \tag{6.4.20}$$

$$y_3' = y_4 + y_6 \tag{6.4.21}$$

$$y_4' = dy_3 + y_7 \tag{6.4.22}$$

$$y_5' = cy_6 + y_{11} \tag{6.4.23}$$

$$y_6' = y_7 + y_8 + y_{12} \tag{6.4.24}$$

$$y_7' = dy_6 + y_9 + y_{13} \tag{6.4.25}$$

$$y_8' = by_6 + y_9 + y_{14} \tag{6.4.26}$$

$$y_9' = by_7 + dy_8 + cy_{10} + y_{15} \tag{6.4.27}$$

$$y_{10}' = y_{16} \tag{6.4.28}$$

$$y_{11}' = -ay_1 + cy_{12} \tag{6.4.29}$$

$$y_{12}' = y_{13} + y_{14} \tag{6.4.30}$$

$$y'_{13} = ey_1 + dy_{12} + y_{15} \tag{6.4.31}$$

$$y'_{14} = ay_3 + by_{12} + y_{15} + y_{17} \tag{6.4.32}$$

$$y'_{15} = ey_2 + ay_4 + by_{13} + dy_{14} + cy_{16} + y_{18} \tag{6.4.33}$$

$$y'_{16} = ey_3 + y_{19} \tag{6.4.34}$$

$$y'_{17} = ay_6 + y_{18} \tag{6.4.35}$$

$$y'_{18} = ey_5 + ay_7 + dy_{17} + cy_{19} \tag{6.4.36}$$

$$y'_{19} = ey_6 + y_{20} \tag{6.4.37}$$

$$y'_{20} = ey_8 - ay_{10} + by_{19} \tag{6.4.38}$$

where the primes indicate differentiation with respect to y, the wall-normal coordinate. Introduction of the second compounds as the unknown of the problem, helps remove the stiffness of the problem, thereby allowing any standard integration procedure to integrate (6.4.19)-(6.4.38). However, we have also mentioned before that the usage of asymptotic boundary conditions at $y \to \infty$ allows us to convert the boundary value problem to an initial value problem- that is discussed next.

6.4.2 Initial Conditions for The Induced System

The property of the fundamental solutions, allows us to truncate the domain of investigation up to Y_∞ and this is used to convert the BVP into an IVP- as shown here. Using (6.4.15) into the definition of the second compounds, as given by (6.4.17), and scaling the expressions by $e^{-(k+Q+S)Y_\infty}$ (for the case of $real(k, Q, S) > 0$) one gets,

$$y_{1\infty} = S^2(k-Q) + Q^2(S-k) + k^2(Q-S) \tag{6.4.39}$$

$$y_{2\infty} = -S^3(k-Q) - Q^3(S-k) - k^3(Q-S) \tag{6.4.40}$$

$$y_{3\infty} = S^4(k-Q) + Q^4(S-k) + k^4(Q-S) \tag{6.4.41}$$

$$y_{4\infty} = -S^5(k-Q) - Q^5(S-k) - k^5(Q-S) \tag{6.4.42}$$

$$y_{5\infty} = S^3(k^2-Q^2) + Q^3(S^2-k^2) + k^3(Q^2-S^2) \tag{6.4.43}$$

$$y_{6\infty} = -S^4(k^2-Q^2) - Q^4(S^2-k^2) - k^4(Q^2-S^2) \tag{6.4.44}$$

$$y_{7\infty} = S^5(k^2-Q^2) + Q^5(S^2-k^2) + k^5(Q^2-S^2) \tag{6.4.45}$$

$$y_{8\infty} = S^4(k^3-Q^3) + Q^4(S^3-k^3) + k^4(Q^3-S^3) \tag{6.4.46}$$

$$y_{9\infty} = -S^5(k^3-Q^3) - Q^5(S^3-k^3) - k^5(Q^3-S^3) \tag{6.4.47}$$

$$y_{10\infty} = S^5(k^4 - Q^4) + Q^5(S^4 - k^4) + k^5(Q^4 - S^4) \tag{6.4.48}$$

$$y_{11\infty} = S^3(kQ^2 - k^2Q) + Q^3(Sk^2 - S^2k) + k^3(QS^2 - SQ^2) \tag{6.4.49}$$

$$y_{12\infty} = S^4(Qk^2 - kQ^2) + Q^4(kS^2 - Sk^2) + k^4(SQ^2 - QS^2) \tag{6.4.50}$$

$$y_{13\infty} = S^5(kQ^2 - Qk^2) + Q^5(Sk^2 - S^2k) + k^5(QS^2 - Q^2S) \tag{6.4.51}$$

$$y_{14\infty} = S^4(kQ^3 - k^3Q) + Q^4(Sk^3 - S^3k) + k^4(-SQ^3 + QS^3) \tag{6.4.52}$$

$$y_{15\infty} = S^5(k^3Q - kQ^3) + Q^5(S^3k - k^3S) + k^5(SQ^3 - QS^3) \tag{6.4.53}$$

$$y_{16\infty} = S^5(kQ^4 - k^4Q) + Q^5(Sk^4 - kS^4) + k^5(QS^4 - SQ^4) \tag{6.4.54}$$

$$y_{17\infty} = S^4(Q^2k^3 - k^2Q^3) + Q^4(k^2S^3 - S^2k^3) + k^4(S^2Q^3 - S^3Q^2) \tag{6.4.55}$$

$$y_{18\infty} = S^5(k^2Q^3 - k^3Q^2) + Q^5(S^2k^3 - k^2S^3) + k^5(S^3Q^2 - S^2Q^3) \tag{6.4.56}$$

$$y_{19\infty} = S^5(Q^2k^4 - k^2Q^4) + Q^5(S^4k^2 - k^4S^4) + k^5(S^2Q^4 - S^4Q^2) \tag{6.4.57}$$

$$y_{20\infty} = S^5(Q^4k^3 - Q^3k^4) + Q^5(S^3k^4 - k^3S^4) + k^5(S^4Q^3 - S^3Q^4) \tag{6.4.58}$$

While evaluating Q and S one can always choose the mode with positive real part, it is not necessarily so while obtaining the response field by integrating (6.4.18) along the Bromwich contour when $real(k) < 0$. In such instances, one can develop similar initial conditions. It is now easy to see from above as to how CMM avoids the *stiffness* of the original problem. While the individual components of the fundamental solutions, as given by (6.4.15) decays with height differently due to the disparate value of the characteristic exponents, the second compounds $\mathbf{y}$, all have the same decay rate given by the exponent $-(|k| + Q + S)$- thereby removing the stiffness. It is for this reason (6.4.19)-(6.4.38) can be simply integrated as IVP from $y = Y_\infty$ to the wall ($y = 0$) by any ordinary integrator. We have used four stage Runge- Kutta method for this purpose.

6.4.3 Dispersion Relation

To solve the stability problem one is required to solve (6.4.19)- (6.4.38) starting from $y = Y_\infty$ using the initial condition given in (6.4.39)- (6.4.58). The dispersion relation can be obtained by satisfying the wall boundary condition as given by (6.4.12) in terms of disturbance velocity components and temperature field. In terms of the fundamental solution components, these conditions at the wall can be written as,

$$a_1\phi_1 + a_3\phi_3 + a_5\phi_5 = 0 \tag{6.4.59}$$

$$a_1\phi_1' + a_3\phi_3' + a_5\phi_5' = 0 \tag{6.4.60}$$

$$h = h_0(constant) \tag{6.4.61}$$

The condition given by (6.4.61) can be rewritten, using (6.4.10) and the fundamental solution components, as

$$a_1(\phi_1^{iv}+a\phi_1-b\phi_1'')+a_3(\phi_3^{iv}+a\phi_3-b\phi_3'')+a_5(\phi_5^{iv}+a\phi_5-b\phi_5'') = ch_0 \tag{6.4.62}$$

Thus, the dispersion relation can be obtained from the characteristic determinant of the linear system formed by (6.4.59), (6.4.60) and (6.4.62). After simplification and using the definition of second compounds, the dispersion relation is obtained as,

$$D_r + iD_i = y_3 - by_1 = 0 \quad at \quad y = 0 \tag{6.4.63}$$

This completes the definition of the stability problem for the mixed convection flow over the horizontal plate. For a given K and Re, one would be required to solve (6.4.19)-(6.4.38), starting with the initial conditions (6.4.39)-(6.4.58) and satisfy (6.4.63) for particular combinations of the eigenvalues obtained as the complex k and ω. We will use the procedure adopted in Sengupta *et al.* (1994) to obtain the eigen-spectrum for the mixed convection case, when the problem is in spatial analysis framework. In the process, it is possible to scan for all the eigenvalues in a limited part of the complex k- plane, without any problem of spurious eigenvalues.

6.4.4 Eigen-function for The Mixed Convection Problem

Having obtained the eigenvalues, it is possible to obtain the eigenfunctions using CMM. The eigenfunction can be written in terms of the decaying fundamental modes as,

$$\phi = a_1\phi_1 + a_3\phi_3 + a_5\phi_5 \tag{6.4.64}$$

For the sixth-order system, one can form the auxiliary system of equations by eliminating a_1, a_3 and a_5 from the definition of the second compounds and

$$\phi' = a_1\phi_1' + a_3\phi_3' + a_5\phi_5' \tag{6.4.65}$$

$$\phi'' = a_1\phi_1'' + a_3\phi_3'' + a_5\phi_5'' \tag{6.4.66}$$

$$\phi''' = a_1\phi_1''' + a_3\phi_3''' + a_5\phi_5''' \tag{6.4.67}$$

$$\phi^{iv} = a_1\phi_1^{iv} + a_3\phi_3^{iv} + a_5\phi_5^{iv} \tag{6.4.68}$$

$$\phi^{v} = a_1\phi_1^{v} + a_3\phi_3^{v} + a_5\phi_5^{v} \tag{6.4.69}$$

For example, using (6.4.64)-(6.4.66) and using the definition of the second compounds, one obtains the following auxiliary equation,

$$y_1\phi''' - y_2\phi'' + y_5\phi' - y_{11}\phi = 0 \tag{6.4.70}$$

If instead one uses (6.4.64), (6.4.65) and (6.4.67), following auxiliary equation is obtained,

$$y_1\phi^{iv} - y_3\phi'' + y_6\phi' - y_{12}\phi = 0 \tag{6.4.71}$$

There are many other possible auxiliary equations that can be used in principle to obtain the eigen functions. In the context of fourth order systems, multiplicity of such equations was considered a source of confusion (see Drazin & Reid (1981))- that was resolved later in Sengupta (1992) by looking at the eigenfunction equations for their correct asymptotic behavior when $y \to Y_\infty$. As the problem allows only three decaying modes for the present case, it is necessary to ensure that the chosen eigenfunction equation also display same asymptotic decay. For example, (6.4.70) displays the correct decay rates of $-|k|$, $-|Q|$ and $-|S|$, while (6.4.71) has the asymptotic variation given by the characteristic exponents as $-|k|$, $-|Q|$, $-|S|$ and $(|k| + |Q| + |S|)$. Thus, (6.4.71) has a spurious violently growing mode and cannot be used. As (6.4.70) already displays the correct solution behavior, we will not look for any other auxiliary equations.

6.5 Results and Discussion

We first obtain the mean flow by solving the coupled ODEs (6.3.11) and (6.3.13) by standard four-stage Runge-Kutta method. These equations have been solved by taking maximum similarity co-ordinate, $\eta_{max} = 12$ equally divided into 4000 sub-intervals. For different Re and K, mean flow has been obtained here. Fixing K, instead of Gr, is motivated by our discussion in the introduction where we have noted that for instability of mixed-convection boundary layers, K is more relevant than Gr. As we have investigated the mixed convection problem in air, we have fixed the value of $Pr = 0.7$ for all cases. Obtained mean-field results for the non-dimensional velocity and temperature are shown in Fig. 6.1.

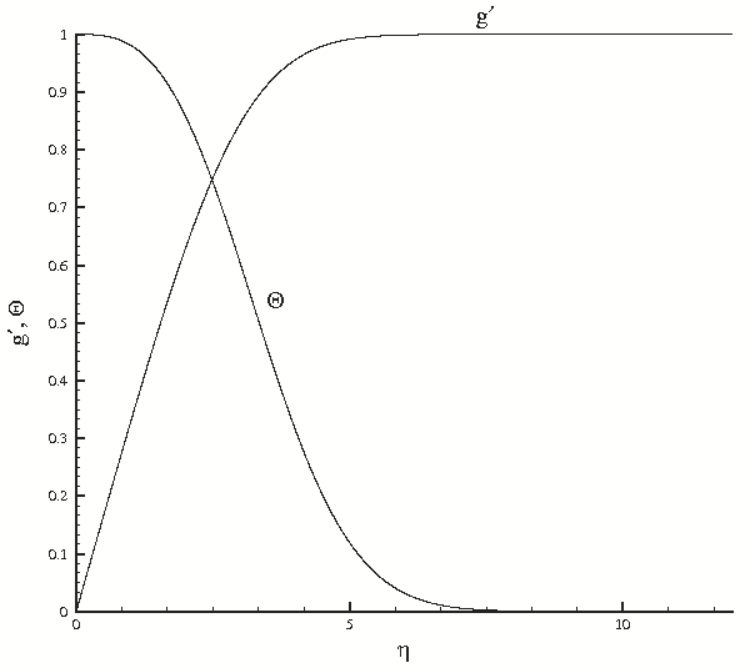

Figure 6.1 Mean flow profile obtained by solving (6.3.11) and (6.3.13) for K = 1.0×10^{-5}

6.5.1 Eigen-spectrum For Mixed Convection Problem

Mean flow is obtained using the similarity co-ordinate η, while the stability equations are solved using the independent variable, $y = y^*/\delta^*$, where y^* is the dimensional height over the plate and δ^* is the displacement thickness of the boundary layer. In terms of η, the displacement thickness is given by,

$$\delta^* = \sqrt{\frac{\nu x}{U_\infty}} \int_0^\infty [1 - g'(\eta)] d\eta = \sqrt{\frac{\nu x}{U_\infty}} C_m \tag{6.5.1}$$

Thus, the two ordinates are related by $y = \eta/C_m$ and C_m depends upon the choice of K. For $K = 0$ (the Blasius profile) this is obtained as 1.72089,

while for $K = 0.1$ this reduces to 1.13831. As all our investigations are related to events on top of the plate, K is non-negative and these two values provide the outer limits. For mixed convection cases under investigation we actually consider K to be very small -of the order of 10^{-6} to 10^{-4}, that is also of the order of the values used in the experimental investigation of Wang (1982). For example, for $K = 1 \times 10^{-5}$ the value of C_m is marginally lower at 1.720703649 and that makes $Y_\infty = 6.97389$.

To obtain the eigen-spectrum for the spatial stability analysis, we solved the stability equations (6.4.19)-(6.4.38) from the free-stream to the wall, for fixed Re, K and $\omega = \omega_0$ and any guess value of complex k. Due to the use of Runge-Kutta method, the stability equations are solved with 2000 sub-intervals between Y_∞ and the wall. For incorrect guess of k, $(D_r + iD_i)$ will not be equal to zero. To obtain approximate values of k quickly, we scan the complex-k plane for points where D_r and D_i are simultaneously zero. Instead of trying to obtain the correct k by Newton-Raphson type procedure, we scan the complex- k plane for points where D_r and D_i are simultaneously zero. This was also the procedure adopted in Sengupta *et* al. (1994) to obtain the eigen-spectrum for Blasius profile. This procedure is fast and pose no difficulties that is associated with matrix or orthogonalization method- allowing correct identification of all the eigen-values simultaneously without requiring any initial guess-values.

For the spatial analysis, we have scanned the region of the complex k-plane: $-1 \leq k_{real} \leq 1$ and $-1 \leq k_{imag} \leq 1$ using 500 and 4000 points in the respective directions. For each combination of (k_{real}, k_{imag}), the value of D_r and D_i have been evaluated numerically from the solution of (6.4.19)-(6.4.38). The zero-contour lines of D_r and D_i are plotted- as shown in Fig. 6.2(a) for $K = 1.0 \times 10^{-5}$, $Re = 1000$ and $\omega_0 = 0.1$.

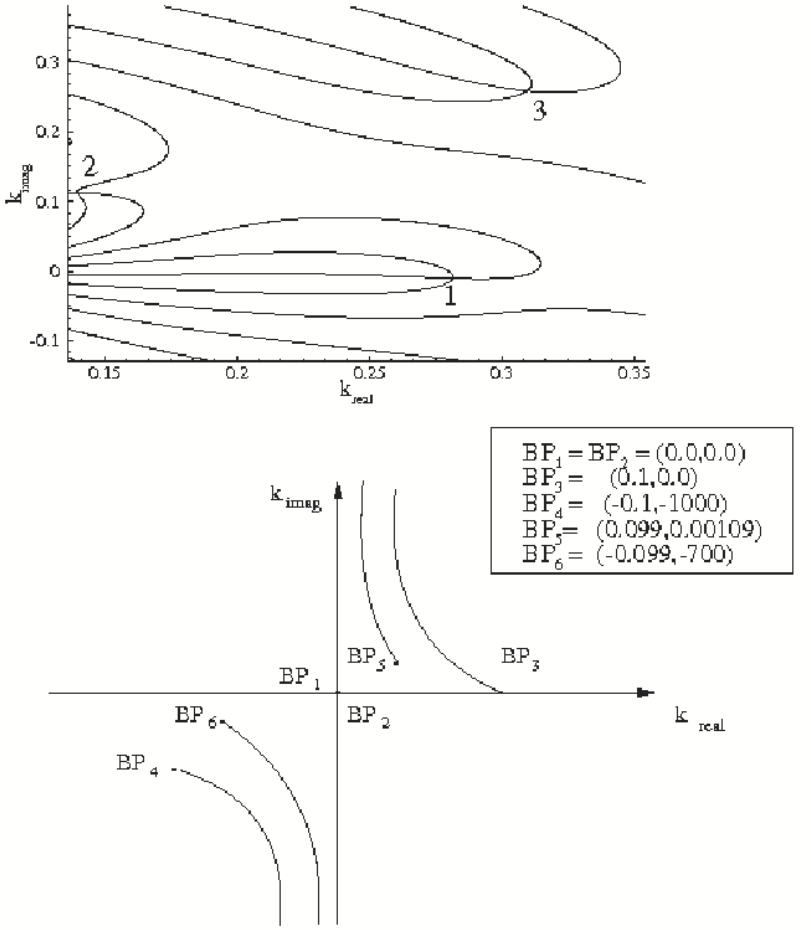

Figure 6.2 Zero-contour lines of D_r and D_i shown plotted in a limited region of the complex wave number plane for the case of Re = 1000, K = 1.0×10^{-5} and $\omega_0 = 0.1$. The eigenvalues are marked as indicated in Table 6.2. (b) Complex k- plane showing all the branch point with coordinates as indicated in the box.

This case is discussed below with respect to Table 6.2. The following procedure is same that was used for the study of the eigen spectrum for Blasius profile in Sengupta *et al.* (1994). In this reference, a fourth order system helped identify the three modes- with one unstable and two stable ones. The present investigation, using the formulation of the sixth order system reproduced the same three eigenvalues with identical wave properties- as given in Table 6.1.

Table-6.1
($Re = 1000$; $K = 0$; $\omega_0 = 0.1$)

Mode	k_{real}	k_{imag}	*Phase speed*	*Group velocity*
1	0.2798275	-0.007287224	0.3573629	0.4199082
2	0.1379587	0.109795	0.7248540	0.3223873
3	0.1221865	0.164828	0.8184210	0.7826533
4	0.2885657	0.287718	0.3465415	0.1160599

We identify these modes, therefore as the hydrodynamic mode. The fourth eigen mode in Table-6.1 is an additional one that can be attributed to the disturbance energy equation, (6.4.11). However, it has to be noted that for $K \neq 0$, such distinction is not desirable as all the modes are coupled together. In the present study, we use the phase speed and group velocity as the relevant wave property. Specifically, the sign of group velocity determines the directionality of the propagation of the disturbance energy (as defined in Brillouin (1960)). Accordingly, all the four modes of Table 6.1, are downstream propagating, with the first mode being only unstable. The match between the present sixth order system results with that obtained earlier for Blasius profile in Sengupta *et al.* (1994) provides the validation for the developed methodology for solving stability equations for the sixth order system.

Next, the eigen-spectrum is obtained for the mixed convection case with $K = 1 \times 10^{-5}$ and $Re = 1000$. For a choice of $\omega_0 = 0.1$, located eigen-values and their wave properties are given in Table 6.2. Here, only three modes are present, with the first mode being unstable, that can be identified with the first hydrodynamic mode of Table 6.1.

Table-6.2
($Re = 1000$; $K = 1.0 \times 10^{-5}$; $\omega_0 = 0.1$)

Mode	k_{real}	k_{imag}	*Phase speed*	*Group velocity*
1	0.2814215	-0.01035186	0.3553388	0.4025252
2	0.1397349	0.1118859	0.7156407	0.3076161
3	0.3095879	0.2579895	0.3230100	0.1498453

While the wave length, phase speed and group velocity is similar for the first modes in Tables 6.1 and 6.2, the spatial growth rate has increased significantly due to added instability via buoyancy effect. The second mode of these two tables are also similarly related, while the third mode of Table 6.1 has disappeared for the case of mixed convection. Disappearance of modes have been identified in Sengupta *et al.* (1997) as related to waves attaining phase speed equal to the free stream speed. The third mode of Table 6.2 can be related to the thermal mode (fourth) of Table 6.1. We note that the thermal mode propagate at lower speeds compared to hydrodynamic modes.

In Table 6.3, eigen-spectrum for a case is tabulated for $K = 1 \times 10^{-5}$, $Re = 1000$ and $\omega_0 = 0.65$. This case, at a high circular frequency, is computed because such parameter combinations correspond to unstable thermal modes occurring for very small wavelength disturbances- as shown and explained later. It is for this reason, here the eigen-spectrum is searched over a larger range of $-2.5 \leq k_{real} \leq 2.5$, while the k_{imag} search space is kept the same. We have used the same number of points in both these directions.

Table-6.3
($Re = 1000$; $K = 1.0 \times 10^{-5}$; $\omega_0 = 0.65$)

Mode	k_{real}	k_{imag}	*Phase speed*	*Group velocity*
1	2.1746912	-0.2976624	0.2988930	0.3206651
2	1.6960187	0.4214139	0.3832504	0.2275976
3	0.9495165	0.2522278	0.6845588	0.9405797
4	0.9101455	0.4832617	0.7141714	4.6808463
5	-2.4431025	-0.2160011	-0.2660551	1.4281580

The tabulated values display five detected eigenmodes with the first eigenmode, a violently unstable thermal mode that moves down-stream. The growth rate is few hundred times higher than the growth rate of most unstable hydrodynamic mode. The second and the third mode in this table

are similar to the damped hydrodynamic modes with smaller wavelength and higher phase speeds. The third mode sends the associated disturbance energy at almost the speed of free-stream. The fourth mode is also a damped mode, but for which the disturbance energy travels at more than four times the free stream speed. Because of its high damping rate and group velocity, this mode will not contribute significantly to the dynamics. The fifth mode is interesting, as this mode is located on the left half of complex k- plane. Such modes have been reported earlier for pure fluid dynamical system in Sengupta *et al* (1997) and very recently by Tumin (2003) for natural convection past inclined plate. However, as k_{real} for this mode is negative, for corresponding disturbances grow with height- instead of the decaying modes that are considered here. We note that the same eigenvalue formulation can be used for both decaying and growing modes with y- as has been established in Sengupta & Nair (1997).

6.5.2 Neutral Curves For Mixed Convection Problem

One of the aim of any instability study is to relate it with the critical values of parameter that marks the onset of the instability. In the present context, one would therefore like to obtain the critical Reynolds number (Re_{cr}) and the corresponding circular frequency (ω_{cr}). Additionally, one would also look for the critical buoyancy parameter (K_{cr}), at which the instability properties change qualitatively, as well as quantitatively. In the previous subsection, we have noted that for $K = 0$, an additional mode is triggered due to the coupling between the energy and momentum equations through convection process for incompressible flows even when the density change due to buoyancy effect is completely ignored. When the heat transfer causes the density to change, as accounted for via Boussinesq approximation, one would be interested in finding K_{cr} that alters the instability of the system dramatically. At a given K, We have noted that there can be more than one unstable modes for a chosen Re, as shown in Table 6.3. This implies that the corresponding neutral curves are multi-lobed. To inspect this and obtaining critical parameters, we obtain neutral curves for different cases of interest. Having obtained the eigen-spectrum for different cases using CMM for the sixth order system, it is straight forward to obtain the spatial eigenvalues for any combinations of Re and ω_0 utilizing Newton-Raphson search procedure.

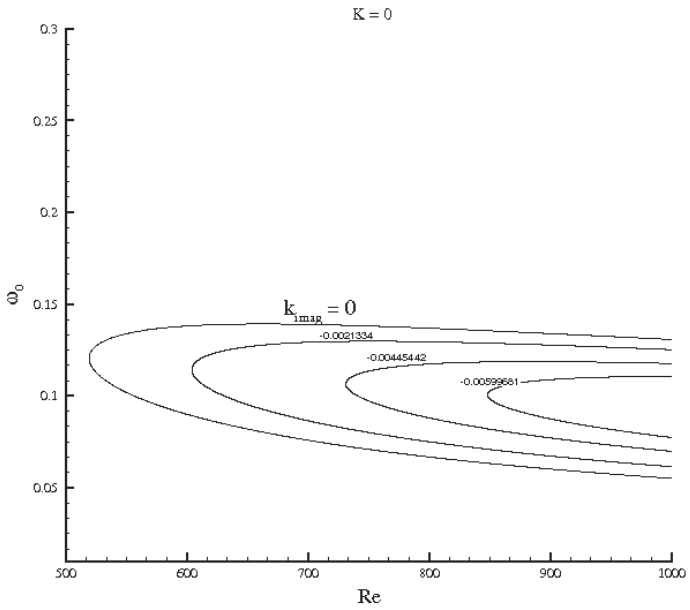

Figure 6.3 Spatial amplification contours shown in $(Re - \omega_0)$ plane for K = 0. For the neutral curve $k_{imag} = 0$ as indicated by the outer contour.

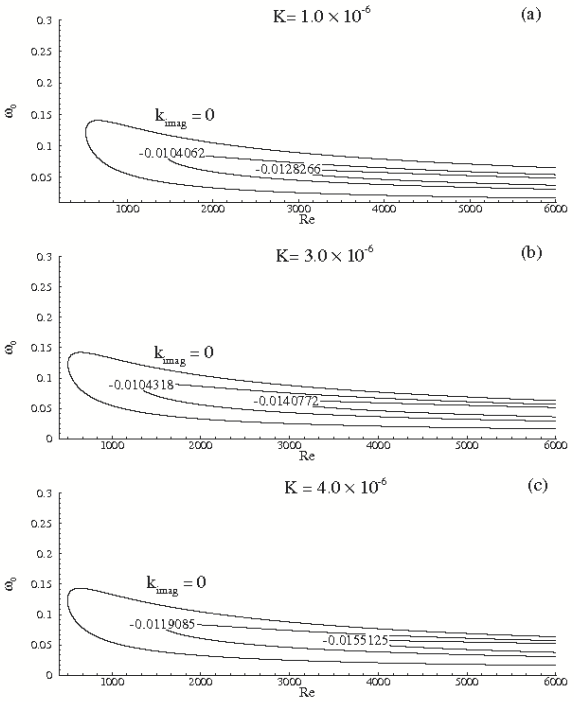

Figure 6.4 Spatial amplification contours shown in $(Re - \omega_0)$ plane for (a) $\mathbf{K} = 1.0 \times 10^{-6}$, (b) $\mathbf{K} = 3.0 \times 10^{-6}$, and (c) $\mathbf{K} = 4.0 \times 10^{-6}$. For the neutral curve $k_{imag} = 0$ as indicated by the outer contour.

First, we obtained the neutral curve for the case of $K = 0$, as shown in Fig. 6.3. From the figure, it is noted that the critical Reynolds number is given by $Re_{cr} = 519.018$ and the corresponding critical circular frequency is $\omega_{cr} = 0.12$- values that are exactly the same for the Blasius profile. We also report such data in Table 6.4 for all the different values of K considered in the present study. Maximum growth rate for spatially growing waves are in the range of $k_{imag} \approx -0.0074$ for the case of Fig. 6.3.

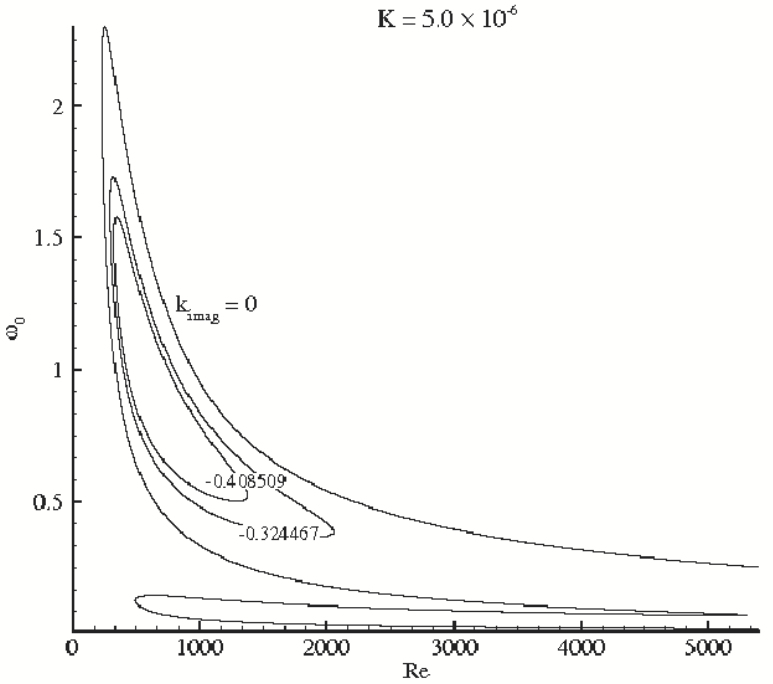

Figure 6.5 Spatial amplification contours shown in $(Re - \omega_0)$ **plane for** $\mathbf{K} = 5.0 \times 10^{-6}$**. For the neutral curve** $k_{imag} = 0$ **as indicated by the outer contour.**

In Fig. 6.4, the neutral curve is shown for the cases of $K = 1 \times 10^{-6}$, 3×10^{-6} and 4×10^{-6}. Here, one notices a slight lowering of the value of Re_{cr} to 513.6 and a marginal increase of ω_{cr} to 0.121 for $K = 1 \times 10^{-6}$. However, while these critical values are seen to change only marginally, it is the maximum growth rate exponent, given by k_{imag} that almost doubles to -0.0135589. All the other relevant wave parameters are given in Table 6.4 for this case.

The case of $K = 5 \times 10^{-6}$ is considered next, for which the neutral curve is shown in Fig. 6.5. One can notice a qualitative change in instability property for this value of buoyancy parameter. The thumb-like neutral curve of the previous cases are replaced by a two-lobed neutral curve. The lower lobe is similar to that shown in Fig. 6.3 and 6.4, with Re_{cr} reducing further to 493.5 and ω_{cr} increasing to 0.127. Thus, one notices that increasing the buoyancy parameter always lead to a decrease in critical Reynolds number for the hydrodynamic mode. It is the second lobe of the neutral curve that is of greater interest in the context of the present problem. There are few aspects about this case. First, it shows instability onset at very low Reynolds number- producing a second Re_{cr} that is found to occur at 230.4999. Secondly, the corresponding circular frequency is 2.17499, about twenty times to that obtained for the hydrodynamic mode. Thirdly, the growth rate of this high frequency mode is eighty times more in the exponents to that for Blasius profile for isothermal flow.

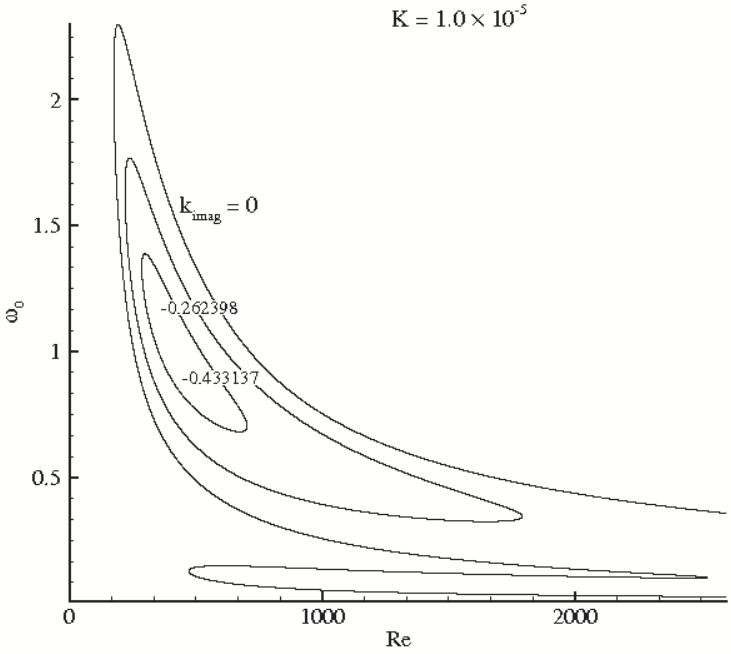

Figure 6.6 Spatial amplification contours shown in $(Re - \omega_0)$ plane for K $= 1.0 \times 10^{-5}$. For the neutral curve $k_{imag} = 0$ as indicated by the outer contour.

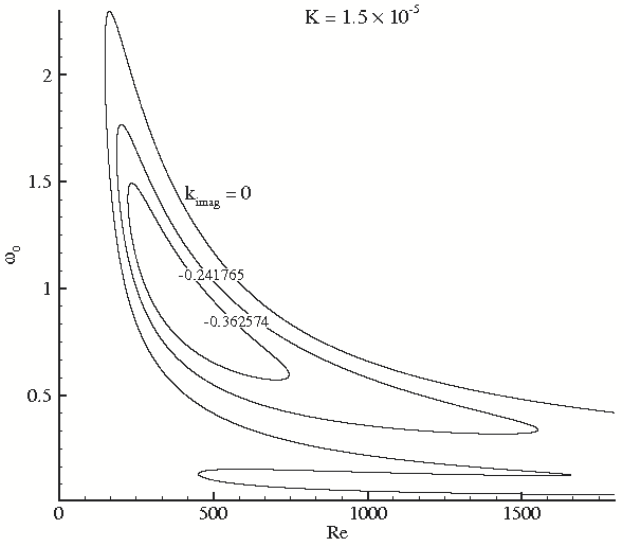

Figure 6.7 Spatial amplification contours shown in $(Re - \omega_0)$ **plane for** $\mathbf{K} = 1.5 \times 10^{-5}$**. For the neutral curve** $k_{imag} = 0$ **as indicated by the outer contour.**

In Figs. 6.6 to 6.9, neutral curves are shown for other cases of Table 6.4, all of which show two-lobed neutral curves. We have noted that the similarity solution shown in Fig. 6.1 indicates an adiabatic wall condition. It was shown by Mack (1969) that supersonic flow past an adiabatic flat plate also displays two-mode neutral curves for Mach number greater than 3.7 and when the Mach number increases further to 4.8 then these two modes merge. These results of supersonic flows are also given in White (1991). It seems that the appearance and subsequent merger of two unstable modes in supersonic flows are related to the basic heat transfer effects studied here for adiabatic flows. From Figs. 6.6 to 6.9, it is seen that both the Re_{cr} progressively reduces as K increases. The frequency for the upper critical Reynolds number increase slightly with K while the frequency corresponding to lower critical Reynolds number remains virtually at the same high value.

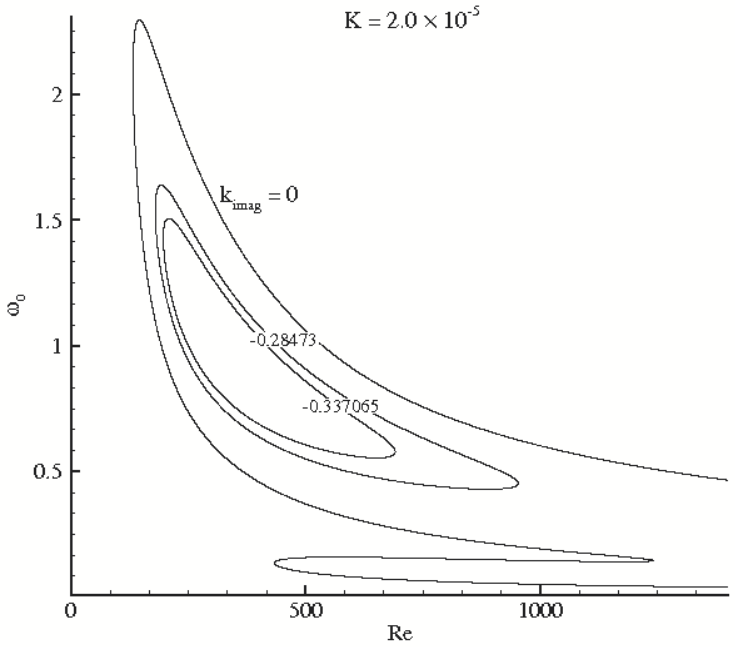

Figure 6.8 Spatial amplification contours shown in $(Re - \omega_0)$ plane for K $= 2.0 \times 10^{-5}$. For the neutral curve $k_{imag} = 0$ as indicated by the outer contour.

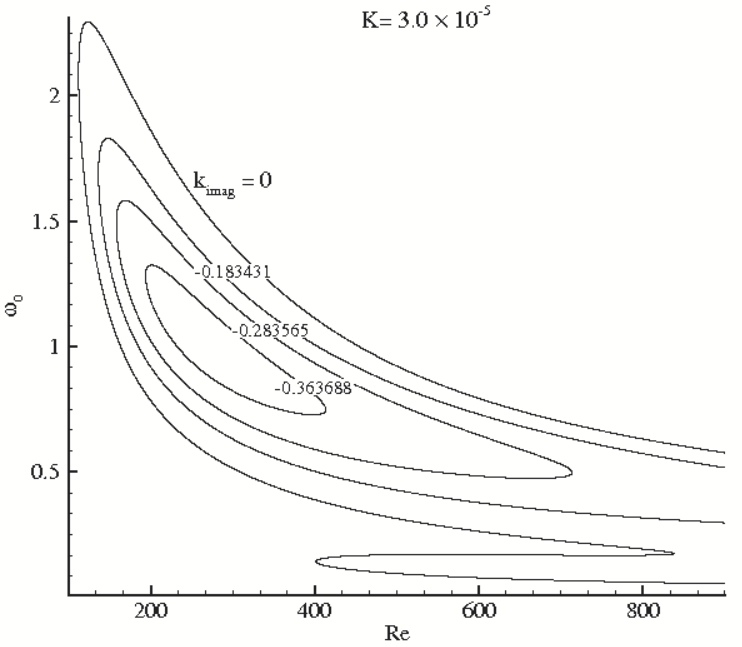

Figure 6.9 Spatial amplification contours shown in $(Re - \omega_0)$ plane for K $= 3.0 \times 10^{-5}$. For the neutral curve $k_{imag} = 0$ as indicated by the outer contour.

All the properties of the neutral curve and the maximum growth rate is noted in Table 6.4- where the two Re_{cr} has been separately identified for the two lobes. The two lobes are connected at $Re_m = 5298.5$ for $K = 5 \times 10^{-6}$. Thus, one can state that this K is the critical parameter when the instability changes heat transfer properties violently.

Table-6.4

Case	K	Re^1_{cr}	Re^2_{cr}	ω^1_{cr}	ω^2_{cr}	Re_m	k_i^{m1}	k_i^{m2}
1	0.0	519.01	–	0.120	–	–	-0.007464	–
2	1.0 X 10^{-6}	513.6	–	0.121	–	–	-0.01355	–
3	5.0 X 10^{-6}	493.5	230.49	0.127	2.174	5298.5	-0.01745	-0.568297
4	1.0 X 10^{-5}	470.9	174.40	0.128	2.160	2524.4	-0.01810	-0.495517
5	1.5 X 10^{-5}	449.7	148.80	0.131	2.182	1658.2	-0.01831	-0.457491
6	2.0 X 10^{-5}	433.5	133.34	0.136	2.211	1240.1	-0.01844	-0.43237
7	3.0 X 10^{-5}	401.1	112.00	0.144	2.104	838.2	-0.01858	-0.399403

In Table 6.4, there are two critical Reynolds number and circular frequencies listed corresponding to the lower and upper lobes of the neutral curves, respectively. Listed k_i^{m1} corresponds to the maximum growth rate exponent of the lower lobe (hydrodynamic mode) and k_i^{m2} corresponds to the maximum growth rate exponent of the upper lobe (thermal mode). All these data are obtained from Figs. 6.3 to 6.9. It is noted that both the critical Reynolds numbers decrease with K. The spatial growth rate exponent for the hydrodynamic mode increases with K. However, the other spatial growth rate exponent has a typical behavior that shows this mode to appear suddenly with a large growth rate, that keeps becoming smaller with increase of K. Interestingly exactly a similar behavior was noted by Mack (1969) for adiabatic supersonic flow past a flat plate (as shown in Figure 1.19 of White (1991))- where it was seen that a second mode appeared at a Mach number of 3.7 with rapid increase of temporal growth rate. This growth rate peaked to a maximum and then decreased smoothly with further increase of Mach number. From Table 6.4 it is found that K plays an identical role for mixed convection problem. The critical value of K is somewhere in between 4×10^{-6} and 5×10^{-6}.

6.5.3 Eigenfunctions of The Mixed Convection Problem

Some representative eigenfunctions have been shown next in Figs. 6.10 and 6.14, that have been obtained by solving (6.4.70) from the wall to the free stream, with a prescribed function value ($\phi_r = 1$) at the wall.

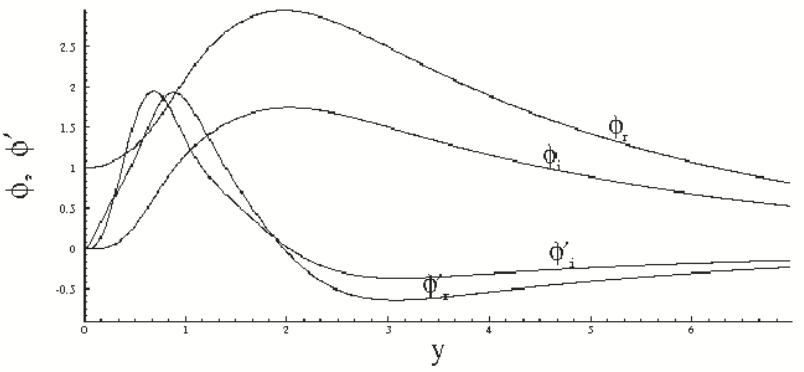

Figure 6.10 Eigenfunction calculated solving equation (6.4.70) for K = 1.0×10^{-6}, Re=1000, and $\omega_0 = 0.1$.

Once again, the use of CMM allows a straight forward integration of the equation without any special treatment. For this equation, the second compounds are the variable coefficients and they were obtained earlier with 2000 interior sub-intervals. Hence the usage of Runge-Kutta method yields solutions at 1000 points located at equal intervals between Y_∞ and zero. It is noted that the eigenfunction is obtained in terms of the three modes that decay with height- whose asymptotic variation is given by (6.4.15). Depending on the eigenvalue, one can associate a physical variable with this eigenfunction. For example, Fig. 6.10 corresponds to a case for which the hydrodynamic mode is predominant and the choice of parameters ($K = 1 \times 10^{-6}$; $Re = 1000$ and $\omega_0 = 0.1$), the eigenfunction represents an unstable mode with the highest growth rate. It is also seen that the depicted eigenfunctions (ϕ and ϕ') represent the normal and streamwise components of disturbance velocity.

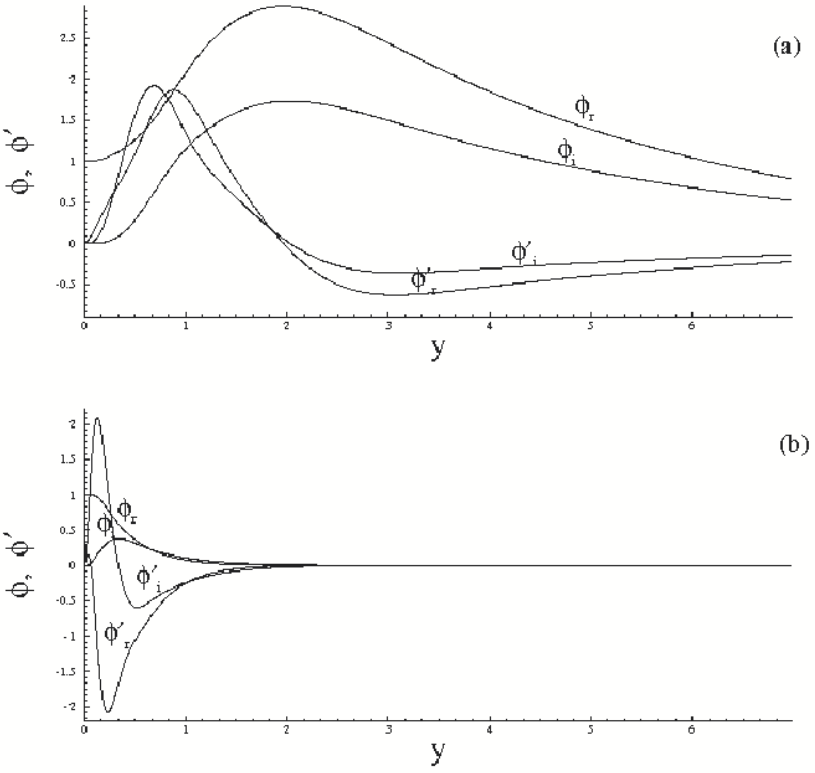

Figure 6.11 Eigenfunction calculated solving equation (6.4.70) for K = 5.0×10^{-6}**, Re=1000 and (a)** $\omega_0 = 0.1$**, and** $\omega_0 = 0.7$.

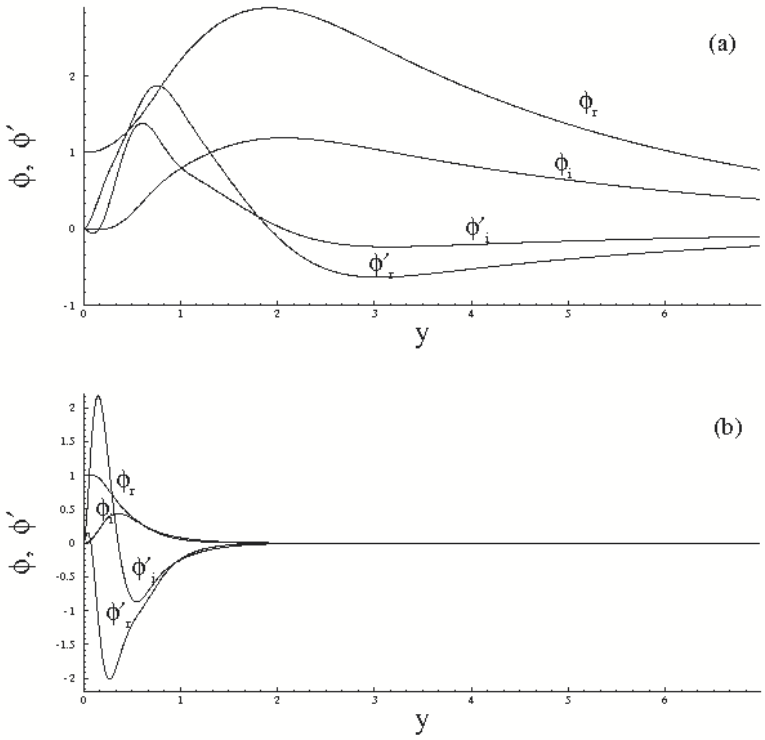

Figure 6.12 Eigenfunction calculated solving equation (6.4.70) for K $= 1.0 \times 10^{-5}$**, and (a) Re=1800,** $\omega_0 = 0.09$**, (b) Re=450,** $\omega_0 = 1.0$.

In Fig. 6.11, two sets of eigenfunctions are shown for the case with $K = 5 \times 10^{-6}$ and $Re = 1000$. In Fig. 6.11(a) the case corresponds to $\omega_0 = 0.1$ for which the hydrodynamic mode attains its maximum growth and thus the eigenfunctions once again represent the disturbance velocity components. In Fig. 6.11(b) the case corresponds to $\omega_0 = 0.7$ and the eigenvalue for this case indicates the thermal mode to be at its maximum growth rate. Hence the plotted function corresponds to the disturbance temperature field.

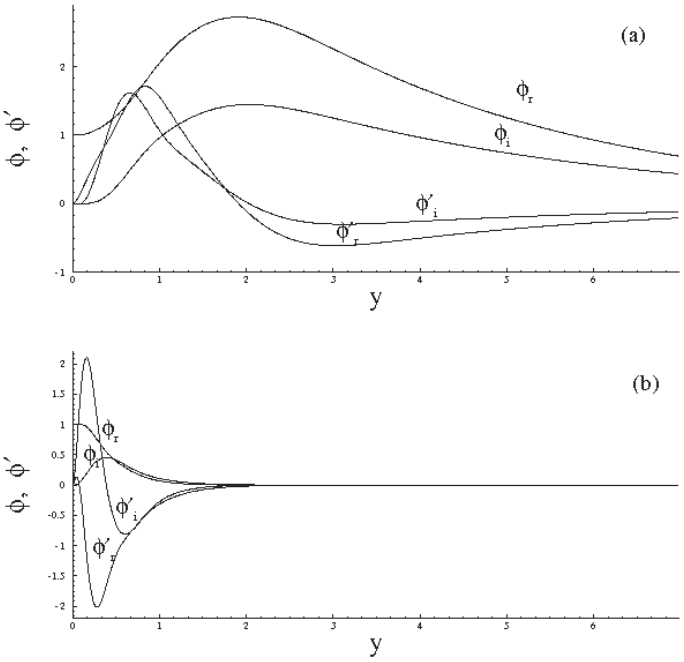

Figure 6.13 Eigenfunction calculated solving equation (6.4.70) for $\mathbf{K = 1.5 \times 10^{-5}}$, and (a) Re=1200, $\omega_0 = 0.1$, (b) Re=400, $\omega_0 = 1.0$

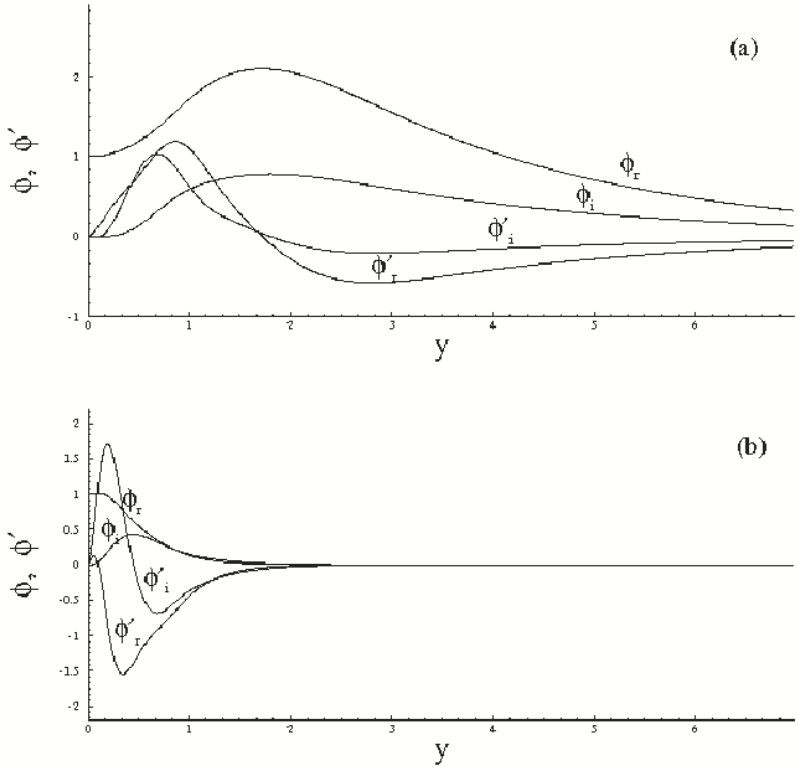

Figure 6.14 Eigenfunction calculated solving equation (6.4.70) for $\mathbf{K} = 3.0 \times 10^{-5}$, and (a) Re=700, $\omega_0 = 0.15$, (b) Re=280, $\omega_0 = 1.0$

In Figs. 6.12 to 6.14, similar eigenfunctions are shown for the identical parameter combinations for which the hydrodynamic and thermal modes are most unstable and thus represents disturbance velocity and temperature fields.

6.6 Conclusions and Outlook

Results of an analysis has been presented here for spatial stability properties of a mixed convection boundary layer developing over a heated horizontal flat plate. A similarity solution (as given by (6.3.11) and (6.3.13)) for the mean flow is used following Schneider (1979). Such boundary layers are characterized by the buoyancy parameter ($K = Gr/Re^{5/2}$) and is solved only for adiabatic wall conditions.

Under the parallel flow approximation, the spatial stability problem has been formulated using the compound matrix method (CMM)- based on previous work of Ng & Reid (1985), Sengupta (1992) and Allen & Bridges (2003) for hydrodynamic stability problems. One of the advantages of CMM is that it allows solving stability problems using traditional ODE solver- as the *stiffness* of the equation is removed at the formulation stage itself. This also allows obtaining the eigen-spectrum without any spurious eigenvalues. Such an analysis for mixed convection boundary layer revealed that there are two types of eigen solutions, that have been termed as hydrodynamic and thermal modes due to physical reasons. Some representative results for eigen-spectrum are shown in Fig. 6.2 and Tables 6.1 to 6.3 for different values of the buoyancy parameter, K. The properties in Table-6.1 for the first three eigen modes match identically with the results published earlier in Sengupta *et al.* (1994) for the stability of Blasius profile obtained by solving a fourth order system. This provides a validation of methodologies developed here for the mixed convection problem. One of the most important findings of the present work is that for $K \geq 5 \times 10^{-6}$, the stability property is seen to change drastically with the appearance of a very unstable thermal mode.

The sudden appearance of a new mode in the present study is similar to what has been reported by Mack (1969) (also reported in White (1991)) for adiabatic supersonic flow past a flat plate when Mach number is increased. Present results show a similar behavior with increase in K for low speed flow, indicating the centrality of heat transfer as the main reason for such sudden appearance of new modes.The neutral curves and spatial growth rates for different values of K have also been calculated and shown in Figs. 6.3 to 6.9. For the reason mentioned above, the qualitative nature of the neutral curve also changed for $K \geq 5 \times 10^{-6}$, with the appearance of two-lobed neutral curves. The lower lobe is similar to what one obtains for isothermal flows and hence termed as the hydrodynamic mode. The upper lobe appears due to the heat transfer and represents high-frequency high growth rate unstable modes. Hence, this mode is termed here as the thermal mode. The growth rate of the thermal mode is seen to be few hundred times more than the most unstable hydrodynamic mode. Various critical parameters associated

with the neutral curves of mixed convection flows are cataloged in Table 6.4. This clearly shows that the critical Reynolds number decreases from 498.3 to 230.49 when K increases from 4×10^{-6} to 5×10^{-6} due to sudden appearance of the thermal mode. The last two columns of Table 6.4 also show relative importance of these two modes in deciding flow transition. Some representative eigenfunctions have been shown in Figs. 6.10 and 6.14 obtained using CMM for the first time. Depending on the values of different parameters, one can associate the eigenfunctions with the velocity and the temperature fields or a combination of the two. Existence of a critical K above which flow transition changes qualitatively and explosively, is a finding of important consequences. This implies that beyond this critical K, heat transfer changes the dynamics of the flow completely. This would be of prime importance, whenever convective heat transfer process is involved in fluid flow - as in atmospheric boundary layer due to man made heat addition, the instability property of the geophysical fluid dynamical system would change dramatically above a critical value of K. It would also be interesting to investigate spatial stability properties of heat convecting flows past vertical and inclined plates. The existence of a violent thermal mode shows the need to re-evaluate transition prediction methodologies for flow problems involving heat transfer.

Chapter 7

COMBUSTION AND CFD FOR COMBUSTION

Dr. Thierry Poinsot
CNRS/Inst. de Mécanique des Fluides de Toulouse
Toulouse, France

7.1 Introduction

The following chapters present an overview of combustion and of CFD (Computational Fluid Dynamics) for combustion. The objective is not to repeat classical textbooks on these topics [379; 306; 288; 334; 340] but to focus on the place of instabilities in reacting flows and in CFD for reacting flows. These instabilities are found at many levels:

- Instabilities exist in individual flame fronts and lead to the formation of cells and of various unstable modes depending on molecular transport of chemical species and heat [379; 266].
- Like any shear flow, reacting flows are submitted to hydrodynamic modes [273; 297] and to vortex formation.
- Acoustics play a major role in reacting flows: by coupling with heat release, they are the source of a major problem in many combustion devices: combustion instabilities [379; 340] which can induce high vibration levels and, in extreme cases, destroy combustion hardware in a few seconds.
- Instabilities are present in the physical problem studied but they are also present in the numerical methods used to simulate these mechanisms. Most high-fidelity numerical schemes required for Computational Fluid Dynamics exhibit low dissipation and therefore multiple non-physical instabilities (wiggles) arise which can require significant efforts to be kept under control [374; 362; 340].
- Finally, CFD for reacting flows are performed today on massively parallel machines: these architectures coupled with centered schemes for turbulent flows lead to an additional type of instability linked to the growth of rounding errors and to a new type of instability where the

solution depends on unexpected parameters such as the commutativity errors of addition, the initial condition or the number of processors.

All these phenomena are 'instabilities' even though they correspond to very different physical mechanisms. In many cases, they can couple: for example, in LES of combustion instabilities, the first issue is to be able to control the non physical waves due to the high-order spatial scheme as well as the rounding errors due to massively parallel computing. These instabilities are discussed in the following chapters, starting with a fast description of the context of combustion and of CFD for combustion (Chapter 7), a discussion of waves in reacting flows (Chapter 8), examples of LES in real combustors (Chapter 9), a discussion of two-phase flow combustion (Chapter 10) and a presentation of rounding errors in LES (Chapter 11). Details on the equations which are solved in LES for reacting flows are given in Chapter 10.

7.2 Combustion and Energy Production

Combustion is the unknown heart of most present problems discussed everyday on global change and pollution issues. More than eighty percent of the energy produced on earth is obtained by burning some fossil fuel. This combustion can be produced by burning wood and producing a few Watts or by running 20 meter long industrial turbines producing 200 MWatts. The processes used for combustion can be simplified and non optimized like for wood combustion or highly technological like the combustion in reciprocating engines. This makes combustion the first contributor to our life style, our energy consumption and to the production of pollutants such as NO_x and of green house gas such as CO_2. This also implies that the most important actions which can improve global weather change problems for example are actions related to reacting flows since they are the major source of the problem and the first place to act. Considering that there is no real substitute for combustion at the moment in many applications (aircrafts, cars, energy production), it also means that the optimization of combustion processes is the most effective method to control global change.

7.3 Combustion and Optimization

The optimization of combustion is an ongoing work since 1900 but recent progresses in this field have been tremendous. In the last twenty years, combustion devices have been optimized in terms of efficiency and pollutant emissions to reach norms which were impossible to imagine before. This has been done by the introduction of electronic monitoring and control (especially for car engines) but also by a better understanding of the combustion

phenomenon and an optimization of the parameters of combustion chambers. These parameters are not only the combustion chamber shape: the fuel injection strategy is a key point to control combustion. Most of the recent progress in the field of Diesel engines is due to the high pressure (2000 atm) injectors used to atomize the fuel before combustion. In the field of gas turbine technology, kerosene is now injected in multiple points, atomized by complex swirler devices. Optimizing a combustion chamber is therefore an extremely difficult process and this complexity is obvious when one considers the results of these optimization processes in combustor designs: while the shapes of most civil aircrafts today look the same, all combustion chambers are different showing that the optimum is by no means simple to define.

What makes combustors optimization even more difficult is the multiple non linearities and instabilities found in reacting flows:

- Clearly, minimizing pollutant is easy to obtain by simply injecting less fuel in a chamber. The problem however is that below a certain equivalence ratio (i.e. below a certain amount of kg of fuel per kg of air), combustion simply stops [379; 306; 340]. The existence of this flammability limit makes optimization delicate because bringing the combustor close to extinction is dangerous (for aircrafts and helicopters for example, that is definitely something which must be avoided for obvious reasons).

- Optimization of combustion devices must be sought for a whole range of operating conditions. Many chambers can be optimized at one regime (for example, idle conditions in a car) but then this will not be efficient for another regime (for example, in full power conditions). Moreover, a chamber can be optimized for a regime (a gas turbine for example) but that is impossible to ignite or too sensitive to sudden flame quenching.

- The most critical problem encountered since the end of the 20th century in the field of gas turbines is instabilities [263; 322; 313; 340]. Most chambers which were optimized to minimize NOx emissions and maximize efficiency since 1990 have been subject to combustion instability problems İn Europe, the LOW NOx projects initiated by the European Commission are now being continued through combustion instability studies because the gains in NOx and efficiency are often wasted by the impact of combustion instabilities. Next Section will focus on this issue.

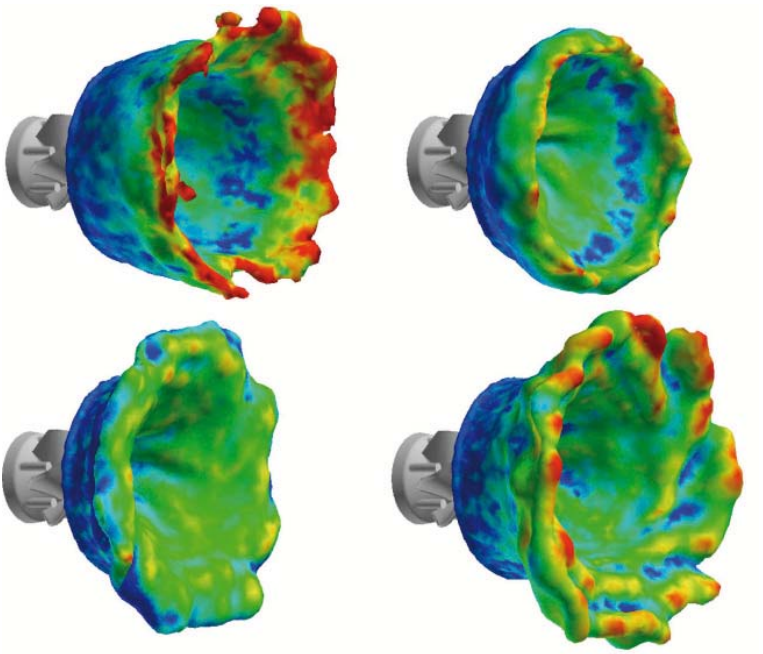

Figure 7.1. Snapshots of flame position (isosurface of temperature) during one oscillation cycle at 120 Hz in an industrial gas turbine [285].

7.4 Combustion and Instabilities

Reacting flows are compressible flows. They exhibit hydrodynamic instabilities (absolute and convective type [297]) but since acoustics are an intrinsic feature of combustion chambers, reacting flows are also submitted to acoustic / combustion instabilities which can be extremely strong [379; 270; 340]. These waves are often coupled to hydrodynamic modes.

The fact that flames can couple with acoustics has been known for a long time [344], even though it is still not fully understood. Since acoustic waves can propagate in any direction in subsonic flows (which is the case in most combustors), they can create a feedback from any point of the flow to any other point, thereby creating multiple paths for absolute instabilities. More importantly, combustion instabilities are difficult to predict and are usually discovered at a late stage during the development of engine programmes so that they represent a significant industrial risk. These instabilities take various forms:

- In steady combustors like gas turbines, instabilities can lead to oscillations of all flow parameters, reaching levels which are incompatible with the normal operation of the chamber. High levels of structural oscillations are found, very high levels of RMS pressure can be observed due to this problem. In a given chamber, while normal turbulent combustion usually leads to 10 to 100 Pa RMS pressure levels, it is not uncommon to see chambers where the RMS pressure reaches 20000 Pa (180 dB) when a combustion instability begins. At these levels, the acoustic velocity associated with the RMS pressure can reach 1 to 20 m/s so that the perturbations induced by the acoustic field are absolutely not negligible. In such cases, the engine structure can fail, the fuel injector can burn, the flame might totally quench or flashback. Flashback is a phenomenon encountered when the acoustic velocity is larger than the mean flow leading to flow reversal in the combustor inlet: in other words, the flow leaves the combustor through the inlet instead of entering it; the flame does the same and ends up upstream of the combustion chamber, in a zone which was not designed to sustain high temperatures. Combustion instabilities have been the source of multiple failures in rocket engines, as early as the Saturn or the Ariane 4 project, in aircraft engines (main chamber of post combustion chamber), in industrial gas turbines, in industrial furnaces, etc. Fig. 7.1 shows an example of simulation of 'mild' oscillation in a gas turbine [285] where the flame position (visualized by an isosurface of temperature colored by axial velocity) pulsates strongly at four instants of a cycle occurring at 120 Hz). For such a mild oscillation, a limit cycle is obtained and the chamber can operate for a long time without problem except for a high noise level.
- In piston engines or in pulse combustors (such as the one used in German V 1 rocket during the second world war) where an external periodic motion or timing is imposed, time averages cannot be used any more and averaging based on realizations must be used. For such flows, instabilities take other forms. The most famous one is cycle-to-cycle variations. Fig. 7.2 shows a simulation of combustion [349] in a four-valve four-stroke engine where all phases are explicitly computed (intake, compression, combustion, exhaust). These cycles are all produced in the same engine and Fig. 7.2 displays the reaction rate at exactly the same crank angle. However, none of these cycles is similar. In some extreme cases, certain cycles can actually not ignite or not burn at all. Such mechanisms, called cycle-to-cycle variations, are still not understood and are the source of major problems: one 'bad' cycle every 100 cycles is enough to increase NOx (nitrogen oxide)

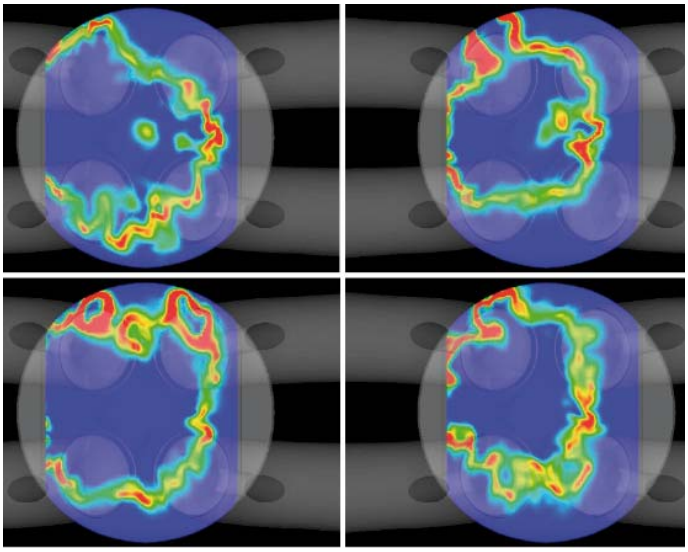

Figure 7.2. Snapshots of reaction rate in a simulation of piston engine at four successive cycles for the same crank angle. None of them is the same.

and CHx (unburnt hydrocarbons) emissions by a factor of 100 or to decrease the power of a Formula One engine by 1 percent. The source of these differences from one cycle to another one is obviously some type of instability. It can be an intrinsic bifurcation of the flow within the chamber or a coupling with the acoustic waves in the intake and exhaust pipes of the engine.

Predicting and controlling combustion instabilities is a major challenge for combustion research. Today, the most promising path is to understand these phenomena using Large Eddy Simulation methods: those are able to predict these combustion oscillations [340; 321; 360] something which was impossible 10 years ago with classical Reynolds Averaged Navier -Stokes methods. The following sections describe turbulent combustion and the various methods used to study combustion numerically.

7.5 Turbulent Combustion

Instabilities are not the only difficulty to study combustion. Almost all combustion devices have high Reynolds number flows where the flow is turbulent. Flames and turbulence exhibit numerous modes of interactions.

Experimentalists have known for a long time that changing the turbulence level before starting combustion in a vessel may change the time needed for total combustion and, accordingly the turbulent flame speed. In his book [307], Laffitte presented combustion times measured in a stirred vessel in 1918 [377; 378] showing that the combustion rate is maximum (the combustion time is minimum) when the reactants are mixed in stoichiometric proportions and increases when the flow becomes turbulent (Fig. 7.3). At that time, Laffitte noted that " the turbulent flame speed was always larger than two times the laminar flame speed." The factor of two observed by Wheeler is not generic of all turbulent flames and more precise measurements lead to multiple empirical and approximate relations [251; 291].

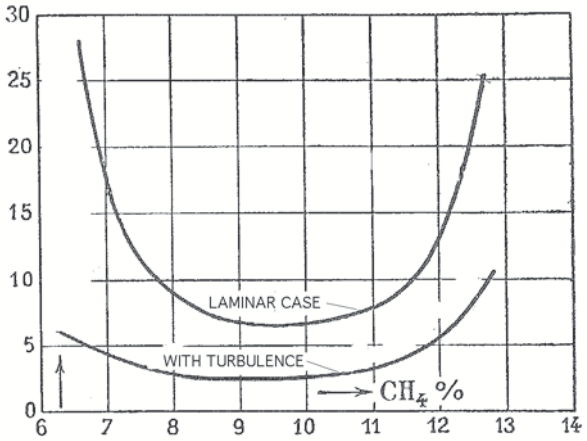

Figure 7.3. The combustion time (the time needed to reach the maximum pressure in a closed vessel) for a methane/air flame with and without turbulence, plotted as a function of the proportion of CH_4 in the reactant mixture, corresponding to the equivalence ratio ϕ (stoichiometric proportions correspond to about 10 % of methane). Time units correspond to 10^{-2} seconds ([377; 307]).

7.6 DNS, LES and RANS for Combustion

Turbulent combustion is encountered in most practical combustion systems such as rockets, internal combustion or aircraft engines, industrial burners and furnaces, while laminar combustion applications are almost limited to candles, lighters and some domestic furnaces. Studying and modeling

turbulent combustion processes is therefore an important issue to develop and improve practical systems (to increase efficiency and reduce fuel consumption and pollutant formation). As combustion processes are difficult to handle using analytical techniques, numerical combustion for turbulent flames is a fast growing area.

The three main numerical approaches used in turbulence combustion modeling are Reynolds averaged Navier Stokes (RANS) where all turbulent scales are modeled, direct numerical simulations (DNS) where all scales are resolved and large eddy simulations (LES) where larger scales are explicitly computed whereas the effects of smaller ones are modeled:

- Reynolds Averaged Navier Stokes (or RANS) computations have historically been the first possible approach because the computation of the instantaneous flow field in a turbulent flame was impossible. Therefore, RANS techniques were developed to solve for the mean values of all quantities. The balance equations for Reynolds or Favre (mass-weighted) averaged quantities are obtained by averaging the instantaneous balance equations. The averaged equations require closure rules: a turbulence model to deal with the flow dynamics in combination with a turbulent combustion model to describe chemical species conversion and heat release. Solving these equations provides averaged quantities corresponding to averages over time for stationary mean flows or averages over different realizations (or cycles) for periodic flows like those found in piston engines (phase averaging). For a stabilized flame, the temperature predicted with RANS at a given point is a constant corresponding to the mean temperature at this point (Fig. 7.4).
- The second level corresponds to large-eddy simulations (LES). The turbulent large scales are explicitly calculated whereas the effects of smaller ones are modeled using subgrid closure rules. The balance equations for large-eddy simulations are obtained by filtering the instantaneous balance equations. LES determine the instantaneous position of a "large scale" resolved flame front but a subgrid model is still required to take into account the effects of small turbulent scales on combustion. LES would capture the low-frequency variations of temperature (Fig. 7.4).
- The third level of combustion simulations is direct numerical simulations (DNS) where the full instantaneous Navier-Stokes equations are solved without any model for turbulent motions: all turbulence scales are explicitly determined and their effects on combustion are captured. DNS would predict all time variations of temperature (Fig. 7.4) exactly like a high-resolution sensor would measure them in an experi-

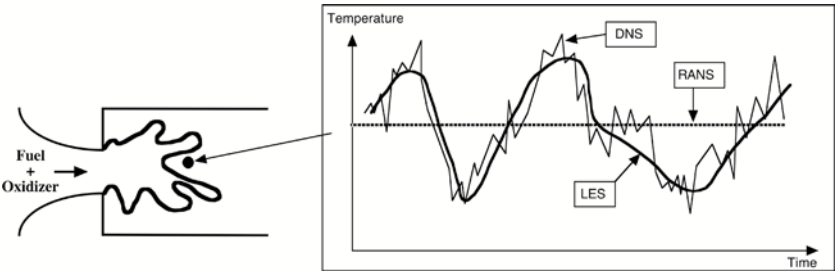

Figure 7.4. Time evolutions of local temperature computed with DNS, RANS or LES in a turbulent flame brush.

ment. Developed in the last twenty years, thanks to the development of high performance computers, DNS have changed the analysis of turbulent combustion but are still limited to simple academic flows (simple geometries and somewhat lower Reynolds numbers).

In terms of computational requirements, CFD for non-reacting and reacting flows follow similar trends: DNS is the most demanding method and is limited to fairly low Reynolds numbers and simplified geometries. LES works with coarser grids (only larger scales have to be resolved) and may be used to deal with higher Reynolds numbers but require subgrid-scale models. The computation quality and the results accuracy are directly linked to the subgrid models. In current engineering practice, RANS is extensively used because it is less demanding in terms of resources but its validity is limited by the closure models describing turbulence and combustion.

The advantage of RANS is its applicability to any configuration and operating conditions: a standard RANS mesh can contain 10^5 points and the domain of calculation may be as large as needed. For example Fig. 7.6a shows an isosurface of mean high temperature (1100 K) in a turbulent premixed flame stabilized by swirl obtained with RANS. The configuration corresponds to a 1:1 burner of a large-scale industrial gas turbine [358]. On the isosurface, the average temperature is 1100 K but RANS does not explicitly solve for possible turbulent fluctuations around this mean value.

Large-eddy simulations are an intermediate tool between DNS and RANS. LES methods have been used extensively in many non reacting flows and have provided reliable predictions in a variety of applications (see for example [295], [325] or [252]). The treatment of reacting flows with similar concepts is less well established. While some advances have been made [303; 286; 300; 283; 287; 323; 373; 254; 261; 337; 358]), research is still required on this topic. It is in particular necessary to construct methods

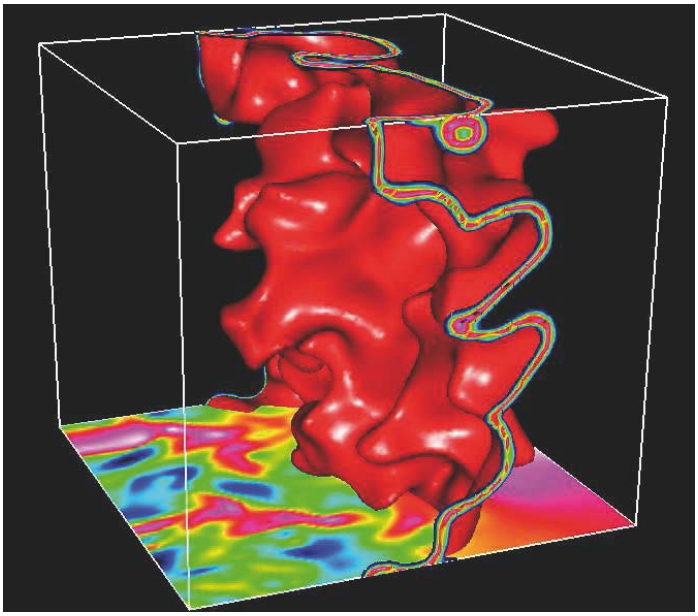

Figure 7.5. DNS of a premixed flame interacting with three-dimensional isotropic turbulence [261]. An isosurface of temperature is visualized. The reaction rate is presented in two planes which are normal to the mean flame front. The vorticity field, corresponding to turbulent motions, is also displayed in the bottom plane.

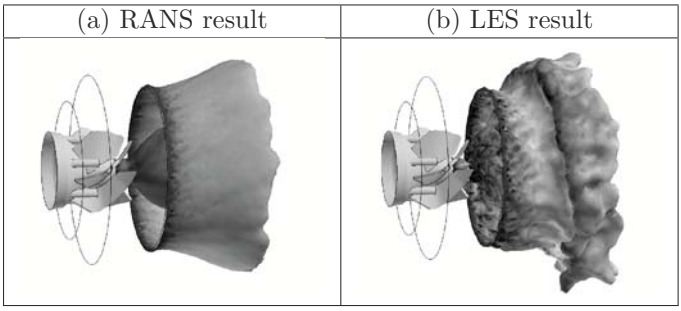

Figure 7.6. Isosurface of temperature (1100 K) during turbulent combustion in a swirled combustor (see geometry in [357]). (a): RANS (mean field), (b): LES (instantaneous field).

for the calculation of the "large scale" flame front and to develop subgrid-scale models. Fig. 7.6b gives an example of instantaneous LES field [357] in the same geometry as the RANS result (Fig. 7.6a). Obviously, the instantaneous flame surface obtained with LES contains much more turbulent scales than the averaged field given by the RANS code.

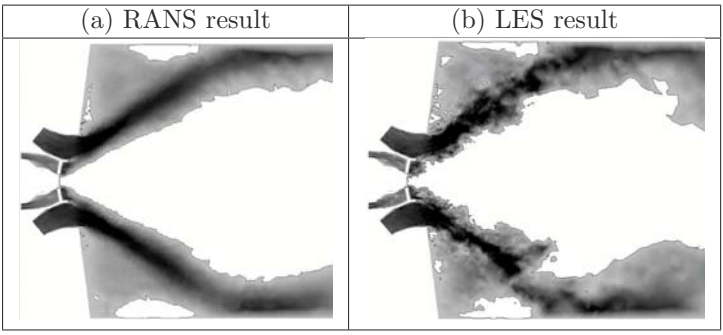

Figure 7.7. Axial velocity fields during turbulent combustion in a swirled combustor (see geometry in [357]). (a): RANS (mean field), (b): LES (instantaneous field). The zones within the black line are backflow regions (A. Giauque, private communication).

The velocity fields obtained by RANS or LES also illustrate the basic differences between the two approaches (Fig. 7.7). While the field of axial velocity obtained with RANS is very smooth (Fig. 7.7a), the LES field exhibits much more small structures: in terms of physics, the LES captures more turbulent activity; in terms of numerical resolution, the grid required for RANS can be very coarse because gradients are small. On the other hand, for LES, the grid must be fine and the numerical method non-dissipative in order to capture the small motions evidenced in Fig. 7.7b. Considering also that RANS codes compute only one state (the converged flow) while LES codes must resolve the flow in time, the cost of a typical LES computation is often 100 to 1000 times higher than a RANS computation. However, despite its cost, LES is well adapted for many combustion studies:

- Large structures in turbulent flows depend on the system geometry whereas small structures are generally assumed to have more universal features. Accordingly, models are probably more suited to describe these small structures.
- Most reacting flows exhibit large scale coherent structures [267]. Such structures are also observed when combustion instabilities occur. These instabilities are due to a coupling between heat release, hydrodynamic

flow field and acoustic waves [340]. They have to be avoided because they induce noise, variations of the system characteristics, large heat transfers and may lead to the system destruction. LES is a powerful tool to predict the occurrence of such instabilities and to numerically test passive or active control systems.

- The knowledge of large-scale turbulent motions may be used to infer the effects of the unresolved smaller ones: for example, during the Kolmogorov cascade, the energy flows from large (resolved) structures to (unresolved) smaller scales. In fact, subgrid scale models are generally based on similarity assumptions between large and small scales.
- Large-eddy simulations also allow a better description of the turbulence/combustion interactions. As large structures are explicitly computed in LES, instantaneous fresh and burnt gases zones, where turbulence characteristics are quite different, are clearly identified, at least at the resolved level (see, for example, Fig. 7.7b). This is a significant advantage of LES compared to RANS in which models have to take into account (at a given spatial location) the probability of being in fresh or in burnt gases.

Chapter 8

WAVES IN REACTING FLOWS

Dr. Thierry Poinsot
CNRS/Inst. de Mécanique des Fluides de Toulouse
Toulouse, France

8.1 Physical Waves In Reacting Flows

A reacting flow can feature multiple waves:

- Hydrodynamic instabilities can be generated in the sheared regions found in all combustors. A specific aspect of many reacting flows is that the baseline flow is swirled [369; 260]. Strongly swirling flows (Fig. 8.1) induce flow reversal and large recirculation zones which, like acoustic waves, favour absolute instabilities. One of these is the PVC (precessing vortex core: Fig. 8.2) which appears in many swirling flows of large intensities and create an oscillation of the flow around the burner axis.
- Acoustic waves are found in all burners. Combustion chambers are necessarily closed domains, surrounded by walls, and therefore prone to develop acoustic eigenmodes [270]. These modes can be longitudinal modes for which the combustor acts like a music instrument (organ for example) resonating with some excitation mechanism. In musical instruments, excitation is produced by vortices induced in the flow; in combustion chambers, unsteady combustion is the excitation source. Modes can also be transverse and lead to higher frequency instabilities. These modes are quite destructive for example in rocket engines or in post combustion chamber of fighter engines.
- Flames are also excellent generators of instabilities. Textbooks [379; 380; 266] describe how the strong density gradients or the differential diffusion of species can lead to flame front instabilities.
- Some instabilities are more 'global' and involve not only the flow but also the structure or the ducts feeding the combustor. For example, the POGO effect in rockets appears when the reacting flow resonates

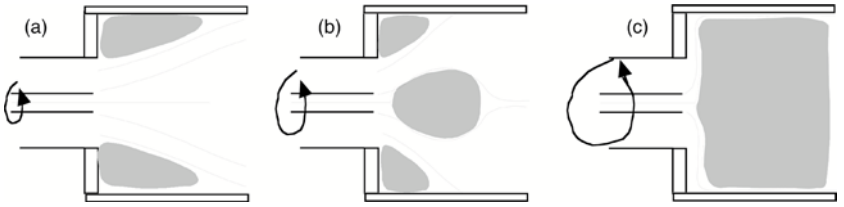

Figure 8.1. Flow topologies in a swirled combustor: (a) low swirl, (b) medium swirl, (c) high swirl. The gray zones correspond to zones of the flow where the velocity is from right to left. For large values of swirl, a recirculation zone occupies most of the chamber and the flow follows the walls.

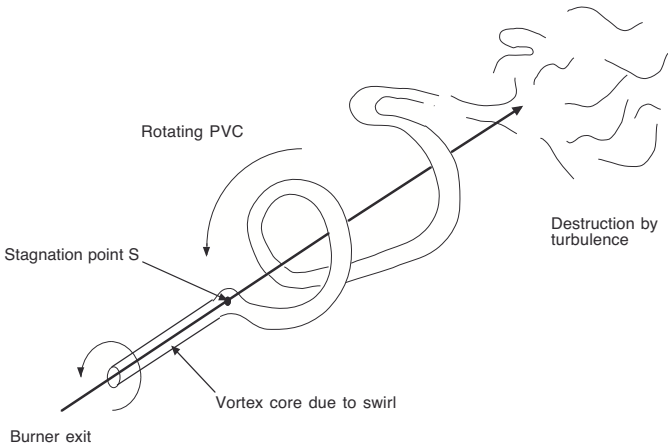

Figure 8.2. Precessing vortex core (PVC): the swirl axis oscillates around the geometrical axis.

with the structure itself and with the feeding lines of the combustor. These instabilities are not studied here.

Many of these instabilities are linked: hydrodynamic instabilities can create vortices in combustion chambers; these vortices contain fuel and oxidizer and can burn after a certain delay, providing the source of excitation for the acoustic mode. this acoustic mode then can trigger new vortices [297].

Like in classical acoustics in cold flows [304], wave equations can also be derived for reacting flows but they are much more complex [270; 340]. Af-

Non-reacting flows	$c^2\nabla^2 p' - \dfrac{\partial^2 p'}{\partial t^2} = -\gamma\bar{p}\nabla\vec{u} : \nabla\vec{u}$
Reacting flows	$\nabla.c^2\nabla p' - \dfrac{\partial^2 p'}{\partial t^2} = -\gamma\bar{p}\nabla u : \nabla u - (\gamma-1)\dfrac{\partial\dot{\omega}_T}{\partial t}$

Table 8.1. Comparison of wave equations for non-reacting and reacting flows: c is the sound speed, $\dot{\omega}_T$ is the heat release due to combustion and $\bar{p}$ the average pressure

ter rather long derivations and some simplifications (for example, low Mach number), a wave equation in a reacting flow can be derived and its comparison with the non reacting case is quite interesting. Table 8.1 compares these wave equations in non-reacting and reacting flows. For the non-reacting case, the $\nabla\vec{u} : \nabla\vec{u}$ term is retained and is responsible for turbulent flow noise. The main complexity brought by combustion is the variable sound speed c_0 which must be kept in the ∇ operator and the additional source term found on the RHS terms for the pressure equation with combustion. This source term is responsible for combustion noise and instabilities. The linearized form of Table 8.1 is sufficient to capture the growth of unstable modes but non-linear extensions are required to describe non-linear effects seen in many limit-cycles.

Two methods can be used to study combustion instabilities:

- LES: the first one is to use brute force and directly solve the Navier Stokes equations with combustion, typically with LES [364; 358; 355].
- Helmholtz solvers: the second one is to solve the wave equation of Table 8.1, providing a model for the unsteady reaction rate $\dot{\omega}_T$ and solving the corresponding equations either in the time domain or in the frequency domain [270; 305; 368; 258; 360; 331].

These two methods are similar to what is found in the study of hydrodynamic instability where LES is replaced most often by DNS and Helmholtz solvers by Orr Sommerfeld solvers. Both methods have already been used and shown to be efficient: more examples will be provided in Chapter 9. They were also compared in a few cases [350; 321]. LES is much more expensive and cannot work if all boundary conditions are not known precisely. This means that impedances of all inlets and outlets for example are required. Helmholtz formulations also need impedances but since they run faster and can provide all modes (and not only the most excited), they are easier to use when impedances are not known precisely.

A useful quantity to study combustion instabilities is the acoustic energy defined by [340]:

$$e_1 = \frac{1}{2}\rho_0 \vec{u}_1^2 + \frac{1}{2}\frac{p'^2}{\rho_0 c_0^2} \tag{8.1}$$

where index 0 refers to mean values and index 1 to perturbations. The conservation equation for e_1 is [340]:

$$\frac{\partial e_1}{\partial t} + \nabla \cdot f_1 = r_1 \quad with \quad r_1 = \frac{(\gamma - 1)}{\gamma \bar{p}} p' \dot{\omega}_T^1 \quad and \quad f_1 = p' \vec{u}_1 \tag{8.2}$$

where the RHS source term r_1 is a correlation between unsteady pressure p' and unsteady heat release $\dot{\omega}_T^1$. This term is due to combustion and can act as a source or a sink term for the acoustic energy. When r_1 is positive, if the pressure oscillations p' are in phase with the unsteady heat release $\dot{\omega}_T^1$, r_1 acts as a source term for the acoustic energy and the instability is locally amplified. On the other hand, if unsteady heat release is maximum when pressure is minimum, the instability decreases. This qualitative criterion for combustion instability is called the Rayleigh criterion [344]. Although this seems a rather natural statement, many experiments do not actually support this result in a straightforward manner. The index r_1 changes with time and with location: some regions of a given combustor usually exciter the oscillation by burning in phase with pressure (positive r_1) while other regions damp the instability by burning out of phase with pressure [341; 353]. The overall effect of flame/acoustics coupling can only be predicted by integrating Eq. (8.2) over space and time to evaluate the instability growth rate.

8.2 Numerical Waves in High-Fidelity Simulations of Reacting Flows

Predicting combustion instabilities requires an accurate computation of all waves mentioned in the previous section. This requires LES formulations. Unfortunately, LES (like DNS and unlike RANS) can propagate other waves: these waves are purely numerical, often called Q waves [374; 362] and they are a significant difficulty for most high-fidelity simulations like LES or DNS. Q waves are produced by sharp gradients, approximate initial conditions, boundary conditions, etc. They interact with the physical waves, making LES difficult and sensitive to unexpected behaviors. This is an unavoidable price to pay for these simulations. Knowing how these numerical waves interact with physics is a necessary exercise but one which is not often discussed because studying wiggles in simulations is not a very exciting topic.

The main reason why numerical waves have not been discussed much in the CFD community is that most RANS codes use excessive artificial viscosity and large turbulent viscosity levels (due to turbulence models) which kills all numerical waves. They also kill all acoustic waves and all hydrodynamic modes and cannot be used for the present needs of combustion research. Methods which can compute accurately waves in reacting flows must use centered schemes and LES (or DNS) formulations in order to avoid damping all waves (physical and numerical). A convenient way to illustrate this point is to compare the various viscosities playing a role in a CFD code:

- The first viscosity is the laminar viscosity ν. This is the only true flow characteristic and it defines the true Reynolds number of the flow: $Re_{real} = UL/\nu$ where U and L are a reference velocity and length of the flow respectively.
- In most CFD codes, a turbulent viscosity ν_t is added. Even though models providing estimates for ν_t justify these formulations through multiple theories, their first interest in terms of numerical method is that they simply allow the computation to be done by adding viscosity thereby decreasing the Reynolds number really seen by the code.
- Many CFD codes[i] also add an artificial viscosity ν_a. This viscosity can be explicit or it can be hidden, for example in the case of upwind schemes. An important dissipation is also introduced by large time steps and implicit schemes which are commonly used in RANS.

The first consequence of the introduction of two additional viscosities ν_t and ν_a to the true viscosity ν is that the Reynolds number really seen by the code is :

$$Re_{code} = UL/(\nu + \nu_t + \nu_a) \tag{8.3}$$

which is much smaller than Re_{real}. In RANS formulations, the turbulent viscosity introduced by models such as the k-ϵ model can reach 1000 times the physical viscosity. To make the code robust and fast, upwinding and large time steps lead to very high levels of artificial viscosity ν_a. As a result, in a RANS calculation of a turbulent flow, the result is steady: in other words, it is laminar. Of course, it is a laminar flow where the local viscosity is tuned to match the mean characteristics of the mean turbulent flow. But the turbulent character of the flow is completely lost. At the other end of the methods spectrum, DNS methods strive to use $\nu_a = \nu_t = 0$ so that $Re_{code} = Re_{real}$: the price to pay is that all scales must now be resolved spatially (requiring small mesh sizes) and temporally (requiring

[i] Certain numerical methods introduce dissipation terms which are not second order and are more difficult to compare to other viscosities: the well known Jameson approach for example uses a second and a fourth-order dissipation. They are not discussed here.

small time steps). LES formulations have to use non zero values for ν_a and ν_t but these must be kept to very small values. If ν_a and ν_t in a LES are not small, the result will be wrong. The flow featured by LES can actually become laminar.

Method	Physical viscosity	Numerical viscosity	Turbulent viscosity	Capacity to propagate waves
DNS	1	0	0	excellent
LES	1	1 to 10	5 to 50	good
RANS	1	10 to 500	100 to 1000	none

Table 8.2. Orders of magnitude of physical, numerical and turbulent viscosity in DNS, LES and RANS codes. All values are scaled by the laminar viscosity.

Table 8.2 shows typical levels of physical viscosity, turbulent viscosity ν_t and artificial viscosity ν_a reached in a combustion chamber for a standard regime. All viscosities are scaled by the physical viscosity. Note that viscosity affects all scales and not only the small scales. For example, acoustic waves are very strongly dissipated in a RANS code because the turbulent viscosity acts on them too. This is a collateral effect of turbulence models formulated using turbulent viscosities but it implies that such methods cannot be used for the present objectives.

A less pleasant implication of Table 8.2 is that, as soon as high-fidelity methods such as DNS or LES are developed, they have to avoid large values of turbulent and artificial viscosities. This requires small mesh sizes, high-order schemes, small time steps [268; 362; 340]. But even after all these improvements, these methods will remain sensitive to numerical waves [363]. In DNS or LES, numerical waves are intrinsic elements of the simulation and must be controlled by something other than viscosity. This usually means significant improvements of initial and boundary conditions and a careful

Chapter 9

LARGE EDDY SIMULATION OF REAL COMBUSTORS

Dr. Thierry Poinsot
CNRS/Inst. de Mécanique des Fluides de Toulouse
Toulouse, France

9.1 Introduction

The examples presented in this chapter [308; 320] are illustrations of the concepts presented in the previous chapters. They correspond to recent numerical analysis of burners which are typical of most modern high-power combustion chambers, especially of gas turbines: the flame is stabilized by strongly swirled flows, the Reynolds numbers are large, the flow field sensitivity to boundary conditions is high, intense acoustic/combustion coupling can lead to self-sustained oscillations. Flames are stabilized by swirl. Swirl also creates specific flow patterns (a Central Toroidal Recirculation Zone called CTRZ) and instabilities (the Precessing Vortex Core called PVC).

The first example is a small-scale laboratory combustor using an aero-engine gas turbine burner (power: 30 kW) while the second one corresponds to a laboratory-scale staged burner in which self-excited instabilities can be easily triggered by changing the outlet acoustic boundary conditions. In staged combustors, fuel and air are premixed but they are introduced into the chamber at different locations and different equivalence ratios so that partially premixed flames are found inside the burner. All combustors are operated at atmospheric pressure.

The flame/turbulence interaction model is the thickened flame model [269] and boundary conditions are specified using the NSCBC method [339; 329]. The turbulence model is the Smagorinski model or the Wale model [330].

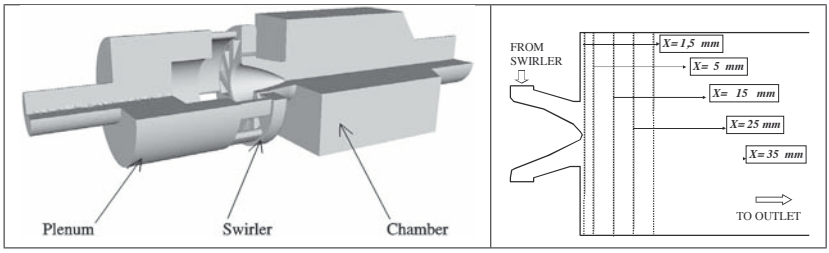

Figure 9.1. Configuration for Case 1 (left). Location of cuts for velocity profiles (right).

9.2 Case 1: Small Scale Gas Turbine Burner

The first example presents typical cold flow fields with swirl (§ 9.2), as well as reacting flow fields (§ 9.2), and compare them with experimental data.

Configuration and Boundary Conditions

The burner of Case 1 uses a swirled injector (Fig. 9.1) where swirl is produced by tangential injection downstream of a plenum. A central hub contributes to flame stabilization. In the experiment methane is injected through holes located in the swirler but mixing is fast so that perfect premixing is assumed for computations. Experiments include LDV (Laser Doppler Velocimetry) measurements for the cold flow as well as a study of various combustion regimes. The dimensions of the combustion chamber are 86 mm $\times$ 86 mm $\times$ 110 mm.

For LES, the critical question of boundary conditions is avoided in Case 1 by extending the computational domain upstream and downstream of the chamber: the swirlers and the plenum are fully meshed and computed and even a part of the outside atmosphere (not shown on Fig. 9.1 for clarity) is meshed to avoid having to specify a boundary condition at the chamber outlet. This procedure is applicable only for certain configurations: a real gas turbine combustion chamber is surrounded by more complex passages for air or by moving parts (the blades of the turbine for example) for which specifying boundary conditions remains much more difficult.

Nonreacting Flow

Average Fields

LES and experimental LDV profiles (measured at DLR Stuttgart) are compared at various sections of the combustion chamber (Fig. 9.1) for average axial (Fig. 9.2), azimuthal (Fig. 9.4), RMS axial (Fig. 9.3) and RMS azimuthal velocities (Fig. 9.5). All mean and RMS velocity profiles are correctly predicted [308]. Considering that this computation has no boundary condition which can be tuned to fit the velocity profiles, these results demonstrate the predictive capacity of LES in such swirling flows (RANS models are usually not well suited to swirling flows). A large central toroidal recirculation zone (evidenced through negative values of the mean axial velocity) develops on the chamber axis. This CTRZ begins at x=2 mm downstream of the hub and is still observed at x=35mm.

Structure of Unsteady Swirling Nonreacting Flows

The RMS fluctuations in both LES and experimental results (Fig. 9.3 and 9.5) are very intense around the axis, close to the injector nozzle (of the order of 20 m/s at $x = 1.5$ mm). These oscillations are typical of most swirled burners. They may be due to:

- a very intense turbulent field,
- an acoustic mode of the chamber or
- a hydrodynamic instability.

First, it is unlikely that random turbulent fluctuations can reach such high values: on the burner axis, Fig. 9.2 and 9.4 show that the mean axial velocity is of the order of 5 m/s and that velocity gradients are not very large. Such a mean flow field cannot explain how the RMS velocity observed on Fig. 9.3 on the axis could be 4 times larger than the mean velocity. Furthermore, spectral analysis of velocity signals in this region reveals that a 540 Hz peak dominates the signal confirming that the source of fluctuations is either acoustic or hydrodynamic type. An useful second step is to compute all acoustic eigenmodes of the rig using a Helmholtz solver. Using the exact geometry of the burner the acoustic eigenmodes of the combustor obtained with such an Helmholtz solver are given in Table 9.1 and none of them matches the 540 Hz frequency. The first mode (172 Hz) is observed neither in LES nor in experiments: this mode is stable. The second mode (363 Hz) is indeed identified in experiments (around 320 Hz) and in LES (around 360 Hz) but only in the plenum and the exhaust pipe. No acoustic mode is identified around 500 Hz. This analysis shows that acoustics are not responsible for the large RMS fluctuations on the burner axis. Finally,

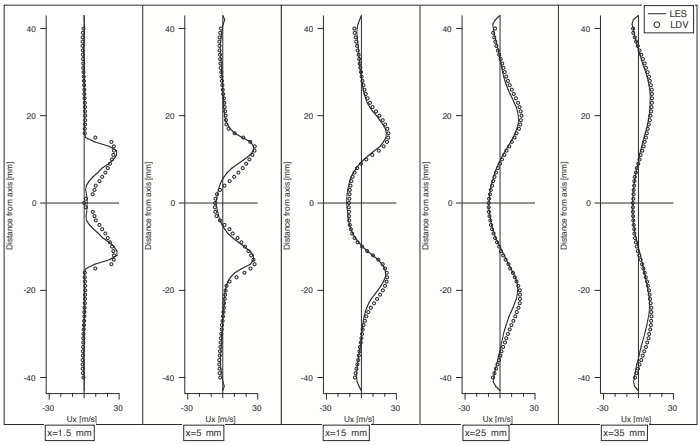

Figure 9.2. Average axial velocity profiles. Circles: LDV; solid line: LES.

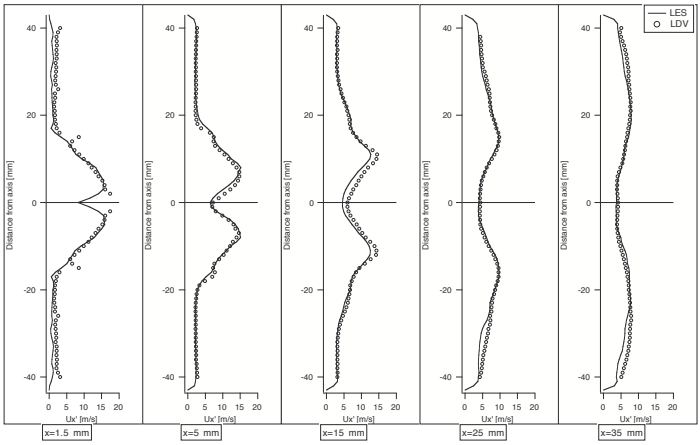

Figure 9.3. RMS axial velocity profiles. Circles: LDV; solid line: LES.

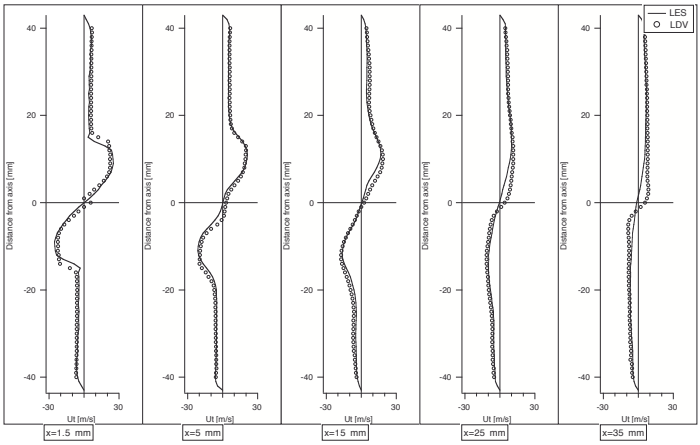

Figure 9.4. Average tangential velocity profiles. Circles: LDV; solid line: LES.

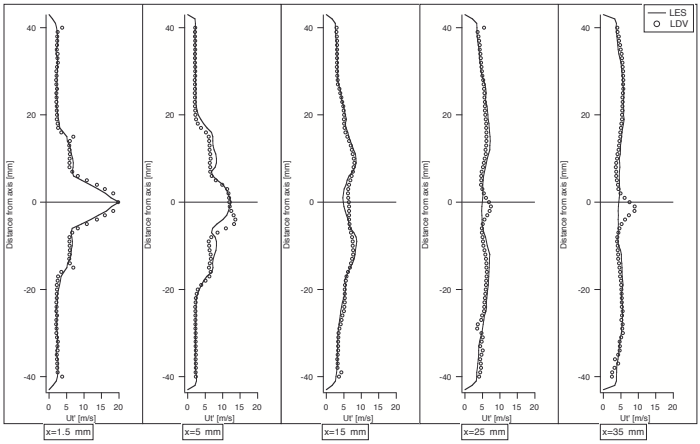

Figure 9.5. RMS tangential velocity profiles. Circles: LDV; solid line: LES.

the existence of a large-scale hydrodynamic structure can be investigated in the LES by plotting an isosurface of low pressure (Fig. 9.6): this diagnostic evidences a large spiral structure rotating around the burner axis at a frequency of 540 Hz. Experimental wall pressure measurements performed inside the chamber also reveal a dominant frequency around 510 Hz. This large hydrodynamic structure called PVC (Precessing Vortex Core) is the actual source of the axis fluctuations observed in Fig. 9.3 and 9.5.

Mode no.	Mode name	Cold flow (Hz)	Reacting flow (Hz)
(1)	Quarter wave	172	265
(2)	Three quarter wave	363	588
(3)	Five quarter wave	1409	1440

Table 9.1. Longitudinal modes of Case 1 predicted by a Helmholtz solver.

Coexistence of Acoustic Modes and Precessing Vortex Core

The previous section shows that two modes control the cold flow structure in Case 1:

- a low amplitude acoustic mode (360 Hz) everywhere in the device and
- a strong hydrodynamic mode (540 Hz) due to the PVC at the burner exit ($0 < x < 5$ cm).

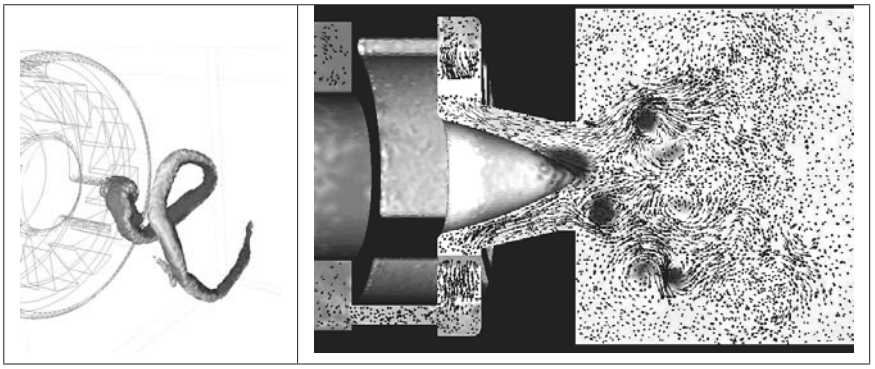

Figure 9.6. Visualization of the PVC mode in Case 1 using an isosurface of low pressure (left) and a field of pressure (gray scale) and velocity vectors in the central plane (right) [308].

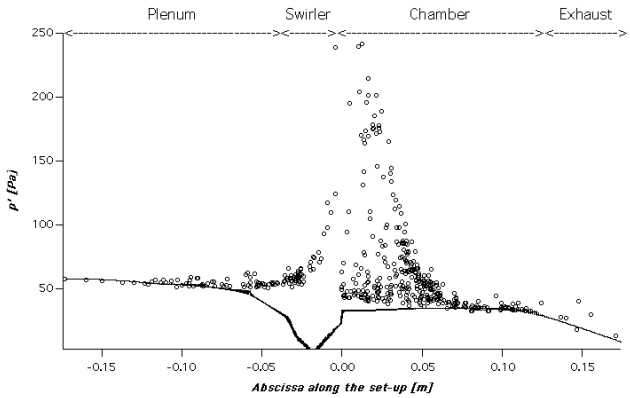

Figure 9.7. Pressure fluctuations amplitude with LES (——) and acoustic code (○) for the non-reacting flow in Case 1[308].

These two modes actually coexist but do not interact. Their respective traces can be found in an analysis of RMS pressure fluctuations because both acoustic and hydrodynamic fluctuations induce pressure perturbations: P' profiles along the burner axis[i], computed both with LES and the Helmholtz solver, are presented in Fig. 9.7. The two codes give similar results in the plenum and in the exhaust, indicating the acoustic nature of the pressure fluctuations in these regions. However, in the swirler and in the first half of the chamber where the PVC is found, the pressure fluctuations given by LES are much larger than the acoustic predictions, because they also contain the effects of the PVC.

The PVC acts acoustically like a rotating solid placed in the flow and partially blocking the swirler exhaust. Such a moving solid acts like an acoustic dipole [336], [304] which radiate weakly: the PVC modifies the pressure field in the chamber but does not affect the pressure field upstream and downstream: this explains why the acoustic mode at 360 Hz is visible and unaffected in the plenum and the exhaust.

[i]Since the acoustic mode structure is longitudinal, P' can be plotted along the burner axis x.

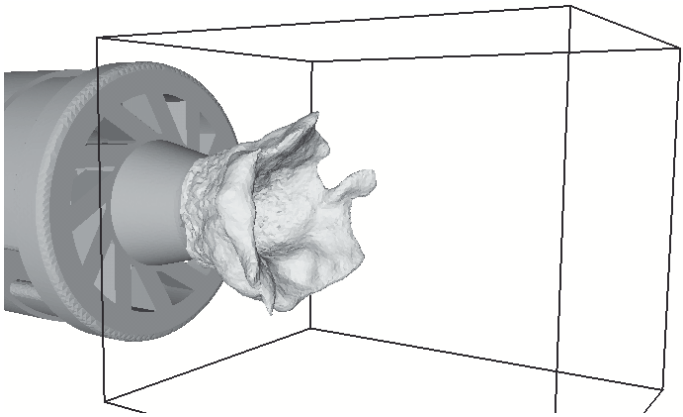

Figure 9.8. Instantaneous 1250 K isosurface (LES data).

Stable Reacting Flow

This section presents results for a stable reacting regime corresponding to an equivalence ratio of 0.75, an air flow rate of 12 g/s, and a thermal power of 27 kW. A snapshot of an instantaneous temperature isosurface (Fig. 9.8) reveals a very compact flame located close to the burner nozzle exit. No comparison is possible with experiments here because temperatures were not measured. The velocity fields, however, were investigated in detail using LDV and are presented in Figs. 9.9 (mean axial velocity), 9.10 (RMS axial velocity), 9.11 (mean tangential velocity) and 9.12 (RMS tangential velocity). The overall agreement between mean LES results and experimental data is good.

Although this regime is considered as a 'stable' case some acoustic activity exists in the burner: two acoustic modes are found experimentally around 300 Hz and 570 Hz and the overall sound level inside the combustor reaches 500 Pa in the LES (more than 140 dB). To identify the nature of these modes, the Helmholtz solver was used with the average temperature field given by LES to identify acoustic eigenmodes with combustion. Table 9.1 confirms that the two frequencies observed in experiments are the two first acoustic modes of the combustor. In LES, a single frequency is observed at 520 Hz, which is close to the second acoustic mode of Table 9.1. To check that the 520 Hz mode found by LES is indeed acoustic, the field of unsteady pressure given by LES is compared to the modal structure

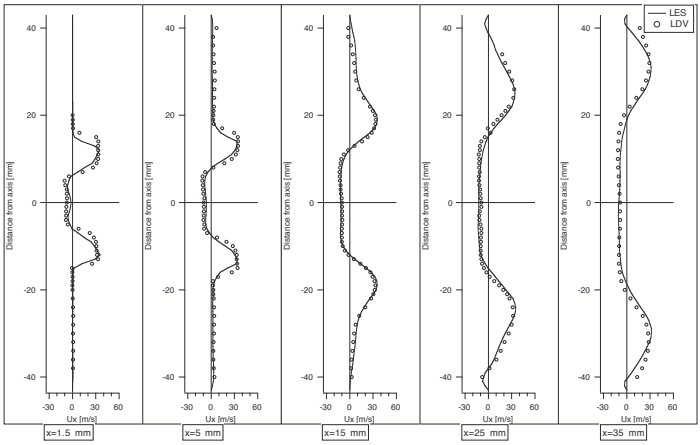

Figure 9.9. Mean axial velocity in the central plane. Circles: LDV; solid line: LES.

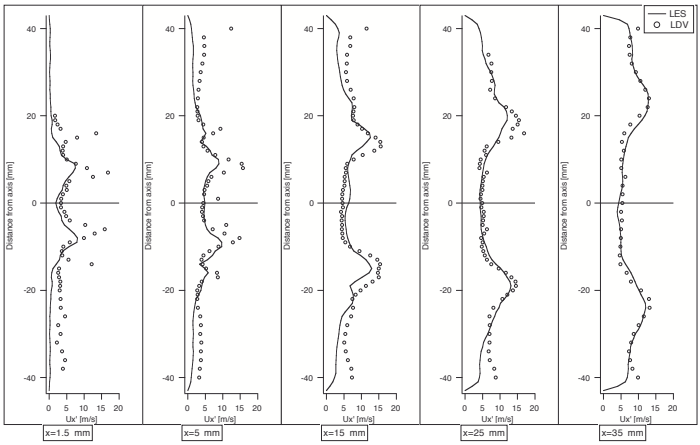

Figure 9.10. RMS axial velocity in the central plane. Circles: LDV; solid line: LES.

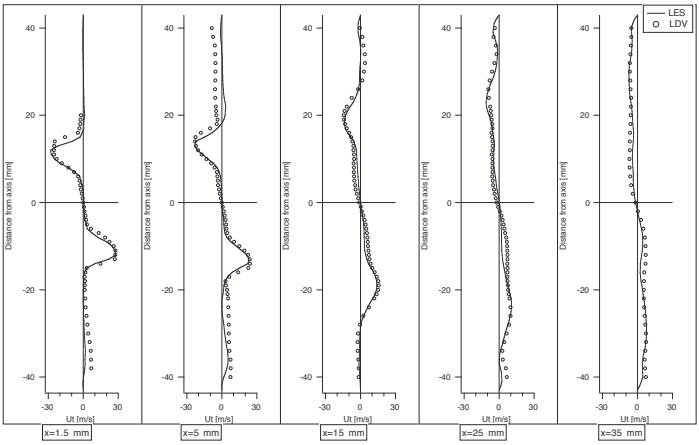

Figure 9.11. Mean tangential velocity in the central plane. Circles: LDV; solid line: LES.

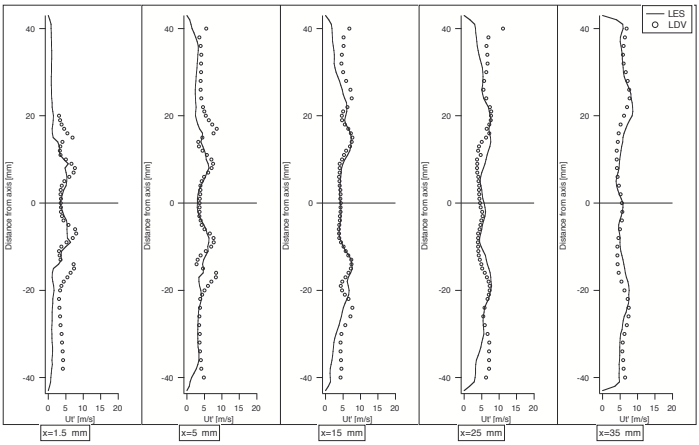

Figure 9.12. RMS tangential velocity in the central plane. Circles: LDV; solid line: LES.

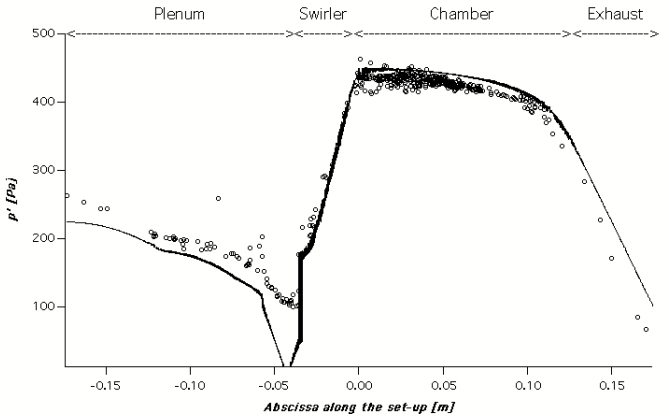

Figure 9.13. Pressure fluctuations amplitude predicted by LES (——) and Helmholtz solver (○) for the reacting flow in Case 1.

predicted by the Helmholtz solver for the 588 Hz mode (Fig. 9.13). Even though the LES signal contains all modes, its shape is clearly close to the structure of the second acoustic mode predicted by the Helmholtz solver. Another major effect of combustion revealed by LES is to damp the PVC observed in the cold flow. The agreement of Fig. 9.13 confirms that the unsteady activity for this reacting regime is controlled everywhere by the acoustic field even though no strong combustion instability is observed.

9.3 Case 2: Self-Excited Staged Burner

Configuration

Fig. 9.14 displays the geometry of Case 2. Swirled premixed (propane and air) gases are introduced tangentially into a long cylindrical duct feeding the combustion chamber to create the swirl required for stabilization.

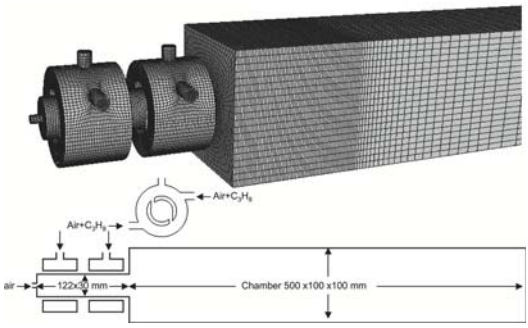

Figure 9.14. Case 2 configuration: a staged swirled combustor.

A specification of the present set-up is that the injection duct is split into two parts to allow staged combustion: the equivalence ratio of the first part (called ϕ_1) can differ from the second part (called ϕ_2). Staged combustion is used in certain burners to control emissions and instabilities. The air flow rates in each section are equal to half the total air flow rate $\dot{m}_{air}$ and the equivalence ratio modulation is obtained by splitting the propane flow rates in different proportions for each section. The global equivalence ratio of the burner ϕ_g is $\phi_g = s\dot{m}_F/\dot{m}_O$ where s is the stoichiometric ratio and $\dot{m}_O$ is the oxygen flow rate ($\dot{m}_O = Y_{ox} * \dot{m}_{air}$). The parameter α used to characterize staging measures the fraction of fuel injected into the first injection section: $\alpha = \dot{m}_F^1/\dot{m}_F$. The equivalence ratios ϕ_1, ϕ_2 and α are linked by $\phi_1 = 2\alpha\phi_g$ and $\phi_2 = 2(1-\alpha)\phi_g$. One specific regime exhibiting large oscillations when the outlet section is acoustically closed is studied here (Table 9.2).

Total flow rate (kg/s)	Mean equivalence ratio	α	ϕ_1	ϕ_2
22.10^{-3}	0.8	0.3	0.5	1.16

Table 9.2. Flow parameters for combustion cases.

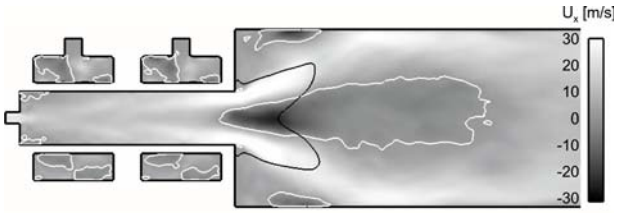

Figure 9.15. Mean axial velocity, white line: $u_x = 0$, black line: T = 1500 K for stable combustion.

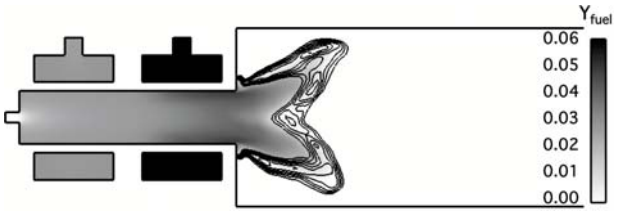

Figure 9.16. Mean fuel mass fraction field, black lines: iso-reaction rate for stable combustion.

Stable Flow

When the outlet is non-reflecting, the flame is stable. The mean axial velocity and fuel mass fraction fields are displayed in Fig. 9.15 and 9.16 [320]: the central recirculation zone (marked by a white line in Fig. 9.15) is filled by burnt gases which provide flame stabilization. Fuel staging is also apparent in Fig. 9.16.

Controlling Oscillations Through Boundary Conditions

The level of reflection of the outlet boundary can be controlled by changing the relaxation coefficient σ of the wave correction [359] which determines the amplitude of the incoming wave entering the computational domain. For small values of σ, the pressure p remains around its target value p_t while letting acoustic wave go out at the same time: the outlet is non reflecting. When large values of σ are specified, the outlet pressure remains strictly equal to p_t and the outlet becomes totally reflecting. The combustion chamber reacts strongly to changes in outlet impedance: for non-reflecting outlet, the flow is stable as seen in § 9.3 and it becomes unstable when the outlet

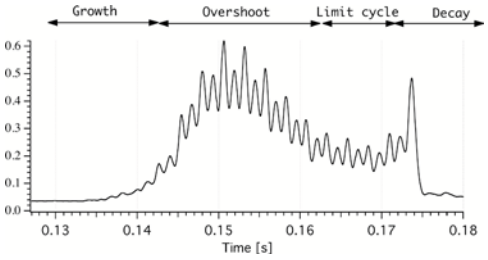

Figure 9.17. Evolution of the acoustic energy vs time for Case 2.

becomes reflecting. To analyze this instability[ii], the following scenario is utilized [320]:

- Starting from a stable flame and a reduced level of fluctuations, the outlet impedance is changed to become reflecting at time $t = 0.127s$. This is obtained by increasing the σ coefficient for the outlet section (Fig. 9.17).
- At time $t = 0.173s$, the outlet impedance is switched again to a non-reflecting condition and the instability disappears.

During these phases, the total acoustic energy is extracted from LES. Fig. 9.17 shows that it first grows, becomes maximum and then decreases slightly to reach a limit cycle at a frequency of 360 Hz mode which is one of the acoustic modes of the combustor [320]. After $t = 0.173$ s, when the outlet becomes non reflecting again, it decays rapidly.

At the limit cycle, the combustor is submitted to a very strong oscillation where the flame periodically contracts on the exit of the burner before expanding through most of the combustion chamber and shrinking again (Fig. 9.18). Snapshots corresponding to a full cycle are displayed in Fig. 9.18 at instants indicated on Fig. 9.19. The vortex criterion of [298] is used to visualize the vortex rings formed at the burner exit. These vortices form a well-defined ring only after their birth (instants 1 to 3) and they degenerate after instant 4 into small scale turbulence. They are created when the inlet acceleration at the burner exit is maximum (just before instant 1). Fig. 9.19 also confirms the intensity of the oscillation: the total reaction rate oscillates between 0.5 and 1.7 times its mean value; the inlet velocity also changes between 0.5 and 1.6 times its mean value: these fluctuating velocities are much larger than typical turbulent velocities and influence the combustion process more than small-scale turbulent motions.

[ii] See animation on http://www.cerfacs.fr/cfd/movies/ECPMod_insta3D.mov.

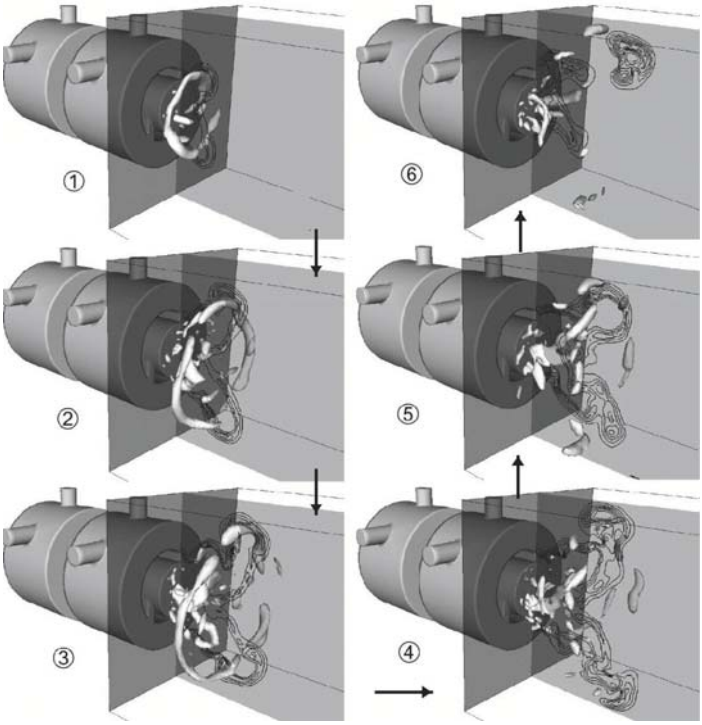

Figure 9.18. Limit cycle for Case 2. Isosurface: Q vortex criterion; black lines: iso-reaction rate.

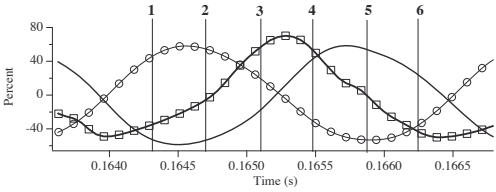

Figure 9.19. Chamber pressure (———), burner inlet velocity (○) and total heat release (—□—) fluctuations normalized by mean values during one period of the limit cycle.

Fig. 9.20 shows that the integral of the Rayleigh source term r_1 defined by Eq. (8.2) is actually not dominant. It is indeed positive and driving the instability most of the time even though it may take negative values for limited times. But the acoustic losses term f_1 given by Eq. (8.2) is also large and provides almost all the damping of the acoustic energy at the limit cycle. This result shows that the amplitude of the limit cycle is controlled mainly by acoustic losses, as expected from the direct observation that changes in acoustic boundary conditions at the outlet could control the oscillation amplitude. This last simple example shows how LES can be used together with budgets of acoustic energy to understand combustion instabilities in combustors. It also demonstrates the importance of acoustics in combustion oscillations and points out an important implication for experimental studies: if acoustic impedances upstream and downstream of the burner are important, it is difficult to take a given burner out of a real gas turbine for example to test it in a laboratory environment where it will be installed in a different set-up. Since acoustic boundary conditions will differ, what will be learned in the laboratory may not be relevant for the full combustor in its real environment.

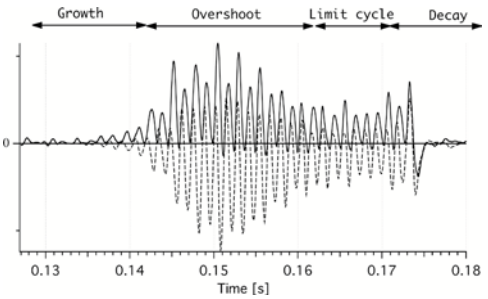

Figure 9.20. RHS terms in the acoustic energy equation for Case 2: Rayleigh criterion (solid); acoustic flux (dotted).

Chapter 10

TWO-PHASE FLOW COMBUSTION

Dr. Thierry Poinsot
CNRS/Inst. de Mécanique des Fluides de Toulouse
Toulouse, France

The previous chapters have discussed examples of instabilities in combustors where the fuel was gaseous. However, in most practical devices, fuel is liquid (gasoline or kerosene) and the problem becomes much more difficult. In this chapter, the specificities of two-phase flow combustion will be discussed and the construction of a numerical tool to perform LES of liquid fuel combustion will be discussed. This chapter will also present the equations solved for gaseous and liquid combustion in more details than the previous ones.

The introduction of a dispersed liquid fuel raises two kinds of problems:

- Liquid fuel sprays are not yet fully understood [310]. The atomization process of a liquid fuel jet [376; 332; 345; 293; 309], the turbulent dispersion of the resulting droplets [256; 253; 262; 333; 319], their interaction with walls [259; 365], their evaporation and combustion [290] are phenomena occurring in LES at the subgrid scale and therefore require accurate modeling.
- The numerical implementation of two-phase flow in LES remains a challenge. The equations for both gaseous and dispersed phases must be solved together at each time step in a strongly coupled manner. This differs again from classical RANS where both phases can be solved in a weakly coupled procedure, bringing first the gas flow to convergence, then calculating the associated dispersed phase and iterating until convergence of both phases.

Attempts to extend RANS formulation to LES of two-phase combustion may be found in [318; 354; 317; 255; 292]. They are all based on a Euler-Lagrange (EL) description of the dispersed phase in which the flow is solved using an Eulerian method and the particles are tracked with a Lagrangian approach. An alternative is the Euler-Euler (EE) description, also called two-fluid approach, in which both the gas and the dispersed phases are

solved using Eulerian formulation.

In RANS codes, the weak numerical coupling of the phases makes the EL method well suited for gas turbine computations, but RANS with the EE approach may also be found for example in simulations of fluidized beds [277; 335] or chemical reactors [284; 272; 289], two examples of two-phase flows with a high load of particles. The experience gained in the development of RANS has led to the conclusions that both approaches are useful and they are both found today in most commercial codes. Moreover, coupling strategies between EE and EL methods within the same application are considered for certain cases. In the framework of LES of gas turbines, it is interesting to compare again EL with EE formulations.

Following the individual trajectory of millions of droplets created by standard injectors implies computer resources that are still far beyond the capacities of computers available today and even in the coming years. To overcome this problem the stochastic Lagrangian approach is usually introduced, where each particle is only a "numerical" particle, representing in fact a statistically homogeneous group of real particles. This reduces the number of particles to compute but implies modeling for these parcels of particles [324]. Moreover in order to reach the accuracy required by LES, the stochastic Lagrangian approach must still involve an important number of particles that make it CPU time-consuming. Another difficult point is that the topology of the flow in dense zones (like near the injectors) differs from a cloud of droplets and a Lagrangian description is not adapted there. Finally the computer implementation of the EL approach is not well-suited to parallel computers: since two different solvers must be coupled, the complexity of the implementation on a parallel computer increases drastically compared to a single-phase code. Two methods may be used for LES: (1) task parallelization in which certain processors compute the gas flow and others compute the droplets flow and (2) domain partitioning in which droplets are computed together with the gas flow on geometrical subdomains mapped on parallel processors. Droplets must then be exchanged between processors when leaving a sub-domain to enter an adjacent domain. For LES, it is easy to show that only domain partitioning is efficient on large grids because task parallelization would require the communication of very large three-dimensional data sets at each iteration between all processors. However, codes based on domain partitioning are difficult to optimize on massively parallel architectures when droplets are clustered in one part of the domain (typically, near the fuel injectors). Moreover, the distribution of droplets may change during the computation: for a gas turbine re-ignition sequence, for example, the chamber is filled with droplets when the ignition begins, thus ensuring an almost uniform droplet distribution; these droplets

then evaporate rapidly during the computation, leaving droplets only in the near injector regions. To preserve a high parallel efficiency on thousands of processors, dynamic load-balancing strategies are required that re-decompose the domain during the computation itself [292].

The EE approach has the important advantage to be straightforward to implement in a numerical tool, and immediately efficient as it allows the use of the same parallel algorithm than for the gas phase [301]. However it requires an initial modeling effort much larger than in the EL method [280] and faces difficulties in handling droplet clouds with extended size distributions. Moreover the resulting set of equations is numerically difficult to handle and requires special care [346].

Throughout this chapter, two-phase flows are treated like mono-disperse sprays, an assumption which is not mandatory in EE methods but which makes their implementation easier. Results also suggest that in many flows, this assumption is reasonable. Considering the lack of information on size distribution at an atomizer outlet in a real gas turbine, this assumption might be a reasonable compromise in terms of complexity and efficiency: tracking multi-disperse sprays with precision makes sense only if the spray characteristics at the injection point are well known. In most cases, droplets are not yet formed close to the atomizer outlet anyway and even the Lagrange description faces difficulties there.

In the context of LES, a new modeling issue appears for two-phase flow simulations, either in the EL or EE formulation, and is linked to the subgrid scale model for the turbulent droplet dispersion. This problem has already been addressed in [278; 279] but is still an open question. However in the case of reacting flows, turbulent droplet dispersion occurs in a very limited zone between the atomizer and the flame and it is greatly influenced by the flame dynamics, therefore limiting the impact of the subgrid scale model.

The EE methodology in LES used throughout this work is taken from previous work [280; 328; 347; 346] where the validity and limitations have been discussed extensively, and it is not the purpose here to discuss further theoretical aspects. Despite the known limitations of such methodology, it is interesting to evaluate the potential and accuracy of the existing models when applied to realistic geometries and flows. This is the objective of the present discussion in the case of aeronautical gas turbines.

The framework and the basic equations for the EE description are first recalled in Section 10.1. The LES filtering procedure for these equations is described in Section 10.1 along with the closure assumptions and models for subgrid terms, including turbulent combustion. The application is a sector of a gas turbine burner for which both the steady flow and an ignition sequence using a spark discharge are computed in Sections 10.2 and 10.2

respectively.

10.1 Equations

Carrier Phase

The set of instantaneous conservation equations in a multi-species reacting gas can be written:

$$\frac{\partial w}{\partial t} + \nabla \cdot F \;=\; S_c + \; S_l \tag{10.1}$$

where w is the vector of the gaseous conservative variables

$$w = (\rho u, \rho v, \rho w, \rho E, \rho_k)^T$$

with respectively ρ, u, v, w, E, ρ_k the density, the three Cartesian components of the velocity vector $\mathbf{u} = (u, v, w)^T$, the total energy per unit mass defined by $E = 1/2\mathbf{u} \cdot \mathbf{u} + E_i$ where E_i is the internal energy, and $\rho_k = \rho Y_k$ where Y_k is the mass fraction of species k. It is usual to decompose the flux tensor F into an inviscid and a viscous component: $F = F(w)^I + F(w, \nabla w)^V$. The three spatial components of the inviscid flux tensor $F(w)^I$ are:

$$\begin{pmatrix} \rho u^2 + P & \rho uv & \rho uw \\ \rho uv & \rho v^2 + P & \rho vw \\ \rho uw & \rho vw & \rho w^2 + P \\ (\rho E + P)u & (\rho E + P)v & (\rho E + P)w \\ \rho_k u & \rho_k v & \rho_k w \end{pmatrix} \tag{10.2}$$

where the hydrostatic pressure P is given by the equation of state for a perfect gas: $P = \rho\, r\, T$, with the gas constant $r = \frac{R}{W} = \sum_{k=1}^{N} \frac{Y_k}{W_k} \mathcal{R}$ and $\mathcal{R} = 8.3143$ J/(mol.K) the universal gas constant. The internal energy E_i is linked to the temperature through the heat capacity of the mixture calculated as $C_p = \sum_{k=1}^{N} Y_k\, C_{p,k}$.

The components of the viscous flux tensor $F(w, \nabla w)^V$ take the form:

$$\begin{pmatrix} -\tau_{xx} & -\tau_{xy} & -\tau_{xz} \\ -\tau_{xy} & -\tau_{yy} & -\tau_{yz} \\ -\tau_{xz} & -\tau_{yz} & -\tau_{zz} \\ -\mathbf{u} \cdot \tau_x + q_x & -\mathbf{u} \cdot \tau_y + q_y & -\mathbf{u} \cdot \tau_z + q_z \\ J_{x,k} & J_{y,k} & J_{z,k} \end{pmatrix} \tag{10.3}$$

It is composed of the stress tensor $\tau = 2\mu(S - 1/3\ \delta_{ij} Tr(S))$ (momentum equations), the energy flux $\mathbf{u} \cdot \tau + q$ (energy equation) and the diffusive flux J_k

(species equations). In the stress tensor expression, $S = 1/2(\nabla\cdot\mathbf{u}+(\nabla\cdot\mathbf{u})^T)$ is the deformation matrix and μ is the dynamic viscosity following a classical power law. The diffusive flux of species k includes a correction velocity V^c that guarantees mass conservation, so that $J_k = -\rho\left(D_k\frac{W_k}{W}\nabla X_k - Y_k V^c\right)$ with $V^c = \sum_{k=1}^{N} D_k\frac{W_k}{W}\nabla X_k$, X_k being the molar fraction of species k. The mixture diffusion coefficient for species k is computed as $D_k = \frac{\mu}{\rho\, Sc_k}$ where the Schmidt number Sc_k is a constant. Finally the heat flux vector q follows a Fourier's law and includes an additional term due to heat transport by species diffusion: $q = -\lambda\,\nabla T + \sum_{k=1}^{N} J_k h_{s,k}$, where $\lambda = \mu C_p/Pr$ is the heat conduction coefficient of the mixture, with the Prandtl number Pr fixed at a constant value.

The chemical part of the source term S_c on the right hand side of Eq. (8.2) adds a term to the energy equation ($\dot{\omega}_T$) and to the species equations ($\dot{\omega}_k$). Chemistry is described by M reactions involving the N reactants $\mathcal{M}_k$ as follows:

$$\sum_{k=1}^{N}\nu'_{kj}\mathcal{M}_k \rightleftharpoons \sum_{k=1}^{N}\nu''_{kj}\mathcal{M}_k, \qquad j = 1, M \tag{10.4}$$

The production/consumption rate $\dot{\omega}_k$ for species k is the sum of the reaction rates $\dot{\omega}_{kj}$ produced by all M reactions:

$$\dot{\omega}_k = \sum_{j=1}^{M}\dot{\omega}_{kj} = W_k\sum_{j=1}^{M}\nu_{kj}\mathcal{Q}_j \tag{10.5}$$

where $\nu_{kj} = \nu''_{kj} - \nu'_{kj}$ and $\mathcal{Q}_j$ is the rate of progress of reaction j and is written:

$$\mathcal{Q}_j = K_{f,j}\prod_{k=1}^{N}\left(\frac{\rho Y_k}{W_k}\right)^{\nu'_{kj}} - K_{r,j}\prod_{k=1}^{N}\left(\frac{\rho Y_k}{W_k}\right)^{\nu''_{kj}} \tag{10.6}$$

The forward reaction rate follows the Arrhenius law: $K_{f,j} = A_{f,j}\exp\left(-\frac{E_{a,j}}{\mathcal{R}T}\right)$ where $A_{f,j}$ and $E_{a,j}$ are the pre-exponential factor and the activation energy. The reverse reaction rate is deduced from the equilibrium relation $K_{r,j} = K_{f,j}/K_{eq}$ where K_{eq} is the equilibrium constant.

The heat release is calculated from the species production/consumption rates as:

$$\dot{\omega}_T = -\sum_{k=1}^{N}\dot{\omega}_k\Delta h^0_{f,k} \tag{10.7}$$

where $\Delta h^0_{f,k}$ is the formation enthalpy of species k.

The second part of the source term S_l is associated to the liquid phase through the drag force and the evaporation. It adds a vector I to the right hand side of the momentum equations, a heat transfer term Π on the energy equation and a mass transfer term Γ on the fuel equation (see Section 10.1).

Dispersed Phase

Eulerian equations for the dispersed phase may be derived by several means. A popular and simple way consists in volume filtering of the separate, local, instantaneous phase equations accounting for the inter-facial jump conditions [274]. Such an averaging approach may be restrictive, because particle sizes and particle distances have to be smaller than the smallest length scale of the turbulence. Besides, it does not account for the Random Uncorrelated Motion (RUM), which measures the deviation of particle velocities compared to the local mean velocity of the dispersed phase [280] (see section 10.1). In the present study, a statistical approach analogous to kinetic theory [265] is used to construct a probability density function (pdf) $\breve{f}_p(\mathbf{c}_p, \zeta_p, \mu_p, \mathbf{x}, t)$ which gives the local instantaneous probable number of droplets with the given translation velocity $\mathbf{u}_p = \mathbf{c}_p$, the given mass $m_p = \mu_p$ and the given temperature $T_p = \zeta_p$. The resulting model leads to conservation equations having the same form as for the gas phase, with the particle number density $\breve{n}_l$, the volume fraction $\breve{\alpha}_l$, the correlated velocity $\breve{u}_l$ (see section 10.1) and the sensible enthalpy $\breve{h}_{s,l}$ (supposed uniform in the droplet, so that in particular the interface temperature T_ζ is equal to the liquid temperature T_l). For a mono-disperse spray, neglecting droplets interaction terms, the conservation equations read:

$$\frac{\partial}{\partial t}\breve{n}_l + \frac{\partial}{\partial x_j}\breve{n}_l\breve{u}_{l,j} = 0 \tag{10.8}$$

$$\frac{\partial}{\partial t}\rho_l\breve{\alpha}_l + \frac{\partial}{\partial x_j}\rho_l\breve{\alpha}_l\breve{u}_{l,j} = -\Gamma \tag{10.9}$$

$$\frac{\partial}{\partial t}\rho_l\breve{\alpha}_l\breve{u}_{l,i} + \frac{\partial}{\partial x_j}\rho_l\breve{\alpha}_l\breve{u}_{l,i}\breve{u}_{l,j} = F_{d,i} - \breve{u}_{l,i}\Gamma - \frac{\partial}{\partial x_j}\rho_l\breve{\alpha}_l\delta\breve{R}_{l,ij} \tag{10.10}$$

$$\frac{\partial}{\partial t}\rho_l\breve{\alpha}_l\breve{h}_{s,l} + \frac{\partial}{\partial x_j}\rho_l\breve{\alpha}_l\breve{h}_{s,l}\breve{u}_{l,j} = -(\Phi + \Gamma h_{s,F}(\breve{T}_l)) \tag{10.11}$$

In these equations, the momentum and heat phase exchange source terms are split in two parts : $I = -F_d + \breve{\mathbf{u}}_l\Gamma$ that includes both the drag force and a momentum transfer due to the mass transfer, and $\Pi = \Phi + \Gamma h_{s,F}(\breve{T}_l)$, where $h_{s,F}(\breve{T}_l)$ is the fuel vapor enthalpy taken at the interface temperature

T_l, that includes conduction and heat transfer linked to the mass transfer. The tensor $\delta\breve{R}_{l,ij}$ corresponds to the random uncorrelated motion (RUM) and is explained in section 10.1.

Note that without source terms (i.e. without evaporation, drag and RUM) the momentum equation Eq. 8.2 is similar to the Burger's equation, known to create shock-like velocity gradients and therefore difficult to handle numerically. The absence of an isotropic pressure-like force can also lead to very high droplet number density gradients. Without the use of shock-capturing numerical schemes it is necessary to add stabilization terms to this equation. This is explained in section 10.1.

The resulting set of equations Eqs. 8.2 to 8.2 is equivalent to the Lagrangian description of the dispersed phase (without collision terms and for mono-disperse sprays) and leads to the same solutions, as shown in [348].

Phase Exchange Source Terms

Mass transfer between the gas and the liquid phases is linked to evaporation, which follows the classical Spalding model [366]. Assuming that the dispersed phase is composed of spherical droplets of pure fuel (denoted with the subscript F), the evaporation rate may be written as :

$$\Gamma = \pi\breve{n}_l d Sh(\rho D_F) ln(1 + B_M) \tag{10.12}$$

where d is the droplet diameter, D_F is the fuel vapor diffusivity and Sh is the Sherwood number that takes into account convective and turbulent effects. A commonly used expression for this number is $Sh = 2.0 + 0.55 Re_d^{1/2} Sc_F^{1/3}$ where $Re_p = d|\mathbf{u} - \breve{\mathbf{u}}_l|/\nu$ is the particle Reynolds number and Sc_F is the fuel vapor Schmidt number. In this definition ν is the carrier phase kinematic viscosity. In Eq. (8.2), one important parameter is the Spalding number $B_M = (Y_{F,\zeta} - Y_F)/(1 - Y_{F,\zeta})$ where $Y_{F,\zeta}$ is the fuel mass fraction at the droplet surface, calculated from the fuel vapor partial pressure at the interface $p_{F,\zeta}$ which is evaluated from the Clausius-Clapeyron relation:

$$p_{F,\zeta} = p_{cc}\ exp\left(\frac{W_F L_v}{\mathcal{R}}\left(\frac{1}{T_{cc}} - \frac{1}{T_l}\right)\right) \tag{10.13}$$

The reference pressure and temperature p_{cc} and T_{cc} correspond to the saturation conditions, and L_v is the latent heat of vaporisation.
The drag force is expressed as:

$$F_d = \frac{\rho_l \breve{\alpha}_l}{\tau_p}\left(u_i - \breve{u}_{l,i}\right) \tag{10.14}$$

introducing the particle relaxation time τ_p:

$$\tau_p = \frac{4\rho_l d^2}{3\rho\nu C_d Re_d} \tag{10.15}$$

itself based on the drag coefficient C_d, which is 0.44 for Re_d greater than 1000 otherwise defined by $C_d = \frac{24}{Re_d}(1 + 0.15\ Re_d^{0.687})$.

Finally, the conductive flux Φ through the interface is calculated as $\Phi = \pi \breve{n}_l d\lambda\ Nu(\breve{T}_l - T)$. In this expression, λ is the carrier phase conductivity and Nu is the Nusselt number usually expressed similarly to the Sherwood number: $Nu = 2.0 + 0.55 Re_d^{1/2} Pr^{1/3}$.

The Random Uncorrelated Motion (RUM)

The averaging operation for the liquid droplet velocity described in the previous section introduces a particle velocity deviation from the mean (or correlated) velocity, noted as $u_p'' = u_p - \breve{u}_l$, and named the random uncorrelated velocity [280]. By definition, the statistical average (based on the particle probability density function) of this uncorrelated velocity is zero: $< u_p'' >= 0$. A conservation equation can be written for the associated kinetic energy $\delta\breve{\theta}_l =< u_{p,i}'' u_{p,i}'' > /2$:

$$\frac{\partial}{\partial t}\rho_l \breve{\alpha}_l \delta\breve{\theta}_l + \frac{\partial}{\partial x_j}\rho_l \breve{\alpha}_l \breve{u}_{l,j} \delta\breve{\theta}_l = -\frac{1}{2}\frac{\partial}{\partial x_j}\rho_l \breve{\alpha}_l \delta\breve{S}_{l,iij} - \frac{2\,\breve{n}_l}{\tau_p}\delta\breve{\theta}_l - \rho_l \breve{\alpha}_l \delta\breve{R}_{l,ij}\frac{\partial \breve{u}_{l,i}}{\partial x_j} - \Gamma\delta\breve{\theta}_l \tag{10.16}$$

where unclosed terms $\delta\breve{R}_{l,ij}$ and $\delta\breve{S}_l$ (called here RUM terms) appear. However the modeling of these terms as proposed for example in [302; 348] is not yet satisfactory and it is still an open and difficult question. In [348] it has been shown that in a configuration representative of industrial flows, the RUM is not essential to capture the mean fields (velocity and mass flux) of the liquid phase, but only influences the particle turbulent agitation. It has been therefore omitted in the applications presented later here.

LES Approach

The two sets of conservative equations defined by Eq. (8.2) and Eqs. (8.2)-(8.2) describe turbulent reacting two-phase flows that require a high grid resolution in order to solve from the smallest to the largest scales. In LES only the largest scales are computed while the smallest scales are modeled.

A spatially localized time independent filter of given size, $\triangle$, is applied to a single realization of the flow.

The filtered quantity $\overline{f}$ is resolved in the numerical simulation whereas $f' = f - \overline{f}$ is the subgrid scale part due to the unresolved flow motion. For variable density ρ, a mass-weighted Favre filtering is introduced so that:

$$\overline{\rho}\widetilde{f} = \overline{\rho f} \tag{10.17}$$

The balance equations for gas phase LES are obtained by filtering the instantaneous balance equation (8.2):

$$\frac{\partial \overline{w}}{\partial t} + \nabla \cdot \overline{F} \;=\; \overline{S}_c + \overline{S}_l \tag{10.18}$$

where the filtered flux tensor $\overline{F}$ can be divided in three parts: the inviscid part $\overline{F}^I$, the viscous part $\overline{F}^V$ and the subgrid scale turbulent part $\overline{F}^t$. The three spatial components of the inviscid and viscous flux tensor use expressions similar to Eqs. 8.2 and 8.2, based on filtered quantities. The subgrid-scale turbulent flux $\overline{F}^t = \overline{\tau}^t$ is a new term introduced by the LES approach and is modeled through the turbulent viscosity concept:

$$\overline{\tau}^t = -\overline{\rho}(\widetilde{\mathbf{u} : \mathbf{u}} - \widetilde{\mathbf{u}} : \widetilde{\mathbf{u}}) = 2\,\overline{\rho}\,\nu_t(\widetilde{S} - \frac{1}{3}\delta_{ij}Tr(\widetilde{S})) \tag{10.19}$$

The turbulent viscosity ν_t is determined using the WALE model [330], similar to the Smagorinski model, but with an improved behavior near solid boundaries. Similarly, a subgrid-scale diffusive flux vector for species $\overline{J_k}^t = \overline{\rho}\,(\widetilde{\mathbf{u}Y_k} - \widetilde{\mathbf{u}}\widetilde{Y_k})$ and a subgrid-scale heat flux vector $\overline{q}^t = \overline{\rho}(\widetilde{\mathbf{u}E} - \widetilde{\mathbf{u}}\widetilde{E})$ appear and are modeled following the same expressions as in section 10.1, using filtered quantities and introducing a turbulent diffusivity $D_k^t = \nu_t / Sc_k^t$ and a thermal diffusivity $\lambda_t = \mu_t \overline{C_p}/Pr^t$. The turbulent Schmidt and Prandtl numbers are fixed to 1 and 0.9 respectively.

In turbulent reacting cases the Dynamically Thickened Flame model [311; 321; 355; 361] is used, where a thickening factor F is introduced to thicken the flame front and the efficiency function $\mathcal{E}$ developed by Colin *et al.* [269] is used to account for subgrid scale wrinkling.

For the dispersed phase, filtered conservative variables and equations are built with the same methodology as for the carrier phase and similarly a particle subgrid stress tensor $\overline{\tau}^t_{l,ij}$ appears :

$$\overline{\tau}^t_{l,ij} = -\bar{n}_l(\widehat{u_{l,i}u_{l,j}} - \hat{u}_{l,i}\hat{u}_{l,j}) \tag{10.20}$$

where the Favre filtered quantities $\hat{f}_l$ are defined as $\bar{n}_l\hat{f}_l = \overline{\breve{n}_l\breve{f}_l}$. By analogy to compressible single phase flows [327; 375], Riber et al. [347] propose

a viscosity model for the SGS tensor $T_{l,ij}$. The trace-free SGS tensor is modeled using a viscosity assumption (compressible Smagorinski model), while the subgrid energy is parametrized by a Yoshizawa model [383] :

$$\overline{\tau}^t_{l,ij} = C_{S,l} 2\Delta^2 \bar{n}_l |\hat{S}_l| (\hat{S}_{l,ij} - \frac{\delta_{ij}}{3} \hat{S}_{l,kk}) - C_{V,l} 2\Delta^2 \bar{n}_l |\hat{S}_l|^2 \delta_{ij} \qquad (10.21)$$

where $\hat{S}_l$ is the filtered particle strain rate tensor, of norm $|\hat{S}_l|^2 = 2\hat{S}_{l,ij}\hat{S}_{l,ij}$. The model constants have been evaluated in a priori tests [328] leading to the values $C_{S,l} = 0.02$, $C_{V,l} = 0.012$. The final set of equations for the gaseous and the dispersed phases is summarized in Table 10.1.

Gas velocity	$\frac{\partial \bar{\rho}\tilde{u}_i}{\partial t} + \frac{\partial \bar{\rho}\tilde{u}_i\tilde{u}_j}{\partial x_j} = -\frac{\partial \bar{P}}{\partial x_i} + \frac{\partial \tilde{\tau}_{ij}+\tau^t_{ij}}{\partial x_j} - F_{d,i} + \hat{u}_{l,i}\Gamma$
Mass fractions	$\frac{\partial \bar{\rho}\tilde{Y}_k}{\partial t} + \frac{\partial \bar{\rho}\tilde{u}_j\tilde{Y}_k}{\partial x_j} = -\frac{\partial \tilde{J}_k + J^t_k}{\partial x_j} + \dot{\omega}^t_k + \delta_{kF}\Gamma,$ for $k = 1, N$
Gas total energy (non chemical)	$\frac{\partial \bar{\rho}\tilde{E}}{\partial t} + \frac{\partial \bar{\rho}\tilde{u}_j\tilde{E}}{\partial x_j} = \frac{\partial (\tilde{\tau}_{ij}+\tau^t_{ij})\bar{u}_i}{\partial x_j} - \frac{\partial \tilde{q}_j + q^t_j}{\partial x_i} + \Phi + \tilde{u}_i(-F_{d,i} + \hat{u}_{l,i}\Gamma) + \dot{\omega}^t_T$
Number density	$\frac{\partial \bar{n}_l}{\partial t} + \frac{\partial \hat{u}_{l,j}\bar{n}_l}{\partial x_j} = 0$
Liquid volume fraction	$\frac{\partial \rho_l \bar{\alpha}_l}{\partial t} + \frac{\partial \hat{u}_{l,j}\rho_l\bar{\alpha}_l}{\partial x_j} = -\Gamma$
Liquid velocity	$\frac{\partial \rho_l\bar{\alpha}_l\hat{u}_{l,i}}{\partial t} + \frac{\partial \rho_l\bar{\alpha}_l\hat{u}_{l,i}\hat{u}_{l,j}}{\partial x_j} = F_{d,i} - \hat{u}_{l,i}\Gamma + \frac{\partial \overline{\tau}^t_{l,ij}}{\partial x_j}$
Enthalpy	$\frac{\partial \rho_l\bar{\alpha}_l\hat{h}_{s,l}}{\partial t} + \frac{\partial \rho_l\bar{\alpha}_l\hat{u}_{l,i}\hat{h}_{s,l}}{\partial x_j} = -(\Phi + \Gamma h_{s,F}(\breve{T}_l))$

Table 10.1. Set of (6+N) conservation equations, where N is the number of chemical species.

Numerical Approach

The solver used for this study is the same as in Chapter 9: a parallel fully compressible code for turbulent reacting two-phase flows, on both structured and unstructured grids. The fully explicit finite volume solver uses a cell-vertex discretization with a Lax-Wendroff centered numerical scheme [296] or a third order in space and time scheme named TTGC [268]. Characteristic boundary conditions NSCBC [339; 329] are used for the gas phase. Boundary conditions are easier for the dispersed phase, except for solid walls where particles may bounce off. In the present study it is simply supposed that the particles stick to the wall, with either a slip or zero velocity.

As pointed out in section 10.1, high velocity and number density gradients may appear, and are difficult to handle with centered schemes. However

the simulations presented in this exercise run smoothly, thanks to at least four reasons:
(1) In the different cases, RUM is not so strong anyway because the small droplets tend to align with the gas flow and the light load avoids particle-particle and particle-wall interactions, that are the main sources of RUM.
(2) In the combustion chamber application, evaporation reduces the numerical stiffness of the problem as it decreases even more the droplet size and the load.
(3) The simulations are all run in the LES framework, i.e. calculating filtered (and by definition smoothened) quantities and introducing sub-grid scale turbulent viscosities.
(4) As is usual with centered schemes, artificial viscosity is used. This is done with great care to preserve accuracy, applying it very locally (using specific sensors) and with the minimum level of viscosity [346].

10.2 Reacting Flow in An Aircraft Combustion Chamber Configuration

The last test case is a 3D sector of 22.5-degrees of an annular combustor at atmospheric pressure. The kerosene Liquid Spray (LS) is located at the center of the main Swirled Inlet (SI). Small holes (H), located around the inlet aim at lifting the flame and protect the injector from high temperatures. The perforations localized on the upper and lower walls are divided in two parts. The primary jets (PJ) bring cold air to the flame in the first part of the combustor where combustion takes place. The dilution jets (DJ) inject air further downstream to reduce and homogenize the outlet temperature to protect the turbine. The Spark Plug (SP) is located under the upper wall between two (PJ). The geometry (Fig. 10.2) also includes cooling films that protect walls from the flame.

The inlet and outlet boundary conditions use characteristic treatments with relaxation coefficients to reduce acoustic reflexion [359; 329]. The SI imposed velocity field mimics the swirler influence. Figure 10.1 displays profiles of the three components of the air velocity as prescribed along the axis of the spray (AB on Fig. 10.2) in reduced units: $u^* = u/U_0$ as a function of $r^* = r/R_0$ where U_0 is the bulk velocity and R_0 is the radius of the SI. The other inlets are simple jets. The injected spray is monodisperse, composed of droplets of diameter of 15 μm. The volume fraction, $\alpha_l \simeq 10^{-3}$, is imposed for a disk of radius $r^* = 0.4$. This corresponds to a lean global stoichiometric ratio of 0.28. At injection, the liquid velocity is equal to the gaseous velocity as the droplet Stokes number, based on the droplet relaxation time, is lower than one. The droplet inlet temperature

Air flow	
Total mass flow rate (g/s)	119
Temperature (K)	525
Pressure (bar)	1
Liquid fuel	
Mass flow rate (g/s)	2.38
Temperature (K)	300
Droplet size (μm)	15

Table 10.2. Flow conditions for the gas turbine configuration.

equals 288 K and the air is at 525 K. No-slip conditions are used on the upper and lower walls while a symmetry condition is used on the sector sides. All conditions are summarized in Table 10.2.

The unstructured mesh is composed of 400,000 nodes and 2,300,000 tetrahedra, which is typical and reasonable for LES of such configuration. The explicit time step is $\Delta t \simeq 0.22\ \mu s$. The mesh is refined close to the inlets and in the combustion zone (Fig. 10.3), leading to a flame thickening factor of the order of 10. A one-step chemical scheme fitted to JP10/air flames is used for chemistry (JP10 is a substitute for kerosene and has the same thermochemical properties). It has been checked that in the simulation the flame mostly burns mixtures with an equivalence ratio in the range between 0.5 and 1, where the chemical scheme is valid.

Steady Spray Flame

First a steady turbulent two-phase flame is calculated. The 15 μm droplet motion follows the carrier phase dynamics so that the Centered Recirculation Zones (CRZ) are similar for gas and liquid, as illustrated on Fig. 10.4, showing the instantaneous backflow lines of both phases, plotted in the vertical central cutting plane. Maintained by this CRZ, the droplets accumulate and the droplet number density, presented with the liquid volume fraction field on Fig. 10.4, rises above its initial value: a zone where the droplet number density n_l is larger than $2n_{l,inj}$ (where $n_{l,inj}$ is its value at injection) is formed downstream of the injector at a distance approximately half of the nozzle diameter (lines with circles on Fig 10.4). The increased residence time of these droplets, whose diameter field is presented

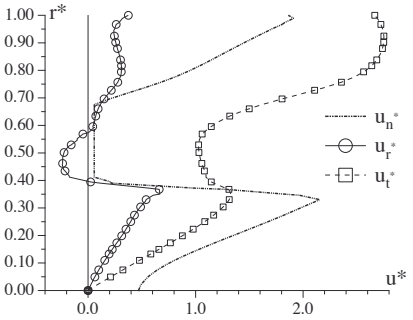

Figure 10.1. Normal, radial and tangential injection velocity profiles for the burner configuration: $r^* = r/R_0$ and $u^* = u/U_0$ where R_0 and U_0 are respectively the SI radius and the bulk velocity.

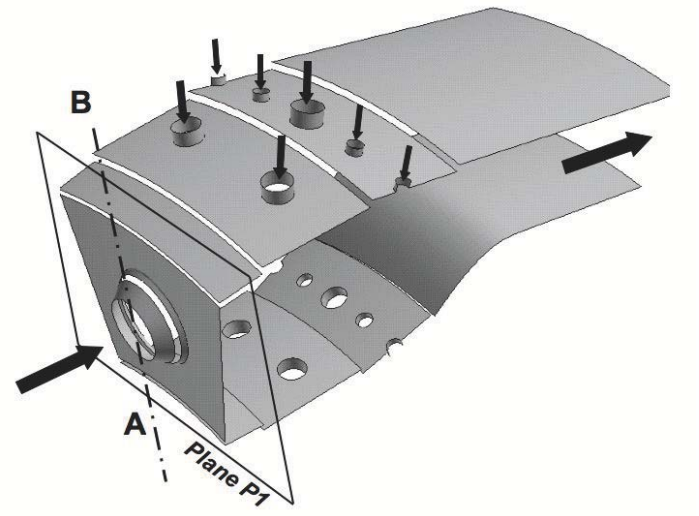

Figure 10.2. Chamber geometry

on Fig. 10.5, increases the local equivalence ratio distribution. The heat transfer linked to the phase change leads to the reduction of the gaseous temperature, as shown by the isoline $T = 450\ K$ on Fig. 10.6, and an increase of the dispersed phase temperature. Thus, the CRZ, by trapping

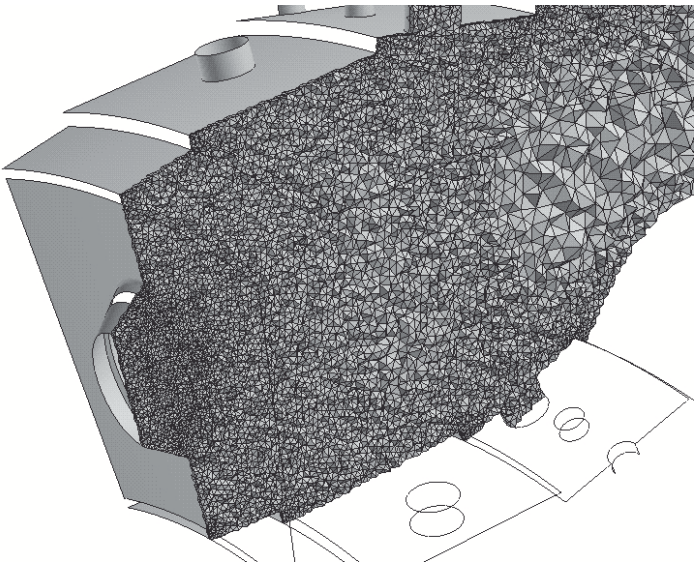

Figure 10.3. Mesh view on central plane

evaporating droplets, stabilizes the vaporised fuel and the flame. The flame front visualized on Fig. 10.6 by the heat release field is influenced by both flow dynamics and evaporation rate. The main phenomena controlling flame stabilization are :

1. the air velocity must be low enough to match the turbulent flame velocity : the dynamics of the carrier phase (and in particular the CRZ) stabilizes the flame front on a stable pocket of hot gases
2. zones where the local mixture fraction is within flammability limits must exist : combustion occurs between the fuel vapour radially dispersed by the swirl and the ambient air, where the equivalence ratio is low enough
3. the heat release must be high enough to maintain evaporation and reaction : the sum of heat flux Π and heat release $\dot{\omega}_T$, plotted on Fig. 10.6, allows to identify the zone (———) where the heat transfer due to evaporation compensates the local heat release : $\Pi + \dot{\omega}_T = 0$.

In the present case, the flame front is stabilized by the CRZ (1) but the heat release magnitude is reduced in the evaporation zone because of both effects (2) and (3). To determine the flame regime (premixed and/or diffusion), the Takeno index $\mathcal{T} = \nabla Y_F.\nabla Y_O$ and an indexed reaction rate $\dot{\omega}_F^* = \dot{\omega}_F \frac{\mathcal{T}}{|\nabla Y_F|.|\nabla Y_O|}$ are used [382]. The flame structure is then divided

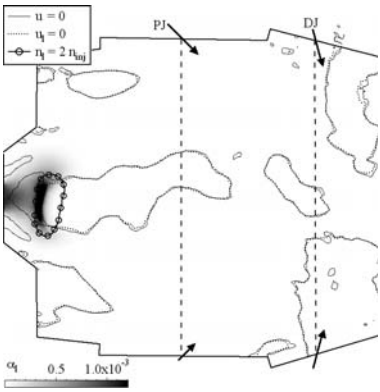

Figure 10.4. Instantaneous field of volume fraction in the central cutting plane of the chamber, with zero-velocity lines and $n_l = 2n_{inj}$ isoline.

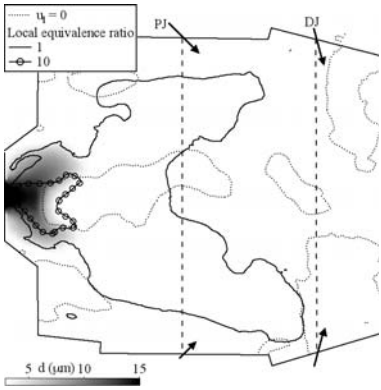

Figure 10.5. Instantaneous field of droplet diameter in the central cutting plane of the chamber, with equivalence ratio isolines for the values 1 and 10.

into two parts : $\dot{\omega}_F^* = +\dot{\omega}_F$ in the premixed regime and $\dot{\omega}_F^* = -\dot{\omega}_F$ in the diffusion regime (Fig. 10.7). In the primary zone, the partially premixed regime dominates because of the unsteady inhomogeneous fuel vapour. In the dilution zone, the unburned fuel reacts with dilution jets through a diffusion flame, as confirmed by the coincidence between the flame and the stoichiometric line. In the review on vortex breakdown, Lucca-Negro & O'Doherty [316] classifies the hydrodynamic instabilities appearing in swirled flows. For high swirl numbers, the axial vortex breaks down at the stagnation point S and a spiral is created around a central recirculation zone CRZ (Fig. 10.8left): this vortex breakdown is the so-called Precessing Vortex Core (PVC) and occurs in a large number of combustors [357]. LES captures the vortex breakdown in the combustor and its frequency is evaluated with the backflow line on a transverse plane (Fig. 10.8right) at six successive times marked with a number from 1 to 6 and separated by 0.5 ms. The turnover time is estimated at $\tau_{PVC} \simeq 3.5$ ms, corresponding to a frequency of $f_{PVC} \simeq 290$ Hz. Moreover, the three rotating motions of the SI, the whole PVC structure and the spiral winding turn in the same direction, as illustrated by the rotating arrows on Fig. 10.8left.

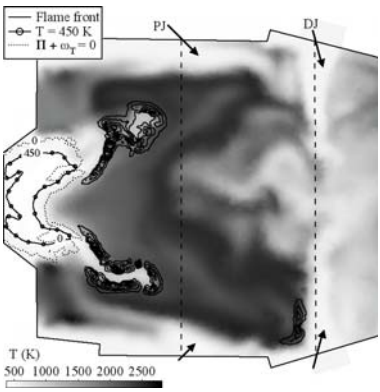

Figure 10.6. Flame front visualized by iso-contours of reaction rate superimposed to the temperature field (gray scale).

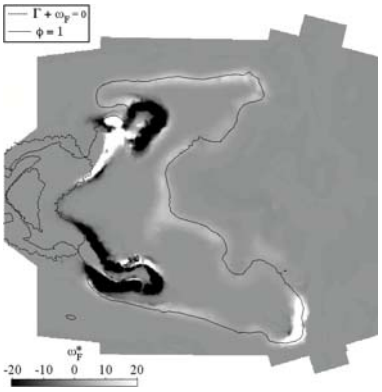

Figure 10.7. Flame structure visualized by the indexed reaction rate. Black zones correspond to premixed flames and white zones to diffusion flames.

The PVC defined on Fig. 10.9a controls the motions of both the Vaporised Fuel (VF) zone and the flame front. Fig. 10.9b displays the temperature field, the maximum fuel mass fraction (white lines) and the flame front (black isolines of reaction rate $\dot{\omega}_F$). In the cutting plane, defined on Fig. 10.9a, the CRZ stabilizes hot gases and enhances evaporation leading to a cold annular zone where the maximum fuel mass fraction precesses. The flame motion follows the PVC and the reaction rate is driven by the fuel vapour concentration.

Ignition Sequence

Ignition sequences can also be simulated with the same LES tool. The numerical method used to mimic an ignition by spark plug in the combustion chamber is the addition of the source term $\dot{\omega}_{spark}$ in Eq. (10.16). This source term, defined by Eq. (10.16), is a Gaussian function located at (x_0, y_0, z_0) near the upper wall between both primary jets and deposited at time $t = t_0 = 0$. The spark duration, typical of industrial spark plugs, is

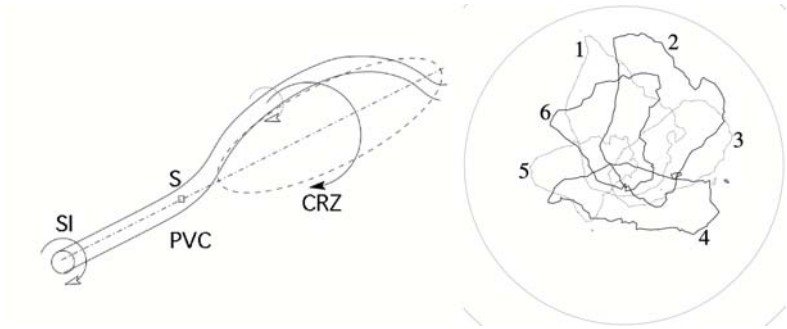

Figure 10.8. Left: Precessing vortex core. Right: Backflow line : transverse cut in plane P1 (Fig 10.2).

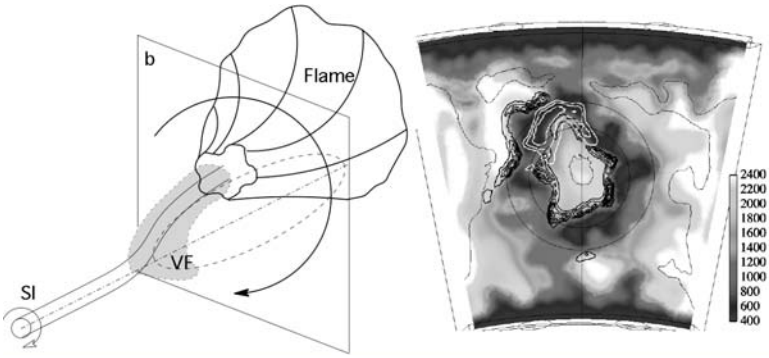

Figure 10.9. PVC influence on evaporation and combustion (left). Fields of temperature and isolines of fuel vapor (white lines) and reaction rate (black lines) (right).

$\sigma_t = 0.04\ ms$. The total deposited energy is $E_{spark} = 150\ J$.

$$\dot{\omega}_{spark} = \frac{E_{spark}}{(2\pi)^2 \sigma_t {\sigma_r}^3} e^{-\frac{1}{2}\left[\left(\frac{t-t_0}{\sigma_t}\right)^2+\left(\frac{x-x_0}{\sigma_r}\right)^2+\left(\frac{y-y_0}{\sigma_r}\right)^2+\left(\frac{z-z_0}{\sigma_r}\right)^2\right]} \qquad (10.22)$$

The temporal evolution of the total (i.e. spatially integrated) power deposited by the spark is presented on Fig. 10.10, along with the total heat release $\dot{\omega}_T$ and the spatially averaged temperature. After a heating phase due to the source term on the energy equation (up to approximately 0.08 ms), the temperature is sufficient to initiate the reaction between fuel vapour and air, leading to a sudden increase of the heat release of the exothermic

reaction. When the spark is stopped (at $\approx 0.18\ ms$), the total heat release decreases, and finally stabilizes at a level corresponding to a propagating flame, while the mean temperature continues to increase: the ignition is successful.

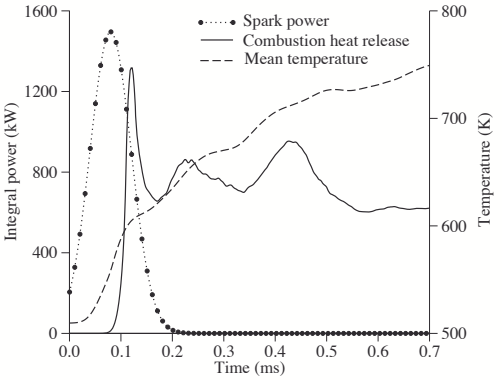

Figure 10.10. Total (spatially integrated) source term $\dot{\omega}_{spark}$, total heat release $\dot{\omega}_T$, and spatially averaged temperature.

The transition from the ignition of the first flame kernel ($t = 0.2\ ms$) to a complete stabilization takes more time (more than $3\ ms$) and is illustrated on the longitudinal central cutting plane identified in Fig. 10.11 with the fuel mass fraction field and the reaction rate isolines. The first image is presented at $t = 0.2\ ms$; successive images are separated by $\Delta t = 0.2\ ms$. At the beginning of the computation, the 15 μm droplets evaporate in the ambient air at $T = 525\ K$ creating a turbulent cloud of vaporised fuel in the whole primary zone. This fuel vapour is trapped by the CRZ and is transported from the evaporation zone to the spark plug area. At $t = 0$, the spark ignition leads to the creation of a hot kernel. The propagation of the flame front created by this pocket of hot gases is highly controlled by the fuel-vapour distribution between $t = 0$ and $t = 1\ ms$. After $t = 0.2\ ms$, this flame loses its spherical shape due to convective effects. The downstream side of the flame front is blown away and extinguishes by lack of fuel while the bottom side is progressing towards the center line where the fuel vapour concentration is high. When entering the CRZ ($t = 1\ ms$), the front is strongly wrinkled by the large turbulent scales of the flow. However, in the upstream region of the CRZ, the low velocities enable to stabilize the edge of

the reacting zone close to the fuel injection ($t = 1$ to $1.4\ ms$). In this region, the flame and the back-flow maintain a high temperature ambient leading to a strong evaporation rate and creating a stable fuel vapour concentrated spot ($t = 1.6$ to $2.4\ ms$). Due to the swirled jet, this fuel vapour is radially dispersed into the air flow and produce a flammable mixture. Burning this mixture, the flame is able to spread in the radial direction and finally occupies a large section of the primary zone ($t = 2.4\ ms$). This last topology corresponds to the steady spray flame described in the previous section.

This ignition sequence shows the important role of the liquid phase, responsible for the great differences with the ignition of a purely gaseous flame. The controlling mechanism is evaporation, that delays the start of the chemical reaction and, together with the droplet turbulent dispersion, modifies the fuel vapor distribution and consequently the flame front propagation. Such a mechanism is difficult to visualize experimentally and, despite the use of simplified models, the simulation provides here a good and new qualitative description of the phenomena.

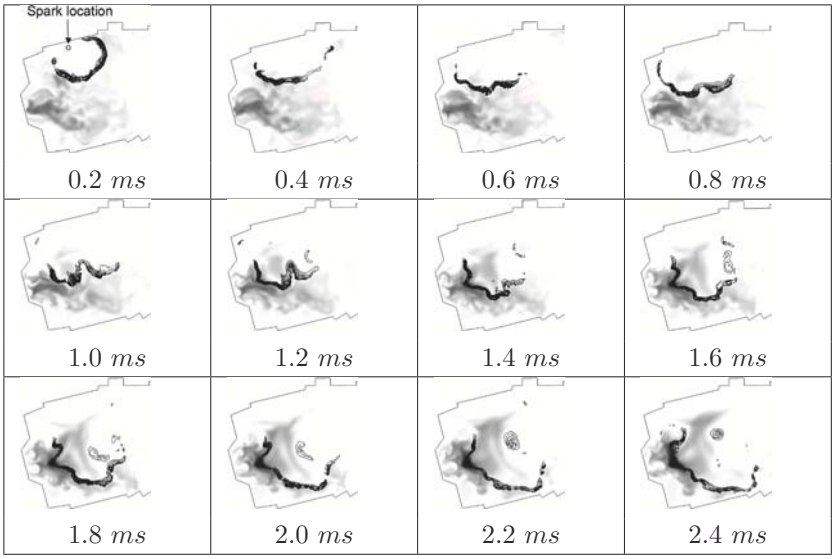

Figure 10.11. Flame front propagation on fuel mass fraction field (white: $0 \rightarrow$ black: 0.35)

Chapter 11

THE GROWTH OF ROUNDING ERRORS IN LES

Dr. Thierry Poinsot
CNRS/Inst. de Mécanique des Fluides de Toulouse
Toulouse, France

11.1 Introduction

Previous chapters have shown the power of Large Eddy Simulation (LES) to predict non-reacting [352; 318] as well as reacting turbulent flows [340; 338; 276; 275; 355]. The main strength of LES compared to classical Reynolds Averaged (RANS) methods is that, like Direct Numerical Simulation (DNS) [342; 326; 372], LES explicitly captures large scale unsteady motions due to turbulence instead of modeling them. LES also captures the multiple instability modes found in reacting flows. An often ignored aspect of this feature is that like DNS, LES is also submitted to a well-known feature of turbulent flows: the exponential separation of trajectories [371] implies that the flow solution exhibited by LES is very sensitive to any "small perturbations". These small perturbations which can induce instabilities can have different sources:

- Rounding errors are the first source of random noise in any finite precision computation: they constitute an unavoidable forcing for the Navier-Stokes equations and may lead to LES variability. The study of error growth in finite precision computations is an important topic in applied mathematics [367; 264] but has found few applications in multidimensional fluid mechanics because of the complexity of the codes used in CFD.
- Initial conditions are a second source of LES results variability: these conditions are often unknown and any small change in initial conditions may trigger significant changes in the LES solution. Boundary conditions, in particular the unsteady velocity profiles imposed at in-

lets and outlets, can have the same effect as initial conditions but are not studied here.

- Due to its large computational resource requirements, modern LES heavily relies on parallel computing. However, in codes using domain decomposition, it is also an additional "noise" source in the Navier-Stokes equations especially at partition interfaces. Even in explicit codes, where the algorithm is independent of the number of processors, the different summation orders with which a nodal value is reconstructed at partition interfaces, may induce non-associativity errors. For example, in explicit codes on unstructured meshes using cell vertex methods [356], the residual at one node is obtained by adding the weighted residuals of the surrounding cells. Additions of only two summands are perfectly associative. Moreover, it must be noted that not all additions of more than two summands generate non-associativity errors. However, in some cases, summation may yield distinct results for floating-point accumulation: the rounding errors in $(a+b)+c$ and in $a+(b+c)$ may be different, in particular if there are large differences in orders of magnitude between the terms [294]. After thousands of iterations, the LES result may be affected. Since these rounding errors are induced by non deterministic message arrival at partition interfaces, it is believed that such behaviour may occur for any unstructured parallel CFD code, regardless of the numerical schemes used. As a consequence, the simulation output might change when run on a different number of processors. The case of implicit codes [318; 282] or in space (such as compact schemes) [312; 250; 363] is not considered here: for such schemes, the methods used to solve the linear system appearing at each iteration [351; 281] depend on the number of processors. Therefore, rounding errors are not the only reason why solutions obtained with different numbers of processors differ.
- Even on a single processor computation, internal parameters of the partitioning algorithm may couple with rounding errors to force the LES solution. For example, a different reordering of nodes using the Cuthill-McKee (CM) or the reverse Cuthill-McKee (RCM) algorithm [271; 314] may produce the same effect as a simple perturbation and can be the source of solution divergence.

Of course, LES/DNS solutions are known to have a meaning only in a statistical manner [343] so that observing that the solution of a given LES/DNS at a given instant changes when the rounding errors or the initial conditions change is not really surprising. It is however a real difficulty in the practical use of LES/DNS because it means that running the same

simulation on two different machines or one machine with a different number of processors or slightly different initial conditions can lead to totally different instantaneous results. For steady flows in the mean, statistics do not depend on these changes and mean profiles must be identical. However, when the objective of the LES is the study of unsteady phenomena such as ignition or quenching in a combustor [364], knowing that results depend on these parameters is certainly a sobering thought for the LES/DNS community and a drawback in terms of industrial exploitation.

This chapter tries to address these issues and answer a simple question which is of interest for all practitioners of LES: how does the solution produced by LES depend on the number of processors used to run the simulation? On the initial condition? On internal details of the algorithm?

The next section gives an example of the effects of the number of processors in a simple case: a rectangular turbulent channel computed with a fully explicit LES code [329]. This example shows that even in an explicit code, running a simulation twice on a different number of processors can lead to totally different instantaneous solutions. The following section then gives a systematic description of the effects of rounding errors in two flows: a turbulent channel and a laminar Poiseuille flow. For all the cases, difference between two instantaneous solutions obtained by changing either the number of processors, the initial condition or the graph ordering is quantified in terms of norms between the two solutions. The effects of time step and machine precision (simple, double and quadruple) are also investigated in this section. All simulations have been performed on an IBM JS21 supercomputer.

11.2 Effects of The Number of Processors on LES

This first example is the LES of a rectangular fully developed turbulent channel of dimensions: 75x25x50 mm (Fig. 11.1). An homogeneous force is applied to a periodic channel flow to provide momentum; random disturbances are added to trigger transition to turbulence. There are no boundary conditions except for the walls in y direction. The Reynolds number is $Re_\tau = \delta u_\tau/\nu = 1500$, where δ is half the channel height and u_τ the friction velocity at the wall: $u_\tau = (\tau_{wall}/\rho)^{1/2}$ with τ_{wall} being the wall stress. The mesh contains 30^3 hexahedral elements, it is not refined at walls. The first grid point is at a reduced distance $y^+ = yu_\tau/\nu \approx 100$ of the wall. The subgrid model is the Smagorinski model and a law-of-the-wall is used at the walls [355]. The CFL number λ controlling the time step Δt is $\lambda = max((u + c)\Delta t/\Delta)$ where u is the local convective velocity, c the speed of sound and Δ the mesh size. For all simulations discussed

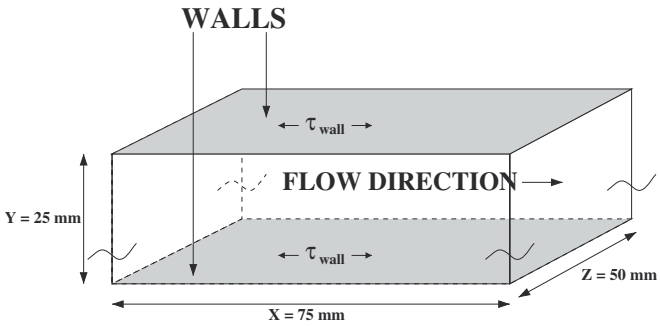

Figure 11.1. Schematic of a periodic channel. The upper and lower boundaries consist of walls, all other boundaries are pairwise periodic.

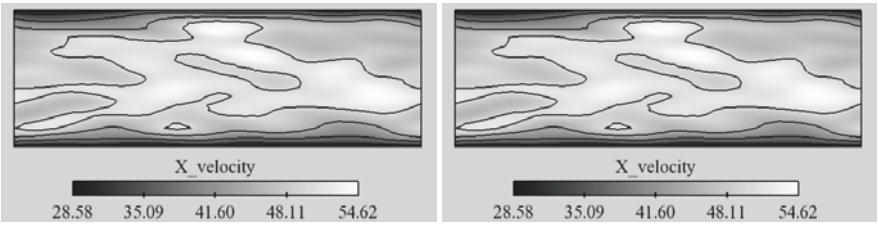

Figure 11.2. Instantaneous field of axial velocity in the central plane of the channel at $t+ = 7.68$. Left) run TC1 (4 processors), right) run TC2 (8 processors).

below, the initial condition corresponds to a snapshot of the flow at a given instant, long after turbulence was initialized so that it is fully established. The computation is performed with an explicit code where domain decomposition is such that the method is perfectly equivalent on any number of processors. The Recursive Inertial Bisection (RIB) [381; 370] algorithm has been used to partition the grid and the Cuthill-McKee algorithm is considered as the default graph reordering strategy. The scheme used here is the Lax-Wendroff scheme [296]. Additional tests were performed using a third-order Taylor-Galerkin scheme in space and time [268] but led to the same conclusions.

Figs. 11.2–11.4 show fields of axial velocity in the central plane of the channel at three instants after the initialization of the run. Two simulations performed on respectively 4 (TC1) and 8 processors (TC2) with identical initial conditions and meshes are compared. The characteristics of all pre-

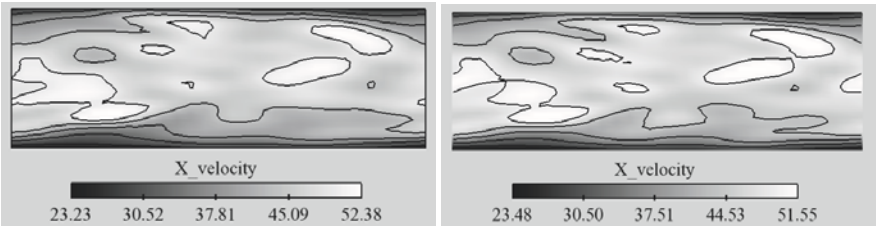

Figure 11.3. Instantaneous field of axial velocity in the central plane of the channel at $t+ = 18.43$. Left) run TC1 (4 processors), right) run TC2 (8 processors).

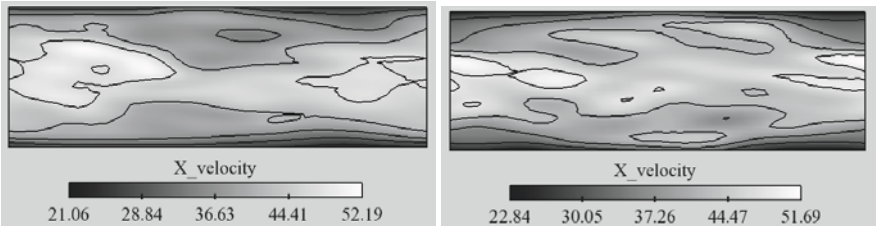

Figure 11.4. Instantaneous field of axial velocity in the central plane of the channel at $t+ = 26.11$. Left) run TC1 (4 processors), right) run TC2 (8 processors).

sented simulations are displayed in Table 11.1 and 11.2. The instants correspond to (in wall units) $t^+ = 7.68$, $t^+ = 18.43$ and $t^+ = 26.11$ respectively where $t^+ = u_\tau t/\delta$. Obviously, the two flow fields observed at $t^+ = 7.68$ are identical. However, at $t^+ = 18.43$, differences start to become visible. Finally, at $t^+ = 26.11$, the instantaneous flow fields obtained in TC1 and TC2 are totally different. Even though the instantaneous flow fields are different, statistics remain the same: mean and root mean square axial velocity profiles averaged over $t^+ \approx 60$ are identical for both simulations, as can be seen in Figs. 11.5.

This very simple example illustrates the main question of the present work: are the results of Figs. 11.2–11.4 reasonable? If it is not a simple programming error (the next section will show that it is not so), can other parameters produce similar effects?

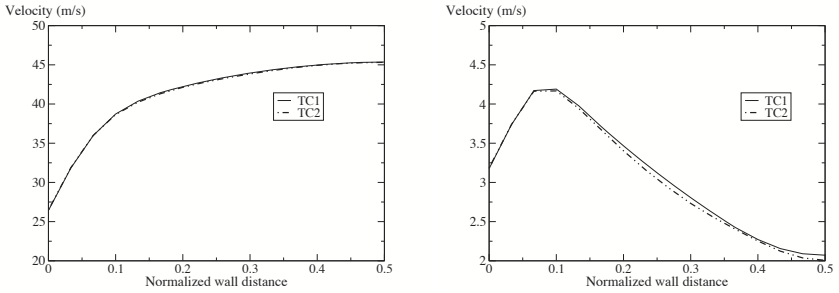

Figure 11.5. Comparison of the mean (left) root mean square (right) velocity profiles for TC1 (4 processors) and TC2 (8 processors) simulations over half channel height.

11.3 Sensitivity of LES in Laminar and Turbulent Flows

To understand how LES can produce diverging instantaneous results such as those shown in the previous section, simple tests were performed to investigate the effects of various aspects of the methodology:

- laminar/turbulent baseline flow,
- number of processors,
- initial condition,
- graph ordering,
- time step,
- machine precision.

For these tests, the objective is to quantify the differences between two LES solutions produced by a couple of simulations in Table 11.1 and 11.2. Let u_1 and u_2 be the scalar fields of two given instantaneous solutions at the same instant after initialization. A proper method to compare the latter is to use the following norms:

$$N_{max} = \max(u_1(\mathbf{x}) - u_2(\mathbf{x})) \quad \textit{and}$$
$$N_{mean} = (\frac{1}{V_\Omega} \int_\Omega (u_1(\mathbf{x}) - u_2(\mathbf{x}))^2 d\Omega)^{\frac{1}{2}} \text{ for } x \in \Omega \tag{11.1}$$

where Ω and V_Ω respectively denote the computational domain and its volume. Both norms (in m/s) will be applied to the axial velocity field so that N_{max} provides the maximum local velocity difference in the field between two solutions while N_{mean} yields a volumetrically averaged difference between the two solutions. The growth of N_{max} and N_{mean} versus the

Table 11.1. Summary of turbulent LES runs (fully developed turbulent channel).

Run Id	Nbr proc	Init. cond.	Precision	Graph ordering	CFL λ
TC1	4	Fixed	Double	CM	0.7
TC2	8	Fixed	Double	CM	0.7
TC3	1	Fixed	Double	CM	0.7
TC4	1	Modif.	Double	CM	0.7
TC5	1	Fixed	Double	RCM	0.7
TC6	4	Fixed	Double	CM	0.35
TC7	8	Fixed	Double	CM	0.35
TC8	4	Fixed	Simple	CM	0.7
TC9	8	Fixed	Simple	CM	0.7
TC10	28	Fixed	Quadr.	CM	0.7
TC11	32	Fixed	Quadr.	CM	0.7

number of iterations will be used as a direct indicator for the divergence of the solutions.

A Fully Deterministic LES?

First, it is useful to indicate that performing any of the LES of Table 11.1 twice on the same machine with the same number of processors, the same initial conditions and the same partition algorithm leads to exactly the same solution, N_{max} and N_{mean} being zero to machine accuracy. In that sense, the LES remains fully deterministic. However, this is true only if the order of operations at interfaces is not determined by the order of message arrival so that summations are always carried out in the same order. Otherwise, the randomness induced by the non deterministic order of message arrival is enough to induce diverging solutions.

Influence of Turbulence

The first test is to compare a turbulent channel flow studied in the previous section and a laminar flow. A three dimensional Poiseuille flow in a pipe geometry was used as test case. The flow is laminar and the Reynolds number based on the bulk velocity and diameter is approximately 500. The bound-

Table 11.2. Summary of laminar runs (Poiseuille flow).

Run Id	Nbr proc	Init. cond.	Precision	Graph ordering	CFL λ
LP1	4	Fixed	Double	CM	0.7
LP2	8	Fixed	Double	CM	0.7

ary conditions are set periodic at the inlet/outlet and no slip at the duct walls, a constant axial pressure gradient is imposed in the entire domain.

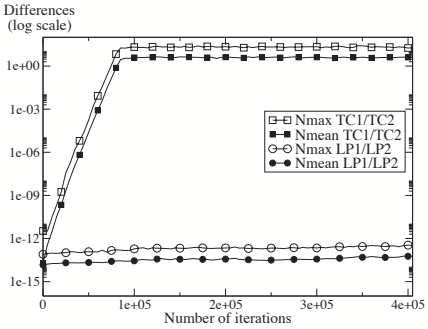

Figure 11.6. Effects of turbulence. Differences between solutions measured by N_{max} (open symbols) and N_{mean} (closed symbols) versus iteration. Squares: differences between TC1 and TC2 (turbulent channel). Circles: differences between LP1 and LP2 (laminar Poiseuille flow).

Figure 11.6 shows the evolutions of N_{max} and N_{mean} versus iteration for runs TC1/TC2 and LP1/LP2. Note that the first point of the graph is the evaluation of the difference after one iteration. The only parameter tested here is a change of the number of processors. As expected from the snapshots of Figs. 11.2–11.4, the turbulent channel simulations are very sensitive to a change in the number of processors and the solutions of TC1 and TC2 diverge rapidly leading to a maximum difference of 20 m/s and a mean difference of 3-4 m/s after 90,000 iterations. On the other hand, the difference between LP1 and LP2 hardly increases and levels off when reaching values of the order or 10^{-12}. This is expected since there is obviously only one stable solution for the Poiseuille flow for infinite times and

laminar flows do not induce exponential divergence of trajectories. However, this simple test case confirms that the turbulent character of the flow is the source of the divergence of solutions. This phenomenon must not be confused with the growth of a hydrodynamic mode, which is induced by the bifurcation in phase space of an equilibrium state of a given physical system. Obviously, such an equilibrium state does not exist for a fully developed turbulent channel flow. In this case, the separation of trajectories is caused by vorticity, which leads to an increase in the number of degrees of freedom in phase space [257] and thus high sensitivity to initial conditions. Moreover, the stagnation of absolute and mean differences between TC1/TC2 simply implies that after 90,000 iterations solutions have become fully uncorrelated and should not be misinterpreted as the saturation of an exponentially growing mode.

The basic mechanism leading to Figs. 11.2–11.4 is that the turbulent flow acts as an amplifier for rounding errors generated by the fact that the mesh is decomposed differently in TC1 and TC2. The source of this difference is the new graph reordering obtained for both decompositions. This implies a different ordering when adding the contributions to a cell residual for nodes inside the sub-domains but mainly at partition interfaces. This random noise roughly starts at machine accuracy (Fig. 11.6) at a few points in the flow and grows continuously if the flow is turbulent.

The growth rate α of the differences between solutions in simulations TC1 and TC2 cannot be estimated in a simple manner. A simplified description for the determination of growth rates of trajectory separation is found in Jimenez [299], it is briefly summarized in the following. For two-dimensional vortical flows, assuming a description of vortices as points with associated circulations and neglecting viscosity, a set of linearized ordinary differential equations can be derived to evaluate the difference between two neighbouring flow field trajectories differing by an arbitrary infinitesimal perturbation δU in the axial velocity. This system admits exponential solutions, the growth rates of which are determined by the real part of the eigenvalues. The evolution of inviscid/conservative systems conserves volume in phase space. As the real part of the eigenvalues describes the separation of trajectories in time, it represents a measure of the evolution of the volume in phase space. Thus, if the sum of the real parts vanishes, then at least one of them has to be positive. At this stage, the number of degrees of freedom of the system imposes topological constraints on the trajectories and can prevent their separation, but a few degrees of freedom suffice for such systems to exhibit chaotic behavior, as was demonstrated by the famous Lorenz attractor [315]. This argument illustrates that the separation of trajectories is a property related to the nature of vorticity and mainly

driven by the number of degrees of freedom in phase space. Therefore, a simple estimate of the growth rate from flow parameters does a priori not seem possible. Although the simplifications in the described analysis are severe, one can suppose that independent of the spatial distribution and amplitude (within the limit of the linearity assumption) of perturbations applied to a given turbulent flow field, the separation of trajectories for various simulations yields similar exponential growth rates, which is confirmed in the following. Moreover, it is a pure physical phenomenon and though induced by rounding errors, the growth rate should not depend on numerical parameters such as machine precision or time step.

Influence of Initial Conditions

The previous section has shown that turbulence combined with a different domain decomposition (i.e. a different number of processors for the following) is sufficient to lead to totally different instantaneous flow realizations. It is expected that a perturbation in initial conditions will have the same effect as domain decomposition. This is verified in runs TC3 and TC4 which are run on one processor only, thereby eliminating issues linked to parallel implementation. The only difference between TC3 and TC4 is that in TC4, the initial solution is identical to TC3 except at one random point where a 10^{-16} perturbation is applied to the streamwise velocity component. Simulations with different locations of the perturbation were run to ensure that their position did not affect results.

Figure 11.7 shows that the growth rate of the difference between TC3 and TC4 is exactly the same as the one observed between TC1 and TC2 (also displayed in Fig. 11.7): two solutions starting from a very slightly perturbed initial condition diverge as fast as two solutions starting from the same solution but running on different numbers of processors. Note that the difference between runs TC1 and TC2 comes from random rounding errors introduced at each time step while TC3 and TC4 differ only through the initial condition: no perturbation is added during the simulation. Still, the differences between TC3 and TC4 increase as fast as those between TC1 and TC2: this confirms that a turbulent flow amplifies any difference in the same manner, whether it is due to rounding errors or to a perturbation of the initial conditions.

Effects of Graph Ordering

It has already been indicated that performing the same simulation twice (with the same number of processors and same initial conditions) leads to

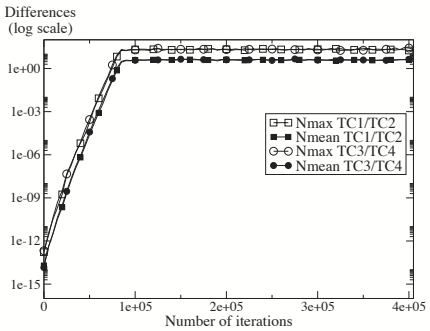

Figure 11.7. Effects of initial conditions. Differences between solutions measured by N_{max} (open symbols) and N_{mean} (closed symbols) versus iteration. Squares: differences between TC1 and TC2 (different numbers of processors). Circles: differences between TC3 and TC4 (different initial conditions).

exactly the same result. However, this is only true as long as exactly the same code is used. It is not verified any more as soon as a modification affecting rounding errors is done in the code. At this point, so many factors affecting rounding errors can be cited that a general discussion is pointless. This chapter will focus on fully explicit codes and on one example only: the order used to add residuals at nodes in a cell vertex scheme. This order is controlled by the developer. For simulation TC5, the ordering of this addition was changed (reverse Cuthill-McKee algorithm): the residual at a given mesh node was assembled by adding the contributions to a cell residual in a different order. This change does not affect the flow data: in TC5 the node residual in a regular tetrahedral mesh is obtained by $1/4(R_1 + (R_2 + (R_3 + R_4))$ where the R_i's are the residuals of the cells surrounding the node and by $1/4(R_4 + (R_3 + (R_2 + R_1))$ in TC3. It has an effect, however, on rounding errors and the cumulated effects of this non-associativity error are what this test tries to isolate. TC5 and TC3 are performed with the same initial condition and run on one processor only. The only difference is the graph reordering strategy.

As shown by Fig. 11.8, the differences between TC5 and TC3 are again similar to those observed between TC1 and TC2 (obtained by changing the number of processors). This confirms that rounding errors (and not the parallel character of the code) are the source of the solution divergence. It

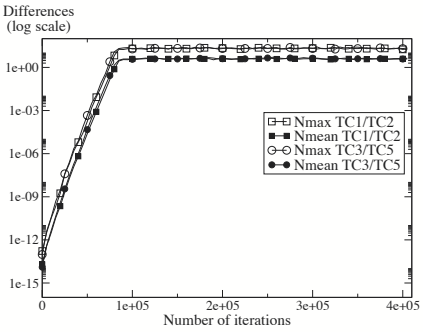

Figure 11.8. Effects of addition order. Differences between solutions measured by N_{max} (open symbols) and N_{mean} (closed symbols) versus iteration. Squares: differences between TC1 and TC2. Circles: differences between TC3 and TC5.

also shows that any modification of the code which can introduce a small modification of the results (within machine accuracy), can then lead to such a divergence, suggesting that repeating an LES simulation with the same code after a few modifications will probably never yield the same instantaneous flow fields, potentially leading to discussions on the validity of the modified code.

Effects of Time Step

It is interesting to verify that numerical aspects do not influence the growth rate of the solutions difference and that the growth rate is only determined by the physical and geometrical parameters of the configuration. On that account, simulations TC6 and TC7 are performed with a time step reduced by a factor 2 compared to simulations TC1 and TC2. TC6 and TC7 are carried out on respectively 4 and 8 processors. The norms between TC6 and TC7 are displayed in Fig. 11.9 and compared to the norms between TC1 and TC2. From the explanations given above, similar growth rates are expected when comparing the growth rates over physical time. The growth rates observed in Fig. 11.9 are indeed very similar. The slight difference is probably due to the variation of the numerical dispersion and dissipation properties of the scheme with the time step [296].

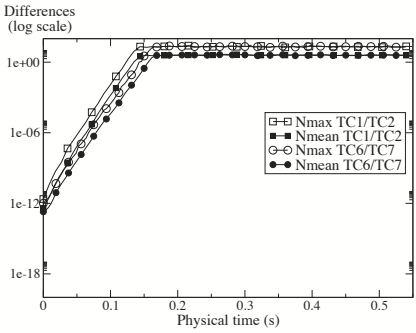

Figure 11.9. Effects of time step. Differences between solutions measured by N_{max} (open symbols) and N_{mean} (closed symbols) versus physical time. Squares: differences between TC1 and TC2 (time step Δt). Circles: differences between TC6 and TC7 (time step $\Delta t/2$).

Effects of Machine Precision

A last test to verify that the divergence between solutions is not due to a programming error but depends primarily on rounding errors is to perform the same computation with simple/quadruple precision instead of double precision. Simulations TC1 and TC2 were repeated using single precision in runs TC8 and TC9 (Table 11.1) and quadruple precision in TC10 and TC11. To compensate for the increase in computational time for quadruple precision simulations, roughly a factor ten compared to double precision, TC10 and TC11 were carried out on respectively 28 and 32 processors in order to yield a reasonable restitution time. Results are displayed in Fig. 11.10 and compared to the difference between TC1 and TC2.

Figure 11.10 shows that the solution differences for TC8/TC9 and TC10/TC11 roughly start from the respective machine accuracies (differences of 10^{-6} for single precision after one iteration, differences of 10^{-30} for quadruple precision after one iteration) and increase exponentially with the same growth rate before reaching the same difference levels for all three cases. This shows that higher precision computations cannot prevent the exponential divergence of trajectories but only delay it.

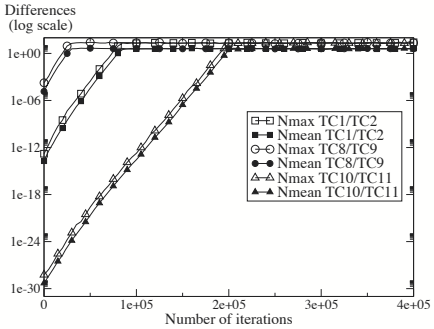

Figure 11.10. Effects of machine accuracy. Differences between solutions measured by N_{max} (open symbols) and N_{mean} (closed symbols) versus iteration. Squares: differences between TC1 and TC2 (double precision). Circles: differences between TC8 and TC9 (single precision). Triangles: differences between TC10 and TC11 (quadruple precision)

11.4 Conclusions

This chapter focused on the sensitivity of instantaneous LES fields to multiple parameters such as number of processors, initial condition, time step, changes in addition ordering of cell residuals for cell vertex methods. The baseline simulation used for the tests was a fully developed turbulent channel. The conclusions are the following:

- Any turbulent flow computed by LES exhibits significant sensitivity to these parameters, leading to instantaneous solutions which can be totally different. Laminar flows are almost insensitive to these parameters.
- The divergence of solutions is due to two combined facts: (1) the exponential separation of trajectories in turbulent flows and (2) the nondeterministic rounding errors induced by different domain decompositions or different ordering of operations. More generally any change in the code lines affecting rounding errors will have the same effects.
- Small changes in initial condition (of the order of machine accuracy at one point of the flow only) produce similar divergence of solutions.
- Working with higher precision machines does not suppress the divergence of solutions but delays it.

These results confirm the expected nature of LES [343] in which solutions are meaningful only in a statistical sense and instantaneous values can not

be used for analysis. However, on a more practical level, they point out various difficulties to develop LES codes:

- Repeating the results of a given LES after modifying the code and verifying that instantaneous solutions have not changed is not always possible. Since any programming error will also lead to a change in instantaneous solutions, identifying errors introduced by new lines will require a detailed analysis based on average fields (and not on instantaneous fields) and a significant loss of time.
- Verifying an LES code on a parallel machine is a difficult task: running the code on different numbers of processors will lead to different solutions and make comparisons impossible.
- Porting a LES code from one machine to another will also produce different solutions for turbulent runs, making comparison and validations of new architectures difficult.

More generally, these results demonstrate that the concept of "quality" in LES will require much more detailed studies and tools than what has been used up to now in Reynolds Averaged simulations. Instabilities appearing in a given LES on a given computer can have sources which were not expected at first sight (like the number of processors). Mastering these instabilities (or at least understanding them) will be an important task to get the full power of LES techniques.

Bibliography

[1] Abbot, I.H. and von Doenhoff, A.E. (1959). *Theory of Wing Section* Dover Publications. New York.

[2] Aizin, L.B. and Polyakov, N.F. (1979). Acoustic generation of Tollmien-Schlichting waves over local unevenness of surfaces immersed in stream. *Preprint 17, Akad. Nauk* USSR, *Siberian Div., Inst. Theor. Appl. Mech., Novosibrisk* (In Russian).

[3] Allen, L.D., and Burrows, F.M. (1956). Flight Experiments on the boundary layer characteristics of a swept back wing. *Cranfield, College of Aero.Rept. No. 104.*

[4] Allen, L. and Bridges, T.J. (2002). Numerical exterior algebra and the compound matrix method, *Numerische Mathematik* **92**:197-232.

[5] Allen, L. and Bridges, T.J. (2003). Hydrodynamic stability of the Ekman boundary layer including interaction with a compliant surface. *Euro. J. Mechanics B/ Fluids* **22**, 239-258.

[6] Anscombe, A. and Illingworth, L.N. (1952). Wind tunnel observations of boundary layer transition on a wing at various angles of sweep back. *ARC R and M 2968.*

[7] Anderson, J.D. Jr. (1991). *Fundamentals of Aerodynamics*, McGraw Hill, New York.

[8] Arnal, D. (1984). Description and prediction of transition in two-dimensional incompressible flow. *AGARD Report No. 709*, **2.1 - 2.71**.

[9] Arnal, D., Coustols, R. and Jullien, J. (1984). Experimental and theoretical study of transition phenomena on infinite swept wing. *La Recherche Aerospatiale* No. **1984-4**, 275-290.

[10] Arnal, D., Habiballah, M. and Coustols, E. (1984a). Laminar instability theory and transition criteria in two- and three-dimensional flow. *La Recherche Aerospatiale* No. **1984-2**.

[11] Arnal, D. (1986). Three-dimensional boundary layer: Laminar-turbulent transition. *AGARD eport No. 741* 1-34.

[12] Arnal, D. and Jullien, J.C. (1987). Three dimensional transition studies at ONERA/CERT. *AIAA Paer No.87-1335.* 87-1335.

[13] Arnal, D., Casalis, G. and Jullien, J.C. (1989). Experimental and theoretical analysis of natural transition on infinite swept wing. In the IUTAM Symp. Proc. on *Laminar- Turbulent Transition* (Eds. D. Arnal, R. Michel), Springer-Verlag, 311-326.

[14] Ashpis, D.E. and Reshotko, E. (1990). Vibrating problem revisited. *J. Fluid Mech.*, **213** 531-547.

[15] Bartlett, D.W. (1975). Application of a supercritical wing to an executive type jet transport model. *N*ASA TM-X 3251, June 1975.

[16] Batchelor, G.K. (1988). *An Introduction to Fluid Dynamics*. Cambridge Univ. Press, U.K.

[17] Bauer, F., Garabedian, P. and Korn, D. (1972). A Theory of Supercritical Wing Sections, With Computer Programs and Examples. Springer Verlag, New York.

[18] Beasley, J.A. (1973). Calculation of the laminar boundary layer and the prediction of transition on a sheared wing. ARC R and M 3787.

[19] Bender, C.M. and Orszag, S.A. (1987). *Advanced Mathematical Methods for Scientists and Engineers*. McGraw Hill Book Co., International Edition, Singapore.

[20] Bers, A. (1975). *Physique des Plasmas*. (Eds. C. Dewitt and J. Peyraud) Gorden and Breach, New York.

[21] Betchov, R. and Criminale, W.O. Jr. (1967). *Stability of Parallel Flows*. Academic press, New York.

[22] Breuer, K.S. and Haritonidis, J.H. (1990). The evolution of a localized disturbance in a laminar boundary layer. Part I. Weak disturbances. *J. Fluid Mech.*, **220**, 569-594.

[23] Breuer, K.S. and Landahl, M.T. (1990). The evolution of a localized disturbance in a laminar boundary layer. Part II. Strong disturbances. *J. Fluid Mech.*, **220**, 595-621.

[24] Breuer, K.S. and Kuraishi, T. (1993). Bypass transition in two and three dimensional boundary layers. *AIAA paper no.* **93-3050**.

[25] Brewstar R.A. and Gebhart B. (1991). Instability and disturbance amplification in a mixed-convection boundary layer. *J. Fluid Mech*, **229**:115-133.

[26] Bridges, T.J. and Morris, P. (1984). Differential eigenvalue problems in which the parameters appear nonlinearly, *J. Comp. Phys.* **55**:437-460.

[27] Brillounin, L. (1960). *Wave Propagation and Group Velocity*. Academic press, New York.

[28] Brinckman, K.W. and Walker, J.D.A. (2001). Instability in a viscous flow driven by streamwise vortices. *J. Fluid Mech.*, **432**, 127-166.

[29] Burrows, F.M. (1956). A theoriretical and experimental study of the boundary layer flow on a 45° swept back wing. *Cranfield College of Aero. Rept.No. 109*.

[30] Buter, T.A. and Reed, H.L. (1993). Numerical investigation of receptivity to freestream vorticity. *AIAA-93-0073*.

[31] Chattopadhyay, M. (2001). Instability and Transition of Wall Bounded Flows by Free-Stream Excitation. M. Eng. Thesis, Dept of Mech. Engg. National University of Singapore.

[32] Chaudhari, M. and Streett, C.L. (1990). Boundary layer receptivity phenomena in three-dimensional and high speed boundary layer. *AIAA-90-5258.*

[33] Chaudhari, M. (1996). Boundary-layer receptivity to three-dimensional unsteady vortical disturbances in free stream. *AIAA-96-0181.*

[34] Chen, T.S., Sparrow, E.M., and Mucoglu, A. (1977). Mixed convection in boundary layer flow on a horizontal plate, *ASME J. Heat Transfer* **99**:66-71.

[35] Chen, T.S. and Moutsoglu. (1979). Wave instability of mixed convection flow on inclined surfaces. *Num. Heat Transfer*, **2**:497-509.

[36] Chen, T.S. and Mucoglu, A. (1979). Wave instability of mixed convection flow over a horizontal flat plate, *Int. J. Heat Mass Transfer* **22**:185-196.

[37] Collis, S.S. and Lele, S.K. (1996). A computational approach to swept leading-edge receptivity. *AIAA-96-0180.*

[38] Crabtree, L.F., Kuchemann, D. and Sowerby, L. (1963). Three-dimensional boundary layers. In *Laminar Boundary Layers.* (Ed.L.Rosenhead) Clarendon Press, U.K.

[39] Croom, C.C. and Holmes, B.J. (1985). Flight evaluation of an insect contamination protection system for laminar flow wings. *SAE Paper No.* 850860.

[40] Crouch, J.D. (1992). Non-localized receptivity of boundary layers. *J. Fluid Mech.*, **244**, 567-581.

[41] Crouch, J.D. (1993). Receptivity to three-dimensional boundary layers. *AIAA-93-0074.*

[42] Dam, R.F., Egmond, J.F. and Sloof J.W. (1994). Optimization of target pressure distribution. In *Optimum Design Methods for Aerodynamics.* AGARD-R-803.

[43] Davies, S.J. and White, C.M. (1928). An experimental study of the flow of water in pipes of rectangular section. *Proc. Royal Soc. London Ser. A* **119**, 92.

[44] Degani, A.T., Walker, J.D.A. and Smith, F.T. (1998). Unsteady separation past moving surfaces. *J. Fluid Mech.*, **375**, 1-38.

[45] Diaz, F., Gavalda, J., Kawall, J.G. and Giralt, F. (1983). Vortex shedding from a spinning cylinder. *Phys. Fluids* **26(12)**, 3454-3460.

[46] Dietz, A.J. (1999). Local boundary layer receptivity to a convected free stream disturbance. *J. Fluid Mech.* **378**, 291-317.

[47] Dipankar, A., Sengupta, T.K. and Talla, S.B. (2007). Suppression of vortex shedding behind a circular cylinder by another control cylinder at low Reynolds numbers. *J. Fluid Mech.* **573**, 171-190.

[48] Dodbele, S.S., Van Dam, C.P., Vijgen, P.M.H.W. and Holmes, B.J. (1987). Shaping of airplane fuselages for minimum drag. *J. Aircraft*, **24(5)**, 298-304.

[49] Doligalski, T.L., Smith C.R., and Walker J.D.A. (1994). Vortex interaction with wall. *Ann. Rev. Fluid Mech.*, **26**, 573-616.

[50] Drazin, P.G. and Reid, W.H. (1981). *Hydrodynamic Stability.* Cambridge Univ. Press, U K.

[51] Dryden, H.L. (1959). Transition from laminar to turbulent flow. In *Turbulent Flows and Heat Transfer, High Speed Aerodynamics and Jet Propulsion.* Edited by C. C. Lin.

[52] Eckert, E.R.G. and Soehngen, E. (1951). Interferometric studies on the stability and transition to turbulence in a free-convection boundary-layer, *Proc. Gen. Disc. Heat Transfer, ASME and IME*, London, pp. 321.

[53] Elsaadawy, E.A. and Britcher, C.P. (2002). The extent of a laminar boundary layer under the influence of a propeller slipstream. AIAA Applied Aerodynamics Conf. paper no. *AIAA 2002-2930.*

[54] Eppler, R. and Somers, D. (1980). A computer program for the design and analysis of low-speed airfolis. *NASA TM-80210.*

[55] Fasel, H. and Konzelmann, U. (1990). Nonparallel stability of a flat plate boundary layers using complete Navier-Stokes equations. *J. Fluid Mech.*, **221**, 331-347.

[56] Fjϕrtoft, R. (1950). Application of integral theorems in deriving criteria of stability for laminar flows and for baroclinic circular vortex. *Geofys. Publ. Oslo* **17(6)**, 1-51.

[57] Fujino, M., Yoshizaki, Y. and Kawamura, Y. (2003). Natural-laminar-flow airfoil development for a lightweight business jet. *J. of Aircraft*, **40(4)**, 609-615.

[58] Fujino, M. and Kawamura, Y. (2003). Wave drag characteristics of an over-the-wing nacelle business-jet configuration. *J. Aircraft*, **40(6)**, 1177-1184.

[59] Gaster, M. (1962). A note on the relation between temporally-increasing and spatially- increasing disturbances in hydrodynamic stability. *J. Fluid Mech.* **14**, 222-224.

[60] Gaster, M. (1965a). A simple device for preventing turbulent contamination on swept leading edges. *J. Roy. Aero. Soc.* **69**, 788-789.

[61] Gaster, M. and Sengupta, T.K. (1993). The generation of disturbance in a boundary layer by wall perturbation: The vibrating ribbon revisited once more. In *Instabilities and Turbulence in Engineering Flows* (eds. D.E. Ashpis, T.B. Gatski and R. Hirsch), 31-49.

[62] Gaster, M., Grosch, C.E. and Jackson, T.L. (1994). The velocity field created by a shallow bump in a boundary layer. ICASE Rept. 94-21, NASA Langley RC, (also published in *Physics of Fluids*), **6(9)**, 3079-3085.

[63] Gebhart, B., Jalurai, Y., Mahajan, R.L., and Sammakia, B. (1988). *Buoyancy-Induced Flows and Transport*. Hemisphere Publication, Washington DC.

[64] Gilpin, R.R., Imura, H. and Cheng, K.C. (1978). Experiments on the onset of longitudinal vortices in horizontal Blasius flow heated from below, *ASME J. Heat Transfer* ***100****:71-77.*

[65] Goldstein, S. (1938). *Modern Development in Fluid Mechanics*, Volume 1 and 2, Clarendon Press, Oxford, U.K.

[66] Golstein, M.E., Sockol, P.M. and Sanz, J. (1983). The evolution of Tollmien- Schlichting waves near a leading edge. Part 2. Numerical determination of amplitudes. *J. Fluid Mechanics*, **129**, 443-453.

[67] Goldstein, M.E. (1983). The evolution of Tollmien- Schlichting waves near a leading edge. *J. Fluid Mech.*, **127**, 59-81.

[68] Goldstein, M.E. (1985). Scattering of acoustic waves into Tollmien-Schlichting waves by small streamwise variation in surface geometry. *J. Fluid Mech.*, **154**, 509-529.

[69] Goldstein, M.E. and Hultgren, L.S. (1989). Boundary-layer respectivity to long-wave free-stream disturbances. *Ann. Rev. Fluid Mech.*, **21**, 137-166.

[70] Gray, W.E. and Fullam, P.W.J. (1950). Comparison of flight and wind tunnel measurements of transition on a highly finished wing (King Cobra). *RAE report no.* 2383, June 1950.

[71] Gregory, N., Stuart, J.T. and Walker, J.S. (1955). On the stability of three dimensional boundary layer with application to the flow due to a rotating disc. *Phil. Trans. Roy. Soc. London*, Series A, **248**, 155-199.

[72] Haaland, S.E. and Sparrow, E.M. (1973). Vortex instability of natural convection flows on inclined surfaces, *Int. J. Heat Mass Transfer* **16**:2355-2367.

[73] Hall, P., Malik, M.R. and Poll, D.I.A. (1984). On the stability of an infinite swept attachment-line boundary layer. *Proc. R. Soc. Lond.* A **395**, 229-245.

[74] Hall, P. and Malik, M.R. (1986). On the instability of three-dimensional attachment-line boundary layer: weakly non-linear theory and numerical approach. *J. Fluid Mech.*, **395**, 229-245.

[75] Hall, P. and Morris, H. (1992). On the instability of boundary layers on heated flat plates, *J. Fluid Mech.* **245**:367-400.

[76] Helmholtz, H. von (1868). On discontinuous movements of fluids. Phil. Mag. **(4)36**, 337-346.

[77] Henningson, D.S., Lundbladh, A. and Johansson, A.V. (1993). A mechanism for bypass transition from localized disturbances in wall-bounded shear flows. *J. Fluid Mechanics*.

[78] Holmes, P., Lumley, J.L. and Berkooz, G. (1996). *Coherent Structures, Dynamical Systems and Symmetry*. Cambridge Univ. Press., U.K.

[79] Homann., F. (1936). Einfluss grosser zahigkeit bei stromung um zylinder. *Firsch. auf dem Gebeite des Ingenieurwesens* **7(1)**, 1-10, 1936.

[80] Huerre, P. and Monkewitz, P.A. (1985). Absolute and convective instabilities in free shear layers. *J. Fluid Mech.* **159**, 151.

[81] Hughes, T.H. and Reid, W.H. (1965). On the stability of the asymptotic suction boundary layer profile. *J. Fluid Mech.*, **23**, 715-735.

[82] Iyer, P.A. and Kelly, R.E. (1974). The instability of the laminar free convection flow induced by a heated, inclined plate, *Int. J. Hear Mass Transfer* **17**:517-525.

[83] Jackson., C.P. (1987). A finite element study of the onset of vortex shedding in flow past variously shaped bodies. *J. Fluid Mech.* **182**, 23-45, 1987.

[84] Jacobs, E.N. (1939). Preliminary report on laminar-flow airfoils and new methods adopted for airfoil and boundary layer investigations. *NACA WR L-345*.

[85] Jacobs, R.G. and Durbin, P.A. (2001). Simulation of bypass transition. *J. Fluid Mech.*, **428**, 185-212.

[86] Jaffe, N.A., Okamura, T.T. and Smith, A.M.O. (1970). Determination of spatial amplification factors and their application to predicting transition. *AIAA*, **8(2)** 301-308.

[87] Jameson, A. (1988). Aerodynamic design via control theory. *J. Scientific Computing*, **3**, 233-260.

[88] Joslin, R.D. (1995). Direct simulation of evolution and control of three-dimensional instabilities in attachment-line boundary layers. *J. Fluid Mech.* **291**, 369-392.

[89] Joslin, R.D. (1996). Simulation of non-linear instabilities in an attachment-line boundary layer. *Fluid Dyn. Res.* **18**, 81-97.

[90] Joslin, R.D. (1998). Aircraft laminar flow control. In *Ann. Rev. Fluid Mech.* **30**, 1-29.

[91] Kaups, K. and Cebeci, T. (1977). Compressible laminar boundary layers with suction on swept and tapered wings. *J. of Aircraft*, **14**(7).

[92] Kelvin, Lord (1871). Hydrokinetic solutions and observations. *Phil Mag.(4)* **42**, 362-377.

[93] Kendall, J.M. (1987). Experimental study of laminar boundary layer receptivity to a traveling pressure field. *AIAA paper no.* 87-1257.

[94] Kendall, J.M. (1990). Boundary layer receptivity to free stream turbulence. *AIAA paper no.* 90-1504.

[95] Kerschen, E.J. (1991). Linear and non-linear receptivity to vortical free-stream disturbances. In *Boundary Layer Stability and Transition to Turbulence*. (eds. D.C. Reda, H.L. Reed & R.K. Kobayashi) *ASME FED* **114**, 43-48.

[96] Klebanoff, P.S. and Tidstrom, K.D. (1959). Evolution of amplified waves leading to transition in a boundary layer with zero pressure gradient. NASA TN D- 195.

[97] Klebanoff, P.S. (1971). Effect of free stream turbulence on the laminar boundary layer, *Bull. Am. Phys. Soc.* **10**, 1323.

[98] Koch, W. (1985). Local instability characteristics and frequency determination of self excited wake flow. *J. Sound and vib.*, **99**, 53-83.

[99] Kosambi, D.D. (1943) Statistics in function space. *J. Indian Math. Soc.* **7**, 76-88.

[100] Kovasznay, L.S.G. (1949). Hot-wire investigation of the wake behind cylinders at low Reynolds numbers. Proc. Roy. Soc. London A. **198**, 174-190.

[101] Landahl, M.T. (1980). A note on an algebraic instability of inviscid parallel shear flows. *J. Fluid Mech.*, **98**, 243-251.

[102] Landahl, M.T. and Mollo-Christensen, E. (1992). *Turbulence and Random Processes in Fluid Mechanics*, Cambridge Univ. Press, U.K.

[103] Landau, L.D. and Lifshitz, E.M. (1959). Fluid Mechanics- vol.6. Addision- Wesley, *Pergamon Press, London.*

[104] Leehey, P. and Shapiro, P. (1979). Leading edge effect in laminar boundary layer excitation by sound. In *Laminar Turbulent Transition (eds. R. Eppler and H. Fasel)*, 321-331, Springer Verlag.

[105] Leib, S.J., Wundrow, D.W. and Goldstein, M.E. (1999). Generation and growth of boundary-layer disturbances due to free-stream turbulence. *AIAA-99-0408.*

[106] Lin, C.C. (1955). *Theory of Hydrodynamic Stability.* Cambridge Univ. Press, Cambridge, U.K.

[107] Lin, N., Reed, H.L. and Saric, W.S. (1992). Effect of leading edge geometry on boundary-layer receptivity to freestream sound. In *Instability, Transition and Turbulence.* (Eds. M.Y. Hussaini, A. Kumar and C.L. Streett), Springer,New York.

[108] Lin, N., Stuckert, G.K. and Herbert, Th. (1995). Boundary layer receptivity to freestream vortical disturbances. *AIAA-95-0772.*

[109] Lim, T.T., Sengupta, T.K. and Chattopadhyay, M. (2004). A visual study of vortex-induced subcritical instability on a flat plate laminar boundary layer. *Expts. In Fluids.* **37**, 47-55.

[110] Liu, X. and Rodi, W. (1991). Experiments on transitional boundary layers with wake induced unsteadiness. *J. Fluid Mech.* **231**, 229-256.

[111] Liu, Z. and Liu, C. (1994). Fourth order finite difference and multigrid methods for modeling instabilities in flat plate boundary layer- 2D and 3D approaches. *Computers and Fluids*, **23**, 955-982.

[112] Lloyd, J.R. and Sparrow, E.M. (1970). On the instability of natural convection flow on inclined plates, *J. Fluid Mech.* **42**:465-470.

[113] Lundbladh, A. and Johansson, A.V. (1991). Direct simulation of turbulent spots in plane Couette flow. *J. Fluid Mech*, **229**, 499-576.

[114] Mack, L.M. (1969). Boundary layer stability theory, *Doc.* ***900-277****, Rev.* A, Jet Prop. Lab, Pasadena, Calif.

[115] Mack, L.M. (1977) Transition and laminar instability. *JPL Publicaion* 77-15.

[116] Mack, L.M. (1984). Boundary layer stability theory. Sppecial course on *Stability and Transition of Laminar Flow.* AGARD Report No.709.

[117] Maddalon, M.D. and Braslow, A.L. (1990) Simulated-airline-service flight tests of laminar-flow control with perforated-surface suction system. *NASA TP 2966.*

[118] Malik, M.R. (1982). COSAL- a black box compressible stability analysis code for transition prediction in three-dimensional boundary layer. *NASA CR 165 925.*

[119] Malik, M.R. and Poll, D.I.A. (1985). Effect of curvature on three-dimensional boundary-layer stability. *AIAA J.*, **23**, 1362-1369.

[120] Masad, J.A. (1996). Effect of surface waviness on transition in three-dimensional boundary layer flow. *NASA CR* 201641.

[121] McGhee, R.J. and Beasley, W.D. (1973) Low-speed aerodynamic characteristics of a 17-percent thick airfoil section designed for general aviation applications. *NASA TN D*-7428.

[122] McGhee, R.J., Beasley, W.D. and Whitcomb, R.T. (1980). NASA low- and medium-speed airfoil development. In *Advanced Technology Airfoil Research* ***II***, NASA CP 2046.

[123] Michel, R. (1952). Etude de la transition sur les profils d'aile-establishment d'un point de transition et calcul de la trainee de profil en incompressible. *ONERA report no.* 1/1578A.

[124] Michel, R., Arnal. D., Coustols, E. and Jullien, J.C. (1984). Experimental and theoretical studies of boundary layer transition on a swept infinite wing. In Proc. of IUTAM Symp. On *Laminar-Turbulent Transition* Novosibirsk, USSR, Springer Verlag.

[125] Miley, S.J. and von Lavante, E. (1985). Propeller propulsion integration- state of technology surveys. *NASA CR-3882.*

[126] Miley, S.J., Howard, R.M. and Holmes, B.J. (1988). Wing laminar boundary layer in the presence of a propeller slipstream. *J.Aircraft*, **25(7)**, 606-611.

[127] Moens, F., Perraud, J., Krumbein, A., Toulorge, T., lannelli, P., Eliasson, P. and Hanifi, A. (2007). Transition prediction and impact on 3D high-lift wing configuration. *AIAA Paper No. 2007-4302.*

[128] Monin, A.S. and Yaglom, A.M. (1971). *Statistical Fluid Mechanics: Mechanics of Turbulence.* The MIT Press, USA.

[129] Moresco, P. and Healey, J.J. (2000). Spatio-temporal instability in mixed convection boundary layers, *J. Fluid Mech.* **402**:89-107.

[130] Morkovin, M.V. (1958). Transition from laminar to turbulent flow - a review of the recent advances in its understanding. *ASME* Tranaction, **80**, 1121-1128.

[131] Morkovin, M.V. (1969). Critical evaluation of transition from laminar to turbulent shear layer with emphasis on hypersonically traveling bodies. *AFFDL-TR*-68-149.

[132] Morkovin, M.V. (1978). Instability, Transition to Turbulence and Predictability. AGARDOGRAPH No. 236,NATO Document.

[133] Morkovin, M.V. (1990). On receptivity to environmental disturbances. In *Instability and Transition, vol. 1 and 2* (eds. MY Hussaini & RG Voigt), 272-280, Springer Verlag, New York.

[134] Morkovin, M.V. (1991). Panoramic view of changes in vorticity distribution in transition instabilities and turbulence. In *Transition to Turbulence (eds. DC Reda, HL Reed and R Kobayashi).* ASME FED Publication, volume **114**, 1-12.

[135] Moutsoglu, A., Chen, T.S. and Cheng, K.C. (1981). Vortex instability of mixed convection flow over a horizontal flat plate, *ASME J. Heat Transfer* **103**:257-261.

[136] Mucoglu, A. and Chen, T.S. (1978). Wave instability of mixed convection flow along a vertical flat plate, *Num. Heat Transfer* **1**:267-283.

[137] Murdock, J.W. (1980). The generation of Tollmien- Schlichting wave by a sound wave. *Proc. R. Soc. London A*, **372**, 517-534.

[138] Murri, D.G., McGhee, R.J., Jordan, F.L., Davis, P.J. and Viken, J.K. (1987). Wind tunnel results of the low speed NLF(1)-0414F airfoil. *NASA CP 2487, Part 3*, 673-695.

[139] Nayfeh, A.H. (1980). Stability of three-dimensional boundary layers. *AIAA J.*, **18**, 406-416.

[140] Nemec, M. and Zingg, D.W. (2002). Newton-Kryolv algorithm for aerodynamic design using the Navier-Stokes equations. *AIAA J.*, **40**(6), 1146-1154.

[141] Ng, B.S. and Reid, W.H. (1980). On the numerical solution of the Orr-Sommerfeld problem: Asymptotic intial conditions for shooting method. *J. Comp. Phys.*, **38**, 275-293.

[142] Ng, B.S. and Reid, W.H. (1985). The compund matrix method for ordinary differential systems. *J. Comp. Phys.* **58**, 209-228.

[143] Nishioka, M. and Sato, H. (1973). Measurements of velocity distributions in the wake of a circular cylinder at low Reynold numbers. *J. Fluid Mech.* **65**, 97-112.

[144] Nishioka, M. and Morkovin, M.V. (1986). Boundary-layer receptivity to unsteady pressure gradients: Experiments and overview. *J. Fluid Mech.*, **171**, 219-261.

[145] Obabko, A.V. and Cassel, K.W. (2002) Navier-Stokes solutions of unsteady separation induced by a vortex. *J. Fluid Mech.* **465**, 99-130.

[146] Obara, C.J., Hastings, E.C., Schoenster, J.A., Parrott, T.L. and Holmes, B.J. (1986). Natural laminar flow flight experiments on a turbine engine nacelle fairing. *AIAA Paper* 86-9756.

[147] Obremski, H.G., Morkovin, M.V. and Landahl, M. (1969). A porfolio of stability characteristics of incompressible boundary layer,*AGARDOGRAPH* No. 134.

[148] Obrist, D. and Schmid, P.J. (2003) On the linear stability of swept attachment-line boundary layer flow. Part 2. Non-modal effect and receptivity. *J. Fluid Mech.* **493**, 31-58.

[149] Orr, W. McF. (1907). The stability or instability of the steady motions of a perfect liquid and of a viscous liquid. Part I: A perfect liquid. Part II A viscous liquid. *Proc. Roy. Irish Acad.* **A27**, 9-138.

[150] Papoulis, A. (1962). *Fourier Integral and Its Applications*. McGraw Hill, New York.

[151] Peridier, V.J., Smith, F.T. and Walker, J.D.A. (1991). Vortex-induced boundary-layer separation. Part 1. The unsteady limit problem. $Re \rightarrow \infty$. *J. Fluid Mech.*, **232**, 99-131.

[152] Peridier, V.J., Smith, F.T. and Walker, J.D.A. (1991a). Vortex-induced boundary-layer separation. Part 2. Unsteady interacting boundary-layer theory. *J. Fluid Mech.* **232**, 133-165.

[153] Pfenninger, W. (1947). Investigations on reductions of friction on wings, in particular by means of boundary layer suction. *NACA TM 1181.*

[154] Pfenninger, W., Gross, L. and Bacon, J. W. Jr. (1957). Experiments on a 30° swept 12% thick symmetrical laminar section in the 5ft by 7ft Michigan tunnel. *Northrop Aircraft Inc. Rep. NAI-57-317* (BLC-93).

[155] Pfenninger, W. (1965) Some results from the X-21A program. Part I. Flow phenomenon at the leading edge of swept of swept wings. *AGARDograph 97.*

[156] Pfenninger, W. and Bacon, J.W. (1969). Amplified laminar boundary-layer oscillation and transition at the front attachment-line of a 45° swept flat-nosed wing with and without suction. In *Viscous Drag Reduction* (Ed. C.S. Wells), 85-105, Plenum Press.

[157] Poll, D.I.A. (1979). Transition in the infinite swept attachment-line boundary layer. Aero. Quart, **30**, 607-629.

[158] Poll, D.I.A. (1985) Some observations of the transition process on the windward face of a long yawed cylinder. *J. Fluid Mech.*, **150**, 329-356.

[159] Poll, D.I.A., Danks, M. and Yardley, M. (1996). The effects of suction and blowing on stability and transition at a swept attachment-line. In *Transitional Boundary Layers in Aeronautics* (Eds.: R. Henkes & J. Van Ingen), Elsevier, Amsterdam, Holland.

[160] Prandtl, L. (1935). In *Aerodynamic Theory* (ed. W.F. Durand) **3**, 178-190. Springer, Berlin.

[161] Prandtl, L. (1946). On boundary layers in three-dimensions. Rept. Aero. Res. Council, London No. 9828.

[162] Provansal, M., Mathis, C. and Boyer, L. (1987). Benard-von Karman instability: transient and forced regimes. *J. Fluid Mech.*, **182**, 1-22.

[163] Rayleigh, L. (1880). On the stability or instability of certain fluid motions. In *Scientific Papers*. **1**, 361-371.

[164] Rayleigh, L. (1887). On the stability or instability of certain fluid motions. In *Scientific Papers*. **3**, 17-23.

[165] Reynolds, O. (1883). An experimental investigation of the circumstances which determine whether the motion of water shall be direct or sinuous and of the law of resistance in parallel channels. *Phil. Trans. Roy. Soc.*, **174**, 935-982.

[166] Robertson, J.M. (1969). *Hydrodynamics in Theory and Application*. Dover Publication, New York.

[167] Robertson, G.E., Seinfeld, J.H. and Leal, L.G. (1973). Combined forced and free convection flow past a horizontal flat plate, *AIChE*, **19(5)**:998-1008.

[168] Robinson, S.K. (1991). Coherent motions in the turbulent boundary layer. *Ann. Rev. Fluid Mech.* **23**, 601-639.

[169] Rogler, H.L. and Reshotko, E. (1975). Disturbances in a boundary layer introduced by a low intensity array of vortices. *SIAM J. Appl. Maths*. **28**, 431-462.

[170] Roshko A. (1954). On the drag and shedding frequency of two-dimensional bluff bodies. *NACA TN. 3169*.

[171] Ruban, A.I. (1985). On the generation of Tollmien- Schlichting waves by sound. *Fluid Dyn.*, **19**, 709-716.

[172] Saric, W.S. and Yeates, L.G. (1985). Experiments on the stability of crossflow vortices in swept-wing flows. *AIAA Pap. No.* 85-0493.

[173] Saric, W.S., White, E.B. and Reed, H.L. (1999). Boundary-layer receptivity to freestream disturbances and its role in transition. *AIAA-99-3788*.

[174] Schlichting, H. (1933). Zur entstehung der turbulenz bei der plattenströmung. *Nach. Gesell. d. Wiss. z. Gött., MPK*, 181-208.

[175] Schlichting, H. (1935). Amplitudenverteilung und energiebilanz der kleinen storungen bei der plattenströmung. *Nach. Gesell. d. Wiss. z. Gött., MPK*, **1**, 47-78.

[176] Schlichting, H. (1979). *Boundary Layer Theory*, McGraw Hill, New York, USA.

[177] Schmid, P.J. (2000). Linear stability theory and bypass transition in shear flows. *Phys. Plasmas.* **7**, 1788.

[178] Schmid, P.J. and Henningson, D.S. (2001). *Stability and Transition in Shear Flow.* Springer Verlag, New York.

[179] Schneider, W. (1979). A similarity solution for combined forced and free convection flow over a horizontal plate, *Int. J. Heat Mass Transfer* **22**:1401-1406.

[180] Schubauer, G.B. and Skramstad, H.K. (1947). Laminar boundary layer oscillations and the stability of laminar flow, *J. Aero. Sci.* **14(2)**:69-78.

[181] Scott, M.R. and Watts, H.A. (1977). Computational solution of linear two point boundary value problems via orthonormalization. *SIAM J. Num. Analysis.* **14**, 40.

[182] Sengupta, T.K. (1991). Impulse response of laminar boundary layer and receptivity. In *Proc. Of* 7^{th} *Inter. Conf. on Numerical Meth. for Laminar and Turbulent Layers.* (Ed. C.Taylor).

[183] Sengupta, T.K. (1992). Solution of the Orr-Sommerfeld equation for high wave numbers. *Comput. and Fluids*, **21(2)**, 302-304.

[184] Sengupta, T.K., Ballav, M. and Nijhawan, S. (1994). Generation of Tollmien-Schlichting waves by harmonic excitation. *Physics Fluids*, **6(3)**, 1213-1222.

[185] Sengupta, T.K., Chattopadhyay, M., Wang, Z-Y. and Yeo, K.S.(2002) By-pass mechanism of transition to turbulence. *J. Fluid Struct.*, **16**, 15-29.

[186] Sengupta, T.K., Chaturvedi, V., Kumar, P. and De, S. (2004). Computation of leading edge contamination. *Comput. Fluids.* **33**, 927-951.

[187] Sengupta, T.K., De, S. and Sarkar, S. (2003). Vortex-induced instability of an incompressible wall-bounded shear layer. *J. Fluid Mech.* **493**, 277-286.

[188] Sengupta, T.K. and De, S (2004). Proper orthogonal decomposition of direct numerical simulation data of by-pass transition. *Comput. Struct.* **82**, 2693-2703.

[189] Sengupta, T.K. and Dipankar, A. (2005). Subcritical instability on the attachment-line of an infinite swept wing. *J. Fluid Mech.* **529**, 147-171.

[190] Sengupta, T.K., Ganeriwal, G and De, S.(2003a). Analysis of central and upwind compact schemes. *J. Comp. Phys.* **192**, 677-694.

[191] Sengupta, T.K., Guntaka, A. and Dey, S. (2004a). Navier-Stokes solution by new compact scheme for incompressible flows. *J. Sci. Comput.* **21**, 269-282.

[192] Sengupta, T.K., Kameswara Rao, A. and Venkatasubbaiah, K. (2006a). Spatio-temporal growth of disturbances in a boundary layer and energy based receptivity analysis. *Physics of Fluids*, **18**, 094101.

[193] Sengupta, T.K., Kameswara Rao, A. and Venkatasubbaiah, K. (2006). Spatiotemporal growing wave fronts in spatially stable boundary layer. *Phys. Rev. Letters*, **96**, 224504.

[194] Sengupta, T.K., Lim, T.T. and Chattopadhyay, M. (2001). An experimental and theoretical investigation of a by-pass transition mechanism. *IIT Kanpur Rept. No. IITK/Aero/AD/2001/02.*

[195] Sengupta, T.K. and Nair, M.T. (1997). A new class of waves for Blasius boundary layer. In Proc. 7^{th} *Asian Cong. Fluid Mech.* 785-788, Allied Publishers, Chennai, India.

[196] Sengupta, T.K., Nair, M.T. and Rana, V. (1997). Boundary layer excited by low frequency disturbances- Klebanoff mode. *J. Fluids Struct.*, **11**, 845-853.

[197] Sengupta, T.K. and Rao, A.K. (2006). Spatio-temporal receptivity of boundary-layers by Bromwich contour integral method. In Proc. Boundary And Interior Layers (BAIL 2006) held at Goettingen, Germany (eds. G. Lube and G. Rapin).

[198] Sengupta, T.K. and Sinha, A.P. (1995). Surface mass transfer: A receptivity mechanism for boundary-layers. In *Proc.* 6^{th} *Asian Cong. Fluid Mech.*, (Eds. Y.T. Chew and C.P. Tso), 1242-1245.

[199] Sengupta, T.K., Sircar, S.K. and Dipankar, A. (2006b). High accuracy compact schemes for DNS and acoustics. *J. Sci. Comput.* **26(2)**, 151-193.

[200] Sengupta, T.K. and Venkatasubbaiah, K. (2006). Spatial stability for mixed convection boundary layer over a heated horizontal plate. *Stud. In Appl. Math.*, **117**, 265-298.

[201] Sengupta, T.K., Wang, Z-Y., Pin, L.Y. and Chattopadhyay, M. (1999). Receptivity to stationary pulsating vortex. In *Proc.* 8^{th} *Asian Cong. Fluid Mech.* (Ed.: E Cui), 959-963.

[202] Sengupta, T.K., Wang, Z-Y., Yeo, K.S. and Chattopadhyay, M. (1999). Receptivity to convected vortices- by-pass route. In *Proc.* 8^{th} *Asian Cong. Fluid Mech.* (Ed.: E Cui), 964-968.

[203] Sewall, W.G., McGhee, R.J., Hahne, D.E. and Jordan, F.L. (1987). Wind tunnel results of the high-speed NLF(1)-0213 airfoil. *NASA CP 2487*, Part 3, 697-726.

[204] Shaukatullah, H. and Gebhart, B. (1978). An experimental investigation of natural convection flow on an inclined surface, *Int. J. Heat Mass Transfer* **21**:1481-1490.

[205] Shu, C. and Chew, Y.T. (1998). On the equivalence of generalized differential quadrature and highest order finite difference scheme. *Comp. Meth. Appl. Mech. Engg.*, **155**, 249-260.

[206] Sirovich, L. (1987). Turbulence and the dynamics of coherent structures. Part I-III. *Quart. J. Appl. Math.* **45(3)**, 561-590.

[207] Smith, A.M.O. and Gamberoni, N. (1956). Transition, pressure gradient and stability theory. *Douglas Aircraft Rept. No. ES-26338.*

[208] Smith, C.R. (1993). Use of 'Kernel' experiments for modeling of near-wall turbulence. In *Near Wall Turbulent Flows* (Eds. R.M.C. So, C.G. Speziale and B.E. Launders), pp 33-42. Elsevier, Amsterdam, Holland.

[209] Smith, C.R., Walker, J.D.A, Haidari, A.H. and Soburn, U. (1991). On the dynamics of near-wall turbulence. *Phil. Trans. R. Soc. Lond. A* **336**, 131-175.

[210] Sommerfeld, A.(1908). Ein Beitrag zur hydrodynamiscen Erklarung der turbulenten Flussigkeitsbewegung. In *Proc.* 4^{th} *Int. Cong. Mathematicians*, Rome, 116-124.

[211] Sommerfeld, A. (1949). *Partial Differential Equation in Physics.* Academic Press, New York.

[212] Spalart, P. (1988). Direct numerical study of leading edge contamination. *AGARD CP **438**, 5.1-5.13.*

[213] Spangler, J.G. and Wells, C.S. Jr. (1968). Effect of freestream disturbances on boundary layer transition. *AIAA J.* **6**, 534-545.

[214] Sparks, S.P. and Miley, S.J. (1983). Development of a propeller afterbody analysis with contracting slipstream. *SAE TP 830743.*

[215] Sparrow, E.M. and Husar, R.B. (1969). Longitudinal vortices in natural convection flow on inclined plates, *J. Fluid Mech.* **37**:251-255.

[216] Sparrow, E.M. and Minkowycz, W.J. (1962). Buoyancy effects on horizontal boundary-layer flow and heat transfer, *Int. J. Heat Mass Transfer*, **5**:505-511.

[217] Srokowski, A.J. and Orszag, S.A. (1977). Mass flow requirements for LFC wing design. *AIAA Paper No.* **77-1222**.

[218] Steinruck, H. (1994). Mixed convection over a cooled horizontal plate: Non-uniqueness and numerical instabilities of the boundary layer equations, *J. Fluid Mech.* **278**:251-265.

[219] Stratford, B.S. (1959). The prediction of separation of the turbulent boundary. *J. Fluid Mech.*, **5**(1), 1-16.

[220] Strykowski, P.J., and Sreenivasan, K.R. (1990).On the formation and suppression of vortex shedding at low Reynolds number. *J. Fluid Mech.*, **218**, 74-104.

[221] Stuart, J.T. (1953). The basic theory of the stability of three-dimensional boundary layer. *ARC 15904*.
[222] Stuart, J.T. (1963). in *Laminar Boundary Layer*. (Ed. L. Rosenhead). Clarendon Press, Oxford, U.K.
[223] Tam, C.K.W. (1971). Directional acoustic radiation from a supersonic jet generated by shear layer instability. *J. Fluid Mech.*, **46**, 757-768.
[224] Tani, I. (1952). On the design of airfoils in which the transition of the boundary layer is delayed. *NACA TM* 1351.
[225] Taylor, G.I. (1936). Statistical theory of turbulence. V Effects of turbulence on boundary layer. *Proc. Roy. Soc. A* 156, no. 888, 307-317.
[226] Taylor, G.I. (1939). Some recent developmetns in the study of turbulence. In *Proc. V^{th} International Con. for Applied Mech.* (eds. J.P. Den Hartog and H. Peters).
[227] Theofilis, V. (1998). On linear and non-linear instability of the incompressible swept attachment-line boundary layer. *J. Fluid Mech.* **355**, 193-227.
[228] Theofilis, V., Fedorov, A., Obrist, D. and Dallmann, U. (2003). The extended Goertler-Haemmerlin model for linear instability of three-dimensional incompressible swept attachment-line boundary layer flow. *J. Fluid Mech.* **487**, 271-313.
[229] Tokumaru, P.T. and Dimotakis, P.E. (1993). The lift of a cylinder rotary motion in a uniform flow. *J. Fluid Mech.* **255**, 1-10.
[230] Tollmien, W. (1931). The production of turbulence. *NACA TM* 609.
[231] Trefethen, L.N., Trefethen, A.E., Reddy, S.C. and Driscoll, T.A. (1993). Hydrodynamic stability without eigenvalues. *Science*, **261**, (5121), 578-584.
[232] Tritton, D.J. (1970). A note on vortex streets behind circular cylinders at low Reynolds numbers. *J. Fluid Mech.* **45(1)**, 203-208.
[233] Tropea, C., Yarin, A.L. and Foss, J.F. (2007). *Springer Handbook of Experimental Fluid Mechanics*. Springer Verlag, Berlin.
[234] Tumin, A. (2003). The spatial stability of natural convection flow on inclined plates, *ASME J.Fluid Engg.* **125**:428-437.
[235] Vander Pol, B. and Bremmer, H. (1959). *Operational Calculus Based on Two-Sided Laplace Integral*, Cambridge University Press, U.K.
[236] Van Driest, E.R. (1951). Turbulent boundary layer in compressible fluids. *J. Aero. Sci.* **18**, 145-160.
[237] Van Ingen, J.L. (1956). A suggested semi-empirical method for the calculation of the boundary layer transition region. *Inst. Of Technology, Dept. of Aeronautics and Engg.Rept. VTH-74*.
[238] Viken, J.K. (1983). Aerodynamic design considerations and theoritical results for a high Reynolds number natural laminar flow airfoil. M.S. Thesis. *The School of Engineering and Applied Science, George Washington Univ, USA*.

[239] Wang, X.A. (1982). An experimental study of mixed, forced, and free convection heat transfer from a horizontal flat plate to air, *ASME J. Heat Transfer* **104**:139-144.

[240] Wazzan, A.R., Gazley, C. Jr. and Smith, A.M.O. (1981). H - R, method for predicting transition. *AIAA J.*, **19**(6), 109-114

[241] Wells, C.S. Jr. (1967). Effects of freestream turbulence on boundary layer transition. *AIAA J.*, **5(1)**, 172-174.

[242] White, F.M. (1991). *Viscous Fluid Flow*, McGraw Hill Int. Edn., New York.

[243] Wiesenfeld, K. and McNamara, B. (1986). Small-signal ampllification in bifurcating dynamical systems. *Physical Review* A **33(1)**, 629-642.

[244] Williamson, C.H.K. (1989). Oblique and parallel modes of vortex shedding in the wake of a circular cylinder at low Reynold numbers. *J. Fluid Mech.* **206**, 579-627.

[245] Wu, R.S. and Cheng, K.C. (1976). Thermal instability of Blasius flow along horizontal plates, *Int. J. Heat Mass Transfer* **19**:907-913.

[246] Wu, X., Jacobs, R.G., Hunt, J.C.R. and Durbin, P.A. (1999). Simulation of boundary layer transition induced by periodically passing wakes. *J. Fluid Mech.* **399**, 109-153.

[247] Zebib, A. (1987). Stability of viscous flow past a circular cylinder. *J. Eng. Math.* **21**, 155-165.

[248] Zuccher, S., Bottaro, A. and Luchini, P. (2006). Algebraic growth in a Blasius boundary layer. *Eur. J. Mech. B/Fluids.* 25,1.

[249] Zuercher, E.J., Jacobs, J.W. and Chen, C.F. (1998). Experimental study of the stability of boundary-layer flow along a heated inclined plate, *J. Fluid Mech.* ***367****:1-25.*

[250] S. S. Abarbanel and A. E. Chertock. Strict stability of high-order compact implicit finite-difference schemes: the role of boundary conditions for hyperbolic PDEs, I. *J. Comput. Phys.*, 160:42–66, 2000.

[251] R. G. Abdel-Gayed, D. Bradley, M. N. Hamid, and M. Lawes. Lewis number effects on turbulent burning velocity. *Proc. Combust. Inst.*, 20: 505–512, 1984.

[252] K. Akselvoll and P. Moin. Large eddy simulation of a backward facing step flow. In W. Rodi and F. Martelli, editors, *Proc. of the 2nd International Symposium on Eng. Turb. Modelling and Exp.*, volume 2, pages 303–313. Elsevier, 1993.

[253] V. M. Alipchenkov and L. I. Zaichik. Modeling of the turbulent motion of particles in a vertical channel. *J. Fluid Dynamics*, 41(4), 2006.

[254] C. Angelberger, D. Veynante, F. Egolfopoulos, and T. Poinsot. Large eddy simulations of combustion instabilities in premixed flames. In *Proc. of the Summer Program*, pages 61–82. Center for Turbulence Research, NASA Ames/Stanford Univ., 1998.

[255] S. V. Apte, M. Gorokhovski, and P. Moin. Large-eddy simulation of atomizing spray with stochastic modeling of secondary breakup. *Int. J. Multiphase Flow*, 29:1503–1522, 2003.

[256] S. V. Apte, K. Mahesh, P. Moin, and J. C. Oefelein. Large-eddy simulation of swirling particle-laden flows in a coaxial-jet combustor. *Int. J. Multiphase Flow*, 29(8):1311–1331, 2003.

[257] H. Aref. Integrable, chaotic and turbulent vortex motion in two-dimensional flows. *Ann. Rev. Fluid Mech.*, 15:345–389, 1983.

[258] L. Benoit and F. Nicoud. Numerical assessment of thermo-acoustic instabilities in gas turbines. *Int. J. Numer. Meth. Fluids*, 47(8-9):849–855, 2005.

[259] M. Benson, T. Tanaka, and J. K. Eaton. Effects of wall roughness on particle velocities in a turbulent channel flow. *J. Fluids Eng.*, 127(2): 250–256, 2005.

[260] P. Billant, J.-M. Chomaz, and P. Huerre. Experimental study of vortex breakdown in swirling jets. *J. Fluid Mech.*, 376:183–219, 1998.

[261] M. Boger, D. Veynante, H. Boughanem, and A. Trouvé. Direct numerical simulation analysis of flame surface density concept for large eddy simulation of turbulent premixed combustion. In *27th Symp. (Int.) on Combustion*, pages 917–927, Boulder, 1998. The Combustion Institute, Pittsburgh.

[262] M. Boivin, O. Simonin, and K. D. Squires. On the prediction of gas-solid flows with two-way coupling using large eddy simulation. *Phys. Fluids*, 12(8):2080–2090, 2000.

[263] S. Candel. Combustion instabilities coupled by pressure waves and their active control. In *24th Symp. (Int.) on Combustion*, pages 1277–1296. The Combustion Institute, Pittsburgh, 1992.

[264] F. Chaitin-Chatelin and V. Frayssé. *Lectures on Finite Precision Computations*. SIAM, Philadelphia, 1996.

[265] S. Chapman and T. G. Cowling. *The Mathematical Theory of Non-Uniform Gases*. Cambridge University Press, cambridge mathematical library edition, 1939 (digital reprint 1999).

[266] P. Clavin. Dynamics of combustion fronts in premixed gases: from flames to detonations. *Proc. Combust. Inst.*, 28:569–586, 2000.

[267] C. M. Coats. Coherent structures in combustion. *Prog. Energy Comb. Sci.*, 22:427 – 509, 1996.

[268] O. Colin and M. Rudgyard. Development of high-order taylor-galerkin schemes for unsteady calculations. *J. Comput. Phys.*, 162(2):338–371, 2000.

[269] O. Colin, F. Ducros, D. Veynante, and T. Poinsot. A thickened flame model for large eddy simulations of turbulent premixed combustion. *Phys. Fluids*, 12(7):1843–1863, 2000.

[270] D. G. Crighton, A. P. Dowling, J. E. Ffowcs Williams, M. Heckl, and F. Leppington. *Modern methods in analytical acoustics*. Lecture Notes. Springer Verlag, New-York, 1992.

[271] E. Cuthill and J. McKee. Reducing the bandwidth of sparse symmetric matrices. In *Proceedings of the 24th National Conference of the ACM*, pages 157–172, 1969.

[272] A. K. Das. *Computational fluid dynamics simulation of gas-solid risers: reactive flow modelling*. Phd thesis, Universiteit Gent, 2002.

[273] P. G. Drazin and W. H. Reid. *Hydrodynamic stability*. Cambridge University Press, London, 1981.

[274] O. A. Druzhinin and S. Elghobashi. On the decay rate of isotropic turbulence laden with microparticles. *Phys. Fluids*, 11(3):602–610, 1999.

[275] C. Duwig, L. Fuchs, P. Griebel, P. Siewert, and E. Boschek. Study of a confined jurbulent jet: influence of combustion and pressure. *AIAA Journal*, 45(3):624–661, 2007.

[276] H. El-Asrag and S. Menon. Large eddy simulation of bluff-body stabilized swirling non-premixed flames. *Proc. Combust. Inst.*, 31:1747–1754, 2007.

[277] H. Enwald, E. Peirano, and A.-E. Almstedt. Eulerian two-phase flow theory applied to fluidization. *Int. J. Multiphase Flow*, 22:21–66, 1996.

[278] P. Fede, O. Simonin, P. Villedieu, and K. D. Squires. Stochastic modeling of the turbulent subgrid fluid velocity along inertial particle trajectories. In *Proc. of the Summer Program*, pages 247–258. Center for Turbulence Research, NASA Ames/Stanford Univ., 2006.

[279] P. Fede, O. Simonin, and L. Zaichik. Pdf approach for the collision modelling in binary mixture of particles. In *Symp. on Fluid-particle Interactions in Turbulence*. ASME-FED, 2006.

[280] P. Février, O. Simonin, and K. Squires. Partitioning of particle velocities in gas-solid turbulent flows into a continuous field and a spatially uncorrelated random distribution: Theoretical formalism and numerical study. *J. Fluid Mech.*, 533:1–46, 2005.

[281] V. Fraysse, L. Giraud, and S. Gratton. A set of flexible-gmres routines for real and complex arithmetics. Technical Report TR/PA/98/20, CERFACS, 1998.

[282] M. Freitag and J. Janicka. Investigation of a strongly swirled premixed flame using les. *Proc. Combust. Inst.*, 31:1477–1485, 2007.

[283] F. Gao. A large-eddy simulation scheme for turbulent reacting flows. *Phys. Fluids*, 5(6):1282–1284, 1993.

[284] J. Gao, C. Xu, S. Lin, and G. Yang. Simulations of gas-liquid-solid 3-phase flow and reaction in FCC riser reactors. *AIChE Journal*, 47(3): 677–692, 2001.

[285] A. Giauque, L. Selle, T. Poinsot, H. Buechner, P. Kaufmann, and W. Krebs. System identification of a large-scale swirled partially premixed combustor using LES and measurements. *J. Turb.*, 6(21):1–20, 2005.

[286] P. Givi. Model-free simulations of turbulent reactive flows. *Prog. Energy Comb. Sci.*, 15:1–107, 1989.

[287] P. Givi. Spectral and random vortex methods in turbulent reacting flows. In F. Williams and Libby P., editors, *Turbulent Reacting Flows*, pages 475–572. Academic Press, 1994.

[288] I. Glassman. *Combustion*. Academic Press, New York, 1987.

[289] A. Gobin, H. Neau, O. Simonin, J.-R. Linas, V. Reiling, and J.-L. Sélo. Fluid dynamic numerical simulation of a gas phase polymerization reactor. *Int. J. Numer. Meth. Fluids*, 43:1199–1220, 2003.

[290] I. Gökalp, C. Chauveau, C. Morin, B. Vieille, and M. Birouk. Improving droplet breakup and vaporization models by including high pressure and turbulence effects. *Atomization and Sprays*, 10:475–510, 2000.

[291] O. Gulder. Turbulent premixed flame propagation models for different combustion regimes. In *23rd Symp. (Int.) on Comb.*, pages 743–835, Orleans, 1990. The Combustion Institute, Pittsburgh.

[292] F. Ham, S. V. Apte, G. Iaccarino, X. Wu, M. Herrmann, G. Constantinescu, K. Mahesh, and P. Moin. Unstructured LES of reacting multiphase flows in realistic gas turbine combustors. In *Annual Research Briefs*, pages 139–160. Center for Turbulence Research, NASA Ames/Stanford Univ., 2003.

[293] Z. Han, S. Parrish, P. V. Farrell, and R. D. Reitz. Modeling atomization processes of pressure-swirl hollow-cone fuel sprays. *Atomization and Sprays*, 7(6):663–684, 1997.

[294] G. Hanrot, V. Lefèvre, D. Stehlé, and P. Zimmermann. Worst cases for a periodic function with large arguments. In Peter Kornerup and Jean-Michel Muller, editors, *Proceedings of the 18th IEEE Symposium on Computer Arithmetic*, pages 133–140, Los Alamitos, CA, 2007. IEEE Computer Society Press.

[295] J. R. Herring, S. A. Orszag, and R. H. Kraichnan. Decay of two-dimensional homogeneous turbulence. *J. Fluid Mech.*, 66:417–444, 1974.

[296] C. Hirsch. *Numerical Computation of Internal and External Flows*. John Wiley, New York, 1988.

[297] C. M. Ho and P. Huerre. Perturbed free shear layers. *J. Fluid Mech.*, 16:365, 1984.

[298] F. Hussain and J. Jeong. On the identification of a vortex. *J. Fluid Mech.*, 285:69–94, 1995.

[299] J. Jiménez. Turbulence and vortex dynamics. Technical Report Ecole Polytechnique, 2004.

[300] K. Kailasanath, J. H. Gardner, E. S. Oran, and J. P. Boris. Numerical simulations of unsteady reactive flows in a combustion chamber. *Combust. Flame*, 86:115–134, 1991.

[301] A. Kaufmann. *Vers la simulation des grandes échelles en formulation Euler/Euler des écoulements réactifs diphasiques*. Phd thesis, INP Toulouse, 2004.

[302] A. Kaufmann, O. Simonin, T. Poinsot, and J. Hélie. Dynamics and dispersion in Eulerian-Eulerian DNS of two-phase flows. In *Proc. of the Summer Program*, pages 381–392. Center for Turbulence Research, NASA Ames/Stanford Univ., 2002.

[303] A. R. Kerstein, W. Ashurst, and F. A. Williams. Field equation for interface propagation in an unsteady homogeneous flow field. *Phys. Rev. A*, 37(7):2728–2731, 1988.

[304] L. E. Kinsler, A. R. Frey, A. B. Coppens, and J. V. Sanders. *Fundamental of Acoustics*. John Wiley, 1982.

[305] W. Krebs, P. Flohr, B. Prade, and S. Hoffmann. Thermoacoustic stability chart for high intense gas turbine combustion systems. *Combust. Sci. Tech.*, 174:99–128, 2002.

[306] K. K. Kuo. *Principles of Combustion*. John Wiley, New York, 1986.

[307] P. Laffitte. *La propagation des flammes dans les melanges gazeux*. Hermann et Cie, Actualites scientifiques et industrielles, PARIS, 1939.

[308] G. Lartigue. *Simulation aux grandes échelles de la combustion turbulente*. Phd thesis, INP Toulouse, 2004.

[309] J. C. Lasheras and E. J. Hopfinger. Liquid jet instability and atomisation in a coaxial gas stream. *Ann. Rev. Fluid Mech.*, 32:275–308, 2000.

[310] A. H. Lefebvre. *Gas Turbines Combustion*. Taylor & Francis, 1999.

[311] J.-Ph. Légier, T. Poinsot, and D. Veynante. Dynamically thickened flame LES model for premixed and non-premixed turbulent combustion. In *Proc. of the Summer Program*, pages 157–168. Center for Turbulence Research, NASA Ames/Stanford Univ., 2000.

[312] S.K. Lele. Compact finite difference schemes with spectral like resolution. *J. Comput. Phys.*, 103:16–42, 1992.

[313] T. Lieuwen and V. Yang. Combustion instabilities in gas turbine engines. operational experience, fundamental mechanisms and modeling. In *Prog. in Astronautics and AeronauticsAIAA*, volume 210, 2005.

[314] W.-H. Liu and A. H. Sherman. Comparative analysis of the cuthill-mckee and the reverse cuthill-mckee ordering algorithms for sparse matrices. *SIAM Journal of Numerical Analysis*, 13(2):198–213, 1976.

[315] E. N. Lorenz. Deterministic nonperiodic flow. *J. Atmos. Sci.*, 20: 130–141, 1963.

[316] O. Lucca-Negro and T. O'Doherty. Vortex breakdown: a review. *Prog. Energy Comb. Sci.*, 27:431–481, 2001.

[317] K. Mahesh, G. Constantinescu, S. Apte, G. Iaccarino, F. Ham, and P. Moin. Progress toward large-eddy simulation of turbulent reacting and non-reacting flows in complex geometries. In *Annual Research Briefs*, pages 115–142. Center for Turbulence Research, NASA Ames/Stanford Univ., 2002.

[318] K. Mahesh, G. Constantinescu, and P. Moin. A numerical method for large-eddy simulation in complex geometries. *J. Comput. Phys.*, 197 (1):215–240, 2004. ISSN 0021-9991.

[319] C. Marchioli, M. Picciotto, and A. Soldati. Particle dispersion and wall-dependent fluid scales in turbulent bounded flow: Implications for local equilibrium models. *J. Turb.*, 7(60):1–12, 2006.

[320] C. Martin, L. Benoit, F. Nicoud, and T. Poinsot. Analysis of acoustic energy and modes in a turbulent swirled combustor. In *Proc. of the Summer Program*, pages 377–394. Center for Turbulence Research, NASA Ames/Stanford Univ., 2004.

[321] C. Martin, L. Benoit, Y. Sommerer, F. Nicoud, and T. Poinsot. Les and acoustic analysis of combustion instability in a staged turbulent swirled combustor. *AIAA Journal*, 44(4):741–750, 2006.

[322] K. McManus, T. Poinsot, and S. Candel. A review of active control of combustion instabilities. *Prog. Energy Comb. Sci.*, 19:1–29, 1993.

[323] S. Menon, P. A. McMurthy, and A. R. Kerstein. A linear eddy mixing model for large eddy simulation of turbulent combustion. In B. Galperin and S.A. Orzag, editors, *Large eddy simulation of complex engineering and geophysical flows*, pages 87 – 314. Cambridge University Press, 1993.

[324] P. Moin. Large eddy simulation of multi-phase turbulent flows in realistic combustors. *Prog. Comput. Fluid Dynamics*, 4:237–240, 2004.

[325] P. Moin and J. Kim. Numerical investigation of turbulent channel flow. *J. Fluid Mech.*, 118:341–377, 1982.

[326] P. Moin and K. Mahesh. Dns: a tool in turbulence research. *Ann. Rev. Fluid Mech.*, 30:539–578, 1998.

[327] P. Moin, K. D. Squires, W. Cabot, and S. Lee. A dynamic subgrid-scale model for compressible turbulence and scalar transport. *Phys. Fluids*, A 3(11):2746–2757, 1991.

[328] M. Moreau, B. Bédat, and O. Simonin. A priori testing of subgrid stress models for euler-euler two-phase LES from euler-lagrange simulations of gas-particle turbulent flow. In *18th Ann. Conf. on Liquid Atomization and Spray Systems*. ILASS Americas, 2005.

[329] V. Moureau, G. Lartigue, Y. Sommerer, C. Angelberger, O. Colin, and T. Poinsot. High-order methods for DNS and LES of compressible multi-component reacting flows on fixed and moving grids. *J. Comput. Phys.*, 202(2):710–736, 2005.

[330] F. Nicoud and F. Ducros. Subgrid-scale stress modelling based on the square of the velocity gradient. *Flow, Turb. and Combustion*, 62(3): 183–200, 1999.

[331] F. Nicoud, L. Benoit, and C. Sensiau. Acoustic modes in combustors with complex impedances and multidimensional active flames. *AIAA Journal*, 45:426–441, 2007.

[332] S. Nukiyama and Y. Tanasawa. Experiments in on the atomization of liquids in air stream. report 3: on the droplet-size distribution in an atomized jet. *Trans. Soc. Mech. Eng. Japan*, 5:62–67, 1939.

[333] B. Oesterlé and L. I. Zaichik. On lagrangian time scales and particle dispersion modeling in equilibrium turbulent shear flows. *Phys. Fluids*, 16(9):3374–3384, 2004.

[334] E. S. Oran and J. P. Boris. *Numerical simulation of reactive flow. 2nd edition.* Cambridge University Press, New-York, 2001.

[335] E. Peirano and B. Leckner. Fundamentals of turbulent gas-solid flows applied to circulating fluidized bed combustion. *Prog. Energy Comb. Sci.*, 24:259–296, 1998.

[336] A. D. Pierce. *Acoustics: an introduction to its physical principles and applications.* McGraw Hill, New York, 1981.

[337] C. D. Pierce and P. Moin. Progress-variable approach for large eddy simulation of non-premixed turbulent combustion. *J. Fluid Mech.*, 504: 73–97, 2004.

[338] H. Pitsch. Large eddy simulation of turbulent combustion. *Ann. Rev. Fluid Mech.*, 38:453–482, 2006.

[339] T. Poinsot and S. Lele. Boundary conditions for direct simulations of compressible viscous flows. *J. Comput. Phys.*, 101(1):104–129, 1992.

[340] T. Poinsot and D. Veynante. *Theoretical and Numerical Combustion.* R.T. Edwards, 2nd edition., 2005.

[341] T. Poinsot, A. Trouvé, D. Veynante, S. Candel, and E. Esposito. Vortex driven acoustically coupled combustion instabilities. *J. Fluid Mech.*, 177:265–292, 1987.

[342] T. Poinsot, S. Candel, and A. Trouvé. Application of direct numerical simulation to premixed turbulent combustion. *Prog. Energy Comb. Sci.*, 21:531–576, 1996.

[343] S. B. Pope. Ten questions concerning the large-eddy simulation of turbulent flows. *New Journal of Physics*, 6:35, 2004.

[344] L. Rayleigh. The explanation of certain acoustic phenomena. *Nature*, July 18:319–321, 1878.

[345] R. D. Reitz and F. V. Bracco. Mechanism of atomization of a liquid jet. *Phys. Fluids*, 25(10):1730–1742, 1982.

[346] E. Riber. *Développement de la méthode de simulation aux grandes échelles pour les écoulements diphasiques turbulents*. Phd thesis, INP Toulouse, 2007.

[347] E. Riber, M. Moreau, O. Simonin, and B. Cuenot. Towards large eddy simulation of non-homogeneous particle laden turbulent gas flows using euler-euler approach. In *11th Workshop on Two-Phase Flow Predictions*, Merseburg, Germany, 2005.

[348] E. Riber, M. García., V. Moureau, H. Pitsch, O. Simonin, and T. Poinsot. Evaluation of numerical strategies for LES of two-phase reacting flows. In *Proc. of the Summer Program*, pages 197–211. Center for Turbulence Research, NASA Ames/Stanford Univ., 2006.

[349] S. Richard, O. Colin, O. Vermorel, A. Benkenida, C. Angelberger, and D. Veynante. Towards large eddy simulation of combustion in spark ignition engines. *Proc. Combust. Inst.*, 31(3059-3066), 2007.

[350] S. Roux, G. Lartigue, T. Poinsot, U. Meier, and C. Bérat. Studies of mean and unsteady flow in a swirled combustor using experiments, acoustic analysis and large eddy simulations. *Combust. Flame*, 141: 40–54, 2005.

[351] Y. Saad. A flexible inner-outer preconditioned gmres algorithm. *SIAM J. Sci. Comput.*, 14:461–469, 1993.

[352] P. Sagaut. *Large eddy simulation for incompressible flows*. Springer, 2002.

[353] J.-M. Samaniego, B. Yip, T. Poinsot, and S. Candel. Low-frequency combustion instability mechanism in a side-dump combustor. *Combust. Flame*, 94(4):363–381, 1993.

[354] V. Sankaran and S. Menon. Les of spray combustion in swirling flows. *J. Turb.*, 3:011, 2002.

[355] P. Schmitt, T. J. Poinsot, B. Schuermans, and K. Geigle. Large-eddy simulation and experimental study of heat transfer, nitric oxide emissions and combustion instability in a swirled turbulent high pressure burner. *J. Fluid Mech.*, 570:17–46, 2007.

[356] T. Schönfeld and M. Rudgyard. Steady and unsteady flows simulations using the hybrid flow solver avbp. *AIAA Journal*, 37(11):1378–1385, 1999.

[357] L. Selle. *Simulation aux grandes échelles des interactions flamme-acoustique dans un écoulement vrillé*. Phd thesis, INP Toulouse, 2004. URL `http://www.cerfacs.fr/ cfdbib/repository/TH_CFD_04_35.pdf`.

[358] L. Selle, G. Lartigue, T. Poinsot, R. Koch, K.-U. Schildmacher, W. Krebs, B. Prade, P. Kaufmann, and D. Veynante. Compressible large-eddy simulation of turbulent combustion in complex geometry on unstructured meshes. *Combust. Flame*, 137(4):489–505, 2004.

[359] L. Selle, F. Nicoud, and T. Poinsot. The actual impedance of non-reflecting boundary conditions: implications for the computation of resonators. *AIAA Journal*, 42(5):958–964, 2004.

[360] L. Selle, L. Benoit, T. Poinsot, F. Nicoud, and W. Krebs. Joint use of compressible large-eddy simulation and helmoltz solvers for the analysis of rotating modes in an industrial swirled burner. *Combust. Flame*, 145 (1-2):194–205, 2006.

[361] A. Sengissen, A. Giauque, G. Staffelbach, M. Porta, W. Krebs, P. Kaufmann, and T. Poinsot. Large eddy simulation of piloting effects on turbulent swirling flames. *Proc. Combust. Inst.*, 31:1729–1736, 2007.

[362] T. K. Sengupta. *Fundamentals of Computational Fluid Dynamics*. Universities Press, Hyderabad (India), 2004.

[363] T. K. Sengupta, G. Ganerwal, and A. Dipankar. High accuracy compact schemes and gibbs' phenomenon. *J. Sci. Comput.*, 21(3):253–268, 2004.

[364] Y. Sommerer, D. Galley, T. Poinsot, S. Ducruix, F. Lacas, and D. Veynante. Large eddy simulation and experimental study of flashback and blow-off in a lean partially premixed swirled burner. *J. Turb.*, 5, 2004.

[365] M. Sommerfeld and J. Kussin. Analysis of collision effects for turbulent gas-particle flow in a horizontal channel. part ii. integral properties and validation. *Int. J. Multiphase Flow*, 29(4):701–718, 2003.

[366] D. B. Spalding. The combustion of liquid fuels. In *4th Symp. (Int.) on Combustion*, pages 847–864. The Combustion Institute, Pittsburgh, 1953.

[367] J. S. Stoer and R. Bulirsch. *An Introduction to Numerical Analysis*. Springer, Berlin, 1980.

[368] S. R. Stow and A. P. Dowling. Modelling of circumferential modal coupling due to helmholtz resonators. In *ASME Paper 2003-GT-38168*, Atlanta, Georgia, USA, 2003.

[369] N. Syred. A review of oscillation mechanims and the role of the precessing vortex core in swirl combustion systems. *Prog. Energy Comb. Sci.*, 32(2):93–161, 2006.

[370] V. E. Taylor and B. Nour-Omid. A study of the factorization fill-in for a parallel implementation of the finite element method. *Int. J. Numer. Meth. Eng.*, 37:3809–3823, 1994.

[371] H. Tennekes and J. L. Lumley. *A first course in turbulence*. M.I.T. Press, Cambridge, 1972.

[372] L. Vervisch and T. Poinsot. Direct numerical simulation of non premixed turbulent flames. *Ann. Rev. Fluid Mech.*, 30:655–692, 1998.

[373] D. Veynante and T. Poinsot. Reynolds averaged and large eddy simulation modeling for turbulent combustion. In J. Ferziger O. Metais, editor, *New tools in turbulence modelling. Lecture 5*, pages 105–135. Les editions de Physique, Springer, 1997.

[374] R. Vichnevetsky and J. B. Bowles. *Fourier analysis of numerical approximations of hyperbolic equations.* SIAM Studies in Applied Mechanics, Philadelphia, 1982.

[375] B. Vreman, B. Geurts, and H. Kuerten. Subgrid modeling in LES of compressible flow. *Appl. Sci. Res.*, 54:191–203, 1995.

[376] C. Weber and Z. Angrew. The decomposition of a liquid jet. *Math. Mech.*, 11:136–154, 1931.

[377] R. V. Wheeler. *J. Chem. Soc.*, 113:840, 1918.

[378] R. V. Wheeler. *J. Chem. Soc.*, 115:81, 1919.

[379] F. A. Williams. *Combustion Theory.* Benjamin Cummings, Menlo Park, CA, 1985.

[380] F. A. Williams. The role of theory in combustion science. In *24th Symp. (Int.) on Combustion*, pages 1–18, Sydney, 1992. The Combustion Institute, Pittsburgh.

[381] R. D. Williams. Performance of dynamic load balancing algorithms for unstructured mesh calculations. *Concurrency: Practice, and Experience*, 3(5):451–481, 1991.

[382] H. Yamashita, M. Shimada, and T. Takeno. A numerical study on flame stability at the transition point of jet diffusion flame. In *26th Symp. (Int.) on Combustion*, pages 27 – 34. The Combustion Institute, Pittsburgh, 1996.

[383] A. Yoshizawa. Statistical theory for compressible turbulent shear flows, with the application to subgrid modeling. *Phys. Fluids*, 29(7): 2152–2164, 1986.